

Synergetic Attenuation of Stray Magnetic Field in Inductive Power Transfer

Ming Lu

Dissertation submitted to the faculty of Virginia Polytechnic Institute and
State University in partial fulfillment of the requirements for the degree of

Doctor of Philosophy

In

Electrical Engineering

Khai D. T. Ngo, Chair

Guo-Quan Lu

Rolando Burgos

Majid Manteghi

Lei Zuo

June 1st, 2017

Blacksburg, Virginia

Keywords: Inductive power transfer; planar coils; high efficiency; proximity-effect loss;
magnetic field; shield; multi-objective optimization; Pareto front;

Synergetic Attenuation of Stray Magnetic Field in Inductive Power Transfer

Ming Lu

Abstract

Significant stray magnetic field exists around the coils when charging the electric vehicles (EVs) with inductive power transfer (IPT), owing to the large air gap between the transmitter and receiver. The methods for field attenuation usually introduce extra losses and reduce the efficiency. This study focuses on the synergetic attenuation of stray magnetic field which is optimized simultaneously with the efficiency. The optimization is realized with Pareto front.

In this dissertation, three methods are discussed for the field attenuation. The first method is to tune the physical parameters of the winding, such as the inner radii, outer radii, distribution of the turns, and types of the litz wires. The second method is to add metal shields around the IPT coils, in which litz wires are used as shields to reduce the shielding losses. The third method is to control the phases of winding currents, which avoids increasing the size and weight of the IPT coils.

To attenuate the stray magnetic field by tuning the physical parameters, the conventional method is to sweep all the physical parameters in finite-element simulation. This takes thousands of simulations to derive the Pareto front, and it's especially time-consuming for three-dimensional simulations. This dissertation demonstrates a faster method to derive the Pareto front. The windings are replaced by the lumped loops. As long as the number of turns for each loop is known, the efficiency and magnetic field are

calculated directly from the permeance matrices and current-to-field matrices. The sweep of physical parameters in finite-element simulation is replaced by the sweep of the turns numbers for the lumped loops in calculation. Only tens of simulations are required in the entire procedure, which are used to derive the matrices. An exemplary set of coils was built and tested. The efficiency from the matrix calculation is the same as the experimental measurement. The difference for stray magnetic field is less than 12.5%.

Metal shields attenuate the stray magnetic field effectively, but generates significant losses owing to the uneven distribution of shield currents. This dissertation uses litz wires to replace the conventional plate shield or ring shield. Skin effect is eliminated so the shield currents are uniformly distributed and the losses are reduced. The litz shields are categorized to two types: shorted litz shield and driven litz shield. Circuit models are derived to analyze their behaviors. The concept of lumped-loop model is applied to derive the Pareto front of efficiency versus stray magnetic field for the coils with litz shield. In an exemplary IPT system, coils without metal shield and with metal shields are optimized for the same efficiency. Both the simulation and experimental measurement verify that the shorted litz shield has the best performance. The stray magnetic field is attenuated by 65% compared to the coils without shield.

This dissertation also introduces the method to attenuate the stray magnetic field by controlling the phases of winding currents. The magnetic field around the coils is decomposed to the component in the axial direction and the component in the radial direction. The axial component decreases with smaller phase difference between windings' currents, while the radial component exhibits the opposite property. Because the axial component is dominant around the IPT coils, decreasing the phase difference is

preferred. The dual-side-controlled converter is applied for the circuit realization. Bridges with active switches are used for both the inverter on the transmitter side and the rectifier on the receiver side. The effectiveness of this method was verified both in simulation and experiment. Compared to the conventional series-series IPT with 90° phase difference between winding currents, stray magnetic field was attenuated by up to 30% and 40% when the phase differences of winding currents are 50° and 40° , respectively.

Furthermore, an analytical method is investigated to calculate the proximity-effect resistance of the planar coils with ferrite plate. The objective of this method is to work together with the fast optimization which uses the lumped-loop model. The existence of the ferrite plate complicates the calculation of the magnetic field across each turn which is critical to derive the proximity-effect resistance. In this dissertation, the ferrite plate is replaced by the mirrored turns according to the method of image. The magnetic fields are then obtained from Ampere's Law and Biot-Savart Law. Up to 200 kHz, the difference of the proximity-effect resistance is less than 15% between calculation and measurement.

Synergetic Attenuation of Stray Magnetic Field in Inductive Power Transfer

Ming Lu

General Audience Abstract

Inductive power transfer for the battery charging of electric vehicles uses loosely coupled coils to replace the cables and plugs. The power is transferred from transmitter to receiver across tens of centimeters. Significant stray magnetic field exists around the coils owing to the large gap, which should be attenuated for the safety consideration of human beings. Three methods are discussed for the field attenuation. The first method is to tune the physical parameters of the winding, such as the inner radii, outer radii, distribution of the turns, and types of the litz wires. The second method is to add metal shields around the IPT coils, in which litz wires are used as shields to reduce the shielding losses. The third method is to control the phases of winding currents, which avoids the increase of the size and weight of the IPT coils.

However, the field attenuation usually comes with reduced efficiency of the system. The work in this dissertation is focused on the synergetic attenuation of stray magnetic field in inductive power transfer for electric vehicles. The optimization is realized with Pareto front. The coils are optimized for low stray magnetic field and high efficiency simultaneously.

Acknowledgement

I'm grateful to all the industry members of the High Density Integration Consortium. Their sponsorship helped me to finish my Ph.D. research on this topic in the past four years. I would also like to show appreciation to GE Appliance and NSF for their sponsorship during my Ph.D. study.

I would like to thank my advisor, Dr. Khai D. T. Ngo, for his guidance, encouragement, and support in my research. His depth of knowledge and rigorous research attitude motivated me to be a better researcher. Everything I've learned from Dr. Ngo will benefit my future career.

I wish to express my sincere gratitude to my committee members: Dr. Guo-Quan Lu, Dr. Rolando Burgos, Dr. Majid Manteghi, and Dr. Lei Zuo. Their comments and help have contributed significantly to the fulfillment of my research.

I would like to express my gratitude to all the great staffs in CPES: Mr. David Gilham, Mr. Igor Cvetkovic, Ms. Trish Rose, Ms. Teresa Shaw, Ms. Marianne Hawthorne, Ms. Linda Long, Ms. Lauren Shutt, and Dr. Wenli Zhang for their help and support.

My study and research were enjoyable and valuable due to the wonderful colleagues at CPES. Discussions with them always led me to approach problems from different perspectives. Mr. Qiong Wang, Mr. Chao Fei, Mr. Jun Wang, Mr. Chi Li, Mr. Wei Zhang, Dr. Milisav Danilovic, Dr. Zhemin Zhang, Dr. Han Cui, Mr. Di Xu, Dr. Jongwon Shin, Mr. Zichen Miao, Mr. Ting Ge, Mr. Chien-An Chen, Dr. Yi Yan, Ms. Yincan Mao, Mr. Yin Wang, Dr. Woochan Kim, Mr. Joseph Kozak, Mr. Xuebing Chen, Mr. Zhongsheng Cao, Dr. Zhengyang Liu, Dr. Xiucheng Huang, Dr. Dongbin Hou, Dr. Yipeng Su, Mr. Yuchen Yang, Mr. Bin Li, Mr. Shishuo Zhao, Mr. Junjie Feng, Mr.

Yadong Lyu, Ms. Bingyao Sun, Dr. Fang Chen, Ms. Ye Tang, Mr. Jianghui Yu, Ms. Christina DiMarino, Ms. Niloofar Rashidimehrabadi, Ms. Qian Li, Mr. Slavko Mocevic.

Thank you all for the help and friendship.

I would like to thank my mother, Jinmei Liu, and my father, Weidong Lu, who have always supported and encouraged me to pursue my further education. They always give me the best suggestions.

Last but not least, I am sincerely grateful to my wife, Xiaoran Yu. Thank you for your love and support. I am so fortunate to have you in my life.

Table of Contents

List of Figures	2
List of Tables	2
Chapter 1. Introduction	1
1.1. Research Background.....	1
1.2. Introduction of Inductive Power Transfer	4
1.2.1. Working Principles	4
1.2.2. Topologies	5
1.2.3. Control Methods	7
1.3. Stray Magnetic Field in Inductive Power Transfer	10
1.4. Methods to Attenuate Stray Magnetic Field	12
1.4.1. Magnetic Shield.....	12
1.4.2. Metal Shield.....	13
1.4.3. Active Shield	17
1.5. Challenges to Attenuate Stray Magnetic Field.....	19
1.5.1. Reduced Efficiency.....	19
1.5.2. Time-Consuming Optimization.....	19
1.5.3. Increased Size and Weight of Coils.....	20
1.6. Research Objectives and Contributions	20
1.6.1. Synergetic Optimization of Efficiency and Stray Magnetic Field	20
1.6.2. Fast Optimization Method	21
1.6.3. Shield Structures with Less Losses	22
1.6.4. Field Attenuation without Increasing Coils Size.....	23
1.6.5. Systematic Procedure to Design IPT Coils.....	23
1.7. Dissertation Outline.....	25

Chapter 2. Baseline Coils Design – Efficiency Maximization without Considering Stray Magnetic Field	27
Nomenclature	27
2.1. Introduction	28
2.2. Design Equations for Converter and Coils.....	30
2.3. Systematic Design of Electrical Parameters.....	39
2.3.1. Operating Condition $f_N = f_{NH}$	41
2.3.2. Operating Condition $f_N = 1$	44
2.4. Physical Realization of Electrical Parameters.....	46
2.4.1. Operating Condition $f_N = f_{NH}$	48
2.4.2. Operating Condition $f_N = 1$	55
2.5. Experimental Verification	61
2.6. Summary	64
Chapter 3. Synergetic Attenuation of Stray Magnetic Field for IPT Coils	66
Nomenclature	66
3.1. Introduction	67
3.2. Pareto Front of Coil-to-Coil Efficiency versus Stray Magnetic Field	69
3.3. Conventional Method to Derive Pareto Front	73
3.4. Fast Method to Derive Pareto Front.....	75
3.4.1. Lumped-loop Model and Turns Vectors	75
3.4.2. Permeance Matrices and Current-to-Field Matrices.....	78
3.4.3. Calculation of Stray Magnetic Field.....	82
3.4.4. Calculation of Coil-to-Coil Efficiency	82
3.4.5. Plotting the Pareto Front.....	83
3.5. Design Example	83
3.6. Experimental Verification	94
3.6.1. Coil-to-Coil Efficiency	94

3.6.2. Stray Magnetic Field	96
3.7. Summary	101
Chapter 4. Approximation of Proximity-Effect Resistance	102
Nomenclature	102
4.1. Introduction	103
4.2. Proximity-Effect Loss of Litz Wire in Inductive Power Transfer	105
4.3. Magnetic Fields across Turns of the Planar Coil with Ferrite Plate.....	106
4.3.1. Components of the Magnetic Field across Each Turn.....	106
4.3.2. Equivalent Structure to Calculate Magnetic Fields	110
4.3.3. Internal Magnetic Field	111
4.3.4. External Magnetic Field	115
4.4. Influence of Ferrite Plate's Size	118
4.5. Experimental Verification	122
4.6. Summary	124
Chapter 5. Attenuation of Stray Magnetic Field with Litz Shield	126
Nomenclature	126
5.1. Introduction	128
5.2. Litz Shield	130
5.2.1. Structures of Litz Shield.....	130
5.2.2. Circuit Models of Coils with Litz Shield.....	133
5.3. Fast Method to Derive Pareto Front.....	139
5.3.1. Lumped-loop Model and Turns Vectors	139
5.3.2. Calculation of Inductances with Permeance Matrices.....	141
5.3.3. Calculation of Stray Magnetic Field with Current-to-Field Matrices	144
5.3.4. Coil-to-Coil Efficiency	146
5.3.5. Summary of the Procedure for the Fast Optimization.....	147
5.4. Design Example for Coils with Shorted Litz Shield	149

5.5. Experimental Verification	161
5.6. Summary	165
Chapter 6. Attenuation of Stray Magnetic Field by Controlling Phases of Winding	
Currents	167
Nomenclature	167
6.1. Introduction	168
6.2. Influence of Currents' Phases on Stray Magnetic Field.....	169
6.3. Circuit Realization with the Dual-Side-Controlled Converter.....	172
6.4. Simulation Verification	177
6.5. Experimental Verification	182
6.6. Summary	189
Chapter 7. Conclusions.....	190
7.1. Introduction	190
7.2. Main Contributions and Conclusions.....	191
List of Publications	194
Appendix A. Matlab Code for Synergetic Optimization.....	196
A.1. Coils without Shield	196
A.2. Coils with Shorted Litz Shield	200
A.3. Coils with Driven Litz Shield.....	207
A.4. Excel Files Imported for Calculation	214
Appendix B. Simulation Tools and Conditions	216
B.1. Directory of raw files for simulation or drawing of each figure	216
B.2. Deriving Permeance Matrices in Ansys Maxwell	218
B.3. Deriving Current-to-Field Matrices in Ansys Maxwell	220
Appendix C. Hardware Setup for Experiment	222
C.1. Layout of the Inverter	222
C.2. Fabrication of 100 W Coils with 3D Printer.....	224

Reference 226

List of Figures

Figure 1-1. The comparison of four methods for wireless power transfer: microwave [12]–[14], laser [15], [16], capacitive power transfer [17]–[21], and inductive power transfer [1]–[11].....	2
Figure 1-2. Historical review for the development of inductive power transfer.	4
Figure 1-3. Working principle of inductive power transfer.	5
Figure 1-4. Basic circuit topologies of inductive power transfer system with: (a) series-series compensation, (b) parallel-series compensation, (c) series-parallel compensation, and (d) parallel-parallel compensation.	6
Figure 1-5. Topology of the series-series inductive power transfer systems with a full bridge inverter.	7
Figure 1-6. The scheme of dual control for the topology in Figure 1-5 [48].	9
Figure 1-7. The circuit topology for the dual-side control [49].	9
Figure 1-8. The architecture of inductive power transfer with a DC-DC stage after the rectifier on the receiver side [50].	10
Figure 1-9. Stray field around planar coils.	10
Figure 1-10. Flux density of stray magnetic field for coils in Figure 1-9 from (a) side view and (b) top view.	11
Figure 1-11. Reference levels of ICNRIP 2010 [39] for the exposure to time varying magnetic fields.	12
Figure 1-12. Magnetic shield with (a) ferrite plate [46] and (b) ferrite bars [49].	13
Figure 1-13. (a) Coils with passive shield. (b) Eddy current flowing through the metal shields.	14
Figure 1-14. Metal shields for (a) circular pad and (b) DD-DDQ pad in references [34] and [35].	15
Figure 1-15. Side view for the flux lines of stray magnetic field for coils (a) with magnetic shield only and (b) with magnetic shield plus metal shield.	15
Figure 1-16. Metal shield with supplied winding current [53].	16
Figure 1-17. Working principle of active shields to attenuate stray magnetic field.	17
Figure 1-18. Active shields with (a) supplied current or (b) tunable capacitors. The current source and the capacitance are actively controlled according to sensed magnetic field.	18
Figure 1-19. Active shield in reference [54].	18
Figure 2-1. The circuit topology with series-series compensation of coils for IPT.	29
Figure 2-2. Output voltage of inverter v_{in_ac} in Figure 2-1 with phase shift.	31
Figure 2-3. Equivalent circuit model of the circuit topology in Figure 2-1.	32

Figure 2-4. Cylindrical 2D model of an exemplary coil to analyze the influence of proximity-effect resistance. Turns number increases from $N = 7$ to $N = 25$ while inner radii and outer radii of the winding are kept the same. The litz wire consists 1650 strands of AWG 44 wires.	37
Figure 2-5. (a) Percentage of the proximity resistance and DC resistance to the total resistance of winding for different turns number N in Figure 2-4 at 100 kHz; (b) normalized impedance Z_N is proportional to N^2 and quality factor Q is proportional to N	38
Figure 2-6. (a) M_V in (2-24), (b) φ_{Zin} in (2-26), and (c) λ_{coil} in (2-25) versus f_N and Z_N when $n = 1$, $k = 0.25$, and $Q = 1000$	40
Figure 2-7. (a) Z_{Nopt} in (2-32) and (b) Q_{ZNopt} for $\lambda_{coil} = 1\%$ versus M_V and k when $f_N = f_{NH}$	43
Figure 2-8. (a) Z_{Nopt} in (2-38) and (b) Q_{ZNopt} for $\lambda_{coil} = 1\%$ versus M_V and k when $f_N = 1$	45
Figure 2-9. (a) Structure of planar coils with spiral winding and (b) simplified coils with single-lumped-turn winding for finite-element simulation.	47
Figure 2-10. (a) Coupling coefficient k and (b) self-inductance L_0 of single-lumped-turn model in Figure 2-9(b) with gap = 100 mm. The gap is 100 mm as shown in Figure 2-9 and TABLE 2-5, and R_{outer} is normalized to gap . The normalized $R_{outer} = 1.25, 2,$ and 3 represent $R_{outer} = 125$ mm, 250 mm, and 300 mm, respectively.	50
Figure 2-11. (a) With simulated k for corresponding R_{inner} and R_{outer} in Figure 2-10(a), Z_{Nopt} is calculated from (2-32) with $f_N = f_{NH}$ and $M_V = 1$; (b) turns number N to realize $Z_N = Z_{Nopt}$ is calculated from (2-39) with Z_{Nopt} in (a) and L_0 in Figure 2-10(b).	51
Figure 2-12. (a) Q_{ZNopt} calculated from $\lambda_{coil} = 1\%$ in (2-30) with $Z_N = Z_{Nopt}$ in Figure 2-11(a) and k in Figure 2-10(a); (b) – (d) the values of Q with different litz wires (660, 1050, 1650, 2625 strands of AWG #44 wire) and turns number N in Figure 2-11(b) for R_{outer} of 125 mm, 200 mm, and 300 mm. Candidates of R_{inner} and R_{outer} are selected for $Q > Q_{ZNopt}$	53
Figure 2-13. Simulation waveforms of inverter output voltage v_{ac_in} and current i_1 , rectifier input voltage v_{out_ac} and current i_2 for circuit topology in Figure 2-1: (a) peak power with $V_{in} = 400$ V, $V_{out} = 400$ V, $I_{out} = 8.2$ A, and $f_s = 100$ kHz; (b) half power with $V_{in} = 400$ V, $V_{out} = 200$ V, $I_{out} = 8.2$ A, and $f_s = 107$ kHz. The square waves are voltages, and the sinusoidal waves are currents. Parameters of the converter and coils are listed in TABLE 2-8.	56
Figure 2-14. (a) Z_{Nopt} versus R_{inner} and R_{outer} with k in Figure 2-10(a) and $M_V = 1$, calculated from (2-38); (b) turns number N to realize $Z_N = Z_{Nopt}$ is calculated from (2-39) with Z_{Nopt} in (a) and L_0 in Figure 2-10(b).	57
Figure 2-15. When $f_N = 1$, (a) Q_{ZNopt} is calculated from $\lambda_{coil} = 1\%$ in (2-34) with $Z_N = Z_{Nopt}$ in Figure 2-14(a) and k in Figure 2-10(a). Q values with different litz wires (660, 1050, 1650, 2625 strands of AWG #44 wire) and turns number N in Figure 2-14(b) for R_{outer} of (b) 125 mm, (b) 200 mm, and (b) 300 mm. Candidates of R_{inner} and R_{outer} to select is when $Q > Q_{Nopt}$	58
Figure 2-16. Simulation waveforms of inverter output voltage v_{ac_in} and current i_1 , rectifier input voltage v_{out_ac} and current i_2 for circuit topology in Figure 2-1 when $f_N = 1$: (a) peak power with	

$V_{in} = 400$ V, $V_{out} = 400$ V, $I_{out} = 8.2$ A, and $f_s = 100$ kHz; (b) half power with $V_{in} = 400$ V, $V_{out} = 200$ V, $I_{out} = 8.2$ A, and $f_s = 100$ kHz. The square waves are voltages, and the sinusoidal waves are currents. Parameters of converter and coils are listed in TABLE 2-9.	60
Figure 2-17. Fabricated coils which were designed for 3.3 kW at $f_N = f_{NH}$ as in TABLE 2-8 following the procedure in TABLE 2-3 and TABLE 2-7 with (a) 4 pieces of 150 mm × 100 mm × 5 mm of EPCOS N95 ferrite plates, (b) winding with 1650/44 litz wire, and (c) 100 mm air gap.....	61
Figure 2-18. (a) Full bridge inverter, (b) rectifier with diode bridges, (c) resonant capacitor bank with 19.8 nF and 1.4 kV voltage rating to test the coils in Figure 2-17.	62
Figure 2-19. Waveforms of inverter and rectifier for circuit topology in Figure 2-1 when $V_{in} = 400$ V, $V_{out} = 400$ V, $I_{out} = 8.2$ A, and $f_s = 100$ kHz.	63
Figure 2-20. Switching frequency and measured coils' efficiency with $I_{out} = 8.2$ A, $V_{out} = 200$ to 400 V, and specifications in TABLE 2-5. Switching frequency were changed from 107 kHz to 100 kHz for different voltage gains and constant output current.....	64
Figure 3-1. Side view of the flux lines of stray magnetic field around the IPT coils.....	70
Figure 3-2. Components of the stray magnetic field – $B_X(t)$, $B_Y(t)$, and $B_Z(t)$ – in three orthogonal directions X, Y, and Z.	71
Figure 3-3 An example of the Pareto front of coil-to-coil efficiency versus stray magnetic field. The front is used to optimize the coils with the structure in Figure 3-2.	72
Figure 3-4. The conventional method to derive the Pareto front of coil-to-coil efficiency versus stray magnetic field, which sweeps the all the physical parameters in finite-element simulation.	74
Figure 3-5. The fast method to derive the Pareto front of coil-to-coil efficiency versus stray magnetic field, using lumped-loop model.	76
Figure 3-6. The lumped-loop model of the coils structure in Figure 3-2, which is used to start the procedure in Figure 3-5 to derive the Pareto front.....	77
Figure 3-7. The cylindrical view of the lumped-loop model in Figure 3-6 to demonstrate the turns vector $[N_{TX1}, N_{TX2}, \dots, N_{TXN}]$ of transmitter and the turns vector $[N_{RX1}, N_{RX2}, \dots, N_{RXN}]$ of the receiver.....	78
Figure 3-8. The elements of permeance matrices in (3-11) – (3-13) for the lumped-loop model, which are derived in one finite-element simulation with unity turn in each loop.	79
Figure 3-9. The elements of current-to-field matrices in (3-20) and (3-21). Index i represents orientations X, Y, and Z in Figure 3-2.....	81
Figure 3-10. The lumped-loop model for the design example, with 10 loops in the transmitter and 10 loops in the receiver.....	85

Figure 3-11. (a) The lumped-loop model to derive the current-to-field matrices; (b) current excitation of loop TX1 with 1 A-turn RMS; (c) the magnetic fields in X, Y, Z directions at the point (0, 100 mm, 0), which are extracted using the fields calculator in Ansys Maxwell.....	87
Figure 3-12. An exemplary lumped-loop model to calculate the inductances, winding currents, and stray magnetic field.....	91
Figure 3-13. Coils with real turns for the lumped-loop model in Figure 3-12, which are used to calculate winding resistances.....	93
Figure 3-14. Comparison of the Pareto fronts derived from the procedures in Figure 3-4 and Figure 3-5. The coils are used with the circuit topology in Figure 2-1, to transfer 100 W power across 40 mm gap. The maximum dimensions of the coils are 100 mm by 100 mm. The red circle on the upper right represents the scaled-down coils in Figure 2-17, which is designed to maximize the efficiency without considering stray magnetic field.	94
Figure 3-15. Fabricated coils of Figure 3-14, using litz wire composed of 100 strands with 0.1 mm strand-diameter and 3C96 ferrite plate with dimensions of 100 mm by 100 mm by 5 mm. .	95
Figure 3-16. (a) Near-field probe and (b) hardware setup up for field measurement.....	97
Figure 3-17. (a) Process of transferring measured field to voltage; (b) values of the voltage-to-field correction versus frequency [89].	98
Figure 3-18. (a) Side view of the coils; (b) quantified stray magnetic fields along Y axis when the measure points are located from 75 mm to 150 mm to the center. The magnetic fields are calculated, simulated, and measured with the coils in Figure 3-12, Figure 3-13, and Figure 3-15, respectively.	99
Figure 3-19. Time-domain waveforms of the stray magnetic fields in Y and Z directions at the points with (a) 100 mm and (b) 150 mm distances to the center of the coils (solid lines: measurement results of the coils in Figure 3-15; dashed lines: calculation results of the lumped-loop model in Figure 3-12).	100
Figure 4-1. (a) Internal field $B_{internal}$ and external field $B_{external}$ across one turn of the planar coil; (b) axial and radial components of $B_{internal}$ and $B_{external}$ at symmetrical points 1 and 1'.	108
Figure 4-2. (a) Cylindrical structure of the planar coils with ferrite plate and (b) its equivalent structure derived from the method of image.....	111
Figure 4-3. Components to calculate the internal fields at symmetrical points 1 and 1': B_{self} generated by the original turn and B_{mirror} generated by the mirrored turn.	113
Figure 4-4. Cross section of the original turn in Figure 4-3 to calculate the internal field in (4-24).....	113
Figure 4-5. Cross sections of the original turn and the mirrored turn in Figure 4-3 to calculate the internal field in (4-26).	114

Figure 4-6. Equivalent structure to calculate the external field on the original turn n for a planar coil with N turns. Turn n is not excited and all the other original turns and mirrored turns are excited with current I .	115
Figure 4-7. The example to calculate external field B across turn n , which is generated by turn m with excitation I . The components of B in the radial and axial directions, B_r and B_a , are calculated from (4-31) and (4-32), respectively.	116
Figure 4-8. Magnetic field dB at the measure point P, generated by the small segment of conductor ds with current excitation I .	116
Figure 4-9. (a) Cylindrical structure of the exemplary coil with ferrite plate; (b) equivalent structure of (a) using the method of image to calculate B^2 .	119
Figure 4-10. Calculated B^2 for the equivalent structure in Figure 4-9(b) and simulated B^2 for the real structure in Figure 4-9(a) with different sizes of ferrite plate.	121
Figure 4-11. Proximity-effect resistance calculated from (4-39) using B^2 in Figure 4-10.	122
Figure 4-12. Fabricated coil of the structure in Figure 4-9 (a) with square ferrite plate of dimensions 100 mm \times 100 mm \times 5 mm.	123
Figure 4-13. ESR and proximity-effect resistance from calculation (dashed lines) and measurement (solid lines) for the coil in Figure 4-12.	124
Figure 5-1. Metal shields with (a) plate structure and (b) ring structure to attenuate stray magnetic fields around the coils.	128
Figure 5-2. Working principle of metal shields to attenuate the stray magnetic field on the side of the coil.	130
Figure 5-3. Top view of current-density vectors for coils with (a) plate shield and (b) ring shield in Figure 5-1.	131
Figure 5-4. Distribution of current-density magnitudes for (a) ring shield and (b) litz shield.	132
Figure 5-5. Structures of the coils with (a) shorted litz shield and (b) driven litz shield.	133
Figure 5-6. (a) Circuit model for the coils with litz shield in Figure 5-5, using four coupled inductors; (b) simplified circuit model with equivalent inductances and resistances, using two coupled inductors.	134
Figure 5-7. (a) An exemplary structure of coils with litz-shield; (b) equivalent self-inductances, (c) equivalent mutual inductances, and (d) equivalent winding resistances calculated for coils without shield, with shorted litz shield, and with driven litz shield.	137
Figure 5-8. The coil-to-coil efficiency calculated from (2-10) with the parameters in Figure 5-7.	138
Figure 5-9. (a) Top view and (b) side view of the lumped-loop model for IPT coils with litz shield. The turns vectors are $[N_{w1,1}, N_{w1,2}, \dots, N_{w1,N}]$ and $[N_{w2,1}, N_{w2,2}, \dots, N_{w2,N}]$ for the windings,	

and $[N_{sh1,1}, N_{sh1,2}, \dots, N_{sh1,M}]$ and $[N_{sh2,1}, N_{sh2,2}, \dots, N_{sh2,M}]$ are for the litz shields. The distribution of turns are represented by turns vectors.	141
Figure 5-10. Permeance matrices \mathbf{L}_{w1} , \mathbf{L}_{w2} , \mathbf{L}_{sh1} , \mathbf{L}_{sh2} , \mathbf{M}_{w1-w2} , $\mathbf{M}_{sh1-sh2}$, \mathbf{M}_{w1-sh1} , \mathbf{M}_{w1-sh2} , \mathbf{M}_{w2-sh1} , and \mathbf{M}_{w2-sh2} of the lumped-loop model in Figure 5-9.	142
Figure 5-11. Current-to-field matrices $\boldsymbol{\alpha}_{w1,i}$, $\boldsymbol{\alpha}_{w2,i}$, $\boldsymbol{\alpha}_{sh1,i}$, $\boldsymbol{\alpha}_{sh2,i}$ of the lumped-loop model in Figure 5-9.	145
Figure 5-12. Procedure to derive the Pareto front of coil-to-coil efficiency versus stray magnetic field for the coils with litz shield, using the concept of lumped-loop model.....	148
Figure 5-13. Lumped-loop model of the design example for the coils with litz shield.....	150
Figure 5-14. Pareto fronts of coil-to-coil efficiency versus stray magnetic field for coils with no shield, plate shield, ring shield, shorted litz shield, and driven litz shield. Horizontal axis is the stray magnetic field at point (0, 100 mm, 0) in Figure 5-13, with 100 W power transferred across 40 mm gap.....	160
Figure 5-15. Fabricated coils for selected structures marked as circles along the Pareto fronts in Figure 5-14, with (a) plate shield, (b) ring shield, (c) shorted litz shield, and (d) driven litz shield. The coils are optimized to transfer 100 W power across 40 mm gap.	161
Figure 5-16. Simulated and measured waveforms of the magnetic fields $B_Y(t)$ and $B_Z(t)$ at the point (0, 100 mm, 0), for the coils in Figure 5-15 with (a) plate shield, (b) ring shield, (c) shorted litz shield, and (d) driven litz shield. The power of 100 W was transferred across 40 mm gap.	163
Figure 5-17. The comparison of $B_Y(t)$ and $B_Z(t)$ at point (0, 100 mm, 0) between the coils without shield and the coils with different shields in Figure 5-15. The stray magnetic fields are measured when 100 W power was transferred across 40 mm gap.	164
Figure 5-18. The quantified stray magnetic fields from measurement along Y axis, with the distance to the center ranging from 75 mm to 150 mm in Figure 5-13.	165
Figure 6-1. The magnetic fields generated by IPT coils from side view. According to superposition, $B_1(t)$ is generated by transmitter current $i_1(t)$, and $B_2(t)$ is generated by receiver current $i_2(t)$. $B_1(t)$ and $B_2(t)$ are decomposed to components $B_{1a}(t)$ and $B_{2a}(t)$ in the axial direction and components $B_{1r}(t)$ and $B_{2r}(t)$ in the radial direction.....	170
Figure 6-2. (a) Phasors representing winding currents $i_1(t)$ and $i_2(t)$, with magnitudes I_1 and I_2 and phase difference θ ; phasors representing stray magnetic fields in (b) axial direction and (c) radial direction.	171
Figure 6-3. Circuit topology of series-series compensation with the dual-side control converter.	172
Figure 6-4. Simulated waveforms of voltages and currents on the inverter side and receiver side in Figure 6-3 ($P_{out} = 3.3$ kW, $V_{in} = 400$ V, $V_{out} = 400$ V, $\varphi = 140^\circ$, $\alpha_1 = \alpha_2 = 126^\circ$).	173
Figure 6-5. Equivalent circuit model of the topology in Figure 6-3.....	174

Figure 6-6. Normalized magnetic field B_N in (6-22) versus φ and a . The measurement position of magnetic field is along the radial axis.....	177
Figure 6-7. Normalized loss in (6-23) versus φ	177
Figure 6-8. Structures and dimensions of the exemplary coils designed for the 3.3 kW IPT system in TABLE 6-1.....	178
Figure 6-9. Positions for field measurement along the radial axis around the coils in Figure 6-8.....	179
Figure 6-10. Simulated values of $a = B_{1r0} / B_{1a0} = B_{2r0} / B_{2a0}$ at the positions for field measurement in Figure 6-9.....	180
Figure 6-11. Simulated B_N (solid lines) and calculated B_N from (6-22) (circles) at the positions for field measurement in Figure 6-9.....	180
Figure 6-12. Waveforms of currents and voltages for the inverter and receiver in Figure 6-3: $\varphi = 90^\circ$, $\theta = 90^\circ$	181
Figure 6-13. Waveforms of currents and voltages for the inverter and receiver in Figure 6-3: $\varphi = 130^\circ$, $\theta = 50^\circ$	181
Figure 6-14. Magnitude of magnetic field around coils from finite-element simulation: $\varphi = 90^\circ$, $\theta = 90^\circ$	182
Figure 6-15. Magnitude of magnetic field around coils from finite-element simulation: $\varphi = 130^\circ$, $\theta = 50^\circ$	182
Figure 6-16. (a) Fabricated coils for the 100 W experimental verification with (b) a gap of 40 mm between transmitter and receiver.....	183
Figure 6-17. A hardware setup for field measurement around the coils.....	184
Figure 6-18. Winding currents when transferring 100 W power with the coils in Figure 6-16 and the hardware in Figure 6-17: (a) $\varphi = 90^\circ$, measurement; (b) $\varphi = 90^\circ$, simulation; ; (c) $\varphi = 130^\circ$, measurement; (d) $\varphi = 130^\circ$, simulation.....	185
Figure 6-19. Points along the radial axis for field measurement for the coils in Figure 6-16....	186
Figure 6-20. Magnetic fields $B_a(t)$ and $B_z(t)$ at the point (0, 100 mm, 0) in Figure 6-19, when transferring 100 W power with the coils in Figure 6-16 and the hardware in Figure 6-17: (a) $\varphi = 90^\circ$, measurement; (b) $\varphi = 90^\circ$, simulation; (c) $\varphi = 130^\circ$, measurement; (d) $\varphi = 130^\circ$, simulation.....	187
Figure 6-21. Comparison of the quantified magnetic field along radial axis in Figure 6-19, between $\varphi = 90^\circ$ and $\varphi = 130^\circ$. The dashed lines are from simulation using Ansys Maxwell. The circles are from measurement.....	188
Figure 6-22. Magnitudes of magnetic field around coils from finite-element simulation: (a) $\varphi = 90^\circ$, $\theta = 90^\circ$; (b) $\varphi = 130^\circ$, $\theta = 50^\circ$	188
Figure A-1. “Litz Wire Datasheet.xls”.....	214

Figure A-2. “Inductance Matrix.xls” (unit: mH).	215
Figure A-3. “Field Matrix.xls” (unit: $\mu\text{T}/\text{Ampere-turn}$).	215
Figure B-1. Lumped-loop model in Ansys Maxwell for coils with litz shield (see TABLE B-1 for the original file).....	218
Figure B-2. Select the eddy current solver for the solution type.	218
Figure B-3. Select eddy current solver for the solution type.	219
Figure B-4. Settings for the analysis.....	219
Figure B-5. Analysis of simulation and the results in matrix.	220
Figure B-6. Analysis of simulation and exporting the results.....	221
Figure B-7. Expressions of the magnetic fields in the calculator.	221
Figure C-1. Complete schematic of the inverter in Figure 2-18(a) (see TABLE B-1 for the original file).	222
Figure C-2. Layout of the inverter in Figure 2-18(a): (a) top layer; (b) layer 2; (c) layer 3; (4) bottom layer (see TABLE B-1 for the original file).	223
Figure C-3. AutoCAD file of the coils’ fixture for 3D printing (see TABLE B-1 for the original file).....	224
Figure C-4. Importing the .stl file in Figure C-3 to Cura for 3D printing.	224
Figure C-5. Settings in Cura for 3D printing.	225

List of Tables

TABLE 2-1. Unknown Parameters for the Design of Coils	34
TABLE 2-2. Normalized Parameters for the Design of Coils	35
TABLE 2-3. Systematic Design of Electrical Parameters, $f_N = f_{NH}$	43
TABLE 2-4. Systematic Design of Electrical Parameters, $f_N = 1$	45
TABLE 2-5. Specifications of IPT Coils for Design	46
TABLE 2-6. Sweep of R_{inner} and R_{outer} in Figure 2-9(b) and Other Background Information	49
TABLE 2-7. Procedure of Physical Realization and Design Results when $f_N = f_{NH}$	54
TABLE 2-8. Parameters of Exemplary Coils Design in TABLE 2-7.....	55
TABLE 2-9. Procedure of Physical Realization and Design Results when $f_N = 1$	59
TABLE 2-10. Parameters of Exemplary Coils Design in TABLE 2-9.....	59
TABLE 2-11. Simulated and Measured Parameters of Coils Designed for $f_N = f_{NH}$ in TABLE 2-8	62
TABLE 3-1. Permeance Matrices \mathbf{L}_{TX} for the Lumped-loop Model in Figure 3-10 (Unit: nH)..	86
TABLE 3-2. Permeance Matrices \mathbf{M} for the Lumped-loop Model in Figure 3-10 (Unit: nH).....	86
TABLE 3-3. Current-to-Field Matrix for the Lumped-loop Model of Transmitter in Figure 3-10 (Unit: $\mu\text{T}/\text{Ampere-Turn}$).....	88
TABLE 3-4. Current-to-Field Matrix for the Lumped-loop Model of Receiver in Figure 3-10 (Unit: $\mu\text{T}/\text{Ampere-Turn}$).....	89
TABLE 3-5. Turns Vectors to be Swept for the Lumped-loop Model in Figure 3-10	90
TABLE 3-6. Inductances, Resistances, and Coil-to-Coil Efficiencies for Coils in Figure 3-12, Figure 3-13, and Figure 3-15	96
TABLE 4-1. Parameters Values to Calculate Magnetic Fields for the Equivalent Structure in Figure 4-9(b)	120
TABLE 4-2. Parameters Values to Calculate Proximity-Effect Loss in (4-39)	122
TABLE 5-1. Permeance Matrices $\mathbf{L}_{w(i)}$ in Figure 5-10 (Unit: nH, $i = 1$ or 2)	151
TABLE 5-2. Permeance Matrix \mathbf{M}_{w1-w2} in Figure 5-10 (Unit: nH).....	152
TABLE 5-3. Permeance Matrices $\mathbf{L}_{sh(i)}$ in Figure 5-10 (Unit: nH, $i = 1$ or 2).....	152
TABLE 5-4. Permeance Matrix $\mathbf{M}_{sh1-sh2}$ in Figure 5-10 (Unit: nH).....	152
TABLE 5-5. Permeance Matrices $\mathbf{M}_{w(i)-sh(i)}$ in Figure 5-10 (Unit: nH, $i = 1$ or 2)	153
TABLE 5-6. Permeance Matrices $\mathbf{M}_{w(i)-sh(j)}$ in Figure 5-10.....	153
TABLE 5-7. Current-to-Field Matrix $\boldsymbol{\alpha}_{w1}$ in Figure 5-11 (Unit: $\mu\text{T}/\text{Ampere-Turn}$)	153
TABLE 5-8. Current-to-Field Matrix $\boldsymbol{\alpha}_{w2}$ in Figure 5-11 (Unit: $\mu\text{T}/\text{Ampere-Turn}$)	154

TABLE 5-9. Current-to-Field Matrix α_{sh1} in Figure 5-11 (Unit: $\mu\text{T}/\text{Ampere-Turn}$).....	154
TABLE 5-10. Current-to-Field Matrix α_{sh2} in Figure 5-11 (Unit: $\mu\text{T}/\text{Ampere-Turn}$)	154
TABLE 5-11. Turns Vectors to Sweep for the Lumped-loop Model in Figure 5-13	156
TABLE 5-12. Turns Vectors for an Exemplary Coil with Shorted Litz Shield with the Lumped-loop Model in Figure 5-13	157
TABLE 5-13. Calculation of Inductances for the Exemplary Coil with Shorted Litz Shield in TABLE 5-12	157
TABLE 5-14. Calculation of Resistances for the Exemplary Coil with Shorted Litz Shield in TABLE 5-12	158
TABLE 5-15. Calculation of Currents for the Exemplary Coil with Shorted Litz Shield in TABLE 5-12	159
TABLE 5-16. Calculation of Stray Magnetic Field for the Exemplary Coil with Shorted Litz Shield in TABLE 5-12	159
TABLE 5-17. Measurement Results for Coils in Figure 5-15.....	162
TABLE 5-18. Weight Breakdown for Transmitter Coil in Figure 5-15, (Ferrite Weight = 240 g)	162
TABLE 6-1. Specifications of the Exemplary 3.3 kW IPT system with Coils in Figure 6-8.....	178
TABLE 6-2. Inductances and Resistances for Coils in Figure 6-16.....	183
TABLE B-1 Directory of Raw Files for Each Figure.....	216

Chapter 1. Introduction

1.1. Research Background

The conventional method to transfer electric power uses wires which are made of conductive materials. The power is transferred to the load with current flowing through wires. Power transfer with wires is simple and efficient, with mature theories.

However, power transfer is preferred to be wireless in some applications. This is called wireless power transfer (WPT). One example is to charge the biomedical implant such as the pacemakers [1]–[5]. With wireless power transfer, patients don't have to suffer surgeries to charge the batteries of the pacemakers. Another example is the battery charging for electric vehicles [6]–[9]. Wireless power transfer is safer than the plug-in method when charging the vehicles in the humid environment. Using wireless power transfer, the vehicles can be charged when they are moving [10], [11]. This helps to reduce the size of battery pack so the weight of the electric vehicles is reduced.

Several methods to achieve wireless power transfer have been investigated: microwave [12]–[14], laser [15], [16], capacitive power transfer [17]–[21], and inductive power transfer. Figure 1-1 shows the comparison of the four methods, including the working principle, the energy form, the distance of power transfer, the power level, and the drawbacks.

The microwave method works based on the electromagnetic radiation, using the energy form of microwave beam. Large amount of energy is transferred with microwave through a long distance for up to kilometers range. The drawbacks of the microwave method are the large antenna size and the serious radio frequency interference.

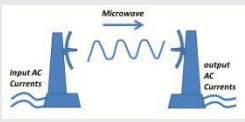
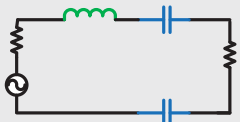
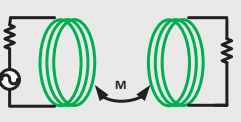
	Microwave	Laser	Capacitive Power Transfer	Inductive Power Transfer
				
Principle	Electromagnetic Radiation	Electromagnetic Radiation	Electric Induction	Magnetic Induction
Energy Form	Microwave beam	Laser beam	Electrical field	Magnetic field
Distance	Far-field (km)	Far-field (km)	Near-field (mm)	Near-field (<10 m)
Power Level	High	High	Low	High Medium Low
Draw-back	<ol style="list-style-type: none"> 1. Large antenna size 2. RF interference 	<ol style="list-style-type: none"> 1. Low conversion efficiency 2. Atmospheric absorption 	<ol style="list-style-type: none"> 1. Limited power 2. Small charging range 	<ol style="list-style-type: none"> 1. EMF trouble 2. Misalignment-sensitive

Figure 1-1. The comparison of four methods for wireless power transfer: microwave [12]–[14], laser [15], [16], capacitive power transfer [17]–[21], and inductive power transfer [1]–[11].

The laser method works based on the electromagnetic radiation, using the energy form of laser beam. Large amount of energy is transferred through a long distance up to kilometers. The drawbacks include the low conversion efficiency between electric power and laser, and the atmospheric absorption.

The capacitive power transfer utilizes the electric induction with coupled electric field. Typically, a small amount of power is transferred in the charging range of millimeters. The power level and transfer distance are the limitation of the capacitive power transfer. Capacitive power transfer can also be used to charge electric vehicles in the power level of kilowatts [20],

[21]. However, since the capacitance value is influenced by the permittivity between the metal plates, humid environment may cause problems for capacitive power transfer when the gap between the transmitter and receiver plates is large.

Inductive power transfer is mostly used for wireless power transfer across the distance which ranges from millimeters to meters. The amount of transferred power is from several watts to tens of kilowatts. The power is transferred according to the coupling of magnetic near field and magnetic resonance. Inductive power transfer has been widely used for the charging of medical implants, electric vehicles, and consumer electronics.

The historic review for the development of inductive power transfer is shown in Figure 1-2. In 1890's, Nikola Tesla managed to light three incandescent lamps wirelessly with the distance up to one hundred feet. His method is to resonate the coils and capacitors [22], [23]. Inductive power transfer was used for biomedical applications in 1960's [24]–[26]. Starting from 1990's, Prof. John Boys and his team in Auckland University made great contributions to the inductive power transfer for electric vehicles [27]–[35]. They incorporated power inverters and resonant circuits to improve the performances of the systems. Since 2000's, Dr. Ron Hui and his team in University of Hong Kong came up with many brilliant ideas to charge the consumer electronics with inductive power transfer [36]–[38].

Although the concept of inductive power transfer is attractive, there are still quiet a few problems. The major problems include: (1) significant stray magnetic field exists around the transmitter and receiver coils, which presents potential hazard to human safety [39]; (2) system performance degrades when there is misalignment between the transmitter and receiver coils; (3) foreign objects between the coils may degrades system performance and causes safety issues

[40]. This dissertation focuses on the attenuation of the stray magnetic field around IPT coils, especially for the application of electric vehicle charging.

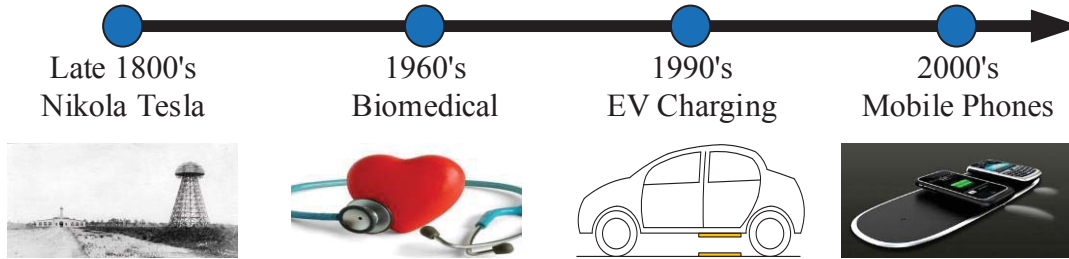


Figure 1-2. Historical review for the development of inductive power transfer.

1.2. Introduction of Inductive Power Transfer

1.2.1. Working Principles

Inductive power transfer is realized by the coupling of magnetic near field and the magnetic resonance. In Figure 1-3, the excitation current in the transmitter coil generates magnetic field in the air. Part of the magnetic field is coupled to the receiver coil and induces voltage. The induced voltage on the receiver then supplies power to the load.

The coupling between the transmitter and receiver coil is weak owing to the large air gap. For the application on EV charging with tens of centimeters' air gap, the coupling coefficient is usually smaller than 0.3. The weak coupling will limit the power transferability and coil-to-coil efficiency of the IPT system. In order to improve the efficiency, the compensation networks are added to both the transmitter side and receiver side [28], [41]. The compensation networks are usually composed of capacitors, which can be either external capacitors or the parasitic capacitors of the coils. The capacitance values are selected according to the resonant frequency

[27], [28]. At the resonance condition, the efficiency is highest because the smallest amount of circulating energy is generated for the desired power transfer.

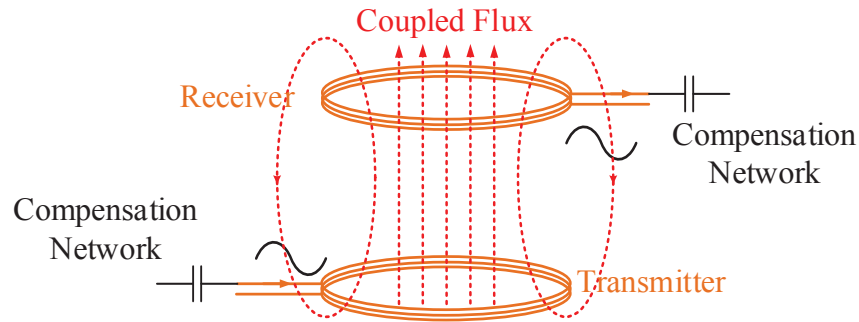


Figure 1-3. Working principle of inductive power transfer.

In some cases, additional coils are inserted between the transmitter and receiver coils to increase the distance of power transfer. Reference [42] applies a 4-coil system and managed to transfer 60 W power through the distance of 2 meters. The resonant frequencies of the 4 coils are tuned to be the same.

1.2.2. Topologies

According to how the compensation networks are connected to the coils, the basic topologies of inductive power transfer systems are categorized as series-series topology, parallel-series topology, series-parallel topology, and parallel-parallel topology [27], [28]. Figure 1-4 shows the four basic topologies. The capacitance values of the compensation capacitors are calculated according to [28].

In these four basic topologies, the series-series compensation is popular for its simplicity. The values of C_1 and C_2 are selected according to the self inductances L_1 and L_2 and the resonant frequency, so they are independent of the load or coupling conditions. The receiver current is

controlled by the input voltage at resonance condition, providing current source behavior.

However, the voltage stress on the resonant capacitors is high for the series-series compensation.

Capacitor banks are applied to deal with the voltage stress for the charging of electric vehicles.

The power transferability is influenced significantly by the coupling between the coils, so

additional control method or specific design of coils is required to deal with the misalignment

between the coils.

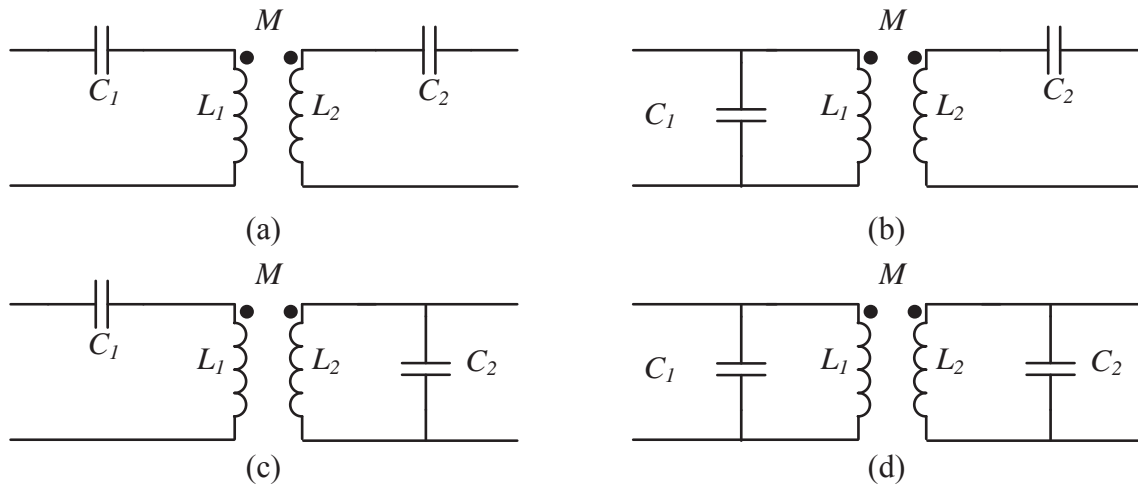


Figure 1-4. Basic circuit topologies of inductive power transfer system with: (a) series-series compensation, (b) parallel-series compensation, (c) series-parallel compensation, and (d) parallel-parallel compensation.

Besides the four basic topologies in Figure 1-4, other topologies have been proposed to overcome different issues in inductive power transfer. A series-parallel-series topology has been discussed in [43], which has high tolerance for misalignment between transmitter and receiver coils. The topology with double-sided LCC compensation network has been demonstrated in [44]. When using the LCC compensation, the transmitter side behaves like a current source, with the switching frequency independent of load or coupling conditions. Reference [45] summarizes

all the topologies with multi-element resonant components, and categorizes them as structures with current-source behavior and with voltage-source behavior.

1.2.3. Control Methods

A full bridge inverter is typically used to supply the AC voltage to the resonant tank, for the application of electrical vehicle charging in kilowatts power. Figure 1-5 is the topology of the series-series inductive power transfer with a full bridge inverter. The power is transferred to the load from the receiver coil. The diodes bridges on the receiver side rectify the receiver current before charging the load. The topology in Figure 1-5 behaves as a DC-DC resonant converter.

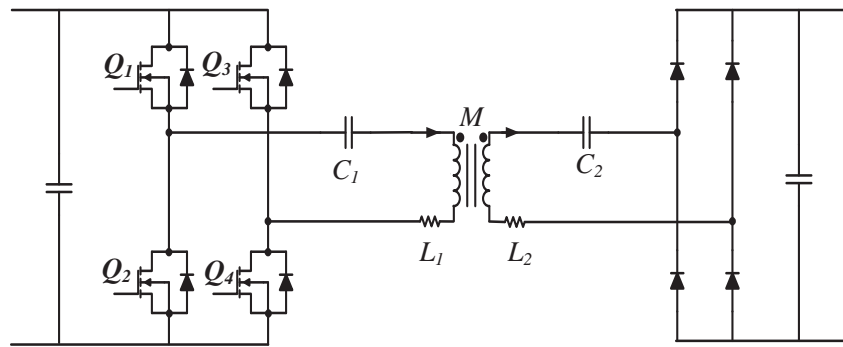


Figure 1-5. Topology of the series-series inductive power transfer systems with a full bridge inverter.

The methods to control the transferred power include phase shift between the bridge legs of the inverter [46], control of the switching frequency [47], a dual control by combining phase shift and switching frequency [48], the dual-side control with active switches on both transmitter and receiver sides [49], and adding a DC-DC stage after the diodes bridges [50].

Phase shift between inverter bridges controls the inverter's output voltage with variable pulse widths, which changes the amplitude of the fundamental voltage and the bulk power transferred

to the load. The full bridge inverter is operated with constant switching frequency when using the phase shift control. However, soft switching is lost for devices of the leading leg, which increases the switching loss.

The transferred power can be controlled by tuning the switching frequency of the full bridge inverter. In this case, complimentary gate signals are supplied to the devices of the inverter, which means Q_1 and Q_4 have the same gate signal, and Q_2 and Q_3 have the same gate signal. The inverter's output voltage is square wave with 50% duty cycle. The switching frequency is selected for inductive operation of the converter, and soft switching is realized for all the switches. However, the converter works off resonance in this condition, resulting in more circulating energy and increased conduction loss.

The dual control combines the phase shift and the frequency control [48]. Its control scheme is shown in Figure 1-6. The zero crossings of the transmitter current are detected to trigger the leading leg (Q_1 and Q_2). The trigger of Q_3 and Q_4 is determined by the pulse width of inverter's output voltage. Zero-voltage switching is realized for all the devices. The converter still works off resonance, but there is less circulating energy compared to the method which uses the frequency control only.

The dual-side control in Figure 1-7 is proposed in [49] to improve the system efficiency over a wide operating range. It achieves high efficiency even with partial load or low coupling. The pulse widths of the inverter's output voltage and the rectifier's input voltage are controlled to realize the optimal efficiency and the required power transfer. Hard switching of the devices and the increased number of active switches are the major concerns of this method.

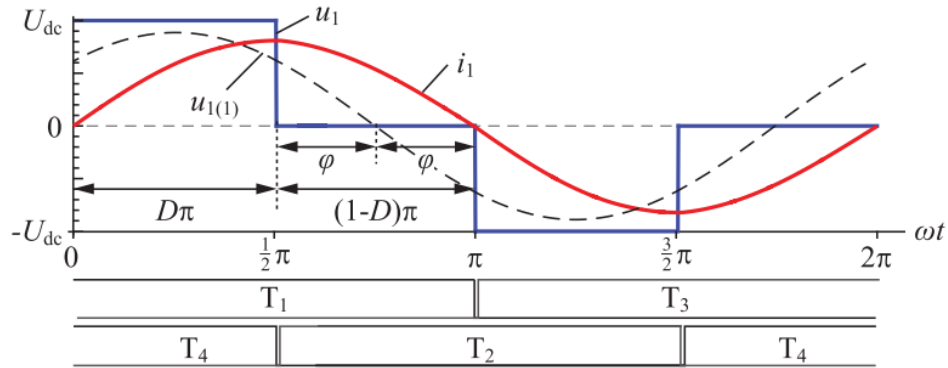


Figure 1-6. The scheme of dual control for the topology in Figure 1-5 [48].

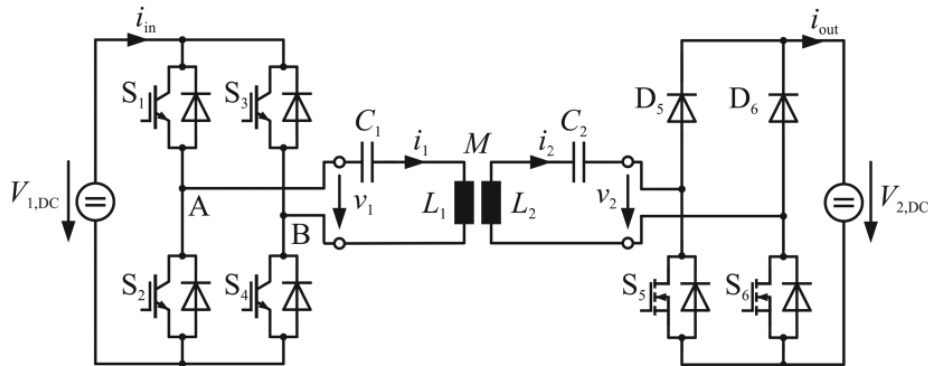


Figure 1-7. The circuit topology for the dual-side control [49].

Figure 1-8 shows the architecture with a DC-DC converter after the rectifier on the receiver side. The DC-DC converter is added in order to achieve the optimal value of equivalent load resistance for higher efficiency. The regulation of the output voltage or output current is easier with the DC-DC converter.

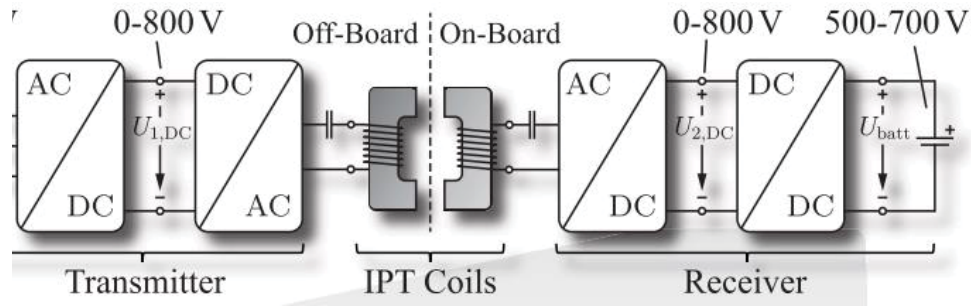


Figure 1-8. The architecture of inductive power transfer with a DC-DC stage after the rectifier on the receiver side [50].

1.3. Stray Magnetic Field in Inductive Power Transfer

The planar coils are popularly used in inductive power transfer, thanks to their low profiles. Because the air gap is comparable with the dimensions of the coils, severe stray magnetic field exists around the coils as shown in Figure 1-9. Plates or bars made of ferrite are usually added to the coils in order to reduce the stray magnetic field and to increase the coupling coefficient between the transmitter and receiver.

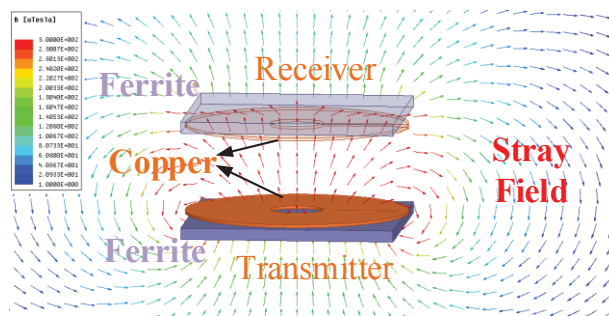


Figure 1-9. Stray field around planar coils.

Figure 1-10 shows the plot of flux density for the stray magnetic field around the planar coils, from top view and side view. The magnetic field are derived from finite-element simulation using Ansys Maxwell [51]. The magnetic field is not severe below the transmitter and above the receiver, because of the ferrite plates. However, the magnitude of the magnetic field is large on the side of the coils, which should be attenuated with extra shield structures.

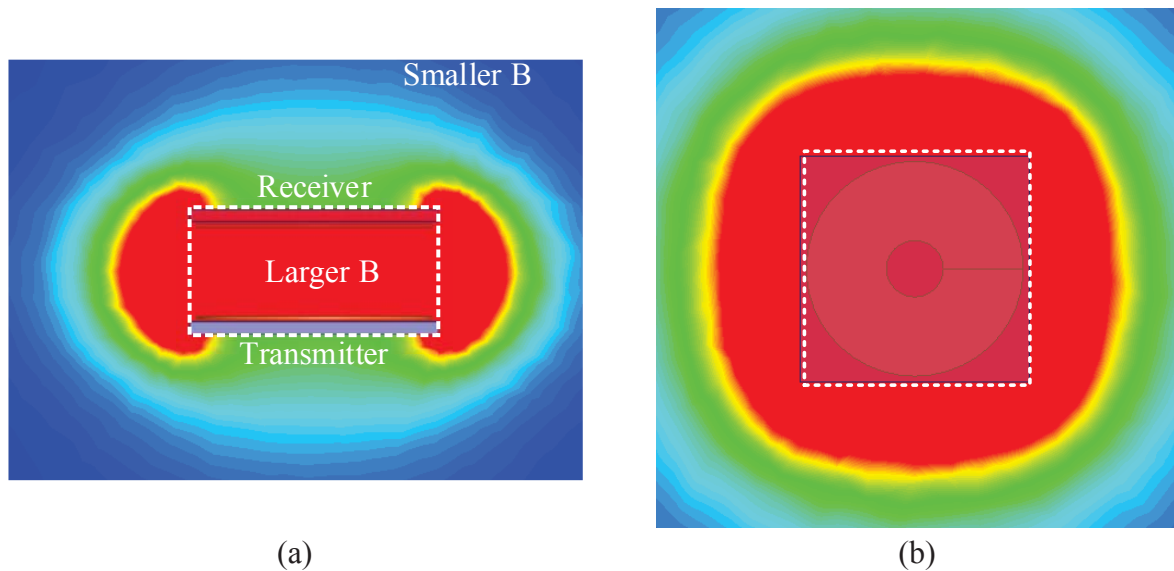


Figure 1-10. Flux density of stray magnetic field for coils in Figure 1-9 from (a) side view and (b) top view.

International Commission on Non-Ionizing Radiation Protection (ICNIRP) reports that the effects such as the stimulation of nervous tissues and the induction in the retina of phosphenes are caused by the exposure to time-varying magnetic field [39]. For safety considerations of human beings, the magnitude of stray magnetic field for the IPT in EV charging should meet the standard of ICNIRP guidelines 2010 [39] in Figure 1-11.

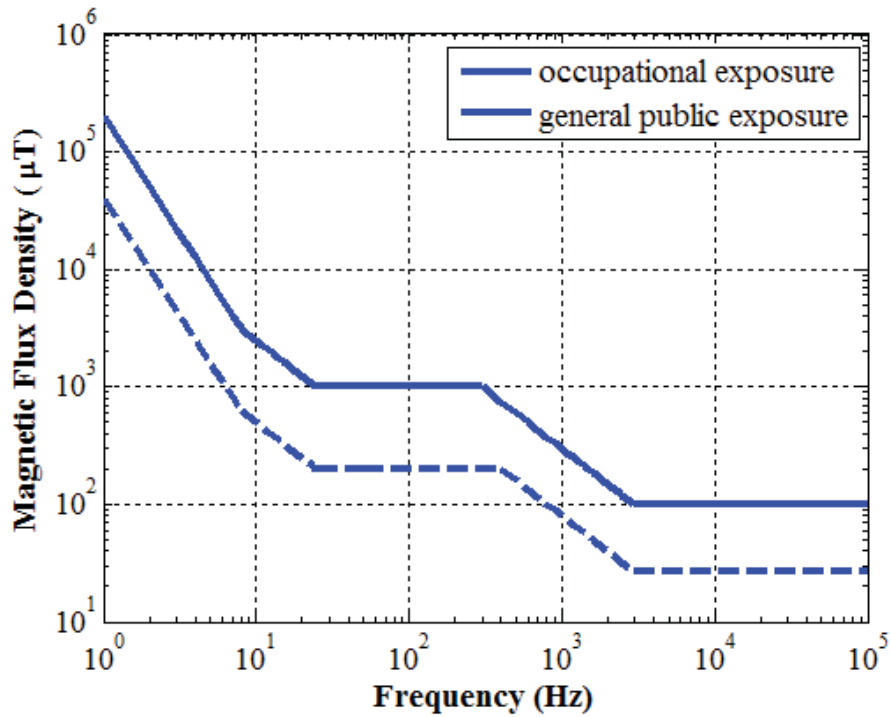


Figure 1-11. Reference levels of ICNRIP 2010 [39] for the exposure to time varying magnetic fields.

1.4. Methods to Attenuate Stray Magnetic Field

1.4.1. Magnetic Shield

As shown in Figure 1-10, adding magnetic materials attenuate the stray magnetic field. The ferrite material is a good candidate for magnetic shield. The most commonly used structures are the ferrite plate in Figure 1-12(a) [46] and the ferrite in Figure 1-12(b) [35], [36], [49].

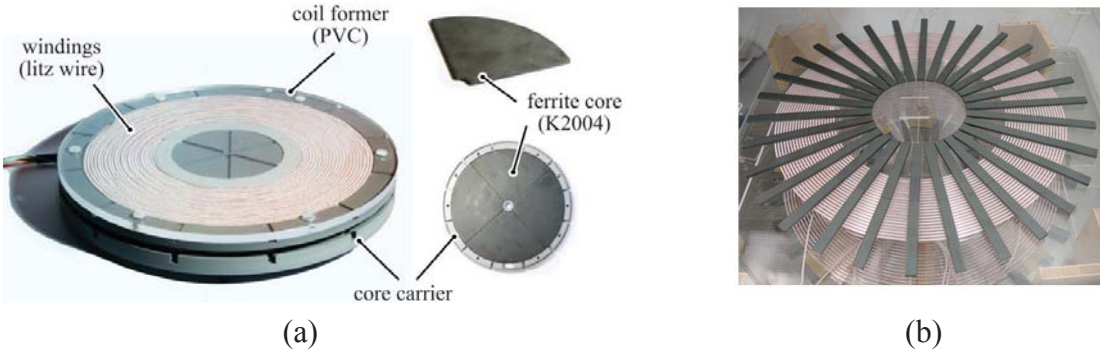


Figure 1-12. Magnetic shield with (a) ferrite plate [46] and (b) ferrite bars [49].

The magnetic shield not only attenuates the stray magnetic field, but also increases the coupling coefficient between transmitter and receiver coils. However, its attenuation is not good enough for the high power applications such as the charging of electric vehicles, especially for the field on the side of the coils [52]. The metal shield or active shield is always applied together with the magnetic shield, which will be demonstrated later on.

1.4.2. Metal Shield

Metal shield is a simple method to attenuate stray magnetic field [34], [35], [53]. It always works together with the magnetic shield. Shield structures made of conductive materials are placed around the IPT coils. The stray magnetic field is attenuated by the current flowing through the metal shield.

The current of the metal shield is either eddy current or winding current. Figure 1-13 shows the how the eddy current attenuates the stray magnetic field. With conductive materials of plate-structure or ring-structure placed around the coils, eddy current on the shield is induced by the stray magnetic field. The eddy current flows in the opposite direction as the winding current, so

the magnetic fields generated by the eddy current and by the winding current cancel each other on the side of the IPT coils.

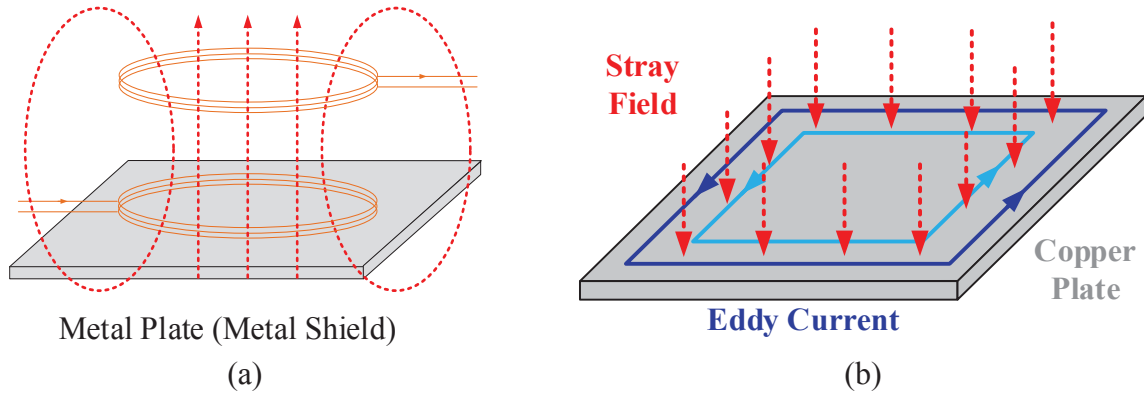


Figure 1-13. (a) Coils with passive shield. (b) Eddy current flowing through the metal shields.

References [34] and [35] apply shield structures in Figure 1-14 to attenuate the stray magnetic field. The shields combine plate structure and ring structure. Figure 1-15 shows the comparison of flux lines for coils with magnetic shield only and with magnetic shield plus metal shield. Stray magnetic field around the coils is obviously reduced by the metal shield.

Reference [53] uses winding current for the metal shield. Figure 1-16 shows the structure and working principle of this method. The cancel coil is connected to the main coil in series, but in the reverse direction. The magnetic fields generated by the main coils and by the cancel coils then attenuates each other on the side of the coils, as shown in Figure 1-16(b).

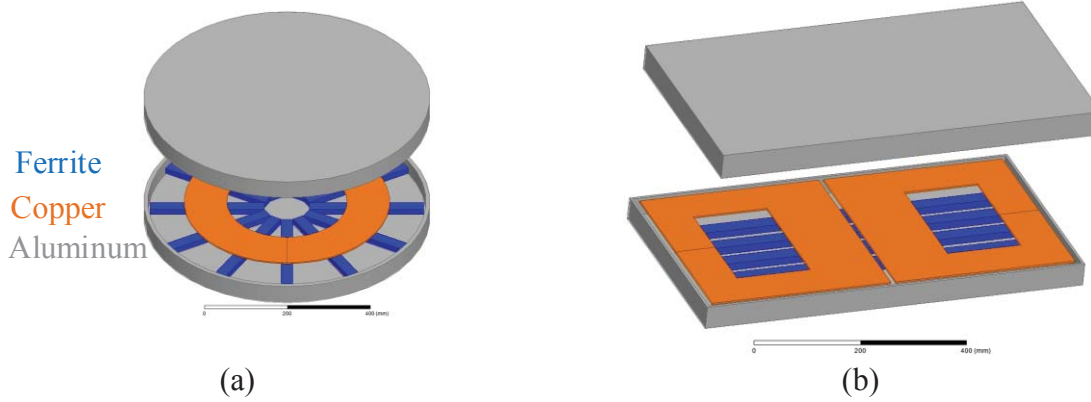


Figure 1-14. Metal shields for (a) circular pad and (b) DD-DDQ pad in references [34] and [35].

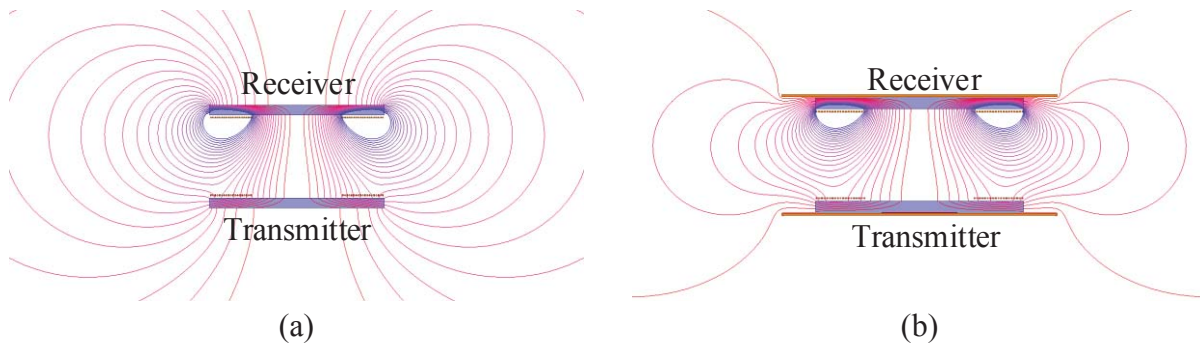


Figure 1-15. Side view for the flux lines of stray magnetic field for coils (a) with magnetic shield only and (b) with magnetic shield plus metal shield.

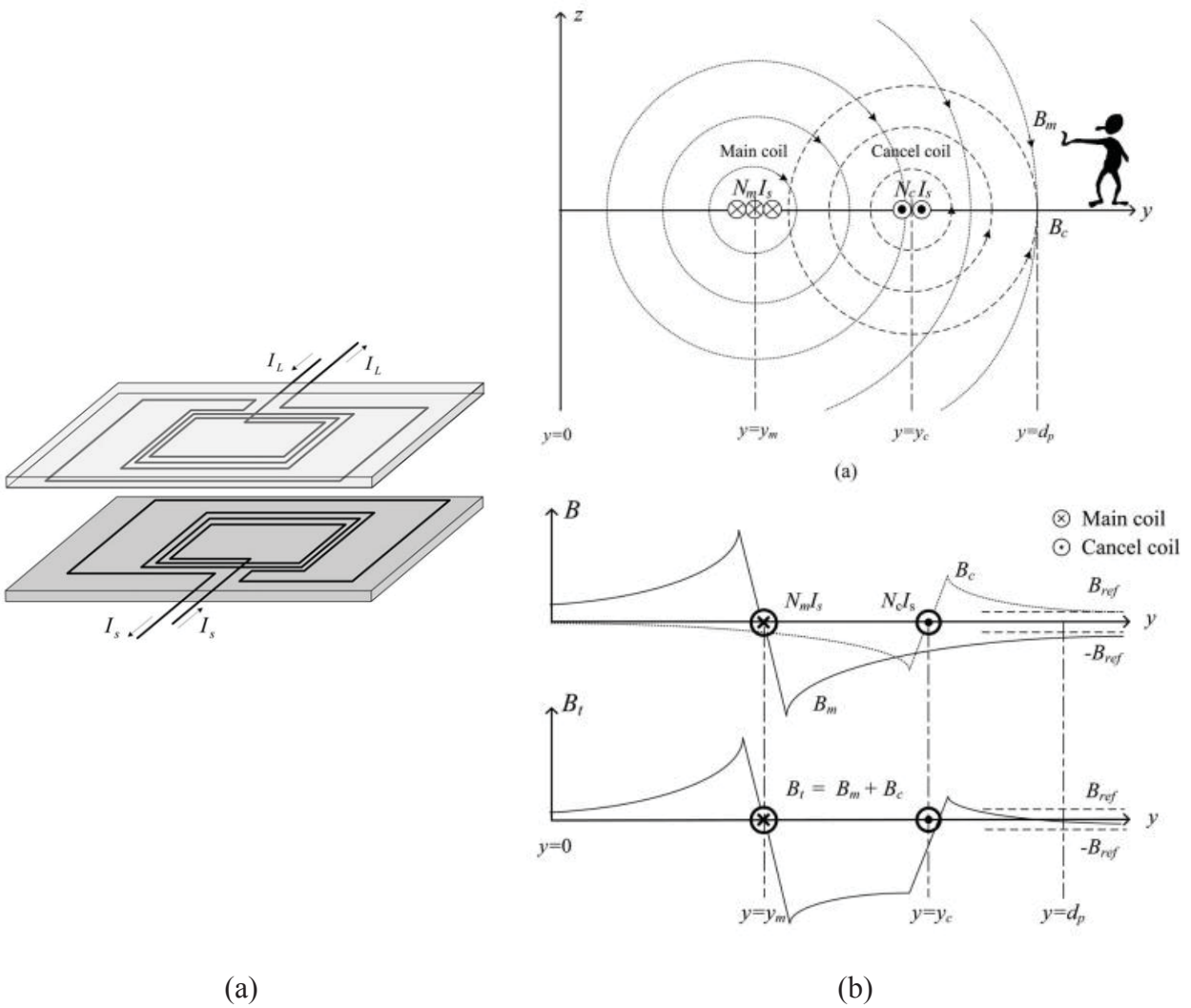


Figure 1-16. Metal shield with supplied winding current [53].

The metal shield effectively attenuates the stray magnetic field with simple implementation. However, it significantly decreases the coil-to-coil efficiency. The size and weight of the coils are increased as well.

1.4.3. Active Shield

Figure 1-17 shows the working principle of the active shield. The coils working as active shields are placed around the power-transfer coils. Field sensors are used to sense the stray magnetic field penetrating the active shields. The phase and magnitude of the shields are calculated and actively controlled according to the sensed field.

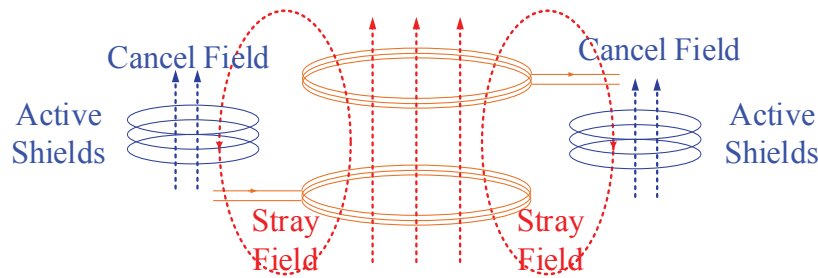


Figure 1-17. Working principle of active shields to attenuate stray magnetic field.

Figure 1-18 illustrates two methods to change the current in the active shields. In Figure 1-18(a), the shield current is directly supplied from an AC current source. In Figure 1-18(b), tunable capacitors are connected to the active shields. Voltage is induced on the active shields by the stray magnetic field. The impedances of the shields are changed by actively tuning the capacitance, which then controls the magnitude and phase of the shielding current for field attenuation.

In reference [54], active shields with tunable capacitors are applied in the inductive power transfer for electric buses. Figure 1-19 shows the architecture of the system. Active shields together with field sensors are placed on the sides of the buses. The capacitor block with active switches are used to realize tunable capacitance.

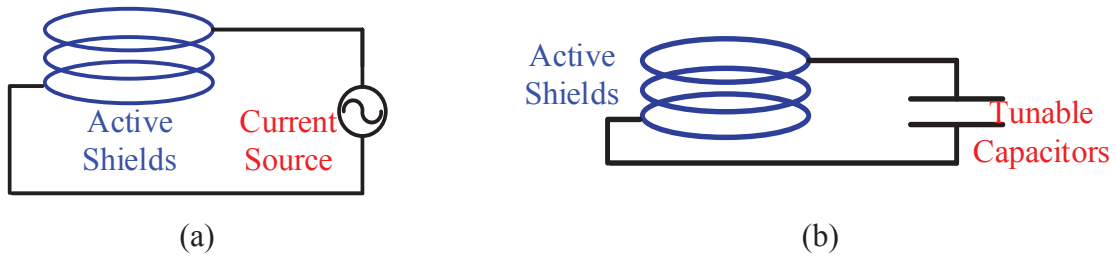


Figure 1-18. Active shields with (a) supplied current or (b) tunable capacitors. The current source and the capacitance are actively controlled according to sensed magnetic field.

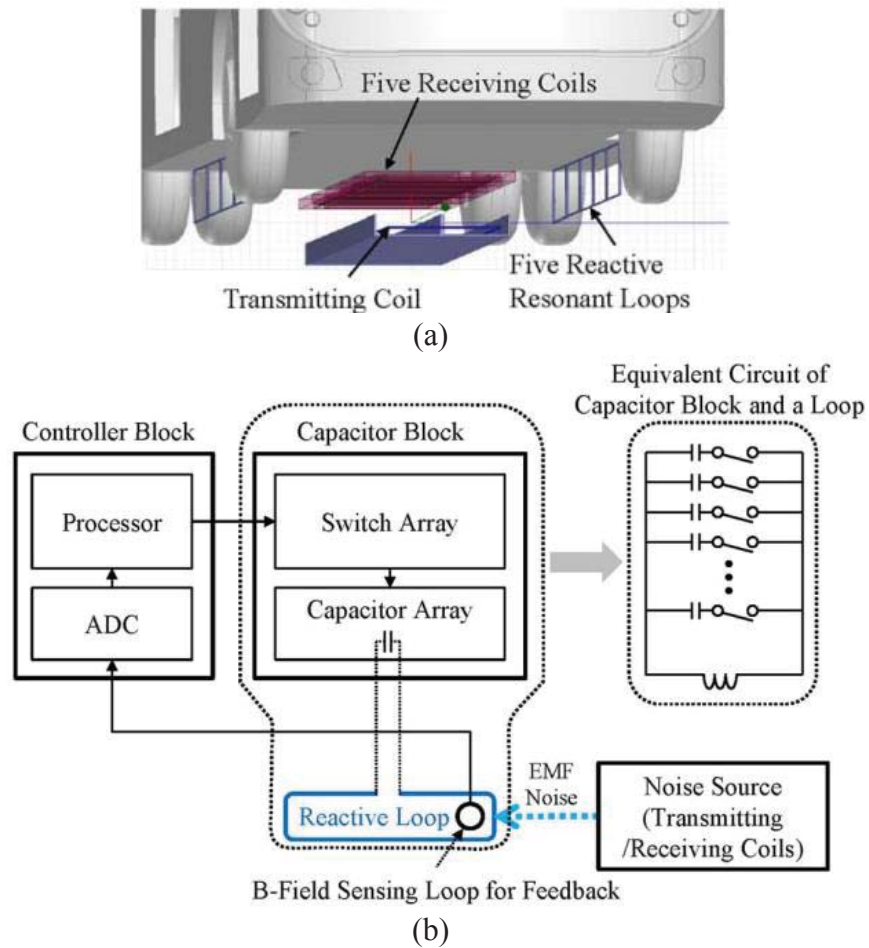


Figure 1-19. Active shield in reference [54].

The disadvantages of the active shields include decreased efficiency, increased size and weight to the system, difficulties for the implementation, the requirement of the field sensors, and complicated control algorithm.

1.5. Challenges to Attenuate Stray Magnetic Field

1.5.1. Reduced Efficiency

The synergetic optimization of the coil-to-coil efficiency and stray magnetic field is required. Although the metal shield in Section 1.4.2 and the active shield in Section 1.4.3 effectively attenuate the stray magnetic field, the efficiency is reduced as the price. The shields bring in extra losses. The conventional metal shields with plate structure or ring structure introduce significant shielding losses owing to the uneven distribution of the shield current. The shields also decrease the coupling coefficient between the coils, resulting in higher winding loss when transferring the same amount of power.

1.5.2. Time-Consuming Optimization

A fast method is needed to realize the synergetic optimization. Pareto front is applied to optimize the coil-to-coil efficiency and stray magnetic field. The front is derived by plotting the results of different structures in a two-dimensional Cartesian coordinate system. In the conventional method, the physical parameters are swept in finite-element simulations. This takes thousands of simulations which is very time-consuming, especially for three-dimensional simulations.

1.5.3. Increased Size and Weight of Coils

A compact structure of IPT coils is preferred in the real application. However, the metal shields and active shields makes the coils bulkier and heavier. A method should be investigated to attenuate the stray magnetic field without increasing the weight and size of the coils.

1.6. Research Objectives and Contributions

1.6.1. Synergetic Optimization of Efficiency and Stray Magnetic Field

The coil-to-coil efficiency is defined as the ratio of the receiver's output power to the transmitter's input power [55]. Losses of the coils contribute 30% to 50% to the total loss of the IPT circuits [46], [49], [56], which means the system's efficiency will be poor if the coil-to-coil efficiency is low. In order to increase the coil-to-coil efficiency, physical parameters of the IPT coils, such as inner radii and outer radii of the windings as well as the distribution of the turns, should be optimized [27], [57], [60].

Magnetic field is dominant compared to electric field in the near-field range where IPT works [61]. Significant stray magnetic field exists around the coils owing to the large air gap between the transmitter and receiver coils. One method to attenuate the stray magnetic field is to optimize the physical parameters of the planar coils [52], [62].

Since both the coil-to-coil efficiency and stray magnetic field are influenced by the physical design of IPT coils, their synergetic optimization is important. Pareto front is suitable for the multi-objective optimization, and it has been used a lot on the design of converters [63], [64]. In this dissertation, synergetic optimization of the coils is realized with Pareto front as well. The fronts are plotted on a two-dimensional Cartesian coordinate system. The horizontal axis and

vertical axis represent magnetic field and efficiency, respectively. The optimal design of the coils should be selected along the fronts.

1.6.2. Fast Optimization Method

One straightforward way to derive the Pareto fronts is to sweep all the physical parameters of the IPT coils in finite-element simulation. The results from the parametric sweep are plotted on the Cartesian coordinate system to derive the Pareto fronts. However, this takes for thousands of simulations, which is very time-consuming, especially when three-dimensional simulations are required [52].

This dissertation demonstrates a faster optimization method which requires only tens of simulations during the entire procedure. The windings are replaced by several lumped loops [65], [66]. The permeance matrices and current-to-field matrices are used to calculate the inductances and stray magnetic fields, respectively. As long as the number of turns for each loop is known, the efficiency and magnetic field are calculated directly from the matrices. Only tens of simulations are implemented to derive the permeance matrices and the current-to-field matrices. Therefore, sweeping the physical parameters in finite-element simulation is replaced by sweeping numbers of turns for the lumped loops in calculation. This makes the optimization fast without losing the accuracy.

An analytical method is investigated to calculate the proximity-effect resistance of the winding, which is used to work together with the fast optimization. The magnetic fields across each turn are critical to calculate the resistance, but the existence of the ferrite plate complicates the derivation of the the magnetic fields. According to the method of image, the ferrite plates are replaced by mirrored turns. Then the magnetic fields are obtained from Ampere's Law and Biot-Savart Law analytically.

1.6.3. Shield Structures with Less Losses

The conventional metal shields cause significant shielding losses, owing to the uneven distribution of shielding current. The skin depth is 0.2 mm for copper and 0.26 mm for aluminum at 100 kHz. Most of the shield current flows on the surface which increases conduction losses. Litz wires are used as metal shields to reduce the shielding losses, in which the shield current are almost uniformly distributed.

Two structures of litz shields are discussed in this dissertation, which are named shorted litz shield and driven litz shield [67]. Turns of litz wires are placed around the windings for shielding purpose. In shorted litz shield, the shield turns of litz wire are self-shortened and not connected to the windings. Eddy current is induced on the shield for field attenuation. In driven litz shield, the shield turns are connected to the windings in series, but in the reverse direction. The induced eddy current in shorted litz shield and the supplied current in driven litz shield are evenly distributed in the shields, so the shield loss should be smaller than that of the plate shield and ring shield.

Circuit models are derived to analyze the behaviors of the coils with litz shields. The litz shields are modeled as inductors coupled with the windings, so the coils with litz shields are represented as four coupled inductors. Currents of windings and shields, equivalent inductances, and equivalent series resistances (ESRs) are all calculated from the circuit models.

Both the coil-to-coil efficiency and the stray magnetic field should be considered during the design of litz shield. Pareto fronts are used for their optimization. The fronts are derived with the concept of lumped-loop model. The windings and litz shields are replaced by several lumped loops. Sweeping geometrical parameters in finite-element simulation is replaced by sweeping the numbers of turns for the lumped loops in calculation. The inductances and stray magnetic fields

are derived from matrices and turns vectors. The resistances of windings and shields are analytically calculated by replacing the ferrite plate with mirrored turns according to the method of image.

1.6.4. Field Attenuation without Increasing Coils Size

To avoid making the coils bulkier, a method to attenuate stray magnetic field by controlling the phases of winding currents is investigated. Magnetic field is decomposed to components in axial and radial directions. The axial component decreases when the phase difference between winding currents is smaller, whereas the axial component exhibits the opposite property. Because the axial component of stray magnetic field on the side of IPT coils is dominant, it's preferred to decrease the phase difference.

The dual-side-controlled converter is applied for the circuit realization. Bridges with active switches are used for both the inverter on the transmitter side and the rectifier on the receiver side. Switching frequency equals the resonant frequency. The magnitudes of winding currents are controlled by pulse-widths of inverter voltage and rectifier voltage. The phases of winding currents are tuned with phases of voltages. Equations are derived from the equivalent circuit model of the converter, and they are used to predict the field attenuation with phases of currents. The increased winding loss is analyzed with the equivalent circuit model.

1.6.5. Systematic Procedure to Design IPT Coils

The requirements of power transferability and efficiency in inductive power transfer are satisfied by proper design of coils. Complex iterations are always required for coils design in IPT because the electrical parameters of coils (such as self-inductance, mutual inductance, and winding resistance) and converters (such as resonant and switching frequencies, and load

conditions) are coupled together. Reference [68] demonstrates an iterative process to optimize the coils' power transferability and efficiency using a design factor. Another method by sweeping parameters is proposed in [57] to minimize transmitter current for high efficiency. One way to avoid iterations is to pre-evaluate the coils' performance using the figure of merit (FOM). Reference [55] describes $k*Q$ as the FOM for IPT coils because it determines the maximum efficiency that the coils can potentially achieve when the system operates at resonant frequency and optimal load conditions, where k is the coupling coefficient and Q is the quality factor of the coil. Coils in [5] and [46] are selected to maximize this FOM. However, in some cases the IPT system is not operating at resonant frequency or the load is not optimal for efficiency. It's not intuitive to use $k*Q$ to predict whether the efficiency meets the requirement under specific conditions.

Coils with high Q are preferred in order to meet efficiency requirement. Coils either with larger size and thicker wire or with special structures such as that in [69] can be applied to achieve high Q , but these may increase the size and weight of coils or complicate the fabrication process. In order to minimize the size and ease the fabrication of the coils, the smallest value of Q to meet efficiency requirement should be derived, based on which the coils are designed and fabricated.

A method is discussed in this dissertation to design the coils for series-series IPT system systematically to meet given specifications. It avoids trial-and-error which is always required in the conventional design method. Requirements of power transferability and efficiency are met with the smallest value of Q . Two possible operating conditions of the series-series IPT are discussed: when the compensation capacitor resonates with self-inductance or resonates with

leakage inductance. The design procedure is good for both cases, and it includes two steps: electrical design and physical realization.

1.7. Dissertation Outline

Chapter 2 demonstrates a systematic procedure which designs the IPT coils to maximize the coil-to-coil efficiency, without considering stray magnetic field. The electrical parameters of IPT coils and converters are normalized to simplify the design process. Physical realization of the electrical parameters is implemented with finite-element simulations. A set of coils with 99% efficiency was developed to transfer 3.3 kW across 100 mm gap.

Chapter 3 investigates how to fast optimize the coils for efficiency and stray magnetic field. The coils with real turns are replaced with lumped-loop model. Turns vectors are used to represent the physical parameters of coils, such as radii of the winding, distribution of the turns, and sizes of litz wires. The inductances and stray magnetic field are calculated using permeance matrices and current-to-field matrices. Only tens of finite-element simulations are required in the entire optimization, so it's much faster than the conventional method which takes thousands of simulations.

Chapter 4 shows the method to approximate the proximity-effect resistance of IPT coils. In order to calculate the proximity-effect loss, magnetic fields across each turn should be derived. The conventional method to derive the magnetic fields is from finite-element simulation. However, it's not suitable to simulate the magnetic fields for all the cases during the optimization process. An analytical method is investigated in this chapter to approximate the magnetic fields with the existence of ferrite plate. The ferrite plate is replaced by mirrored turns, according to the method of image. After that, the magnetic field is analytically derived from Ampere's law and

Biot-Savart law. The difference of the proximity-effect resistance between calculation and measurement is less than 15% for a set of exemplary coils.

Chapter 5 discusses litz shields for IPT coils which have smaller shielding losses than the conventional metal shields. Two structures of litz shields are discussed, namely shorted litz shield and driven litz shield. The equivalent circuit models are given to analyze the behavior of the coils with litz shields. The optimization for the efficiency and field attenuation is realized using the concept of lumped-loop model which is mentioned in Chapter 3. With the same efficiency, shorted litz shield attenuated the stray magnetic field by up to 65% compared to the coils without metal shield.

Chapter 6 illustrates a method to attenuate the stray magnetic field without increasing the size and weight of the coils. The stray magnetic field is attenuated by controlling the phases of winding currents of the transmitter and receiver. In order to realize this, full bridges with active switches are implemented on both sides. The phases and amplitudes of winding currents are controlled by proper switching sequence of the bridges. Compared to the conventional series-series IPT which has 90° phase difference between winding currents, stray magnetic field is attenuated by up to 30% and 40% when the phases differences of winding currents are 50° and 40° , respectively. The comparison of the methods in Chapter 5 and Chapter 6 shows metal shield has better performance for field attenuation than the method of phase control, but these two methods can be combined for further attenuation of stray magnetic field.

Chapter 2. Baseline Coils Design – Efficiency Maximization without Considering Stray Magnetic Field

Nomenclature

f_0	Resonant frequency in (2-1).
f_N	Normalized switching frequency in TABLE 2-2.
f_{NH}	Normalized switching frequency for constant voltage gain in (2-27).
f_s	Switching frequency of the inverter.
I_{out}	Output current in Figure 2-1.
k	Coupling coefficient between transmitter and receiver.
L_0	Self-inductance of the simplified model with one turn in Figure 2-9(b).
L_1	Self-inductance of transmitter.
L_2	Self-inductance of receiver.
M	Mutual inductance between transmitter and receiver.
M_V	Voltage gain in (2-4).
n	Turns ratio of receiver coil over transmitter coil.
N_1	Turns number of transmitter.
N_2	Turns number of receiver.
Q_1	Quality factor of transmitter in TABLE 2-2.
Q_2	Quality factor of receiver in TABLE 2-2.
$Q_{Z_{Nopt}}$	The smallest value of Q for the required efficiency when $Z_N = Z_{Nopt}$.

r_1	ESR of transmitter at switching frequency.
r_2	ESR of receiver at switching frequency.
R_{inner}	Inner radius of the winding.
R_{Lac}	Equivalent load resistance in Figure 2-3.
R_{outer}	Outer radius of the winding.
V_{in}	Input DC voltage in Figure 2-1.
V_{in_ac}	Amplitude of the sinusoidal voltage source in Figure 2-3.
V_{out}	Output DC voltage in Figure 2-1.
V_{out_ac}	Amplitude of the load voltage in Figure 2-3.
$Z_{in,\omega}$	Input impedance of the equivalent circuit model in Figure 2-3.
Z_{N1}	Normalized impedance of transmitter to load in TABLE 2-2.
Z_{N2}	Normalized impedance of receiver to load in TABLE 2-2.
Z_{Nopt}	Optimal value of Z_N for maximum efficiency in (2-32) and (2-38).
α	Pulse-width of inverter output voltage in Figure 2-2.
λ_{coil}	Loss factor of the coils in (2-5).
φ_{Zin}	Phase of $Z_{in,\omega}$ in (2-6).
ω_0	Resonant angular frequency.
ω_s	Switching angular frequency.

2.1. Introduction

Loosely coupled coils are applied in inductive power transfer (IPT) systems to replace the cables and plugs in the conventional charging method for electric vehicles (EVs) [6]–[9]. Power is transferred through a distance up to tens of centimeters based on magnetic resonance and near-

field coupling. Advantages of IPT include convenience for drivers, safety for charging in humid environment, and potential of dynamic charging when vehicles are moving [10], [11].

Figure 2-1 shows the circuit topology with series-series compensation. Switching frequency and inverter output voltage can be tuned for different conditions to realize desired power transfer [46], [48]. Coils are crucial to the performance of series-series IPT system [70], [71]. The requirements of power transferability and efficiency are satisfied by proper design of coils.

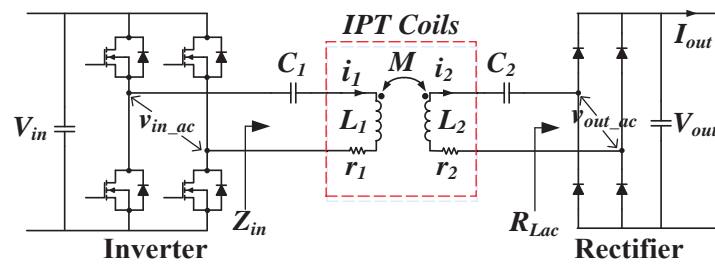


Figure 2-1. The circuit topology with series-series compensation of coils for IPT.

Trial-and-error is always required for coils design in IPT because the electrical parameters of coils (e.g. self-inductance, mutual inductance, and winding resistance) and converters (e.g. resonant and switching frequencies, and load conditions) are coupled together. The objective of this chapter is to systematically design the coils for series-series IPT system to meet the given specifications. The requirements of power transferability and efficiency are met with the smallest value of Q . Two possible operating conditions of series-series IPT are discussed: when the compensation capacitor resonates with self-inductance or with leakage inductance. The design procedure is good for both cases, and it includes two steps: electrical design and physical realization.

Electrical parameters are normalized and then systematically designed, which makes the design faster and more generalized. Normalized parameters include normalized impedance Z_N , coil quality factors Q , normalized switching frequency f_N , coupling coefficient k , and turns ratio n . Power transferability is determined by n . Optimal Z_N is selected to meet the efficiency requirement with the smallest value of Q . Because all the electrical parameters are normalized, the equations and plots are generalized and they are good to use for different specifications.

Physical realization is implemented after electrical design. Planar coils with spiral winding and ferrite plate are mostly used for IPT due to low profile [29], [35]. Finite-element simulations are used to derive plots of electrical parameter (such as coupling coefficient and self-inductance) versus physical parameters (such as inner radii and outer radii of winding). Then turns number to realize optimal Z_N and wire size to satisfy Q are calculated and selected from these plots.

Section 2.2 analyzes IPT with simplified circuit model and introduces design equations with normalized parameters. Section 2.3 presents the procedure to systematically design electrical parameters for efficient power transfer with smallest Q . Section 2.4 demonstrates the physical realization of coils using generalized plots derived from finite-element simulation. In Section 2.5, the coils for a 3.3 kW IPT system with dimensions of 250 mm \times 250 mm and an air gap of 100 mm were built for experimental verification. The coils' loss factor of 1.1% was achieved which was designed for 1%.

2.2. Design Equations for Converter and Coils

Figure 2-1 shows the circuit topology with series-series compensation of coils for IPT. Resonant frequency f_0 of C_1 and L_1 is the same as that of C_2 and L_2

$$\frac{1}{\sqrt{L_1 C_1}} = \frac{1}{\sqrt{L_2 C_2}} = 2\pi f_0 \quad (2-1)$$

where L_1 and L_2 are the self-inductances of transmitter and receiver coils, respectively.

Switching frequency and phase-shift between legs are two commonly used methods to regulate output [46]–[49]. Switching frequency moves the operating point of the system and minimizes the effect when coupling or load condition changes. Phase-shift controls the inverter output voltage as shown in Figure 2-2, and it directly regulates the bulk power transferred to the load. Both methods can be used in coordination to control the power transfer and maintain the efficiency.

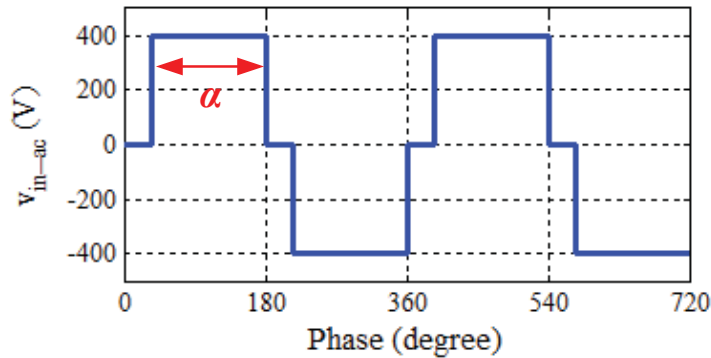


Figure 2-2. Output voltage of inverter v_{in_ac} in Figure 2-1 with phase shift.

Simplified circuit model in Figure 2-3 is used for analysis. Under the first harmonic approximation, input DC voltage source and inverter are modeled as sinusoidal voltage source $v_{in_ac, \omega}(t)$ with peak amplitude $(4/\pi)V_{in}$, switching angular frequency $\omega_s = 2\pi f_s$, and pulse-width α . Passive rectifier and load are modeled with equivalent resistor R_{Lac} . Expressions of $v_{in_ac, \omega}(t)$ and R_{Lac} are

$$v_{in_ac,\omega}(t) = \frac{4}{\pi} V_{in} \sin\left(\frac{\alpha}{2}\right) \cdot e^{j\omega t} \quad (2-2)$$

$$R_{Lac} = \frac{8}{\pi^2} \cdot \frac{V_{out}}{I_{out}} \quad (2-3)$$

where V_{in} , V_{out} , I_{out} and are input voltage, output voltage, and output current in Figure 2-1; α is the pulse-width of inverter output voltage in Figure 2-3.

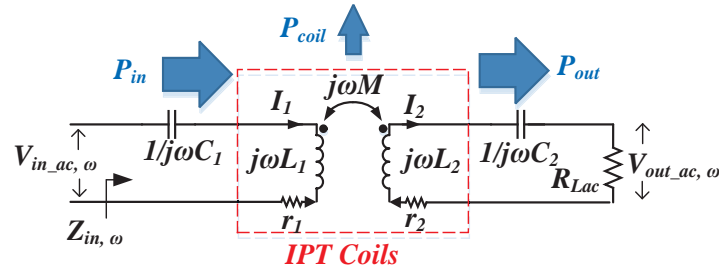


Figure 2-3. Equivalent circuit model of the circuit topology in Figure 2-1.

Voltage gain M_V in Figure 2-3 is defined as the ratio of $V_{out_ac,\omega}$ over $V_{in_ac,\omega}$ as

$$M_V = \left| \frac{V_{out_ac,\omega}}{V_{in_ac,\omega}} \right| = \frac{V_{out}}{V_{in} \sin\left(\frac{\alpha}{2}\right)} \quad (2-4)$$

When phase-shift is not used, α is 180° and M_V equals the ratio of V_{out} over V_{in} .

The loss factor λ_{coil} of coils is determined in (2-5) as the ratio of coils' loss P_{coil} over the transferred power P_{out} in Figure 2-3. The loss factor should be small for high efficiency of coils.

$$\lambda_{coil} = \frac{P_{coil}}{P_{out}} \quad (2-5)$$

When MOSFETs are used in the inverter, high current stress and turn-on loss are caused by the reverse-recovery of body diode of the opposite switch if zero-voltage turn-on is lost.

Inductive impedance $Z_{in,\omega} = R_{Zin,\omega} + jX_{Zin,\omega}$ in Figure 2-3 for soft-turn-ons of switches is equivalent to positive φ_{Zin} . The phase angle of $Z_{in,\omega}$ equals

$$\varphi_{Zin} = \arctan\left(\frac{X_{Zin,\omega}}{R_{Zin,\omega}}\right) \quad (2-6)$$

Equations (2-7) and (2-8) are derived from Figure 2-3 to analyze the behavior of the circuit.

$$V_{in_ac,\omega} = \left[r_1 + j \cdot \left(\omega_s L_1 - \frac{1}{\omega_s C_1} \right) \right] I_1 - j \cdot \omega_s M \cdot I_2 \quad (2-7)$$

$$0 = j \cdot \omega_s M \cdot I_1 - \left[r_2 + R_{Lac} + j \cdot \left(\omega_s L_2 - \frac{1}{\omega_s C_2} \right) \right] I_2 \quad (2-8)$$

where L_1 and L_2 are the self-inductances; M is the mutual inductance; r_1 and r_2 are the equivalent series resistances (ESR) of transmitter and receiver coils at switching frequency; C_1 and C_2 are the resonant capacitors; R_{Lac} is the equivalent load resistance in (2-3); I_1 and I_2 are the currents of transmitter and receiver coils, respectively.

Expressions of M_V , λ_{coil} , and φ_{Zin} in (2-4) – (2-6) are derived from (2-7) and (2-8) [9], [47] as

$$M_V = \frac{\omega_s M \cdot R_{Lac}}{\left| \begin{array}{l} \left(\omega_s M \right)^2 + r_1 \cdot (r_2 + R_{Lac}) - \left(\omega_s L_1 - \frac{1}{\omega_s C_1} \right) \left(\omega_s L_2 - \frac{1}{\omega_s C_2} \right) \\ + j \cdot \left[r_1 \left(\omega_s L_2 - \frac{1}{\omega_s C_2} \right) + (r_2 + R_{Lac}) \left(\omega_s L_1 - \frac{1}{\omega_s C_1} \right) \right] \end{array} \right|} \quad (2-9)$$

$$\lambda_{coil} = \frac{r_2}{R_{Lac}} + \frac{r_1}{R_{Lac}} \cdot \frac{\left(r_2 + R_{Lac} \right)^2 + \left(\omega_s L_2 - \frac{1}{\omega_s C_2} \right)^2}{\left(\omega_s M \right)^2} \quad (2-10)$$

$$\varphi_{Zin} = \arctan \frac{\left(\omega_s L_1 - \frac{1}{\omega_s C_1} \right) \left[(r_2 + R_{Lac})^2 + \left(\omega_s L_2 - \frac{1}{\omega_s C_2} \right)^2 \right] - (\omega_s M)^2 \left(\omega_s L_2 - \frac{1}{\omega_s C_2} \right)}{r_1 \left[(r_2 + R_{Lac})^2 + \left(\omega_s L_2 - \frac{1}{\omega_s C_2} \right)^2 \right] + (\omega_s M)^2 (r_2 + R_{Lac})} \quad (2-11)$$

There are eight unknown parameters in (2-9) – (2-11) which are listed in TABLE 2-1. They are calculated to meet the requirements of power transferability and efficiency. This results in complicated iterations. The parameters in TABLE 2-1 are normalized as shown in TABLE 2-2 in order to simplify the design procedure. The number of unknowns for calculation is reduced from eight to six.

TABLE 2-1. Unknown Parameters for the Design of Coils

Parameters	Symbols
Self-inductance of coil 1	L_1
Self-inductance of coil 2	L_2
Mutual inductance	M
ESR of coil 1 at switching frequency	r_1
ESR of coil 2 at switching frequency	r_2
Load resistance	R_{Lac}
Resonant angular frequency	$\omega_0 = 2\pi f_0$
Switching angular frequency	$\omega_s = 2\pi f_s$

TABLE 2-2. Normalized Parameters for the Design of Coils

Normalized Parameters	Symbols
Coupling coefficient	k
Normalized switching frequency	$f_N = f_s / f_0$
Normalized impedance of transmitter coil to load	$Z_{N1} = \omega_s L_1 / R_{Lac}$
Quality factor of transmitter coil	$Q_1 = \omega_s L_1 / r_1$
Normalized impedance of receiver coil to load	$Z_{N2} = \omega_s L_2 / R_{Lac}$
Quality factor of receiver coil	$Q_2 = \omega_s L_2 / r_2$

Coupling coefficient k is used to define the coupling condition of coils as

$$k = \frac{M}{\sqrt{L_1 L_2}} \quad (2-12)$$

The self-inductances L_1 and L_2 and the mutual inductance M are derived from finite-element simulation or analytical equations [72]–[76].

Equations (2-9) – (2-11) are represented as (2-13) – (2-15), using the normalized parameters listed in TABLE 2-2.

$$M_V = \sqrt{\frac{Z_{N2}}{Z_{N1}}} \frac{k}{\sqrt{\left[k^2 \cdot Z_{N2} + \frac{Q_2 + Z_{N2}}{Q_1 \cdot Q_2} - \left(1 - \frac{1}{f_N^2} \right)^2 Z_{N2} \right]^2 + \left[\left(1 + \frac{Z_{N2}}{Q_1} + \frac{Z_{N2}}{Q_2} \right) \left(1 - \frac{1}{f_N^2} \right) \right]^2}} \quad (2-13)$$

$$\lambda_{coil} = \frac{Z_{N2}}{Q_2} + \frac{Z_{N2}}{k^2 \cdot Q_1} \left(\frac{1}{Z_{N2}} + \frac{1}{Q_2} \right)^2 + \frac{Z_{N2}}{k^2 \cdot Q_1} \left(1 - \frac{1}{f_N^2} \right)^2 \quad (2-14)$$

$$\varphi_{Zin} = \arctan \left\{ \left(1 - \frac{1}{f_N^2}\right) \frac{\left[\left(1 - \frac{1}{f_N^2}\right)^2 - k^2 + \left(\frac{1}{Z_{N2}} + \frac{1}{Q_2}\right)^2 \right] \cdot Q_1}{\left(1 - \frac{1}{f_N^2}\right)^2 + k^2 \cdot Q_1 \cdot \left(\frac{1}{Z_{N2}} + \frac{1}{Q_2}\right) + \left(\frac{1}{Z_{N2}} + \frac{1}{Q_2}\right)^2} \right\} \quad (2-15)$$

To simplify the design, equations (2-13) and (2-15) are replaced with (2-16) and (2-17), with the assumption that $Z_{N1} \ll Q_1$ and $Z_{N2} \ll Q_2$. In most cases this assumption is reasonable because coils' ESR should be small for high efficiency.

$$M_V \approx \sqrt{\frac{Z_{N2}}{Z_{N1}}} \frac{k}{\sqrt{\left[k^2 - \left(1 - \frac{1}{f_N^2}\right)^2 \right]^2 Z_{N2}^2 + \left(1 - \frac{1}{f_N^2}\right)^2}} \quad (2-16)$$

$$\varphi_{Zin} \approx \arctan \left\{ \left(1 - \frac{1}{f_N^2}\right) \frac{1 - k^2 \cdot Z_{N2}^2 + \left(1 - \frac{1}{f_N^2}\right)^2 \cdot Z_{N2}^2}{k^2 \cdot Z_{N2}} \right\} \quad (2-17)$$

When geometries of transmitter and receiver coils are the same, L_1 and L_2 are proportional to N^2 , where N is the turns number of litz wire. In this case, Z_{N1} and Z_{N2} are proportional to N^2 as well. The relationship between Q_1 , Q_2 and N is more complicated because both DC loss and proximity effect contribute to the value of Q . The DC resistance is proportional to N since it's related to the length of the coil. The proximity effect is proportional to N^3 because it's proportional to the square of the magnetic field as well as the length of the coil [77]–[79]. However, the proximity effect is weak in the frequency range where IPT works for EV charging. Besides, the coil size for EV application is large, so usually limited number of turns is needed for the desired inductance value. This further weakens the proximity effect. Figure 2-4 shows an exemplary planar coil. The percentages of its proximity resistance and DC resistance to its

winding resistance versus N at 100 kHz is plotted in Figure 2-5(a). The proximity effect is not significant. Figure 2-5 (b) shows that Z_N is roughly proportional to N^2 and Q is proportional to N .

Therefore, the relationship of Q_1, Q_2, Z_{N1}, Z_{N2} is

$$\frac{Q_2}{Q_1} = \sqrt{\frac{Z_{N2}}{Z_{N1}}} = n \quad (2-18)$$

where n is the turn ratio of receiver coil over transmitter coil as

$$n = \frac{N_2}{N_1} \quad (2-19)$$

To simplify the design process, Z_{N1} and Z_{N2} are represented with Z_N as

$$Z_{N1} = Z_N \quad (2-20)$$

$$Z_{N2} = n^2 \cdot Z_N \quad (2-21)$$

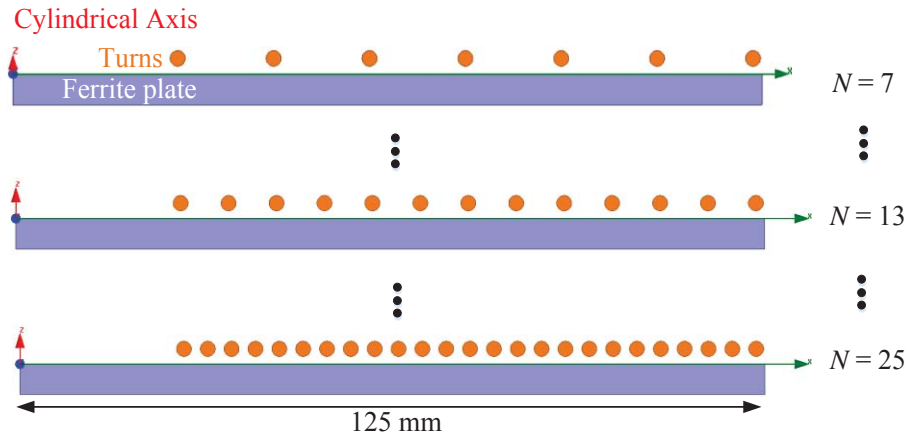


Figure 2-4. Cylindrical 2D model of an exemplary coil to analyze the influence of proximity-effect resistance. Turns number increases from $N = 7$ to $N = 25$ while inner radii and outer radii of the winding are kept the same. The litz wire consists 1650 strands of AWG 44 wires.

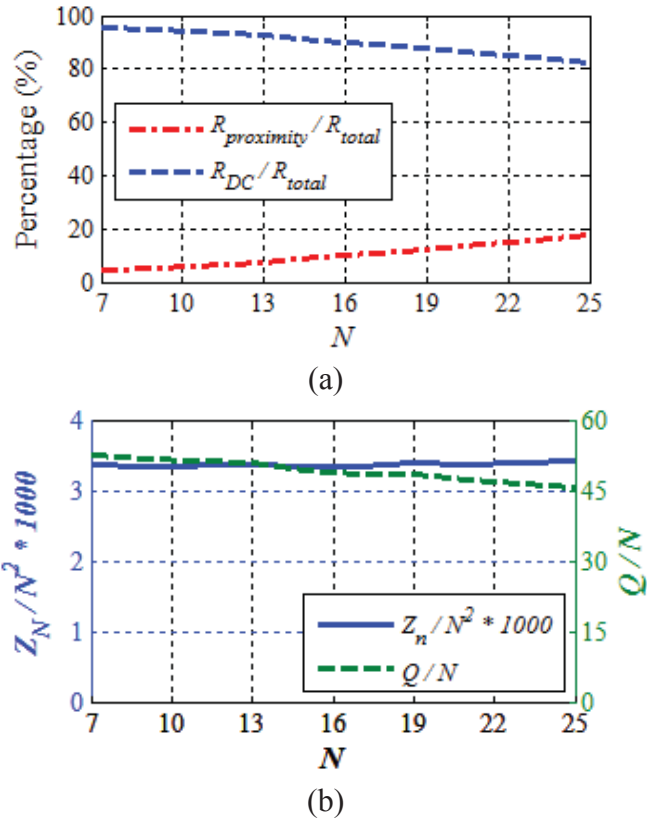


Figure 2-5. (a) Percentage of the proximity resistance and DC resistance to the total resistance of winding for different turns number N in Figure 2-4 at 100 kHz; (b) normalized impedance Z_N is proportional to N^2 and quality factor Q is proportional to N .

Similarly, Q_1 and Q_2 are represented with Q as

$$Q_1 = Q \quad (2-22)$$

$$Q_2 = n \cdot Q \quad (2-23)$$

Equations of M_V , λ_{coil} , and φ_{Zin} in (2-14), (2-16), and (2-17) are simplified with Z_N , Q , and n in (2-20) - (2-23) as

$$M_V = n \cdot \frac{k}{\sqrt{\left[k^2 - \left(1 - \frac{1}{f_N^2} \right)^2 \right]^2 \cdot n^4 \cdot Z_N^2 + \left(1 - \frac{1}{f_N^2} \right)^2}} \quad (2-24)$$

$$\lambda_{coil} = n \cdot \frac{Z_N}{Q} + \frac{Z_N}{k^2 \cdot Q} \cdot \left(\frac{1}{n \cdot Z_N} + \frac{1}{Q} \right)^2 + n^2 \cdot \frac{Z_N}{k^2 \cdot Q} \cdot \left(1 - \frac{1}{f_N^2} \right)^2 \quad (2-25)$$

$$\varphi_{Zin} = \arctan \left\{ \left(1 - \frac{1}{f_N^2} \right) \frac{1 - k^2 \cdot n^4 \cdot Z_N^2 + \left(1 - \frac{1}{f_N^2} \right)^2 \cdot n^4 \cdot Z_N^2}{k^2 \cdot n^2 \cdot Z_N} \right\} \quad (2-26)$$

The six unknowns in TABLE 2-2 are now further reduced to five: coupling coefficient k , normalized switching frequency f_N , normalized impedance Z_N , coil quality factor Q , and turns ratio n . The feasibility to systematically design the normalized parameters is demonstrated in the next session.

2.3. Systematic Design of Electrical Parameters

Normalized parameters k , f_N , Z_N , Q , and n are designed in this section for power transferability and efficiency. Figure 2-6 shows M_V in (2-24), φ_{Zin} in (2-26), and λ_{coil} in (2-25) versus f_N and Z_N .

A series-series IPT can be designed with the compensation capacitors resonating with leakage inductances or with self-inductances. When the normalized switching frequency f_N equals f_{NH} , the capacitors resonate with the leakage inductances. When the normalized switching frequency $f_N = 1$, the capacitors resonate with the self-inductances. The value of f_{NH} is derived from equation (38) in [80] as

$$f_{NH} = \frac{1}{\sqrt{1-k}} \quad (2-27)$$

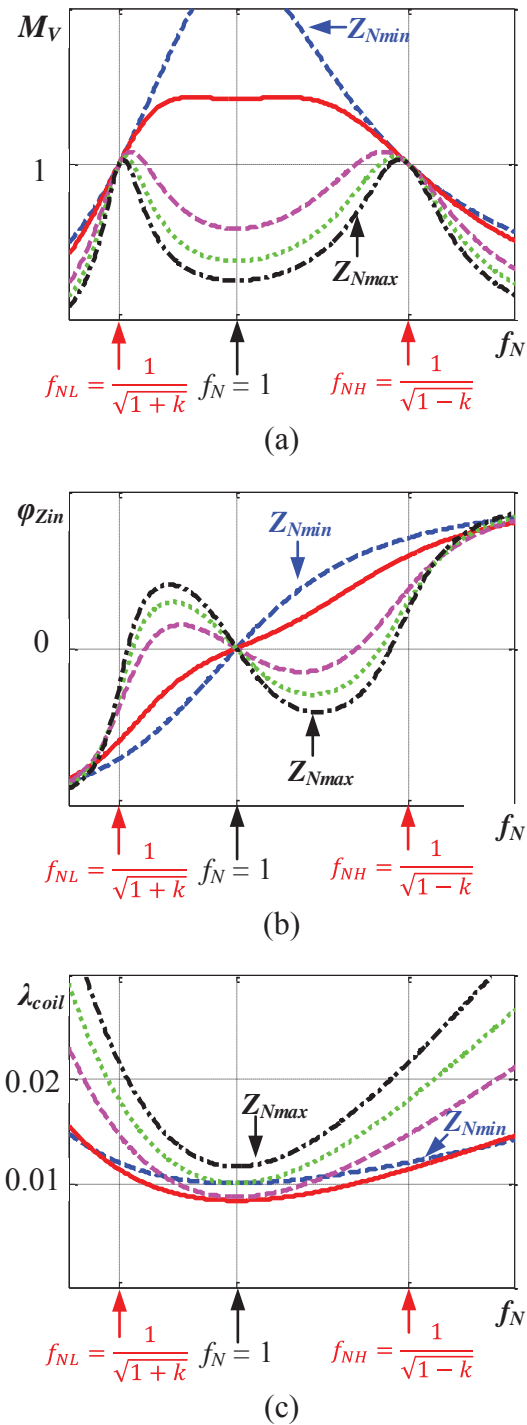


Figure 2-6. (a) M_V in (2-24), (b) ϕ_{Zin} in (2-26), and (c) λ_{coil} in (2-25) versus f_N and Z_N when $n = 1$, $k = 0.25$, and $Q = 1000$.

2.3.1. Operating Condition $f_N = f_{NH}$

When the switching frequency is no lower than f_{NH} , the highest output voltage is achieved at $f_N = f_{NH}$. Smaller output voltages are realized with either phase-shift or setting $f_N > f_{NH}$. The benefits of operating at f_{NH} include easier controllability of output voltage [80] and avoidance of bifurcation when load condition changes [28], [57], [81]. The bifurcation generates two peaks of M_V as shown in Figure 2-6 with Z_{Nmax} , which complicates the control. The major disadvantages to operate at $f_N = f_{NH}$ include the dependence of f_{NH} on the values of k and higher λ_{coil} compared to $f_N = 1$. The higher λ_{coil} at $f_N = f_{NH}$ is also shown in Figure 2-6(c) and discussed in [82].

Voltage gain M_V in (2-24), phase φ_{Zin} of input impedance in (2-26), and loss factor λ_{coil} in (2-25) are calculated with $f_N = f_{NH}$ as

$$M_V = n \quad (2-28)$$

$$\varphi_{Zin} = \arctan\left(\frac{1}{k \cdot n^2 \cdot Z_N}\right) \quad (2-29)$$

$$\lambda_{coil} = M_V \cdot \frac{Z_N}{Q} + M_V^2 \cdot \frac{Z_N}{Q} + \frac{Z_N}{k^2 \cdot Q} \left(\frac{1}{M_V \cdot Z_N} + \frac{1}{Q} \right)^2 \quad (2-30)$$

Equation (2-28) demonstrates that the power transferability is realized by simply choosing the turns ratio n of the coils. Equation (2-29) shows φ_{Zin} is always positive when $f_N = f_{NH}$ for different load conditions.

Ideally, Q should be as high as possible to reduce the loss factor in (2-30) for high efficiency. This is not practical in many cases because either special structure of coils or customized thicker wire should be applied to increase Q . It's important to calculate the smallest value of Q that satisfies the efficiency requirement. The loss factor λ_{coil} is determined by Z_N and Q . For each Q , the smallest λ_{coil} is achieved when partial derivative of (2-30) to Z_N equals to zero as

$$\partial\lambda_{coil}/\partial Z_N = 0 \quad (2-31)$$

The solution of (2-31), which is represented as Z_{Nopt} , is derived as

$$Z_{Nopt} = \frac{1}{k \cdot M_V \cdot \sqrt{M_V + M_V^2}} \quad (2-32)$$

The smallest value of Q to meet efficiency requirement is when $Z_N = Z_{Nopt}$. In (2-32), Z_{Nopt} is independent of Q , and it's determined by k and M_V only. This means Z_N and Q can be optimized sequentially. Figure 2-7(a) shows Z_{Nopt} versus M_V and k . Because M_V is selected from specifications, Z_{Nopt} is only determined by k .

The smallest value of Q for the required λ_{coil} , which is represented as Q_{ZNopt} , is calculated from (2-30) with k , M_V , and $Z_N = Z_{Nopt}$. As an example, Q_{ZNopt} for $\lambda_{coil} = 1\%$ is plotted in Figure 2-7(b) versus k and M_V . The requirement for λ_{coil} is realized when $Q > Q_{ZNopt}$. Figure 2-7(b) shows that the value of Q_{ZNopt} should be larger than 1200 to realize $\lambda_{coil} < 1\%$ when k is lower than 0.2. The size of coils should be optimized to increase k and to achieve required λ_{coil} with practical value of Q which is usually smaller than 1200. Physical realization of coils is discussed in detail in Section 2.4.

Up to now, normalized parameters n , Z_{Nopt} , and Q_{ZNopt} have been derived to meet the requirement of power transferability and efficiency when $f_N = f_{NH}$ for different k . The derived equations and plots in this section are valid for different converter specifications. TABLE 2-3 summarizes the systematic design of electrical parameters.

TABLE 2-3. Systematic Design of Electrical Parameters, $f_N = f_{NH}$

Parameters	Methods
n	$M_V = n$
$Z_N = Z_{Nopt}$	$Z_{Nopt} = \frac{1}{k \cdot M_V \cdot \sqrt{M_V + M_V^2}}$
Q_{ZNopt} for λ_{coil}	$\lambda_{coil} = M_V \cdot \frac{Z_N}{Q} + M_V^2 \cdot \frac{Z_N}{Q} + \frac{Z_N}{k^2 \cdot Q} \left(\frac{1}{M_V \cdot Z_N} + \frac{1}{Q} \right)^2$

(a)

(b)

Figure 2-7. (a) Z_{Nopt} in (2-32) and (b) Q_{ZNopt} for $\lambda_{coil} = 1\%$ versus M_V and k when $f_N = f_{NH}$.

2.3.2. Operating Condition $f_N = 1$

When switching frequency equals the resonant frequency, the compensation capacitors resonate with self-inductances of the coils. In this case f_N equals 1. The procedure of coils design for $f_N = 1$ is the same as $f_N = f_{NH}$ but with different equations.

When $f_N = 1$, M_V , λ_{coil} , and φ_{Zin} in (2-24) – (2-26) are simplified as

$$M_V = \frac{1}{k \cdot Z_N \cdot n} \quad (2-33)$$

$$\lambda_{coil} = n \cdot \frac{Z_N}{Q} + \frac{Z_N}{k^2 \cdot Q} \cdot \left(\frac{1}{n \cdot Z_N} + \frac{1}{Q} \right)^2 \quad (2-34)$$

$$\varphi_{Zin} = 0 \quad (2-35)$$

The optimal Z_N , when the efficiency requirement is satisfied with the smallest value of Q , is derived by equating $\partial \lambda_{coil} / \partial Z_N$ to zero as

$$Z_{Nopt} = \frac{1}{k} \cdot n^{\frac{3}{2}} \quad (2-36)$$

The voltage gain M_V when $Z_N = Z_{Nopt}$ is derived by combining (2-33) and (2-36) as

$$M_V = \sqrt{n} \quad (2-37)$$

Then Z_{Nopt} is represented with k and M_V by combining (2-36) and (2-37) as

$$Z_{Nopt} = \frac{1}{k \cdot M_V^3} \quad (2-38)$$

Equation (2-38) shows Z_{Nopt} is independent of Q . This means Z_N and Q can be optimized sequentially. The smallest value of Q when $Z_N = Z_{Nopt}$, which is represented as Q_{ZNopt} , is calculated from (2-34) for the required λ_{coil} . Figure 2-8 shows Z_{Nopt} and Q_{ZNopt} versus M_V and k .

TABLE 2-4. Systematic Design of Electrical Parameters, $f_N = 1$

Parameters	Methods
n	$M_V = \sqrt{n}$
$Z_N = Z_{Nopt}$	$Z_{Nopt} = \frac{1}{k \cdot M_V^3}$
$Q_{ZNopt} \text{ for } \lambda_{coil}$	$\lambda_{coil} = n \cdot \frac{Z_N}{Q} + \frac{Z_N}{k^2 \cdot Q} \cdot \left(\frac{1}{n \cdot Z_N} + \frac{1}{Q} \right)^2$

(a)

(b)

Figure 2-8. (a) Z_{Nopt} in (2-38) and (b) Q_{ZNopt} for $\lambda_{coil} = 1\%$ versus M_V and k when $f_N = 1$.

2.4. Physical Realization of Electrical Parameters

Analytical or numerical approaches are usually used for physical realization of the electrical parameters such as inductances and resistances. Analytical equations have been proposed to calculate the inductances of planar coils with air core [72] and infinite-size ferrite plate [73]–[76]. There is no simple analytical model for planar coils with finite-size ferrite plate. Numerical method is more suitable in this case.

Physical parameters of coils, such as inner radii and outer radii of winding R_{inner} and R_{outer} , number of turns N , and wire size, are optimized in ANSYS Maxwell [51] to achieve $Z_N = Z_{N_{opt}}$ and $Q > Q_{Z_{N_{opt}}}$. The values of $Z_{N_{opt}}$ and $Q_{Z_{N_{opt}}}$ are plotted in Figure 2-7 and Figure 2-8. The procedure is demonstrated for the circuit topology in Figure 2-1 with specifications in TABLE 2-5. The peak value of output power is 3.3 kW. Input voltage is 400 V. Output voltage increases from 200 V to 400 V. Output current is constant to be 8.25 A. Switching frequency is 100 kHz at peak power. Loss factor λ_{coil} of coils is designed to be less than 1% at peak power.

TABLE 2-5. Specifications of IPT Coils for Design

Parameters	Values
V_{in} in Figure 2-1	400 V
V_{out} in Figure 2-1	200 – 400 V
I_{out} in Figure 2-1	8.25 A
f_s	100 kHz
λ_{coil} at peak power	< 1%
Air Gap	100 mm

The ground clearance for electric vehicles is usually larger than 140 mm. The exemplary set of coils specified in TABLE 2-5 is a scaled-down version of the coils in practical application. The air gap between transmitter and receiver coils is limited to 100 mm because the size of coils is reduced under this condition. The scaled-down coils are used herein to verify the design method. The design procedure is the same when the gap between coils is increased for real application.

A typical set of planar coils is shown in Figure 2-9(a). A circular spiral winding is placed above a square ferrite plate. Circular winding is chosen because of its easy fabrication. The choice of square ferrite plate is for its easy accessibility with commercial products. Coils with different shapes such as those in [35], [83], [84] are also applicable following this design procedure. Single layer of winding is mostly used in practice for inductive power transfer, in order to control the thickness of the planar coils and the parasitic capacitance.

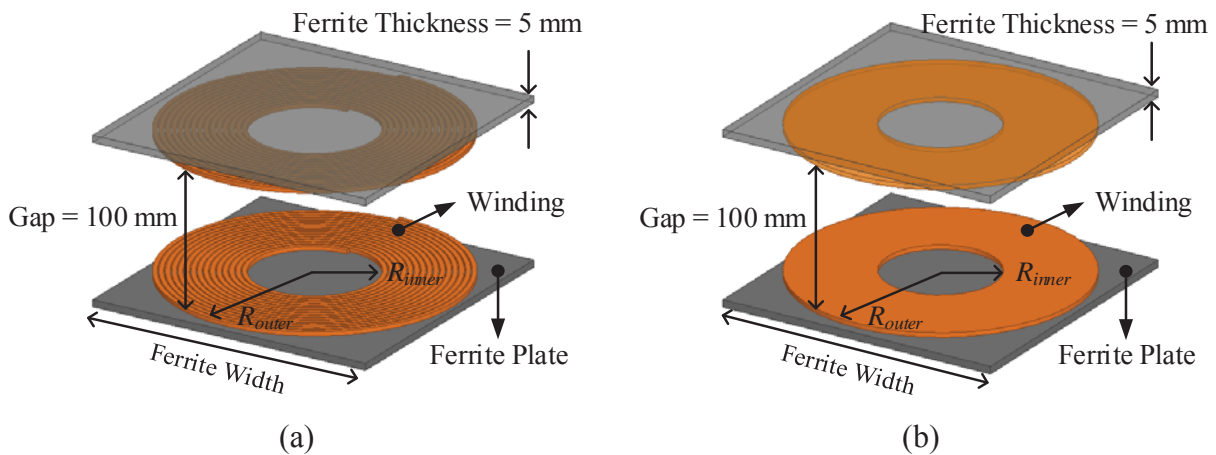


Figure 2-9. (a) Structure of planar coils with spiral winding and (b) simplified coils with single-lumped-turn winding for finite-element simulation.

The physical realization of coils includes two steps. The first step is to sweep physical parameters R_{inner} and R_{outer} in finite-element simulation and to plot electrical parameters k and L versus R_{inner} and R_{outer} . The second step is to sequentially select R_{inner} , R_{outer} , turns number N , and wire size from the plots, in order to realize the desired electrical parameters for $Z_N = Z_{Nopt}$ and $Q > Q_{ZNopt}$.

2.4.1. Operating Condition $f_N = f_{NH}$

The gap between the coils is 100 mm in this example, determined by the specifications in TABLE 2-5. A 5 mm thick ferrite plate is used according to the commercialized N95 plates, and the spacing between the ferrite and winding is set to be 1.25mm. Spiral winding with litz wire in Figure 2-9(a) is lumped to one flat turn in finite-element simulation with the same R_{inner} and R_{outer} as depicted in Figure 2-9(b). Simulation time is reduced by more than half with this simplification. The accuracy of the simulated inductances and magnetic field using the simplified model is good enough for the physical design of coils [83].

With a 100 mm gap between coils, R_{outer} and R_{inner} are parametrically swept in finite-element simulation as shown in TABLE 2-7. The ferrite width equals twice of R_{outer} , in order to achieve the highest k and Q within limited dimensions [71]. The simulation results of coupling coefficient k and one-turn self-inductance L_0 of the simplified model in Figure 2-9(b) are plotted in Figure 2-10 versus different R_{outer} and R_{inner} .

TABLE 2-6. Sweep of R_{inner} and R_{outer} in Figure 2-9(b) and Other Background Information

Parameters	Values
R_{outer}	100 mm, 125 mm, 200 mm, 300 mm, 400 mm
R_{inner}	From $R_{outer} * 0.1$ to $R_{outer} * 0.9$, step = $R_{outer} * 0.1$
Gap	100 mm
Ferrite thickness	5 mm

The coupling coefficient k is the same for coils in Figure 2-9(a) and Figure 2-9(b). Self-inductance L for the coils with N turns of winding in Figure 2-9(a) is derived from the self-inductance L_0 of the simplified model with one turn in Figure 2-9(b) as

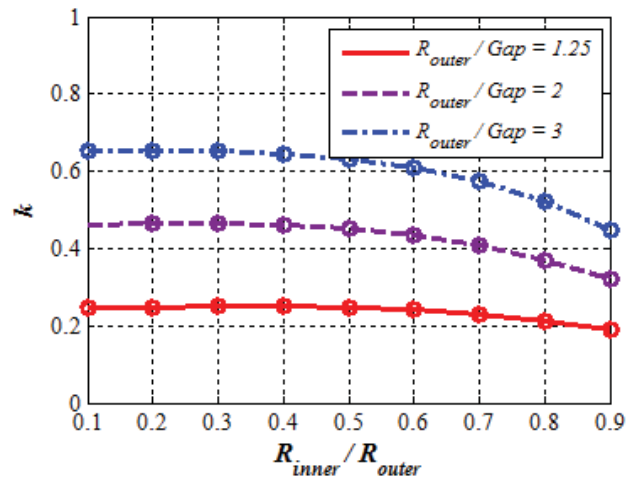
$$L = N^2 \cdot L_0 \quad (2-39)$$

The normalized impedance of the coils in Figure 2-9(a) is calculated from the simplified coils in Figure 2-9(b) as

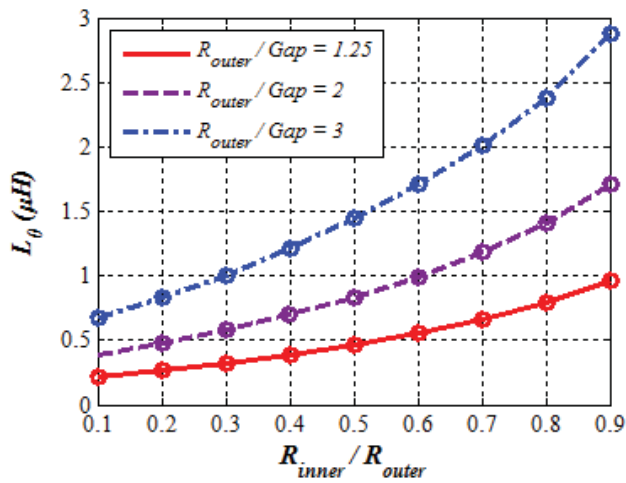
$$Z_N = \frac{\omega_s \cdot N^2 \cdot L_0}{R_{Lac}} \quad (2-40)$$

Physical parameters, including inner radii R_{inner} , outer radii R_{outer} , turns number N , and size of litz wire, are selected sequentially to realize $Z_N = Z_{Nopt}$ and $Q > Q_{ZNopt}$.

Equation (2-32) shows that Z_{Nopt} is determined by M_V and k . Specifications in TABLE 2-5 determines $M_V = 1$, assuming phase shift is not used for peak power. The values of k for different R_{outer} and R_{inner} are plotted in Figure 2-10(a). Then the values of Z_{Nopt} for different R_{outer} and R_{inner} are calculated from (2-32) with $M_V = 1$ and k in Figure 2-10(a). They are plotted in Figure 2-11(a).

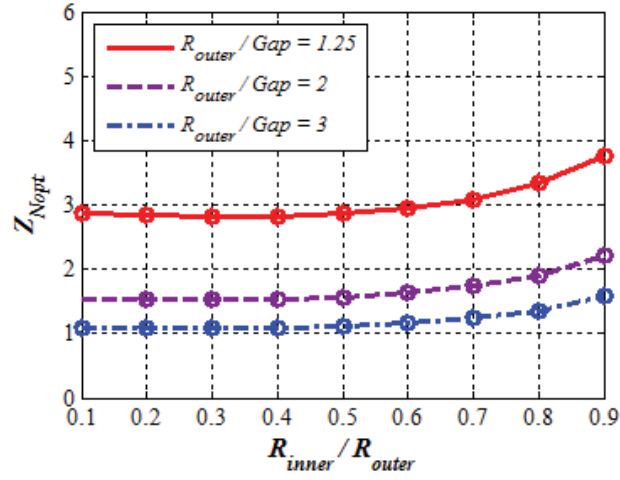


(a)

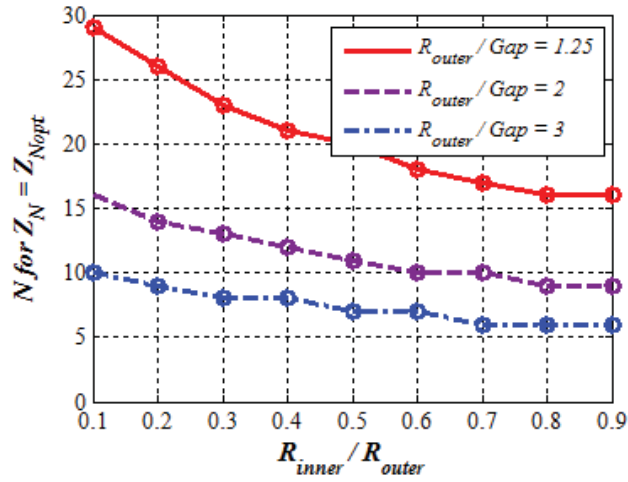


(b)

Figure 2-10. (a) Coupling coefficient k and (b) self-inductance L_0 of single-lumped-turn model in Figure 2-9(b) with gap = 100 mm. The gap is 100 mm as shown in Figure 2-9 and TABLE 2-5, and R_{outer} is normalized to gap. The normalized $R_{outer} = 1.25, 2,$ and 3 represent $R_{outer} = 125$ mm, 250 mm, and 300 mm, respectively.



(a)



(b)

Figure 2-11. (a) With simulated k for corresponding R_{inner} and R_{outer} in Figure 2-10(a), Z_{Nopt} is calculated from (2-32) with $f_N = f_{NH}$ and $M_V = 1$; (b) turns number N to realize $Z_N = Z_{Nopt}$ is calculated from (2-39) with Z_{Nopt} in (a) and L_0 in Figure 2-10(b).

The turns number N to realize $Z_N = Z_{Nopt}$ is calculated from (2-40) and plotted in Figure 2-11(b). The values of Z_{Nopt} and L_0 for different R_{outer} and R_{inner} are plotted in Figure 2-11(a) and Figure 2-10(b), respectively. Switching frequency f_s is 100 kHz, and R_{Lac} is 39 Ω at peak power calculated from (2-3) with $V_{in} = 400$ V and $V_{out} = 400$ V. There are some variations between Z_N

calculated from (2-40) and Z_{Nopt} because N should be an integer, but the variation is small so $Z_N \approx Z_{Nopt}$.

The smallest values of Q to satisfy $\lambda_{coil} < 1\%$, which is represented as Q_{ZNopt} , is derived from (2-30) with $M_V = 1$, k in Figure 2-10(a), and $Z_N = Z_{Nopt}$ in Figure 2-11(a). The results of Q_{ZNopt} are plotted for different R_{outer} and R_{inner} in Figure 2-12(a). When the size of coils is increased, the coupling coefficient is higher, which helps to transfer the power more efficiently. Therefore, the value of Q_{ZNopt} is smaller for coils with larger size.

The self-inductance L is derived from (2-39) with L_0 in Figure 2-10(b) and N in Figure 2-11(b). The mutual inductance M is derived from (2-12) with k in Figure 2-10(a) and L . Inductances are used to calculate or simulate winding currents i_1 and i_2 from Figure 2-3. After that, i_1 and i_2 are imported as stranded excitations to coils in Figure 2-9(b) in finite-element simulation. Winding loss $P_{winding}$ is calculated based on the method proposed in [78]. Core loss P_{core} is derived from simulation directly. The equivalent series resistances of coils are determined from:

$$r = (P_{winding} + P_{core}) / I^2 \quad (2-41)$$

The numbers and diameters of strands for the litz wire are swept to guarantee that Q is larger than the Q_{ZNopt} in Figure 2-12(a). The swept candidates of litz wire are selected according to the commercialized products from the manufacturers. The diameters of strand are chosen for negligible skin effect at 100 kHz, so AWG 40, 42, 44, 46, 48 are all taken into consideration. Strands with AWG larger than 48 are not considered because of the cost. Numbers of strands for sweep are selected from the manufactures' datasheet. Figure 2-12(b)-(d) plots the quality factors for litz wires with 660, 1050, 1650, and 2625 strands of AWG 44, calculated from the definition of Q in TABLE 2-2 with L in (2-39), $f_s = 100$ kHz, and r in (2-41). The values of Q with the litz

wires are compared with Q_{ZNopt} for $\lambda_{coil} = 1\%$, for different values of R_{outer} such as 125 mm in Figure 2-12(b), 200 mm in Figure 2-12(c), and 300 mm in Figure 2-12(d). The missing circles for some values of R_{inner} means the wire is too thick for winding with single layer to realize the optimal turns. Values of R_{outer} , R_{inner} , and wire size that produce $Q > Q_{ZNopt}$ in Figure 2-12(b)-(d) are the candidates that satisfy the requirements of $M_V = 1$ and $\lambda_{coil} < 1\%$ when $f_N = f_{NH}$. The corresponding turns number N is found in Figure 2-11(b).

(a)

(b)

(c)

(d)

Figure 2-12. (a) Q_{ZNopt} calculated from $\lambda_{coil} = 1\%$ in (2-30) with $Z_N = Z_{Nopt}$ in Figure 2-11(a) and k in Figure 2-10(a); (b) – (d) the values of Q with different litz wires (660, 1050, 1650, 2625 strands of AWG #44 wire) and turns number N in Figure 2-11(b) for R_{outer} of 125 mm, 200 mm, and 300 mm. Candidates of R_{inner} and R_{outer} are selected for $Q > Q_{ZNopt}$.

TABLE 2-7 summarizes the design procedure and results of the example when $f_N = f_{NH}$. The voltage gain M_V is 1 and the switching frequency f_s is 100 kHz at peak power, according to the specifications in TABLE 2-5. The equivalent load resistance R_{Lac} at peak power equals 39 Ω , calculated from (2-3) with $V_{in} = 400$ V and $V_{out} = 400$ V.

Outer radii R_{outer} , inner radii R_{inner} , and strands number of litz wire are selected to guarantee $Q > Q_{Z_{Nopt}}$ from Figure 2-12(b)-(d). Corresponding k is known from Figure 2-10(a). Optimal normalized impedance Z_{Nopt} is calculated from (2-32) with k and $M_V = 1$. Turns number N for $Z_N = Z_{Nopt}$ is calculated from (2-40) with Z_{Nopt} in Figure 2-11(a) and L_0 in Figure 2-10(b).

The designed values of the exemplary coils are listed in TABLE 2-7. The loss factor λ_{coil} is 1% when $f_N = f_{NH}$, with $M_V = 1$, $k = 0.247$, $Z_N = 2.8$, and $Q = 1043$. Inductances and ESR, resonant frequency, and resonant capacitances for the designed coils in TABLE 2-7 are listed in TABLE 2-8.

TABLE 2-7. Procedure of Physical Realization and Design Results when $f_N = f_{NH}$

Parameters	Design Methods	Values
R_{outer}	$Q > Q_{Z_{Nopt}}$ in Figure 2-12 ($Q = 1043$)	125 mm
R_{inner}	$Q > Q_{Z_{Nopt}}$ in Figure 2-12	62.5 mm
<i>Strands number</i>	$Q > Q_{Z_{Nopt}}$ in Figure 2-12	1650
k	Figure 2-10(a) at $R_{inner} = 62.5$ mm, $R_{outer} = 125$ mm	0.247
Z_{Nopt}	(2-32) with $k = 0.247$ and $M_V = 1$	2.8
N	(2-40) with $Z_{Nopt} = 2.8$ and L_0 in Figure 2-10(b)	20
λ_{coil}	(2-30) with $Z_N = 2.8$, $Q = 1043$, $k = 0.247$, $M_V = 1$	1%

TABLE 2-8. Parameters of Exemplary Coils Design in TABLE 2-7

Parameters	Values
L_1, L_2 (μH)	175, 175
M (μH)	43
f_0 (kHz)	88
C_1, C_2 (nF)	19.2, 19.2
r_1, r_2 (m Ω) at 100 kHz	104, 104

The designed coils are simulated with the circuit topology in Figure 2-1, with $V_{in} = 400$ V and $I_{out} = 8.2$ A. Output voltage varies from 400 V to 200 V. Figure 2-13 shows the simulation waveforms when $V_{out} = 400$ V and $V_{out} = 200$ V using the parameters in TABLE 2-8. Switching frequency is 100 kHz when $V_{out} = 400$ V and is 107 kHz when $V_{out} = 200$ V.

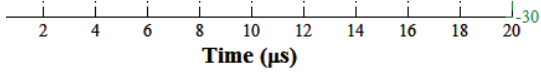
2.4.2. Operating Condition $f_N = 1$

The physical parameters, including inner radii R_{inner} , outer radii R_{outer} , turns number N , and size of litz wire, are selected sequentially to realize $Z_N = Z_{Nopt}$ and $Q > Q_{ZNopt}$ when $f_N = 1$.

The values of Z_{Nopt} for different R_{outer} and R_{inner} are calculated from (2-38) with $M_V = 1$ and k in Figure 2-10(a), as shown in Figure 2-14(a). The turns number N to realize $Z_N = Z_{Nopt}$ is calculated from (2-40) and plotted in Figure 2-14 (b).

Values of Q_{ZNopt} for $\lambda_{coil} = 1\%$ is derived from (2-34) with $Z_N = Z_{Nopt}$. The results of Q_{ZNopt} are plotted for different R_{outer} and R_{inner} in Figure 2-15(a). Coil quality factors with four types of litz wires, e.g. 660, 1050, 1650, and 2625 strands of AWG #44 wires, are compared with Q_{ZNopt} in Figure 2-15(b)-(d), with R_{outer} of 125 mm, 200 mm, and 300 mm. Values of R_{outer} , R_{inner} , and wire

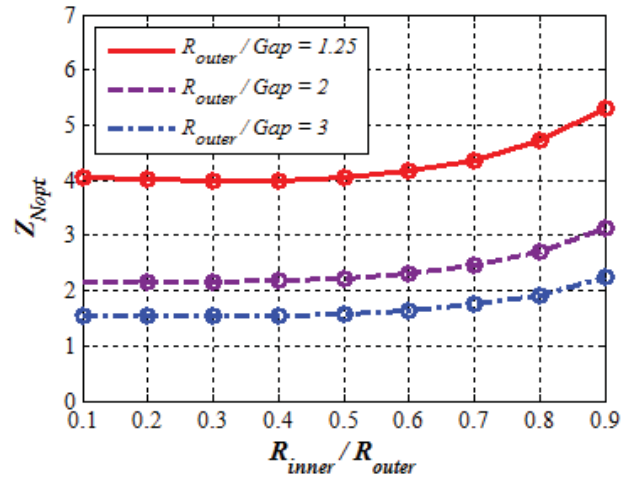
size that produce $Q > Q_{ZNopt}$ in Figure 2-15(b)-(d) are the candidates that satisfy the requirements of power transferability and efficiency. The corresponding turns number N is found in Figure 2-14(b).



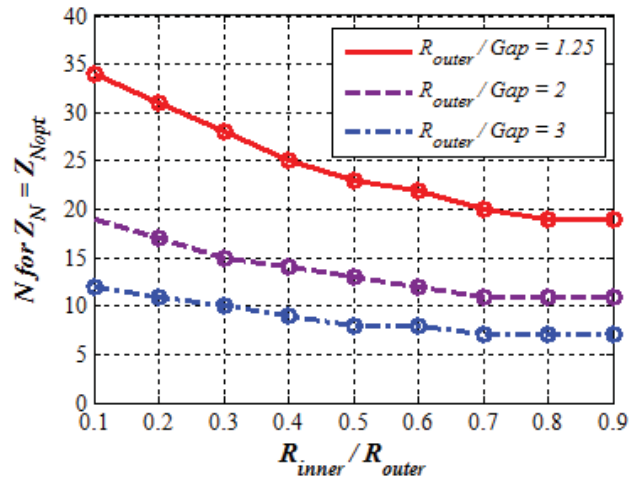
(a)

(b)

Figure 2-13. Simulation waveforms of inverter output voltage v_{ac_in} and current i_1 , rectifier input voltage v_{out_ac} and current i_2 for circuit topology in Figure 2-1: (a) peak power with $V_{in} = 400$ V, $V_{out} = 400$ V, $I_{out} = 8.2$ A, and $f_s = 100$ kHz; (b) half power with $V_{in} = 400$ V, $V_{out} = 200$ V, $I_{out} = 8.2$ A, and $f_s = 107$ kHz. The square waves are voltages, and the sinusoidal waves are currents. Parameters of the converter and coils are listed in TABLE 2-8.



(a)



(b)

Figure 2-14. (a) $Z_{N_{opt}}$ versus R_{inner} and R_{outer} with k in Figure 2-10(a) and $M_V = 1$, calculated from (2-38); (b) turns number N to realize $Z_N = Z_{N_{opt}}$ is calculated from (2-39) with $Z_{N_{opt}}$ in (a) and L_0 in Figure 2-10(b).

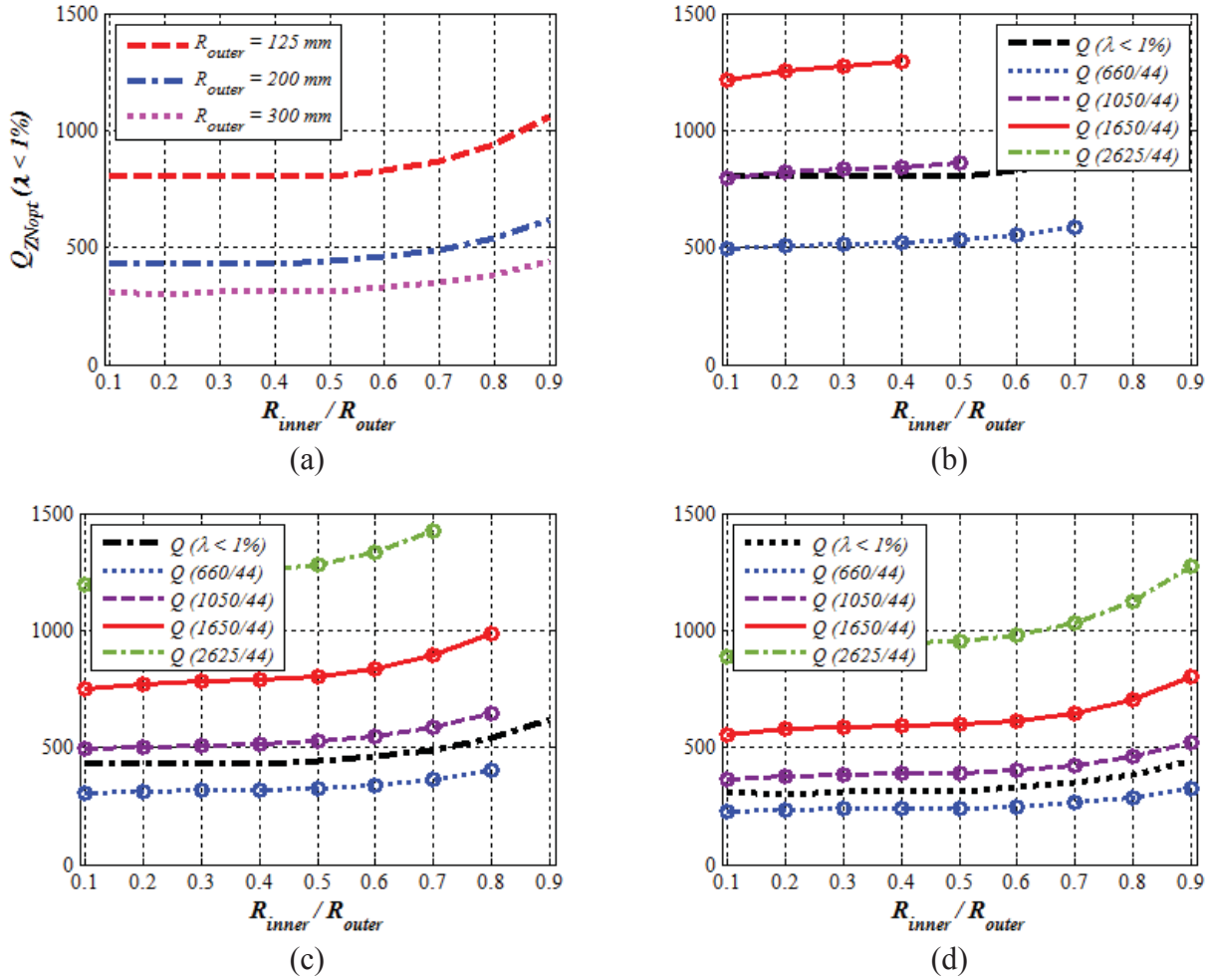


Figure 2-15. When $f_N = 1$, (a) $Q_{Z_{Nopt}}$ is calculated from $\lambda_{coil} = 1\%$ in (2-34) with $Z_N = Z_{Nopt}$ in Figure 2-14(a) and k in Figure 2-10(a). Q values with different litz wires (660, 1050, 1650, 2625 strands of AWG #44 wire) and turns number N in Figure 2-14(b) for R_{outer} of (b) 125 mm, (b) 200 mm, and (b) 300 mm. Candidates of R_{inner} and R_{outer} to select is when $Q > Q_{Nopt}$.

TABLE 2-9 summarizes the procedure of physical realization when $f_N = 1$. Corresponding inductances and ESR, resonant frequency, and resonant capacitance are listed in TABLE 2-10.

TABLE 2-9. Procedure of Physical Realization and Design Results when $f_N = 1$

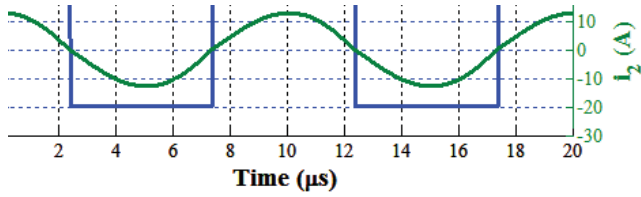
Parameters	Design Methods	Values
R_{outer}	$Q > Q_{Z_{Nopt}}$ in Figure 2-15 ($Q = 861$)	125 mm
R_{inner}	$Q > Q_{Z_{Nopt}}$ in Figure 2-12	62.5 mm
Strands number	$Q > Q_{Z_{Nopt}}$ in Figure 2-15	1050
k	Figure 2-10(a) at $R_{inner} = 62.5$ mm, $R_{outer} = 125$ mm	0.247
Z_{Nopt}	(2-38) with $k = 0.247$ and $M_V = 1$	4.0
N	(2-40) with $Z_{Nopt} = 4.0$ and L_0 in Figure 2-10(b)	23
λ_{coil}	(2-34) with $Z_N = 4.0$, $Q = 861$, $k = 0.247$, $M_V = 1$	1%

TABLE 2-10. Parameters of Exemplary Coils Design in TABLE 2-9

Parameters	Methods
L_1, L_2 (μH)	249, 249
M (μH)	62
f_0 (kHz)	100
C_1, C_2 (nF)	10.2, 10.2
r_1, r_2 (m Ω), at 100 kHz	182, 182

Designed coils are simulated with the circuit topology in Figure 2-1, with $V_{in} = 400$ V and $I_{out} = 8.2$ A. Output voltage varies for different load conditions by phase-shifting inverter voltage. Figure 2-16 shows simulation waveforms with the coils in TABLE 2-10, when output

voltage is 400 V and at half power when output voltage is 200 V. Switching frequency is fixed at 100 kHz for different load conditions.



(a)

(b)

Figure 2-16. Simulation waveforms of inverter output voltage v_{ac_in} and current i_{l1} , rectifier input voltage v_{out_ac} and current i_2 for circuit topology in Figure 2-1 when $f_N = 1$: (a) peak power with $V_{in} = 400$ V, $V_{out} = 400$ V, $I_{out} = 8.2$ A, and $f_s = 100$ kHz; (b) half power with $V_{in} = 400$ V, $V_{out} = 200$ V, $I_{out} = 8.2$ A, and $f_s = 100$ kHz. The square waves are voltages, and the sinusoidal waves are currents. Parameters of converter and coils are listed in TABLE 2-9.

2.5. Experimental Verification

Following the procedure in TABLE 2-7, coils with 62 mm R_{inner} , 125 mm R_{outer} , and 20 turns of 1650/44 litz wire were selected and built as shown in Figure 2-17. The 250 mm \times 250 mm ferrite plate was composed of four pieces of 150 mm \times 100 mm \times 5 mm of EPCOS N95 ferrite [85]. The gap between coils was set to be 100 mm. The measured parameters are listed in TABLE 2-11. All the values in TABLE 2-11 were measured in the presence of both transmitter and receiver coils as shown in Figure 2-17(c).

Figure 2-18 shows the full-bridge inverter, rectifier, and bank of resonant capacitors to test the coils. The inverter was built with STY139N65M5 from STMicroelectronics. Its schematics and PCB layout is provided in Appendix C. The fast recovery epitaxial diodes DSEI120-06A from IXYS were used for the rectifier. Resonant capacitance is 19.8 nF for both C_1 and C_2 .

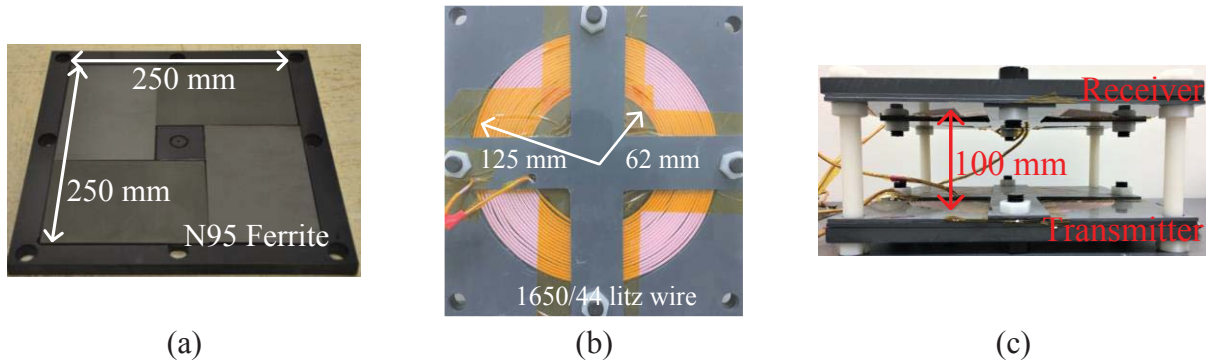
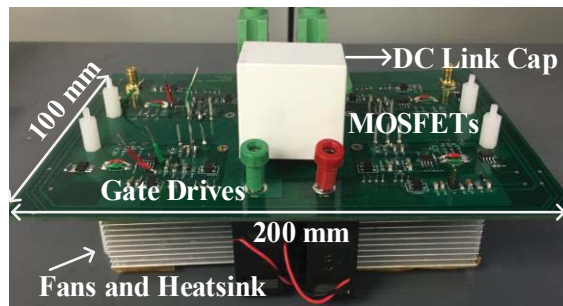


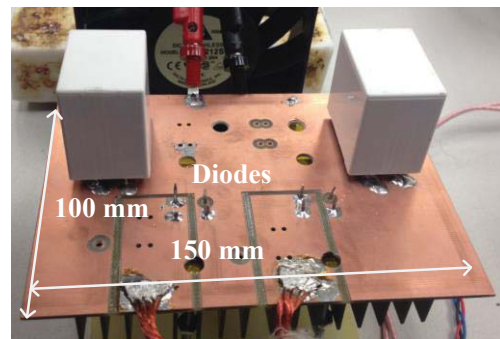
Figure 2-17. Fabricated coils which were designed for 3.3 kW at $f_N = f_{NH}$ as in TABLE 2-8 following the procedure in TABLE 2-3 and TABLE 2-7 with (a) 4 pieces of 150 mm \times 100 mm \times 5 mm of EPCOS N95 ferrite plates, (b) winding with 1650/44 litz wire, and (c) 100 mm air gap.

TABLE 2-11. Simulated and Measured Parameters of Coils Designed for $f_N = f_{NH}$ in TABLE 2-8

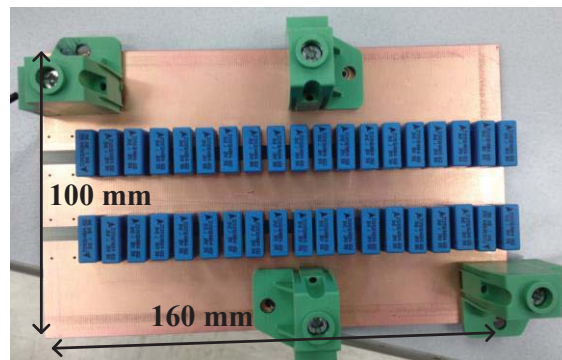
Parameters	Simulated Values	Measured Values
L_1, L_2 (μH)	175, 175	166, 163
M (μH)	43	39
k	0.247	0.25
r_1, r_2 ($\text{m}\Omega$), at 100 kHz	104, 104	110, 108



(a)



(b)



(c)

Figure 2-18. (a) Full bridge inverter, (b) rectifier with diode bridges, (c) resonant capacitor bank with 19.8 nF and 1.4 kV voltage rating to test the coils in Figure 2-17.

The measured waveforms of inverter output voltage v_{in_ac} and current i_I , as well as rectifier input voltage v_{out_ac} and current i_2 at peak power are shown in Figure 2-19. Voltage gain M_V is 1 with $V_{in} = 400$ V and $V_{out} = 400$ V. Voltages v_{in_ac} and v_{out_ac} were measured with Tektronix THDP0200 voltage differential probes, current i_I was measured with PEM CWT015 Rogowski coil, and current i_2 was measured with Tektronix A6302 current probe and Tektronix TM503B current probe amplifier. On the transmitter side, i_I is lagging v_{in_ac} because switching frequency is designed to be higher than resonance frequency on purpose. Zero-voltage turn-on is realized for all the devices under all the load conditions as in (2-29) and Figure 2-6(b). The trade-off is higher turn-off loss of inverter devices and higher conduction loss due to circulating energy.

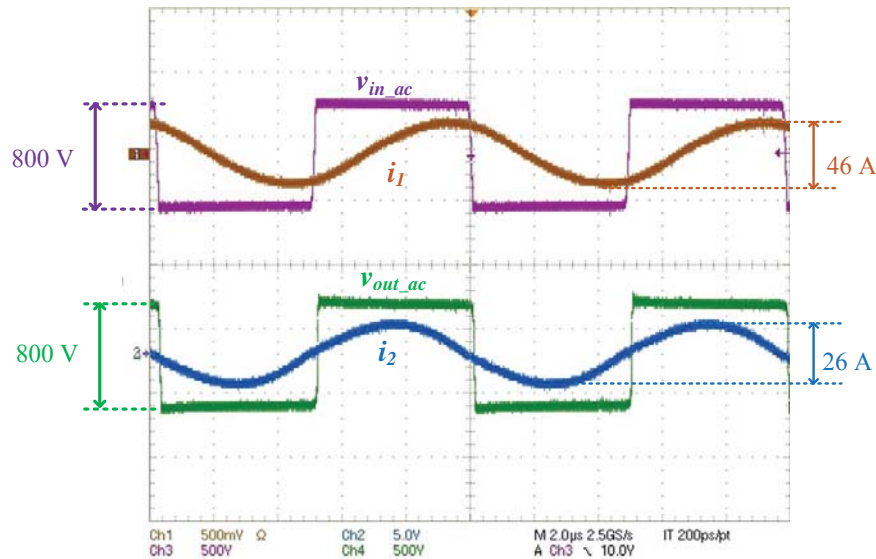


Figure 2-19. Waveforms of inverter and rectifier for circuit topology in Figure 2-1 when $V_{in} = 400$ V, $V_{out} = 400$ V, $I_{out} = 8.2$ A, and $f_s = 100$ kHz.

Switching frequency f_s was changed for different output voltages in experiment without phase-shift for inverter output voltage. Figure 2-20 shows f_s and λ_{coil} in experiment for different load conditions. Loss factor of coils at peak power is 1.1%. In Figure 2-20, coils' efficiency

increases with output voltage because switching frequency is going closer to resonant frequency. Figure 2-19 and Figure 2-20 verify that desired power transferability and loss factor, as well as ZVS turn-on of inverter devices, are satisfied following the design method. The end-to-end efficiency of the circuit in Figure 2-1 is 95.9% at peak power with the fabricated coils.

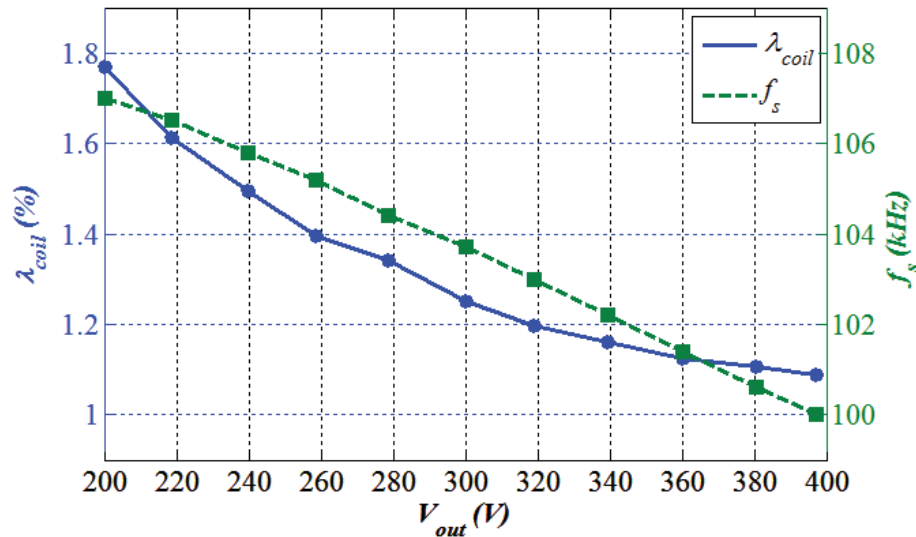


Figure 2-20. Switching frequency and measured coils' efficiency with $I_{out} = 8.2$ A, $V_{out} = 200$ to 400 V, and specifications in TABLE 2-5. Switching frequency were changed from 107 kHz to 100 kHz for different voltage gains and constant output current.

2.6. Summary

Coils' parameters were designed systematically to satisfy the requirement of power transferability and efficiency for series-series inductive power transfer system. The parameters were normalized as coupling coefficient k , normalized switching frequency f_N , normalized impedance Z_N , coil quality factors Q , and turns ratio n . The power transferability is determined by n when geometries are the same for transmitter and receiver coils. Efficiency requirement is

satisfied by choosing $Z_N = Z_{N_{opt}}$ and making $Q > Q_{Z_{N_{opt}}}$, where $Z_{N_{opt}}$ is the optimal value of the normalized impedance, and $Q_{Z_{N_{opt}}}$ is the Q value for desired loss factor of coils λ_{coil} when $Z_N = Z_{N_{opt}}$. Physical realization for designed electrical parameters were optimized by parametric sweep in finite-element simulation. Inner radii and outer radii of the winding, R_{inner} and R_{outer} , as well as the size of litz wire, were selected for $Q > Q_{Z_{N_{opt}}}$. Number of turns N is chosen for $Z_N = Z_{N_{opt}}$.

Following this procedure, a set of coils was designed for the operating condition when the compensation capacitor resonates with leakage inductance. In order to meet the efficiency specification when transferring 3.3 kW power across 100 mm gap, the coils dimensions should be no smaller than 250 mm × 250 mm. Litz wire with strands of AWG 44 is selected for negligible skin effect, and either 1650 or 2625 strands should be chosen to guarantee the coil quality factor. The coils were built and tested in a series-series IPT system rated at 3.3 kW, for the operating condition $f_N = f_{NH}$. The coil-to-coil efficiency reached 98.9% at 100 kHz for peak power. The operating frequency should range between 100 kHz – 107 kHz to realize the requirements of power transferability. Soft-turn-ons were achieved for switches.

The design procedure in this chapter focuses on maximizing the efficiency of the coils. The stray magnetic field is not considered. The coils design following the procedure are used as the baseline design, which will be compared with the coils optimized for both efficiency and field attenuation in the later chapters.

Chapter 3. Synergetic Attenuation of Stray Magnetic Field for IPT Coils

Nomenclature

B	Quantified magnetic field.
$B_{RXn,i}$	Stray magnetic field in the i orientation generated by loop n of the receiver, with $i = X, Y, \text{ or } Z$ in Figure 3-2.
$B_{TXn,i}$	Stray magnetic field generated in the i orientation by loop n of the transmitter, with $i = X, Y, \text{ or } Z$ in Figure 3-2.
B_X	Stray magnetic field in X direction.
B_Y	Stray magnetic field in Y direction.
B_Z	Stray magnetic field in Z direction.
d_c	Strand diameter of litz wire.
f_0	Resonant frequency.
f_s	Switching frequency of the inverter.
I_{out}	Output current in Figure 2-1.
I_{RX}	RMS value of receiver current.
I_{TX}	RMS value of transmitter current.
L_1	Self-inductance of transmitter.
L_2	Self-inductance of receiver.
L_{RXn}	Self-inductance of loop n in the receiver in Figure 3-8.
l_t	Average length of one turn.
L_{TXn}	Self-inductance of loop n in the transmitter in Figure 3-8.

M	Mutual inductance between transmitter and receiver.
$M_{RXn-RXm}$	Mutual inductance between loops n and m in the receiver in Figure 3-8.
$M_{TXn-RXm}$	Mutual inductance between loop n in the transmitter and loop m in the receiver in Figure 3-8.
$M_{TXn-TXm}$	Mutual inductance between loops n and m in the transmitter in Figure 3-8.
$N_{RX(m)}$	Turns number of loop m in the receiver in Figure 3-7.
$N_{TX(m)}$	Turns number of loop m in the transmitter in Figure 3-7.
P_e	Proximity-effect loss of a turn.
r_1	ESR of transmitter at switching frequency.
r_2	ESR of receiver at switching frequency.
R_{inner}	Inner radius of the winding.
R_{Lac}	Equivalent load resistance in Figure 2-3.
R_{outer}	Outer radius of the winding.
$\alpha_{RXn,i}$	Current-to-field coefficient for loop n of the receiver in Figure 3-9, with $i = X, Y, \text{ or } Z$ in Figure 3-2.
$\alpha_{TXn,i}$	Current-to-field coefficient for loop n of the transmitter in Figure 3-9, with $i = X, Y, \text{ or } Z$ in Figure 3-2.
θ	Phase difference between transmitter and receiver currents.
ω_0	Resonant angular frequency.
ω_s	Switching angular frequency.
ρ_c	Resistivity of copper.

3.1. Introduction

Both the coil-to-coil efficiency and stray magnetic field are influenced by the physical design of IPT coils. Their synergetic optimization is important. The coil-to-coil efficiency is defined as

the ratio of the receiver's output power to the transmitter's input power as shown in Figure 2-3 [55]. The physical parameters of the IPT coils should be optimized to increase the coil-to-coil efficiency, such as inner radii and outer radii of the windings, the distribution of the turns, and the type of litz wires [27], [57]–[60], [62], [65]. Significant stray magnetic field exists around the coils since the gap between the transmitter and receiver is comparable to the dimensions of the coils. The objective of this chapter is to attenuate the stray magnetic field by optimizing the physical parameters of the planar coils.

Pareto fronts are used for the multi-objective optimization in this chapter. The fronts are plotted on a two two-dimensional Cartesian coordinate system. The horizontal axis and vertical axis represent the quantified value of the magnetic field and the coil-to-coil efficiency, respectively. The optimal designs should be selected along the fronts.

In the conventional way [52] to derive the Pareto fronts, all the physical parameters of the planar coils are swept in finite-element simulation. The simulation results of the magnetic fields and efficiencies for all the swept cases are plotted on the Cartesian coordinate system, from which the Pareto fronts are derived using mathematical software such as Matlab. The main drawback of this method is that it takes thousands of simulations which is very time-consuming, especially when three-dimensional simulations are required.

This chapter demonstrates a method of fast optimization. The key concept of this method is the lumped-loop model, in which the windings of the planar coils are replaced by several lumped loops. As long as the number of turns for each loop is know, the inductances and stray magnetic fields are calculated with the permeance matrices and current-to-field matrices, respectively. The coil-to-coil efficiency is then derived with the inductances and the winding resistances. The winding resistances are calculated analytically using the method that will be illustrated in

Chapter 4. Only tens of simulations are required during the entire optimization, which are used to derive the permeance matrices and current-to-field matrices. By replacing the parametric sweep in finite-element simulation by sweeping the numbers of turns for the lumped loops in calculation, the method in this chapter makes the optimization faster than the conventional method without losing the accuracy.

Section 3.2 introduces optimizing the coil-to-coil efficiency and stray magnetic field of the IPT coils with Pareto fronts. Section 3.4 demonstrates how to use the lumped-loop model to derive the fronts. Section 3.5 uses a design example to describe the detailed procedure of the fast optimization. In this example, the coils are optimized to transfer 100 W power across 40 mm gap, and the maximum dimensions of the coils are limited to be 100 mm × 100 mm. The Pareto front derived from the lumped-loop model matches well with that derived from parametric sweep in finite-element simulation. In Section 3.6, an optimal design selected along the front in Section 3.5 was fabricated and tested in experiment to verify the accuracy of the calculation results with permeance matrices and current-to-field matrices. The coil-to-coil efficiencies from calculation and measurement are the same, and the difference for stray magnetic field is less than 12.5%.

3.2. Pareto Front of Coil-to-Coil Efficiency versus Stray Magnetic Field

Stray magnetic field is defined as the magnetic field around the IPT coils. Its flux lines are shown in Figure 3-1. The stray magnetic field at one point represents either the leakage field or the coupling field, depending on its distance to the coils.

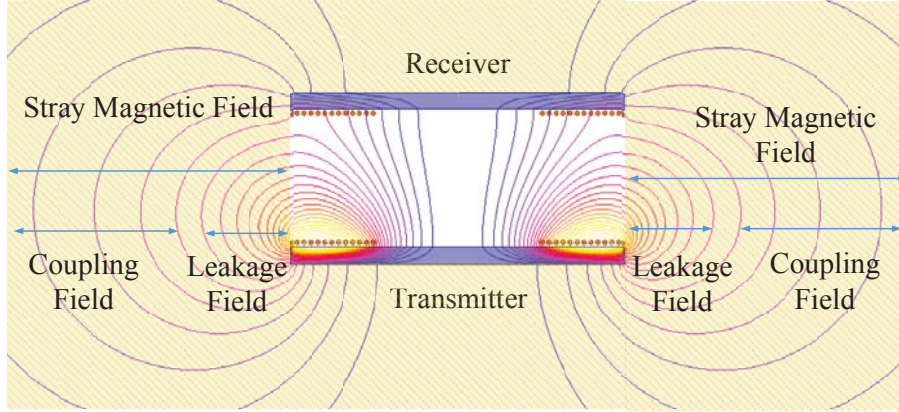


Figure 3-1. Side view of the flux lines of stray magnetic field around the IPT coils

The stray magnetic field is generated by the winding currents of the transmitter and receiver together. The winding currents are sinusoidal in IPT application, and their expressions are

$$i_{TX}(t) = \sqrt{2}I_{TX} \cdot \sin(\omega_s t) \quad (3-1)$$

$$i_{RX}(t) = \sqrt{2}I_{RX} \cdot \sin(\omega_s t + \theta) \quad (3-2)$$

where ω_s is the switching radial frequency; I_{TX} and I_{RX} are the RMS values of winding currents. For series-series compensation, θ is 90° when switching frequency equals resonant frequency, and the winding currents are derived from the simplified circuit model in Figure 2-3 as

$$I_{TX} = \frac{(r_2 + R_{Lac})}{\omega M} \frac{\pi}{2\sqrt{2}} I_{out} \quad (3-3)$$

$$I_{RX} = \frac{\pi}{2\sqrt{2}} I_{out} \quad (3-4)$$

In Figure 3-2, the magnetic field $B(t)$ at the point for measurement is decomposed into $B_i(t)$ ($i = X, Y, Z$) in three orthogonal directions X, Y, and Z. According to superposition, $B_i(t)$ includes $B_{TX,i}(t)$ and $B_{RX,i}(t)$, which are generated by the transmitter and receiver currents, respectively. $B_{TX,i}(t)$ and $B_{RX,i}(t)$ are proportional to $i_{TX}(t)$ and $i_{RX}(t)$.

$$B_{TX,i}(t) = \alpha_{TX,i} \cdot i_{TX}(t) \quad (3-5)$$

$$B_{RX,i}(t) = \alpha_{RX,i} \cdot i_{RX}(t) \quad (3-6)$$

where $\alpha_{TX,i}$ and $\alpha_{RX,i}$ are the current-to-field coefficients, which will be discussed in details in Section 3.4. The time-varying magnetic fields $B_i(t)$ are calculated from $B_{TX,i}(t)$ and $B_{RX,i}(t)$ as

$$B_i(t) = B_{TX,i}(t) + B_{RX,i}(t) = \sqrt{2}(\alpha_{TX,i} \cdot I_{TX}) \sin(\omega_s t) + \sqrt{2}(\alpha_{RX,i} \cdot I_{RX}) \sin(\omega_s t + \theta) \quad (3-7)$$

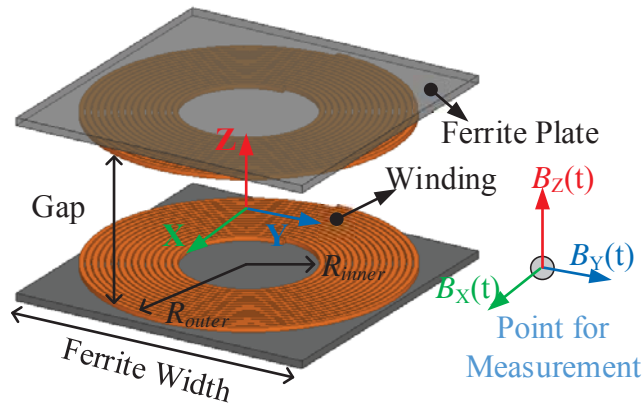


Figure 3-2. Components of the stray magnetic field – $B_X(t)$, $B_Y(t)$, and $B_Z(t)$ – in three orthogonal directions X, Y, and Z.

Equation (3-7) verifies that $B_i(t)$ is sinusoidal with switching frequency. In this dissertation, the magnetic field $B_i(t)$ is quantified with

$$B = \sqrt{\sum_{i=X,Y,Z} B_i^2} \quad (3-8)$$

where B_i is the RMS value of the sinusoidal $B_i(t)$. According to (3-7) and (3-8), the stray magnetic field is determined by winding currents $i_{TX}(t)$ and $i_{RX}(t)$ and the current-to-field coefficients $\alpha_{TX,i}$ and $\alpha_{RX,i}$

The coil-to-coil efficiency is defined as the ratio of the receiver's output power to the transmitter's input power. Both the stray magnetic field and coil-to-coil efficiency are influenced

by the design of IPT coils. Their synergetic optimization is realized with Pareto front. The front is plotted on a two-dimensional Cartesian coordinate. The horizontal axis and vertical axis represent magnetic field and coil-to-coil efficiency, respectively. The optimal designs of the coils should be selected along the fronts.

Figure 3-3 shows an example of the Pareto front of coil-to-coil efficiency versus stray magnetic field. The front is used to optimize the coils with the structure in Figure 3-2. The coils are designed to transfer 100 W power across 40 mm gap, using the series-series compensation in Figure 2-1. The maximum dimensions of each coil are 100 mm by 100 mm.

Figure 3-3 An example of the Pareto front of coil-to-coil efficiency versus stray magnetic field. The front is used to optimize the coils with the structure in Figure 3-2.

Each marker in Figure 3-3 represents the coil-to-coil efficiency and stray magnetic field for one set of physical parameters of the coils, including inner radii and outer radii of the winding, the distribution of turns, and the type of litz wire. After all the physical parameters are swept and all the markers are plotted, the Pareto front is derived on the upper left of all the markers, as shown in Figure 3-3.

3.3. Conventional Method to Derive Pareto Front

Figure 3-4 summarizes the conventional method to derive the Pareto front, in which all the physical parameters are swept in the finite-element simulations. The procedure starts off by drawing the model of the coils in simulation. After that, the physical parameters are swept, including the inner radii and outer radii of the windings, the distribution of the turns, and the types of litz wire.

Two simulations are required to get the efficiency and magnetic field for each set of the physical parameters. The objective of the first simulation is to simulate the inductances L_1 , L_2 , M as well as the magnetic fields across each turn. The inductances are used to calculate the winding currents $i_{TX}(t)$ and $i_{RX}(t)$. The magnetic fields across each turn are used to calculate the winding resistances r_1 and r_2 from (3-22). The coil-to-coil efficiency is then derived from (2-10). The second simulation excites the windings with $i_{TX}(t)$ and $i_{RX}(t)$ to obtain the stray magnetic field.

With these two simulations, the coil-to-coil efficiency and stray magnetic field of the corresponding set of physical parameters are marked on the Cartesian coordinate such as that in Figure 3-3. After the results of all the physical parameters are calculated and simulated, the Pareto front is derived using Matlab.

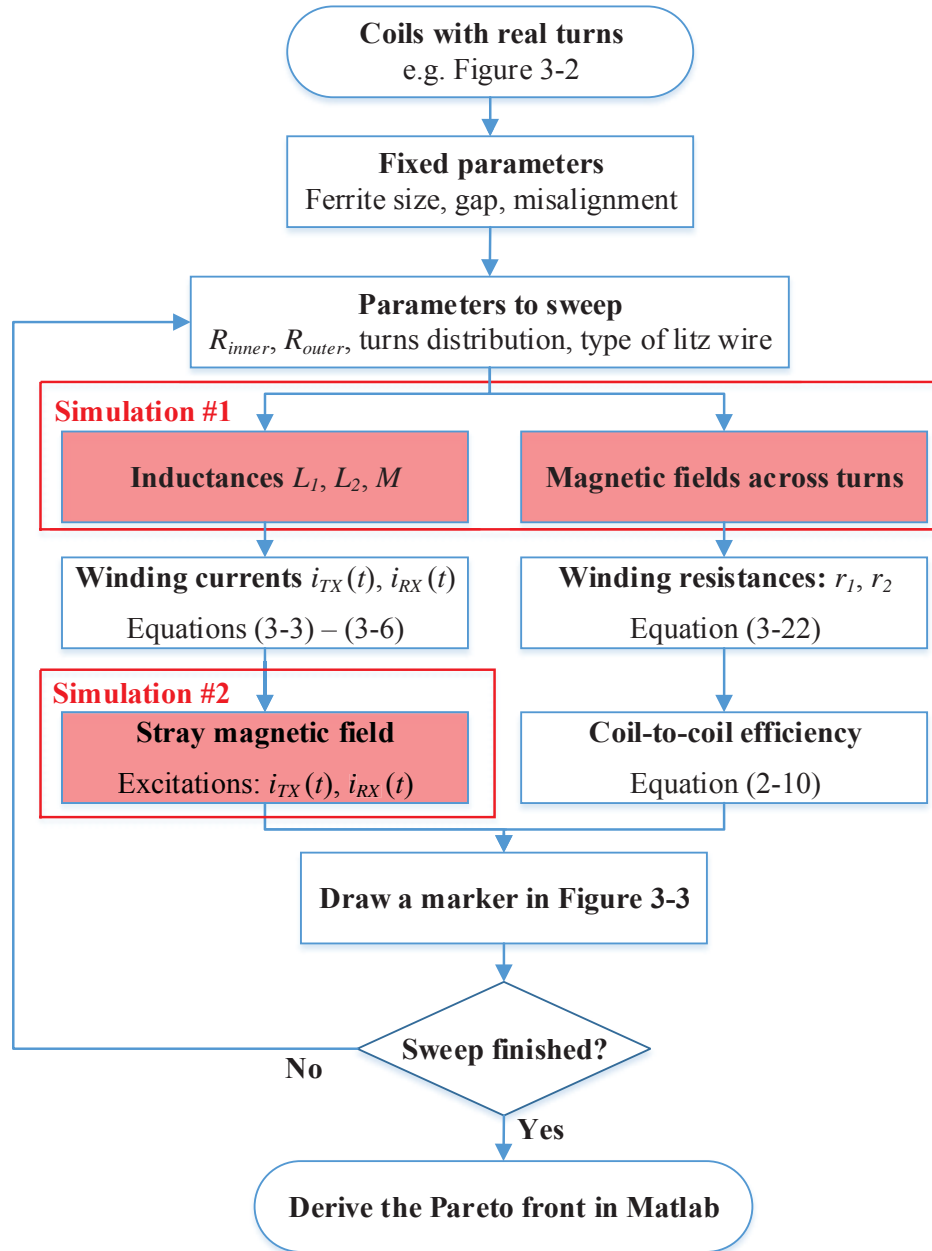


Figure 3-4. The conventional method to derive the Pareto front of coil-to-coil efficiency versus stray magnetic field, which sweeps the all the physical parameters in finite-element simulation.

However, the method in Figure 3-4 asks for thousands of simulations, which is very time-consuming. This is because the finite-element simulations are inside the iteration of the

parametric sweep. If M sets of parameters are swept, a total number of $2M$ simulations are required to derive the Pareto front. The simulations should be taken out of the iteration to make the optimization faster. This is realized with the concept of lumped-loop model, which will be demonstrated in Section 3.4.

3.4. Fast Method to Derive Pareto Front

Figure 3-5 shows the procedure of the fast method to derive the Pareto front [66]. Because the finite-element simulation is taken out of the iteration, only tens of simulations are required in the entire procedure. All the simulations are implemented before the iteration starts. They are used to derive the permeance matrices and current-to-field matrices.

There are five major steps in this procedure: determine the lumped-loop model, derive the permeance matrices and current-to-field matrices from finite-element simulations, calculate the stray magnetic field, calculate the coil-to-coil efficiency, and derive the Pareto front using Matlab. Details about each step will be demonstrated in the following parts.

3.4.1. Lumped-loop Model and Turns Vectors

The procedure in Figure 3-5 starts with replacing the original coils with the lumped-loop model. The original winding of turns in Figure 3-2 is replaced by several lumped loops. Each loop is composed of certain number of turns. Figure 3-6 shows the lumped-loop model of the coils structure in Figure 3-2. Several loops are distributed on top of the ferrite plate with equal spacing.

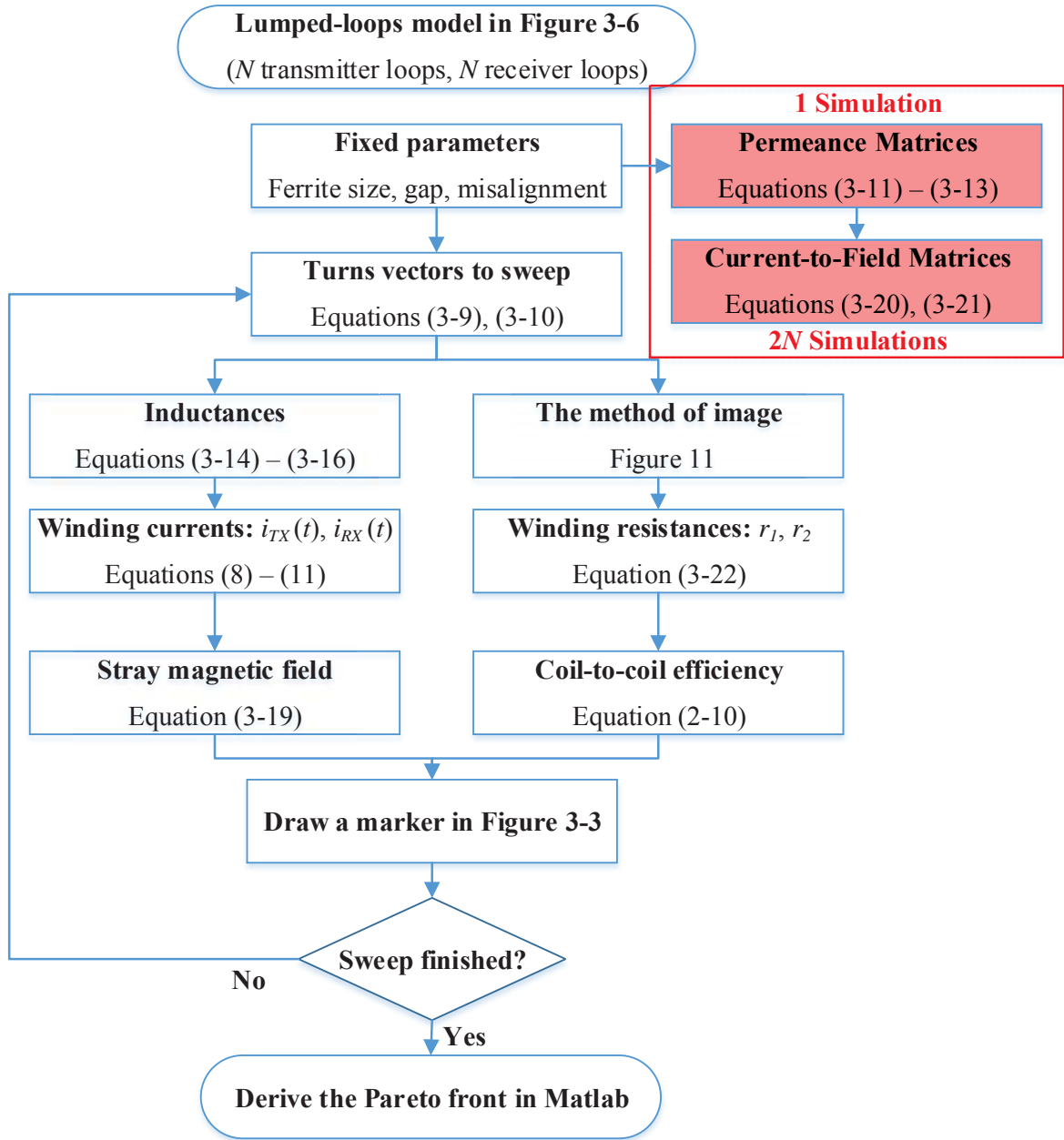


Figure 3-5. The fast method to derive the Pareto front of coil-to-coil efficiency versus stray magnetic field, using lumped-loop model.

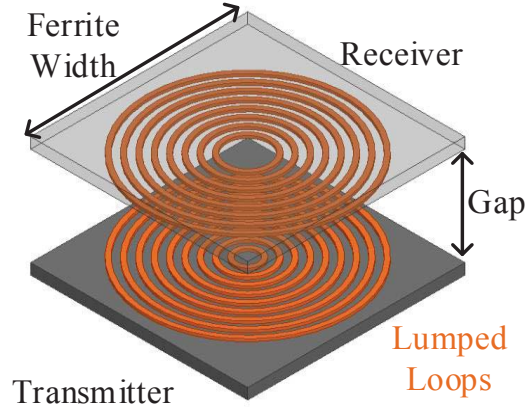


Figure 3-6. The lumped-loop model of the coils structure in Figure 3-2, which is used to start the procedure in Figure 3-5 to derive the Pareto front.

Turns vectors \vec{N}_{TX} and \vec{N}_{RX} are used to describe the number of turns for each loop.

$$\vec{N}_{TX} = [N_{TX1} \quad N_{TX2} \quad \cdots \quad N_{TXN}] \quad (3-9)$$

$$\vec{N}_{RX} = [N_{RX1} \quad N_{RX2} \quad \cdots \quad N_{RXN}] \quad (3-10)$$

where $N_{TX(m)}$ and $N_{RX(m)}$ represent the turns number of the loop in the transmitter and receiver, respectively, with $m = 1, 2, \dots, N$. Loop 1 represents the outermost loop, while loop N represents the innermost loop. Figure 3-7 shows the definitions of the turns vector, using the cylindrical view of the lumped-loop model in Figure 3-6.

The physical parameters of the coils, such as inner radii, outer radii, and distribution of turns, are equivalent to the turns vectors. In Figure 3-7, the loops with dashed circles are assigned zero turn to realize the labeled inner radii and outer radii of the winding. The numbers of turns for the loops with solid circles represent the distribution of turns in the original coils. Therefore, by using the lumped-loop model and turns vectors, the sweep of the physical parameters is equivalent to the sweep of the elements of the turns vectors in (3-9) and (3-10).

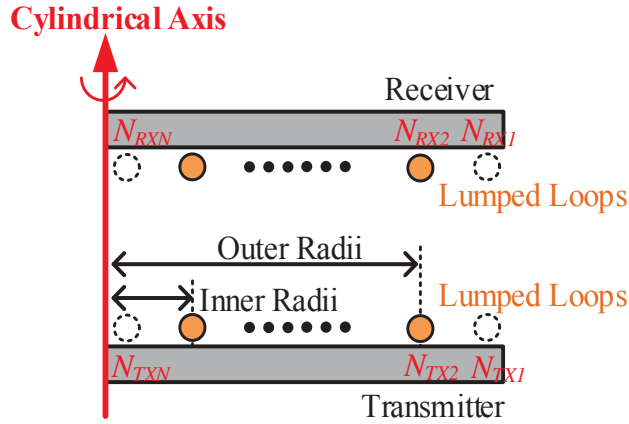


Figure 3-7. The cylindrical view of the lumped-loop model in Figure 3-6 to demonstrate the turns vector $[N_{TX1}, N_{TX2}, \dots, N_{TXN}]$ of transmitter and the turns vector $[N_{RX1}, N_{RX2}, \dots, N_{RXN}]$ of the receiver.

3.4.2. Permeance Matrices and Current-to-Field Matrices

The permeance matrices and current-to-field matrices are used to calculate the inductances and stray magnetic fields from the turns vectors of the lumped-loop model. Figure 3-5 shows that $2N + 1$ simulations are required to derive the permeance matrices and the current-to-field matrices, when there are N loops in the lumped-loop model of each coil.

3.4.2.1. Permeance Matrices

The definitions of permeance matrices is explained in Figure 3-8. In this lumped-loop model, each loop is assumed to have one turn. The permeance matrices \mathbf{L}_{TX} , \mathbf{L}_{RX} , and \mathbf{M} are defined as

$$\mathbf{L}_{TX} = \begin{bmatrix} L_{TX1} & M_{TX1-TX2} & \cdots & M_{TX1-TXN} \\ M_{TX2-TX1} & L_{TX2} & \cdots & M_{TX2-TXN} \\ \vdots & \vdots & \ddots & \vdots \\ M_{TXN-TX1} & M_{TXN-TX2} & \cdots & L_{TXN} \end{bmatrix} \quad (3-11)$$

$$\mathbf{L}_{RX} = \begin{bmatrix} L_{RX1} & M_{RX1-RX2} & \cdots & M_{RX1-RXN} \\ M_{RX2-RX1} & L_{RX2} & \cdots & M_{RX2-RXN} \\ \vdots & \vdots & \ddots & \vdots \\ M_{RXN-RX1} & M_{RXN-RX2} & \cdots & L_{RXN} \end{bmatrix} \quad (3-12)$$

$$\mathbf{M} = \begin{bmatrix} M_{TX1-RX1} & M_{TX1-RX2} & \cdots & M_{TX1-RXN} \\ M_{TX2-RX1} & M_{TX2-RX2} & \cdots & M_{TX2-RXN} \\ \vdots & \vdots & \ddots & \vdots \\ M_{TXN-RX1} & M_{TXN-RX2} & \cdots & M_{TXN-RXN} \end{bmatrix} \quad (3-13)$$

where L_{TXn} is the self-inductance of corresponding loop n in the transmitter; $M_{TXn-TXm}$ is the mutual inductance between loops n and m in the transmitter; L_{RXn} is the self-inductance of corresponding loop n in the receiver; $M_{RXn-RXm}$ is the mutual inductance between loops n and m in the receiver; $M_{TXn-RXm}$ is the mutual inductance between loop n in the transmitter and loop m in the receiver.

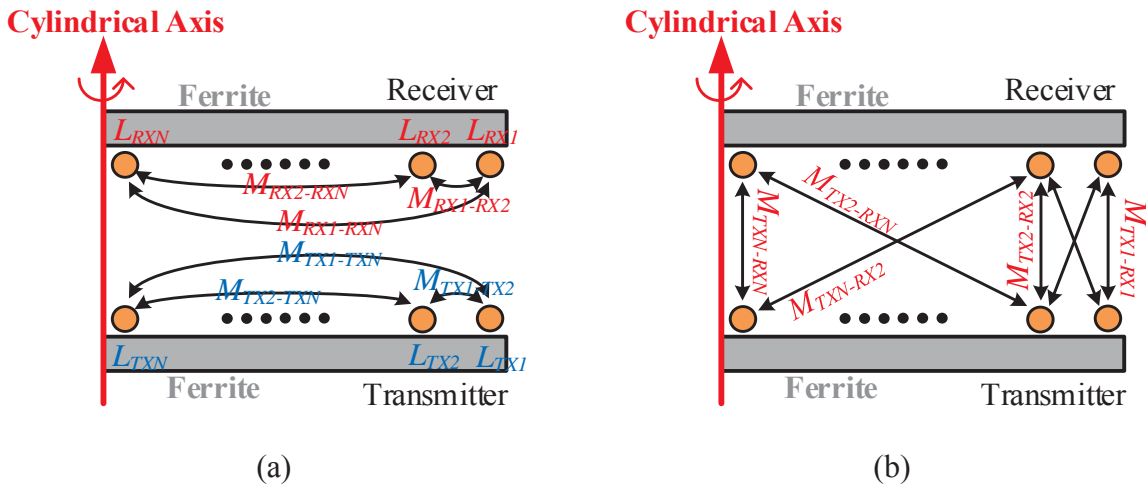


Figure 3-8. The elements of permeance matrices in (3-11) – (3-13) for the lumped-loop model, which are derived in one finite-element simulation with unity turn in each loop.

All the elements of the permeance matrices in (3-11) – (3-13) are derived from one finite-element simulation of the lumped-loop model in Figure 3-8, with one turn for each loop.

The inductances L_1 , L_2 and M of the coils are calculated with the turns vectors \vec{N}_{TX} and \vec{N}_{RX} and the permeance matrices \mathbf{L}_{TX} , \mathbf{L}_{RX} , and \mathbf{M} .

$$L_1 = \vec{N}_{TX} \mathbf{L}_{TX} \vec{N}_{TX}^T \quad (3-14)$$

$$L_2 = \vec{N}_{RX} \mathbf{L}_{RX} \vec{N}_{RX}^T \quad (3-15)$$

$$M = \vec{N}_{TX} \mathbf{M} \vec{N}_{RX}^T \quad (3-16)$$

3.4.2.2. Current-to-Field Matrices

The current-to-field matrices are used to calculate the stray magnetic field from winding currents and turns vectors. The similar concept has been described in [86].

Figure 3-9 shows the cylindrical view of the lumped-loop model. The stray magnetic field $B_i(t)$ at the point of measurement equals the summation of the magnetic fields generated by all the loops in the transmitter and receiver coils. Since the magnetic field is proportional to the winding current, the magnetic field $B_{TXn,i}(t)$ generated by loop n of the transmitter coil is calculated as

$$B_{TXn,i}(t) = \alpha_{TXn,i} N_{TXn} i_{TX}(t) \quad (3-17)$$

where $\alpha_{TXn,i}$ is the current-to-field coefficient for loop n of the transmitter; N_{TXn} is the number of turns for this loop; $i_{TX}(t)$ is the winding current of transmitter; i represents the orientations X, Y, or Z in Figure 3-2.

Similarly, the magnetic field $B_{RXn,i}(t)$ generated by loop n of the receiver coil is calculated as:

$$B_{RXn,i}(t) = \alpha_{RXn,i} N_{RXn} i_{RX}(t) \quad (3-18)$$

According to superposition, the stray magnetic fields $B_i(t)$ at the point for measurement is

$$B_i(t) = \sum_{n=1}^N \alpha_{TXn,i} N_{TXn} i_{TX}(t) + \sum_{n=1}^N \alpha_{RXn,i} N_{RXn} i_{RX}(t) = \bar{\mathbf{a}}_{TX,i} \bar{N}_{TX}^T i_{TX}(t) + \bar{\mathbf{a}}_{RX,i} \bar{N}_{RX}^T i_{RX}(t) \quad (3-19)$$

where $\bar{\mathbf{a}}_{TX,i}$ and $\bar{\mathbf{a}}_{RX,i}$ are current-to-field matrices in X, Y, Z orientations for transmitter and receiver, respectively. They are composed of the current-to-field coefficients in (3-17) and (3-18) as

$$\bar{\mathbf{a}}_{TX,i} = [\alpha_{TX1,i} \quad \alpha_{TX2,i} \quad \cdots \quad \alpha_{TXN,i}] \quad (3-20)$$

$$\bar{\mathbf{a}}_{RX,i} = [\alpha_{RX1,i} \quad \alpha_{RX2,i} \quad \cdots \quad \alpha_{RXN,i}] \quad (3-21)$$

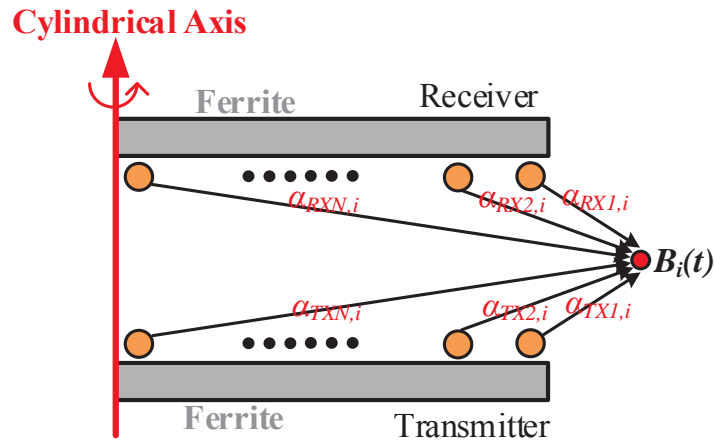


Figure 3-9. The elements of current-to-field matrices in (3-20) and (3-21). Index i represents orientations X, Y, and Z in Figure 3-2.

The current-to-field coefficient of one loop in Figure 3-9 is derived by setting 1 Ampere-turn to this loop and setting 0 Ampere-turn to all the others. If there are N loops for transmitter and N loops for receiver, $2N$ simulations are required to derive all the elements in the current-to-field matrices.

3.4.3. Calculation of Stray Magnetic Field

For each set of turns vectors, the self-inductances L_1 , L_2 and mutual inductance M are calculated from (3-14) – (3-16) with permeance matrices. The winding currents $i_{TX}(t)$ and $i_{RX}(t)$ are derived from (3-1) – (3-4) with the inductances. The stray magnetic fields in X, Y, Z directions are calculated from (3-19) with the winding currents, turns vectors, and current-to-field matrices.

3.4.4. Calculation of Coil-to-Coil Efficiency

The coil-to-coil efficiency is calculated from (2-10) with inductances and winding resistances. The winding resistances r_1 and r_2 include DC part and AC part. The DC resistance is analytically calculated from physical parameters of the litz wire, including the cross-sectional area and length. The AC resistance is mostly caused by the proximity effect when litz wire is used for the coils. Several methods have been proposed to calculate the proximity-effect loss [78], [79], [87], [88]. The method in [78] is applied here with

$$P_e = \frac{\pi l_t N d_c^4}{64 \rho_c} \left\langle \left(\frac{dB(t)}{dt} \right)^2 \right\rangle \quad (3-22)$$

where P_e is the proximity-effect loss of a turn; l_t is the average length of the turn; N is the number of strands; d_c is the diameter of the strand; ρ_c is resistivity of copper; $B(t)$ is the time-varying flux density across the turn; $\langle x \rangle$ is the spatial average over the turn's cross section; \bar{x} is the time average.

The magnetic field across each turn is needed to calculate the proximity-effect resistance in (3-22). To analytically calculate these fields, the lumped-loop model is translated back to the

original coils with real turns, according to the turns vectors. Details are demonstrated in Section 4.3 to approximate the fields across the turns.

3.4.5. Plotting the Pareto Front

After the coil-to-coil efficiencies and stray magnetic fields are calculated for all the turns vectors, the results are marked on the two-dimensional Cartesian coordinate system. Then the Pareto front is derived from all these markers, as shown in Figure 3-3. In this dissertation, the Pareto fronts are derived with Matlab, using the code in Appendix A.

3.5. Design Example

A design example is demonstrated in this section to explain how to use the fast method to optimize the coil-to-coil efficiency and stray magnetic field.

The coils are designed for the series-series compensation with the circuit topology in Figure 2-1. The power of 100 W is transferred across 40 mm gap, with 35 V output voltage on the load and 100 kHz switching frequency of the full bridge inverter. The structure of the coils is the same as Figure 3-2. The dimensions of the 3C96 ferrite plate are 100 mm by 100 mm, with the thickness of 5 mm. The maximum dimensions of each coil are limited to be no larger than the ferrite plate.

The steps to derive the Pareto front for the synergetic optimization include two parts. The first part requires finite-element simulations: determine the lumped-loop model, extract the permeance matrices from one simulation, and extract the current-to-field matrices from several simulations. The second part is done with Matlab: sweep the turns vectors of the lumped-loop model, calculate the inductances, winding currents, and the stray magnetic field, approximate the

winding resistances, calculate the coil-to-coil efficiency, and finally derive the Pareto front. The Matlab code is provided in Appendix B.

1. Determine the lumped-loop model

Figure 3-10 shows the lumped-loop model for the design example. The original structure of the coils is the same as Figure 3-2. There are 10 lumped loops for the transmitter and 10 lumped loops for the receiver. The loops are labeled as TX1 to TX10 and RX1 to RX10. The loops TX1 and RX1 are the outermost loops, with 48 mm radii. The loops TX10 and RX10 are the innermost loops, with 10 mm radii. All the loops are distributed with equal spacing of 4.2 mm, which is about one tenth of the radius for the outermost loop. The wire thickness is set to be 1.2 mm. The influence on inductances and stray magnetic field of wire thickness is ignored because it's much smaller compared to the gap.

2. Extract the permeance matrices from one finite-element simulation

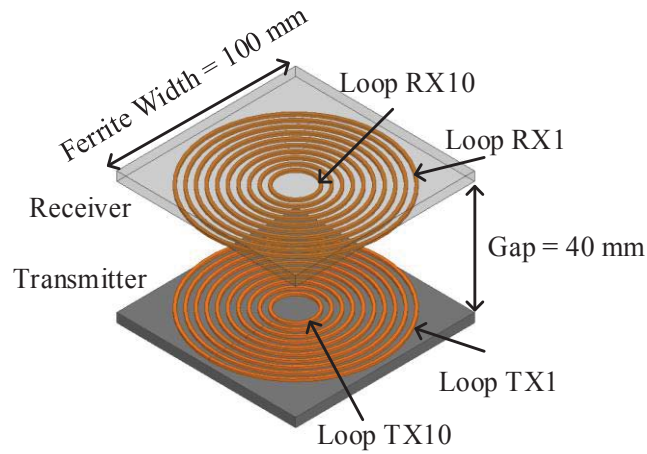
After the lumped-loop model is determined in Figure 3-10, the permeance matrices are derived from one finite-element simulation. In Ansys Maxwell, all the 20 loops are excited with stranded excitation. The permeance matrices are extracted directly from the solution.

The lumped loops models of the transmitter and receiver are the same, so the permeance matrices \mathbf{L}_{TX} and \mathbf{L}_{RX} equal each other. TABLE 3-1 lists the elements of the 10 by 10 matrix \mathbf{L}_{TX} . The elements of \mathbf{L}_{RX} are the same as those of \mathbf{L}_{TX} . TABLE 3-2 shows the elements of the 10 by 10 matrix \mathbf{M} .

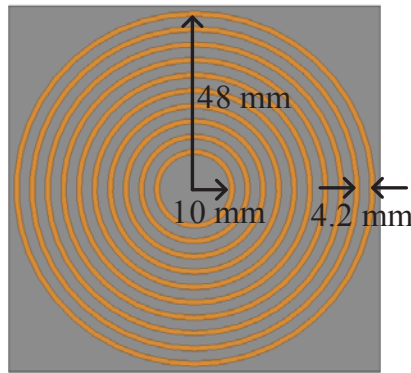
3. Extract the current-to-field matrices from finite-element simulations

The current-to-field matrices are extracted from 20 finite-element simulations. The stray magnetic field is optimized for the point (0, 100 mm, 0) in Figure 3-11(a). When deriving the current-to-field coefficients of one loop, the RMS value of the excitation in this loop is 1

Ampere-turn, and all the other loops are supplied with 0 Ampere-turn. The current-to-field coefficients equal the RMS values of the magnetic fields in X, Y, or Z directions, when the RMS value of the excitation is 1 Ampere-turn.



(a)



(b)

Figure 3-10. The lumped-loop model for the design example, with 10 loops in the transmitter and 10 loops in the receiver.

TABLE 3-1. Permeance Matrices L_{TX} for the Lumped-loop Model in Figure 3-10 (Unit: nH)

	TX1	TX2	TX3	TX4	TX5	TX6	TX7	TX8	TX9	TX10
TX1	400	242	167	120	87	61	42	27	16	8
TX2	242	369	220	149	104	72	49	31	18	9
TX3	167	220	332	194	128	86	57	36	21	10
TX4	120	149	194	291	164	105	67	42	24	11
TX5	87	104	128	164	249	135	82	49	28	13
TX6	61	72	86	105	135	206	106	60	33	15
TX7	42	49	57	67	82	106	165	80	41	19
TX8	27	31	36	42	49	60	80	125	54	23
TX9	16	18	21	24	28	33	41	54	88	32
TX10	8	9	10	11	13	15	19	23	32	54

TABLE 3-2. Permeance Matrices M for the Lumped-loop Model in Figure 3-10 (Unit: nH)

	TX1	TX2	TX3	TX4	TX5	TX6	TX7	TX8	TX9	TX10
RX1	66	62	56	48	40	31	23	16	10	5
RX2	62	59	54	47	39	31	23	16	10	5
RX3	56	54	50	44	37	30	23	16	10	5
RX4	48	47	44	40	34	28	21	15	9	5
RX5	40	39	37	34	30	24	19	13	8	4
RX6	31	31	30	28	25	20	16	12	7	4
RX7	23	23	23	21	19	16	13	9	6	3
RX8	16	16	16	15	13	12	9	7	4	2
RX9	10	10	10	9	8	7	6	4	3	2
TX10	5	5	5	5	4	4	3	2	2	1

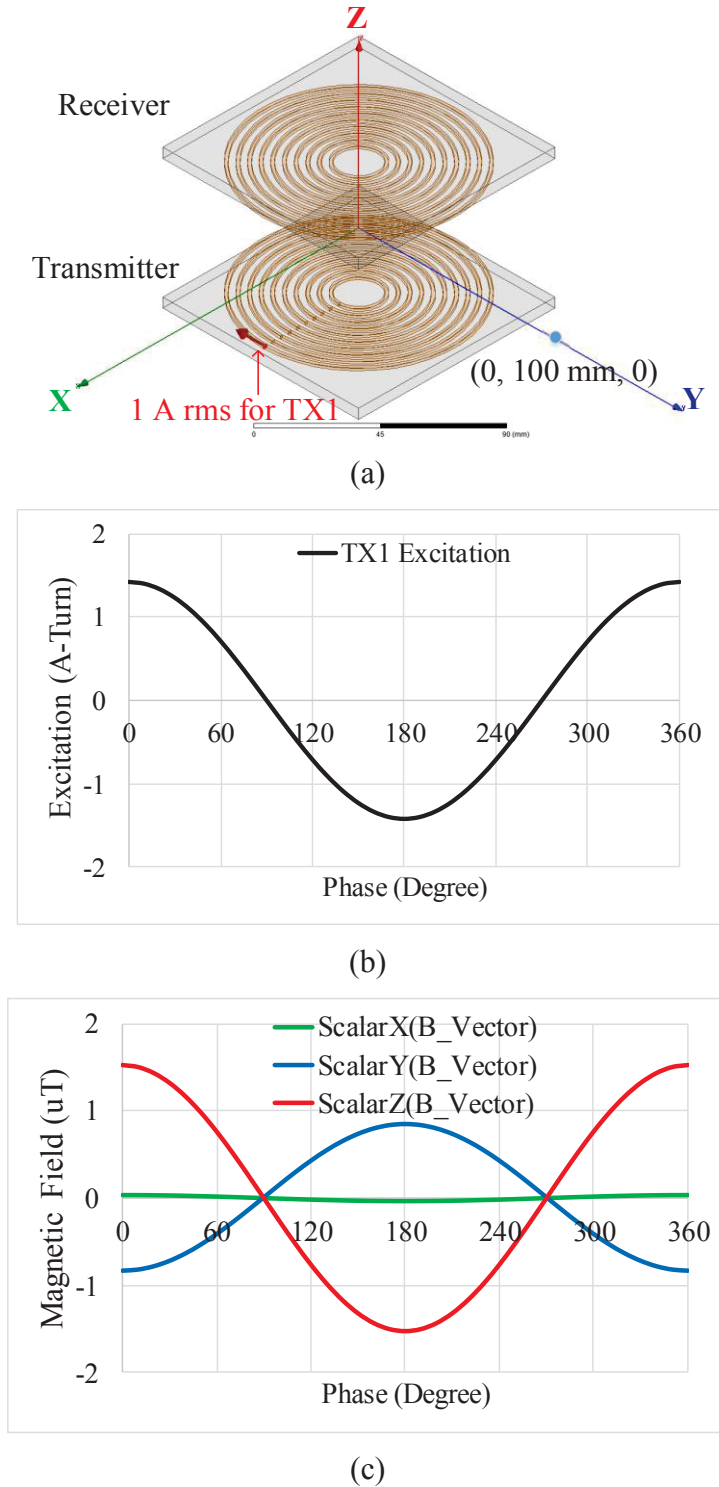


Figure 3-11. (a) The lumped-loop model to derive the current-to-field matrices; (b) current excitation of loop TX1 with 1 A-turn RMS; (c) the magnetic fields in X, Y, Z directions at the point (0, 100 mm, 0), which are extracted using the fields calculator in Ansys Maxwell.

Figure 3-11(a) shows how to excite the loop TX1 to derive the corresponding current-to-field coefficients. The excitation of 1 Ampere-turn in Figure 3-11(b) is supplied to TX1, and all the other loops are supplied with 0 Ampere-turns. In Ansys Maxwell, the magnetic field is decomposed to components in X, Y, and Z directions, with the commands ScalarX(B_Vector), ScalarY(B_Vector), and ScalarZ(B_Vector) in the Fields Calculator. The waveforms of the magnetic fields are plotted in Figure 3-11(c). The current-to-field coefficients for the loop TX1 equal the ratio of the magnetic fields in Figure 3-11(c) over the current excitation in Figure 3-11(b). The horizontal axis of Figure 3-11(b) and (c) is the phase from 0° to 360° which is equivalent to one period of time.

Following the similar procedure, finite-element simulations are implemented to derive the current-to-field coefficients for the other loops. TABLE 3-3 and TABLE 3-4 list the elements of the current-to-field matrices $\vec{u}_{TX,i}$ and $\vec{u}_{RX,i}$.

TABLE 3-3. Current-to-Field Matrix for the Lumped-loop Model of Transmitter in Figure 3-10 (Unit: $\mu\text{T}/\text{Ampere-Turn}$)

	TX1	TX2	TX3	TX4	TX5	TX6	TX7	TX8	TX9	TX10
X	0.021	0.006	0.000	0.007	0.011	0.005	0.008	0.007	0.001	0.001
Y	-0.594	-0.394	-0.229	-0.185	-0.123	-0.067	-0.049	-0.029	-0.019	-0.01
Z	1.083	0.906	0.688	0.620	0.521	0.359	0.255	0.174	0.096	0.07

TABLE 3-4. Current-to-Field Matrix for the Lumped-loop Model of Receiver in Figure 3-10 (Unit: $\mu\text{T}/\text{Ampere-Turn}$)

	RX1	RX2	RX3	RX4	RX5	RX6	RX7	RX8	RX9	RX10
X	0.021	0.006	0.000	0.007	0.011	0.005	0.008	0.007	0.001	0.001
Y	0.594	0.394	0.229	0.185	0.123	0.067	0.049	0.029	0.019	0.01
Z	1.083	0.906	0.688	0.620	0.521	0.359	0.255	0.174	0.096	0.07

In the previous steps, 1 simulation is used to extract the permeance matrices, and 20 simulations are used to extract the current-to-field matrices. A total number of 21 finite-element simulations are required during the entire optimization. All the following steps will be realized using Matlab.

4. Sweep the turns vectors in the lumped-loop model

There are 10 loops for both the transmitter and receiver in the lumped-loop model of Figure 3-10, so the turns vectors are:

$$\vec{N}_{TX} = [N_{TX1} \quad N_{TX2} \quad \cdots \quad N_{TX10}] \quad (3-23)$$

$$\vec{N}_{RX} = [N_{RX1} \quad N_{RX2} \quad \cdots \quad N_{RX10}] \quad (3-24)$$

The turns vectors are swept to derive the Pareto fronts. In this example, the winding turns are assumed to be evenly distributed. TABLE 3-5 lists how to sweep the elements of the turns vectors.

The outermost loop is swept to represent the outer radii of the winding. For the transmitter, its outermost loop N_{TX0} is swept from N_{TX1} to N_{TX5} , whereas the outermost loop of the receiver N_{RX0} is swept from N_{RX1} to N_{RX5} .

The innermost loops N_{TXi} and N_{RXi} are selected according to the outermost loops N_{TXo} and N_{RXo} , respectively. The innermost loop of the transmitter, N_{TXi} , is selected by sweeping from $N_{TX(o+1)}$ to N_{TX10} , whereas the innermost loop of the receiver, N_{RXi} , is selected by sweeping from $N_{RX(o+1)}$ to N_{RX10} .

TABLE 3-5. Turns Vectors to be Swept for the Lumped-loop Model in Figure 3-10

Procedure	Swept Values
The outermost loop of transmitter $N_{TX(o)}$	$o = 1$ to 5
R_{outer} of the transmitter	$50 \text{ mm} - (o - 1) * 4.2 \text{ mm}$
The innermost loop of transmitter $N_{TX(i)}$	$i = (o + 1)$ to 10
R_{inner} of the transmitter	$50 \text{ mm} - (i - 1) * 4.2 \text{ mm}$
Wire Diameter D	0.9 mm to 6 mm
Sweep the turns number of the transmitter	From 1 to floor $[(R_{outer} - R_{inner}) / D]$
The outermost loop of receiver $N_{RX(o)}$	$o = 1$ to 5
R_{outer} of the receiver	$50 \text{ mm} - (o - 1) * 4.2 \text{ mm}$
The innermost loop of receiver $N_{RX(i)}$	$i = (o + 1)$ to 10
R_{inner} of the receiver	$50 \text{ mm} - (i - 1) * 4.2 \text{ mm}$
Sweep the turns number of the receiver	From 1 to floor $[(R_{outer} - R_{inner}) / D]$

The turns number is swept according to the wire diameter D . In this example, litz wires with AWG #38 strands are selected. The strand numbers are selected from 40, 66, 100, 162, 260, 420, 660, 1050, 1650. The corresponding wire diameters are 0.9 mm, 1.1 mm, 1.5 mm, 1.9 mm, 2.3 mm, 2.9 mm, 3.8 mm, 4.8 mm, and 6 mm. The maximum number of turns, N_{max} , is calculated

from the innermost loop, outermost loop and D . The number of turns is swept from 1 to N_{max} . All these turns are evenly distributed between the loops N_{TXi} and N_{TXo} , or between the loops N_{RXi} and N_{RXo} . The other loops are assigned zero turns.

5. Calculate the inductances with lumped-loop model

For each set of turns vectors, the inductances are calculated with the permeance matrices in TABLE 3-1 and TABLE 3-2, using (3-14) – (3-16). For the example of Figure 3-12,

$N_{TXo} = N_{TX2}$, $N_{TXi} = N_{TX9}$, $N_{RXo} = N_{RX2}$, $N_{RXi} = N_{RX9}$. There are 21 turns for the transmitter and 21 turns for the receiver. The corresponding turns vectors of the example are:

$$\vec{N}_{TX} = [0 \quad 2.3 \quad 2.3] \quad (3-25)$$

$$\vec{N}_{RX} = [0 \quad 2.3 \quad 2.3] \quad (3-26)$$

The inductances of the lumped-loop model in Figure 3-12 is calculated as $L_1 = L_2 = 36.9 \mu\text{H}$, and $M = 8.6 \mu\text{H}$.

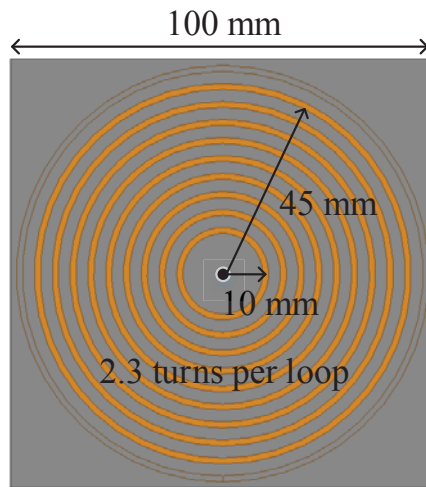


Figure 3-12. An exemplary lumped-loop model to calculate the inductances, winding currents, and stray magnetic field.

6. Calculate the winding currents from the inductances

For the example in Figure 3-12, the winding currents are derived from (3-1) – (3-4) as:

$$i_{TX}(t) = 8 \cdot \sin(2\pi \cdot 100k \cdot t) \quad (3-27)$$

$$i_{RX}(t) = 4.5 \cdot \sin(2\pi \cdot 100k \cdot t + \pi/2) \quad (3-28)$$

7. Calculate the stray magnetic field with lumped-loop model

The stray magnetic fields in X, Y, Z directions at the point (0, 100 mm, 0) are calculated from (3-19), with the winding currents in (3-27) and (3-28), turns vectors in (3-25) and (3-26), and current-to-field matrices in TABLE 3-3 and TABLE 3-4. The RMS values of calculated $B_Y(t)$ and $B_Z(t)$ are 17.9 μT and 55.4 μT , respectively. The magnitude of $B_X(t)$ is negligible due to symmetry. The quantified magnetic field is 58.1 μT at the point (0, 100 mm, 0).

8. Approximate the winding resistances

In order to calculate the winding resistances, the lumped-loop model in Figure 3-12 is translated back to the coils with real turns as shown in Figure 3-13, according to the turns vectors in (3-25) and (3-26). The inner radius is 10 mm and the outer radius is 45 mm. When the litz wire is composed of 100 strands with 0.1 mm strand-diameter, the calculated winding resistance is 100 m Ω . Detailed procedure will be demonstrated in Chapter 4.

9. Calculate the coil-to-coil efficiency

The coil-to-coil efficiency of the exemplary coils in Figure 3-12 and Figure 3-13 is calculated from (2-10), with inductance $M = 8.6 \mu\text{H}$ and winding resistances $r_1 = r_2 = 100 \text{ m}\Omega$. The calculated efficiency is 95.7%.

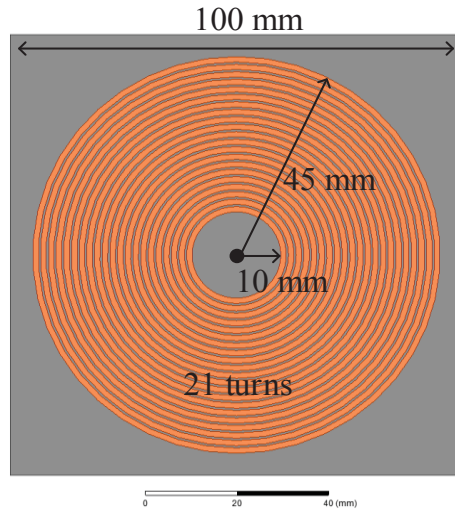


Figure 3-13. Coils with real turns for the lumped-loop model in Figure 3-12, which are used to calculate winding resistances.

10. Derive the Pareto front

The efficiency and stray magnetic field for the exemplary coils in Figure 3-12 and Figure 3-13 is marked on the two-dimensional Cartesian coordinate in Figure 3-19. After all the turns vectors in TABLE 3-5 are swept, the Pareto front is derived in Matlab. The solid line in Figure 3-14 is derived using the method of lumped-loop model. The dashed line is derived following the procedures in Figure 3-4 by sweeping physical parameters in finite-element simulations. The results are almost the same, which proves the accuracy of the method using the lumped-loop model.

The red circle on the upper right of Figure 3-14 represents the scaled-down coils of Figure 2-17, which is designed to maximize the efficiency without considering stray magnetic field. Although the efficiency of the red circle almost reaches the maximum, its stray magnetic field is $10 \mu\text{T}$ higher than the optimal design which is located along the Pareto front with similar efficiency.

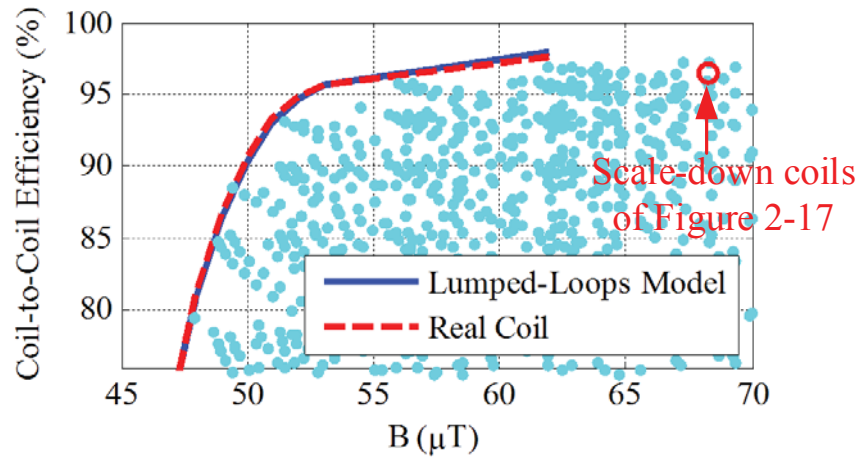


Figure 3-14. Comparison of the Pareto fronts derived from the procedures in Figure 3-4 and Figure 3-5. The coils are used with the circuit topology in Figure 2-1, to transfer 100 W power across 40 mm gap. The maximum dimensions of the coils are 100 mm by 100 mm. The red circle on the upper right represents the scaled-down coils in Figure 2-17, which is designed to maximize the efficiency without considering stray magnetic field.

3.6. Experimental Verification

3.6.1. Coil-to-Coil Efficiency

The exemplary coils in Figure 3-12 and Figure 3-13 locates along the Pareto front in Figure 3-14, which means it is one of the optimal designs. Figure 3-15 is the coil fabricated according to Figure 3-13. A 3C96 ferrite plate with dimensions of 100 mm by 100 mm by 5 mm is placed underneath the winding. The fixture of the winding was made with PLA using the 3D printer, and the fabrication procedure is provided in Appendix C.

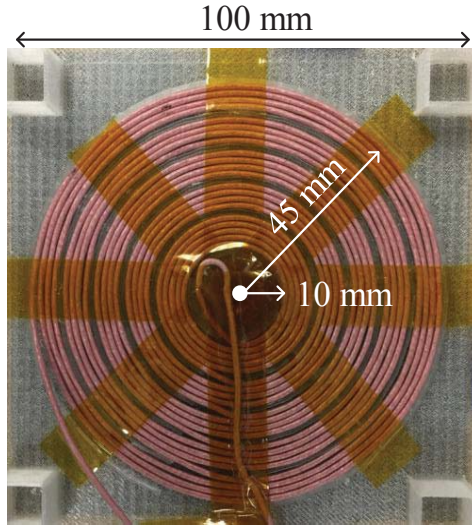


Figure 3-15. Fabricated coils of Figure 3-14, using litz wire composed of 100 strands with 0.1 mm strand-diameter and 3C96 ferrite plate with dimensions of 100 mm by 100 mm by 5 mm.

TABLE 3-6 shows the inductances and winding resistances of the coils in Figure 3-12, Figure 3-13, and Figure 3-15, which are derived from matrix calculation, finite-element simulation, and measurement, respectively. The matrix calculation and simulation results are almost the same. The maximum difference between calculation and measurement is 4% for inductances and 6% for winding resistances. One reason for the error is the deviation of turns' radius during the fabrication process. As shown in Figure 3-15, the fixture of the winding makes the turns unevenly distributed. This is caused by the resolution of the 3D printer, which is not fine enough to make a slot for each turn.

The coil-to-coil efficiencies in TABLE 3-6 are calculated from (2-10) with the inductances and winding resistances. All the coils in Figure 3-15 achieve 95.7% efficiency for the same specifications in Figure 3-3.

TABLE 3-6. Inductances, Resistances, and Coil-to-Coil Efficiencies for Coils in Figure 3-12, Figure 3-13, and Figure 3-15

Parameters	Matrix Calculation Figure 3-12	Simulation Figure 3-13	Measurement Figure 3-15
L_1, L_2 (μH)	36.9, 36.9	36.8, 36.8	35.4, 36.0
M (μH)	8.6	8.6	8.7
r_1 and r_2 ($\text{m}\Omega$), at 100 kHz	100, 100	100, 100	102, 106
Coil-to-coil efficiency	95.7%	95.7%	95.7%

3.6.2. Stray Magnetic Field

Near-field probe Langer EMV LF-R 50 [89] is selected for the measurement of magnetic field. The probe is designed with 10 mm loops as in Figure 3-16(a). It's used to measure magnetic field from 100 kHz to 50 MHz.

When the probe is placed into the magnetic field as shown in Figure 3-16(b), the voltage which is induced on the probe loops with spatial directions is calculated from Faraday's law with

$$v_{ind,i}(t) = \frac{d}{dt} \iint \vec{B}(t) d\vec{A}_i = NA \frac{d}{dt} B_i(t), i = X, Y, Z \quad (3-29)$$

where N is the turns number of loops in field probe, A is loop area; $B_i(t)$ is the magnetic field flowing through the field.

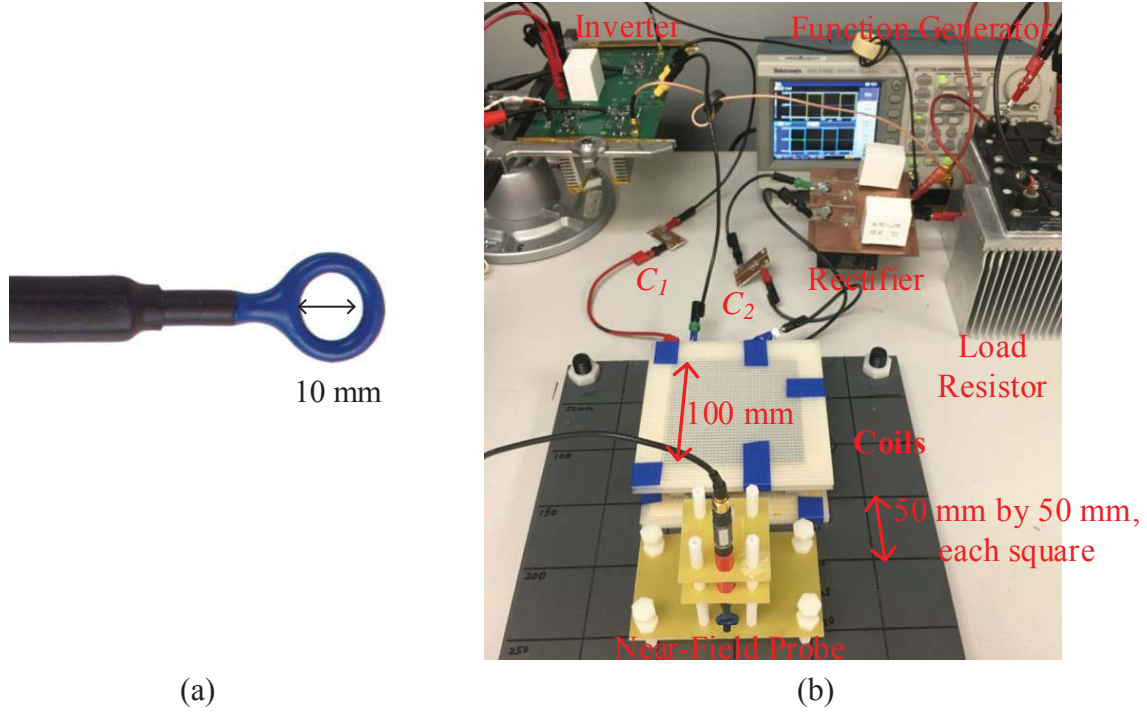


Figure 3-16. (a) Near-field probe and (b) hardware setup for field measurement.

The induced voltage $v_{ind,i}(t)$ goes through calibration network, which is integrated with the probe and is used to improve the performance of frequency response. The waveform of the calibrated voltage $v_i(t)$ is displayed on the oscilloscope after the calibration network. This process is demonstrated in Figure 3-17(a). With the correction values in Figure 3-17(b) which are supplied by the manufacture, the information of magnetic field $B_i(t)$ is calculated from $v_i(t)$ as

$$B_i(\omega) = \mu_0 \cdot v_i(\omega) \cdot 10^{\frac{CorrectionValue(\omega)}{20}} \quad (3-30)$$

where μ_0 is the permeability of air; ω is the radial frequency of the signal; v_i is the RMS value of the induced voltage on the oscilloscope for the magnetic field in one spatial direction; B_i is the RMS value of the magnetic field in one spatial direction; the correction value is plotted in Figure 3-17(b).

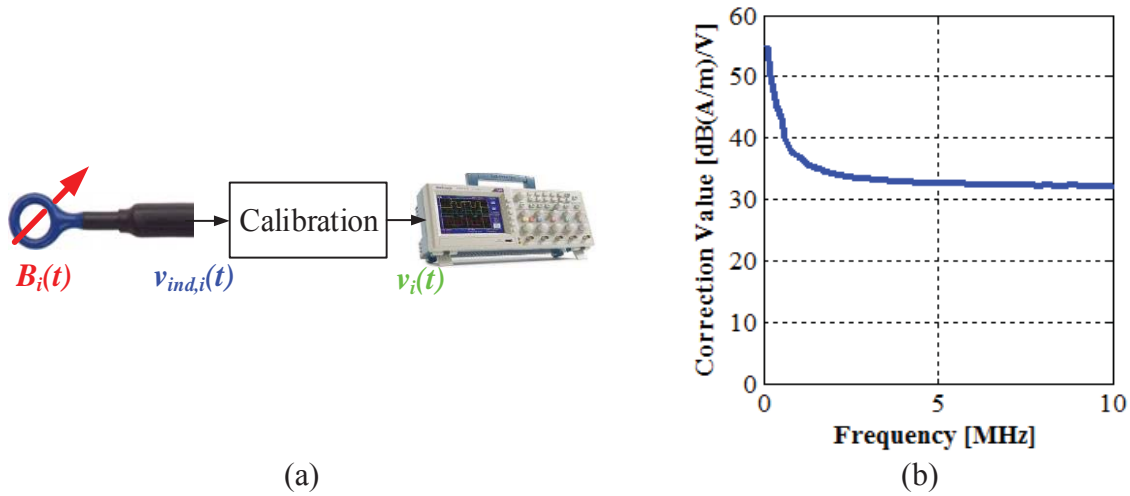
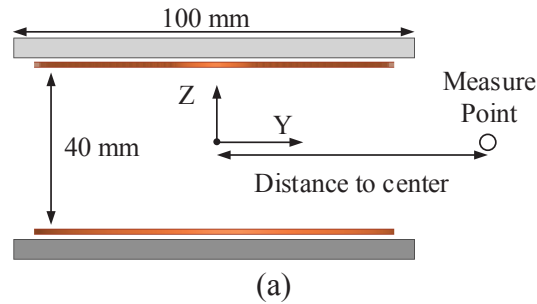


Figure 3-17. (a) Process of transferring measured field to voltage; (b) values of the voltage-to-field correction versus frequency [89].

The hardware setup for the field measurement is shown in Figure 3-16(b). At each position, the near-field probe is used to measure the magnetic fields $B_X(t)$, $B_Y(t)$, and $B_Z(t)$ in X, Y, and Z directions. The quantified magnetic fields were calculated according to (3-8).

With 40 mm gap between transmitter and receiver coils, the magnetic fields along Y axis in Figure 3-18(a) were calculated, simulated, and measured for the coils in Figure 3-12, Figure 3-13, and Figure 3-15, respectively. The distances from the measure points to the center range from 75 mm to 150 mm. The comparison of the quantified magnetic field is shown in Figure 3-18(b), which shows that the difference between the measurement and calculation is less than 12.5%. One reason of the error is cause by the fabrication process using 3D printer, as domenstrated in 3.6.1. Another reason is that the probe has a 10 mm diameter as in Figure 3-16(a). The measured field is the spatial average of the field penetrating the probe instead of the field at one point.



(b)

Figure 3-18. (a) Side view of the coils; (b) quantified stray magnetic fields along Y axis when the measure points are located from 75 mm to 150 mm to the center. The magnetic fields are calculated, simulated, and measured with the coils in Figure 3-12, Figure 3-13, and Figure 3-15, respectively.

Figure 3-19(a) and (b) show the time-domain waveforms of stray magnetic fields in Y and Z directions at two points along the Y-axis. One point is 100 mm away from the center, and the other one is 150 mm away from the center. The dashed lines are the calculated results of the lumped-loop model in Figure 3-12 with the turns vectors in (3-25) and (3-26) and the current-to-field matrices in TABLE 3-3. The solid lines are the measured results of the coils in Figure 3-15 using the hardware setup in Figure 3-16. The calculated waveforms match well with the measured waveforms. The magnetic fields are not purely sinusoidal owing to the harmonics in

winding currents. However, the influence of this non-sinusoidal effect is negligible when quantifying the magnetic fields.

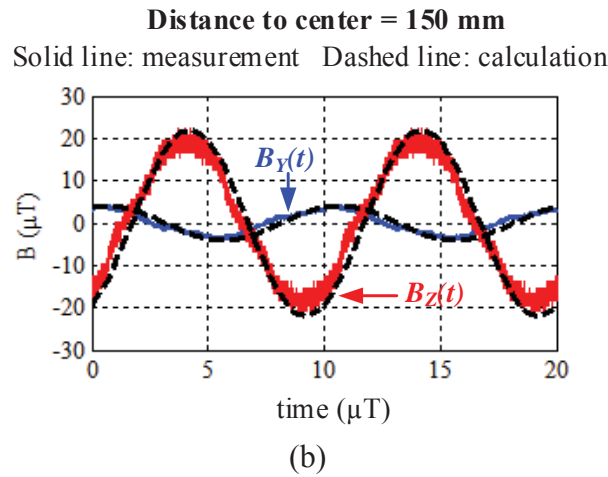
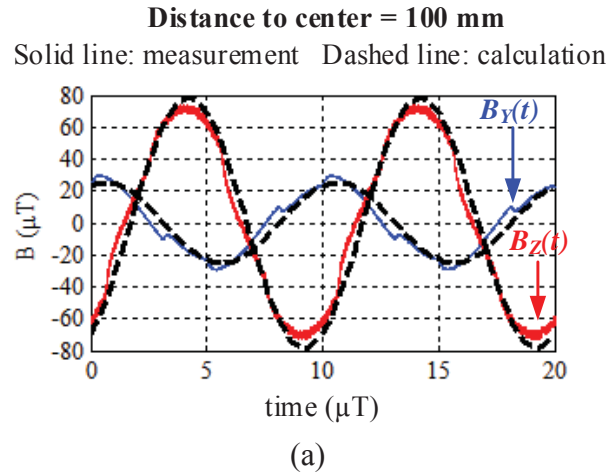


Figure 3-19. Time-domain waveforms of the stray magnetic fields in Y and Z directions at the points with (a) 100 mm and (b) 150 mm distances to the center of the coils (solid lines: measurement results of the coils in Figure 3-15; dashed lines: calculation results of the lumped-loop model in Figure 3-12).

3.7. Summary

This chapter discusses the synergetic attenuation of stray magnetic field when designing IPT coils for high efficiency. Pareto front is applied for the optimization. A fast method for optimization is described, using the concept of lumped-loop model. The coil-to-coil efficiency and stray magnetic field are calculated with permeance matrices, current-to-field matrices, and turns vectors. The turns vectors are swept to get the Pareto front. Only tens of simulations are required during the entire procedure, so this method is much faster than the conventional method which requires thousands of simulations.

Detailed procedure of the optimization is demonstrated using an example. The coils are used in the series-series compensation to transfer 100 W power across 40 mm gap. The dimensions of each coil are 100 mm by 100 mm. The Pareto front derived from the lumped-loop model matches well with that derived from parametric sweep in finite-element simulation. An exemplary set of coils located along the front was fabricated and tested in experiment. The coil-to-coil efficiencies are the same for calculation and experimental measurement, and the difference for stray magnetic fields from calculation and measurement is less than 12.5%.

In this chapter, the analytical method to calculate winding resistance is not discussed. All the details for the resistance calculation will be demonstrated in Chapter 4.

Chapter 4. Approximation of Proximity-Effect Resistance

Nomenclature

a	Radius of turn m in Figure 4-7.
$B_{external}$	External field across a turn in Figure 4-1, generated by all the other turns.
$B_{external-r}$	Component of $B_{external}$ in the radial direction in Figure 4-1.
$B_{external-a}$	Component of $B_{external}$ in the axial direction in Figure 4-1.
$B_{internal}$	Internal field across a turn in Figure 4-1, generated by the turn itself.
$B_{internal-r}$	Component of $B_{internal}$ in the radial direction in Figure 4-1.
$B_{internal-a}$	Component of $B_{internal}$ in the axial direction in Figure 4-1.
B_{mirror}	Magnetic field generated by the mirrored turn in Figure 4-3.
$B_{m-mirror}$	The magnetic fields generated by the mirrored turn m in Figure 4-6.
$B_{m-original}$	The magnetic fields generated by the original turn m in Figure 4-6.
$B_{r, m-mirror}$	Component of $B_{m-mirror}$ in the radial direction in Figure 4-6.
$B_{r, m-original}$	Component of $B_{m-original}$ in the radial direction in Figure 4-6.
B_{self}	Magnetic field generated by the original turn in Figure 4-3.
$B_{a, m-mirror}$	Component of $B_{m-mirror}$ in the axial direction in Figure 4-6.
$B_{a, m-original}$	Component of $B_{m-original}$ in the axial direction in Figure 4-6.
d	Distance between the centers of the original turn and the corresponding mirrored turn.
d_c	Strand diameter of litz wire.

I	Peak value of winding current.
l_t	Average length of a turn.
P_e	Proximity-effect loss of a turn.
R	Radius of the turn's cross section in Figure 4-4 and Figure 4-5.
r	Distances in radial direction between the center of turn m and the measure point of turn n in Figure 4-7.
r_e	Proximity-effect resistance of a turn.
R_{inner}	Inner radius of the winding.
R_{outer}	Outer radius of the winding.
z	Distances in axial direction between the center of turn m and the measure point of turn n in Figure 4-7.
μ_0	Permeability of free space.
ρ_c	Resistivity of copper.
ω	Radial frequency of winding current [rad/s].

4.1. Introduction

Because of the low coupling caused by the air gap, the efficiency of an IPT system is significantly influenced by the winding resistances of the coils. Litz wire is popularly used to reduce the winding loss. The winding resistance of the litz wire include DC part and AC part. The DC resistance is analytically calculated from the physical parameters of the wire, such as the cross-section area and the length. The AC resistance is caused by the skin effect and the proximity effect, which is generated by the eddy current in the wire [90], [91]. When the strand diameter of the litz wire is properly selected, the skin-effect loss is negligible. The proximity-effect loss is inevitable for planar coils, and several methods have been proposed to calculate it [78], [79], [87], [88]. The proximity-effect loss is proportional to the square of magnetic fields

across the turns of winding. The derivation of the magnetic fields is essential to calculate the proximity-effect resistance of litz wire.

The magnetic fields across turns can be derived using either numerical method or analytical method. Numerical method with finite-element simulation [51] generates accurate results, but it is time-consuming, especially for three-dimensional simulations. Things get even worse when the coils are optimized with parametric sweep, which has been discussed in Chapter 3. Analytical method is faster to calculate the magnetic field, and it is more suitable for the optimization procedure of coils such as the fast method in Figure 3-5.

However, when the ferrite plate with finite size is placed below the planar winding, the analytical equations become complicated [73]–[76] or less accurate [92]. The objective of this chapter is to demonstrate an analytical method that is simple and accurate to calculate the magnetic fields across turns of planar coil with ferrite plate. This method should work well together with the concept of the lumped-loop model in Chapter 3.

The method of image [93]–[96] is applied for field calculation in this chapter. The ferrite with sufficiently high magnetic permeability is modeled as a perfect magnetic conductor (PMC). Setting tangential H fields at the interface to zero, the PMC can be modeled using just a single mirror image. Therefore, the ferrite plate is replaced by the mirrored turns, which have the same current as the original turns. The magnetic field across one turn is decomposed into internal field and external field. The internal field is generated by the turn itself, and it's calculated from Ampere's Law [97]. The external field is generated by all the other turns, and it's calculated from Biot-Savart Law [98]. The proximity-effect resistance is derived directly with internal and external fields. Thanks to the sinusoidal currents in inductive power transfer, the analytical equations to calculate the magnetic fields are further simplified.

It's found that the size of the ferrite plate has negligible influence on the proximity-effect resistance as long as it is larger than the size of the winding. This requirement is reasonable in inductive power transfer for EV charging. The size of ferrite plate is always designed to be no smaller than the winding, in order to increase the coupling [46], [71] and to reduce the field emission [62] within the limited dimensions.

Section 4.2 introduces the equations to calculate the proximity-effect loss of litz wire in inductive power transfer. Section 4.3 presents the method to calculate the equivalent structure of planar coils with ferrite plate and the magnetic fields across the turns of winding. Section 4.4 demonstrates the influence of ferrite size on the proximity-effect resistance. In Section 4.5, the accuracy of the calculation is verified by comparing with the measurement results.

4.2. Proximity-Effect Loss of Litz Wire in Inductive Power Transfer

Different methods have been proposed to calculate the proximity-effect loss of litz wire [78], [79], [87], [88]. The proximity-effect loss is caused by the proximity effect at strand level and bundle level. Bundle level effects relate to current circulating in paths involving multiple strands, whereas strand-level effects take place within individual strands.

The bundle-level effect is negligible since it is controlled by the twisting or weaving pattern of the litz wire. The strand-level effect is dominant, and (3-22) is applied in this dissertation to calculate the proximity-effect loss in strand-level [78].

The spatial average of $\overline{(dB(t)/dt)^2}$ over the cross section of the turn should be derived to calculate the proximity-effect loss according to (3-22). Finite-element simulation is accurate to do so, but it's not suitable for the optimization of coils. The objective of this chapter is to investigate a simple and accurate method to calculate $\left\langle \overline{(dB(t)/dt)^2} \right\rangle$.

For the IPT circuit in Figure 2-1, the winding current is almost sinusoidal, expressed as

$$i(t) = I \cdot \sin(\omega t) \quad (4-1)$$

where I is the peak value of winding current, and ω is the radial frequency of the inverter's switching frequency. Because magnetic field is proportional to current, the field generated by the current in (4-1) is sinusoidal as well:

$$B(t) = B \cdot \sin(\omega t) \quad (4-2)$$

where B is the peak value of the magnetic field, and ω is the radial frequency of winding current in (4-1). The value of $\overline{\left(\frac{dB(t)}{dt}\right)^2}$ is calculated from (4-2) as

$$\overline{\left(\frac{dB(t)}{dt}\right)^2} = \frac{\omega^2}{2} \cdot B^2 \quad (4-3)$$

The spatial average $\left\langle \overline{\left(\frac{dB(t)}{dt}\right)^2} \right\rangle$ over the cross section of the turn is simplified from (4-3)

as

$$\left\langle \overline{\left(\frac{dB(t)}{dt}\right)^2} \right\rangle = \frac{\omega^2}{2} \cdot \langle B^2 \rangle \quad (4-4)$$

According to (3-22) and (4-4), the proximity-effect loss of the litz wire in IPT application is calculated as

$$P_e = \frac{\pi l_t N d_c^4 \omega^2}{128 \rho_c} \cdot \langle B^2 \rangle \quad (4-5)$$

4.3. Magnetic Fields across Turns of the Planar Coil with Ferrite Plate

4.3.1. Components of the Magnetic Field across Each Turn

The magnetic field across one turn is composed of the internal field $B_{internal}(t)$ and the external field $B_{external}(t)$, as shown in Figure 4-1(a). The internal field is generated by the turn itself. It's

determined by the current distribution of the turn. The external field is generated by all the other turns. It's roughly uniform across the turn, because the cross section of the turn is much smaller than the dimensions of the coil. Since $B_{internal}(t)$ and $B_{external}(t)$ are both generated by the winding current in (4-1), their time-domain waveforms are sinusoidal with the same phase as the winding current. In the following discussion, $B_{internal}(t)$ and $B_{external}(t)$ are represented by their peak magnitudes $B_{internal}$ and $B_{external}$.

An axis of symmetry is drawn across the turn in Figure 4-1(a), in the same direction as the axial axis. The pair of points 1 and 1' in Figure 4-1(b) are symmetrical about this axis. The internal field is decomposed to $B_{internal-a}$ and $B_{internal-r}$, where $B_{internal-a}$ is the component in the axial direction, and $B_{internal-r}$ is the component in the radial direction. Similarly, the external field is decomposed to $B_{external-a}$ and $B_{external-r}$. Their relationships are

$$B_{internal}^2 = B_{internal-r}^2 + B_{internal-a}^2 \quad (4-6)$$

$$B_{external}^2 = B_{external-r}^2 + B_{external-a}^2 \quad (4-7)$$

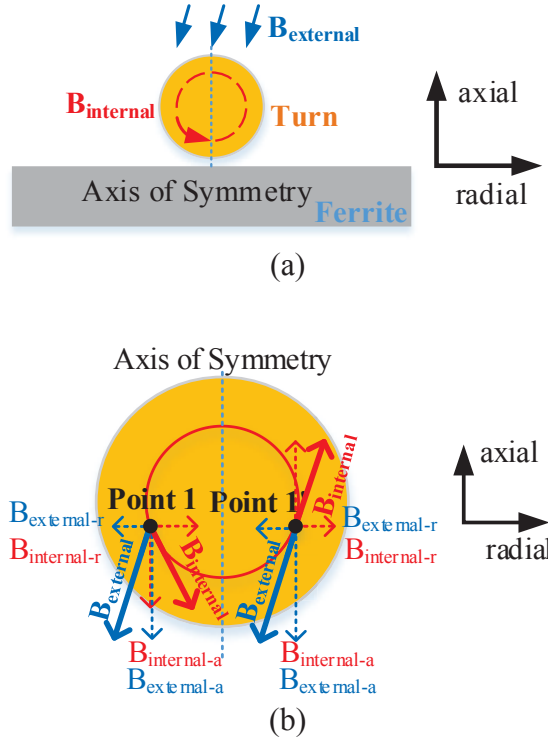


Figure 4-1. (a) Internal field $B_{internal}$ and external field $B_{external}$ across one turn of the planar coil; (b) axial and radial components of $B_{internal}$ and $B_{external}$ at symmetrical points 1 and 1'.

Thanks to the symmetry, the magnitude and direction of $B_{internal-r}$ and the magnitude of $B_{internal-a}$ at point 1 are the same as those at point 1', whereas the direction of $B_{internal-r}$ at point 1 is opposite to that at point 1'. For the external field, both $B_{external-r}$ and $B_{external-a}$ at point 1 are the same as those at point 1' because the external field is almost uniformly distributed across one turn when the cross section of the turn is much smaller than the dimensions of the coil. Owing to the influence of the ferrite plate, $B_{external-a}$ is more dominant than $B_{external-r}$.

According to Figure 4-1(b), the magnetic fields $B_{P1}(t)$ at point 1 and $B_{P1'}(t)$ at point 1' are derived as

$$B_{P1} = \sqrt{(B_{internal-a} + B_{external-a})^2 + (B_{internal-r} - B_{external-r})^2} \quad (4-8)$$

$$B_{P1'} = \sqrt{(B_{internal-a} - B_{external-a})^2 + (B_{internal-r} + B_{external-r})^2} \quad (4-9)$$

The summation of B^2 at points 1 and 1' is derived from (4-6) – (4-9) to be

$$B_{P1}^2 + B_{P1'}^2 = 2(B_{internal}^2 + B_{external}^2) \quad (4-10)$$

Because there are infinite pairs of symmetrical points like points 1 and 1', $\left\langle \overline{\left(\frac{dB(t)}{dt}\right)^2} \right\rangle$ in

(3-22) is derived from all these pairs as:

$$\left\langle \overline{\left(\frac{dB(t)}{dt}\right)^2} \right\rangle = \frac{\sum_{n=1}^{\infty} \left[\overline{\left(\frac{dB_{Pn}(t)}{dt}\right)^2} + \overline{\left(\frac{dB_{Pn'}(t)}{dt}\right)^2} \right] \cdot dS}{S} \quad (4-11)$$

where dS is the differential area of each point, and S is the cross-sectional area of the turn. With

the similar calculation procedure as (4-3), $\overline{\left(\frac{dB_{Pn}(t)}{dt}\right)^2}$ and $\overline{\left(\frac{dB_{Pn'}(t)}{dt}\right)^2}$ are represented as:

$$\overline{\left(\frac{dB_{Pn}(t)}{dt}\right)^2} = \frac{\omega^2}{2} \cdot B_{Pn}^2 \quad (4-12)$$

$$\overline{\left(\frac{dB_{Pn'}(t)}{dt}\right)^2} = \frac{\omega^2}{2} \cdot B_{Pn'}^2 \quad (4-13)$$

Equation (4-11) is simplified from (4-12) and (4-13) to be

$$\left\langle \overline{\left(\frac{dB(t)}{dt}\right)^2} \right\rangle = \frac{\omega^2}{2} \cdot \frac{\sum_{n=1}^{\infty} (B_{Pn}^2 + B_{Pn'}^2) \cdot dS}{S} \quad (4-14)$$

According to (4-10), B_{Pn}^2 and $B_{Pn'}^2$ are represented by $B_{internal}^2$ and $B_{external}^2$, so (4-14) is

simplified as

$$\left\langle \left(\frac{dB(t)}{dt} \right)^2 \right\rangle = \frac{\omega^2}{2} \cdot \left(\frac{\sum_{n=1}^{\infty} 2B_{internal}^2 \cdot dS}{S} + \frac{\sum_{n=1}^{\infty} 2B_{external}^2 \cdot dS}{S} \right) \quad (4-15)$$

The components on the right side of (4-15) equal the spatial average of $B_{internal}^2$ and $B_{external}^2$ across the turn, with

$$\frac{\sum_{n=1}^{\infty} 2B_{internal}^2 \cdot dS}{S} = \langle B_{internal}^2 \rangle \quad (4-16)$$

$$\frac{\sum_{n=1}^{\infty} 2B_{external}^2 \cdot dS}{S} = \langle B_{external}^2 \rangle \quad (4-17)$$

According to (4-16) and (4-17), (4-15) is simplified as

$$\left\langle \left(\frac{dB(t)}{dt} \right)^2 \right\rangle = \frac{\omega^2}{2} (\langle B_{internal}^2 \rangle + \langle B_{external}^2 \rangle) \quad (4-18)$$

Equation (4-18) proves that $B_{internal}$ and $B_{external}$ are decoupled. They should be derived separately to calculate $\left\langle \left(\frac{dB(t)}{dt} \right)^2 \right\rangle$ for the proximity-effect loss in (3-22).

4.3.2. Equivalent Structure to Calculate Magnetic Fields

When the ferrite plate is placed below the winding as shown in Figure 4-2(a), the analytical equations to calculate $\left\langle \left(\frac{dB(t)}{dt} \right)^2 \right\rangle$ become complicated or less accurate compared to the case with air core. According to the method of image, the equivalent structure in Figure 4-2(b) is derived by replacing the ferrite plate with mirrored turns.

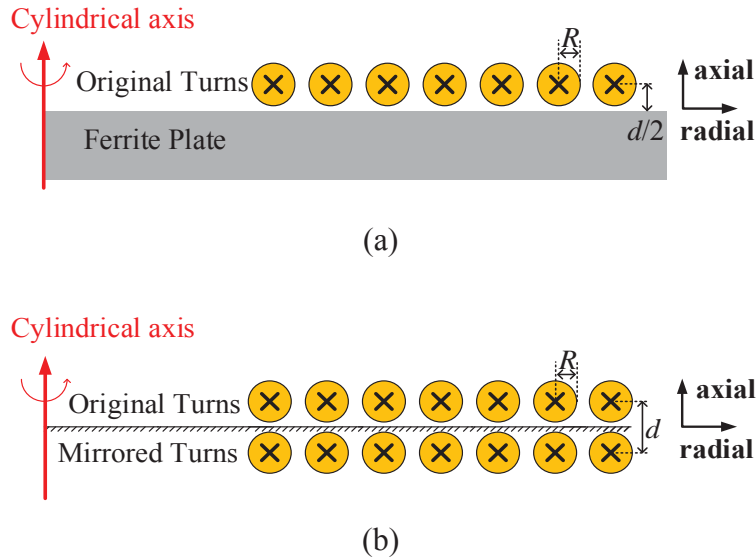


Figure 4-2. (a) Cylindrical structure of the planar coils with ferrite plate and (b) its equivalent structure derived from the method of image.

The original turns and the mirrored turns are symmetrical about the upper surface of ferrite plate. They have the same dimensions and excitations. Since the equivalent structure is composed of windings with air core, the magnetic fields across the original turns are calculated directly using Ampere's Law and Biot-Savart Law. Detailed calculation will be demonstrated in 4.3.3 and 4.3.4.

4.3.3. Internal Magnetic Field

Only the original turn and its mirrored turn are considered when calculating the internal magnetic field $B_{internal}$ of one turn. As shown in Figure 4-3, there are two components for $B_{internal}$ – B_{self} which is generated by the original turn and B_{mirror} which is generated by its mirrored turn.

The axis of symmetry in the horizontal axis is drawn in Figure 4-3 across the original turn. Points 1 and 1' are symmetrical about this axis. The magnitudes of B_{self} at point 1 and 1' are the same, but the magnitudes of B_{mirror} are different. Field B_{self} is decomposed into radial component

B_{self-r} and axial component B_{self-a} as (4-19), while field B_{mirror} is mostly in the radial direction across the original turn.

$$B_{self}^2 = B_{self-r}^2 + B_{self-a}^2 \quad (4-19)$$

The magnitudes of B_{self-r} and B_{self-a} at point 1 are the same as those at point 1'. The values of B_{mirror} at the two points are different, and they are expressed as $B_{mirror-P1}$ and $B_{mirror-P1'}$, respectively. According to Figure 4-3, the magnetic fields $B_{P1}(t)$ at point 1 and $B_{P1'}(t)$ at point 1' are calculated as

$$B_{P1} = \sqrt{(B_{self-r} + B_{mirror-P1})^2 + B_{self-a}^2} \quad (4-20)$$

$$B_{P1'} = \sqrt{(B_{self-r} - B_{mirror-P1'})^2 + B_{self-a}^2} \quad (4-21)$$

The summation of B^2 at points 1 and 1' is derived from (4-20) and (4-21) as

$$B_{P1}^2 + B_{P1'}^2 = 2B_{self}^2 + (B_{mirror-P1}^2 + B_{mirror-P1'}^2) \quad (4-22)$$

Following the similar procedure in (4-10) – (4-18), $\left\langle \left(\frac{dB_{internal}(t)}{dt} \right)^2 \right\rangle$ is derived from all the symmetrical pairs of points, which is

$$\left\langle \left(\frac{dB_{internal}(t)}{dt} \right)^2 \right\rangle = \frac{\omega^2}{2} \langle B_{internal}^2 \rangle = \frac{\omega^2}{2} (\langle B_{self}^2 \rangle + \langle B_{mirror}^2 \rangle) \quad (4-23)$$

Equation (4-23) shows that $\langle B_{self}^2 \rangle$ and $\langle B_{mirror}^2 \rangle$ are decoupled, and they should be derived separately to calculate $\langle B_{internal}^2 \rangle$.

In order to calculate $\langle B_{self}^2 \rangle$, only the original turn is excited. The flux density $B_{self}(r)$ of the differential ring in Figure 4-4 is calculated using Ampere's Law, with

$$\frac{B_{self}(r)}{\mu_0} \cdot 2\pi r = I \cdot \frac{r^2}{R^2} \quad (4-24)$$

where r is the radius of the differential ring; I is the peak value of the current excitation in the original turn; μ_0 is the permeability of free space; R is the radius of the turn's cross section.

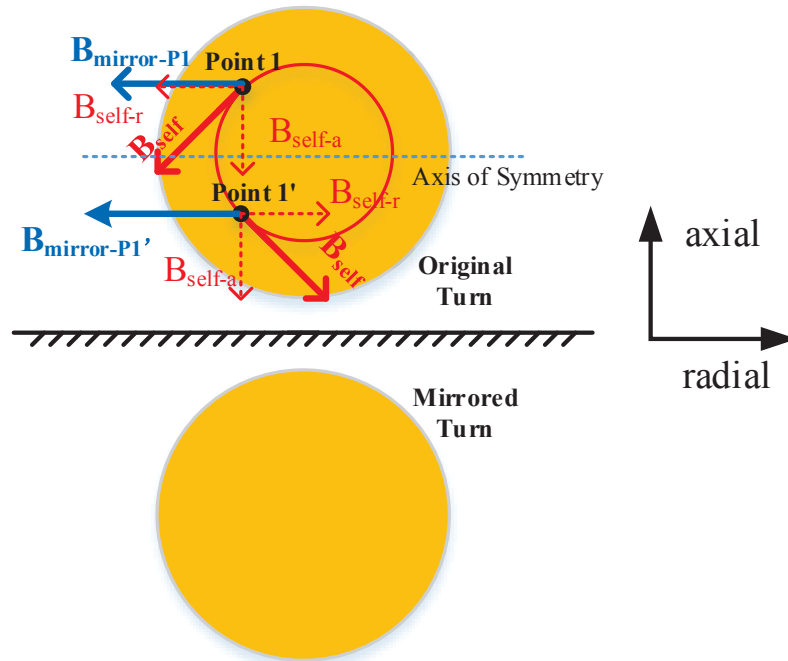


Figure 4-3. Components to calculate the internal fields at symmetrical points 1 and 1': B_{self} generated by the original turn and B_{mirror} generated by the mirrored turn.

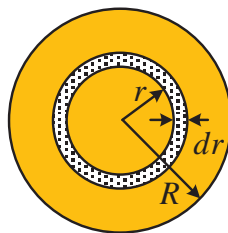


Figure 4-4. Cross section of the original turn in Figure 4-3 to calculate the internal field in (4-24).

By integrating (4-24) over the cross-sectional area of the original turn, $\langle B_{self}^2 \rangle$ is

$$\langle B_{self}^2 \rangle = \frac{\int_0^R \left(\frac{\mu_0 I}{2\pi r} \cdot \frac{r^2}{R^2} \right)^2 (2\pi r \cdot dr)}{\pi R^2} \quad (4-25)$$

where R is the radius of the cross section.

Only the mirrored turn is excited to derive $\langle B_{mirror}^2 \rangle$. The flux density of the differential strip in Figure 4-5 is calculated using Ampere's Law, and $\langle B_{mirror}^2 \rangle$ is derived by integrating flux density over the cross section of the original turn, with

$$\langle B_{mirror}^2 \rangle = \frac{\int_{-R}^R \left[\frac{\mu_0 I}{2\pi (d+x)} \right]^2 (2\sqrt{R^2 - x^2} \cdot dx)}{\pi R^2} \quad (4-26)$$

where d is the distance between the centers of the original turn and the mirrored turn; x is the distance between the centers of the differential strip and the mirrored turn.

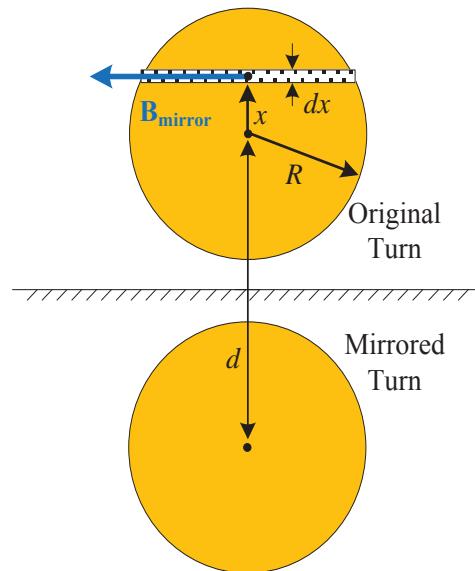


Figure 4-5. Cross sections of the original turn and the mirrored turn in Figure 4-3 to calculate the internal field in (4-26).

4.3.4. External Magnetic Field

Figure 4-6 shows the equivalent structure to calculate $\langle B_{external}^2 \rangle$ across the original turn n of a planar coil. There are N turns totally. The ferrite plate is replaced with the mirrored turns. In the equivalent structure, turn n is not excited so its mirrored turn is not drawn. All the other original turns and mirrored turns are excited with sinusoidal current.

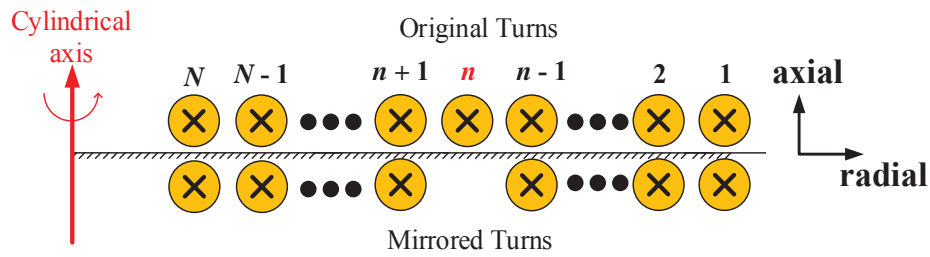


Figure 4-6. Equivalent structure to calculate the external field on the original turn n for a planar coil with N turns. Turn n is not excited and all the other original turns and mirrored turns are excited with current I .

The magnetic fields generated by the original turn m and the mirrored turn m are represented as $B_{m-original}$ and $B_{m-mirror}$, respectively. $B_{m-original}$ and $B_{m-mirror}$ are decomposed into components in the radial direction, $B_{r, m-original}$ and $B_{r, m-mirror}$, and components in the axial direction, $B_{a, m-original}$ and $B_{a, m-mirror}$. Then $\langle B_{external}^2 \rangle$ across turn n is calculated by summing up all the fields generated by other turns in Figure 4-6 as

$$\langle B_{external}^2 \rangle = \left(\sum_{\substack{m=1 \\ m \neq n}}^N B_{r, m-original} + \sum_{\substack{m=1 \\ m \neq n}}^N B_{r, m-mirror} \right)^2 + \left(\sum_{\substack{m=1 \\ m \neq n}}^N B_{a, m-original} + \sum_{\substack{m=1 \\ m \neq n}}^N B_{a, m-mirror} \right)^2 \quad (4-27)$$

The values of $B_{r, m-original}$, $B_{r, m-mirror}$, $B_{a, m-original}$ and $B_{a, m-mirror}$ are calculated from Biot-Savart Law. Figure 4-7 shows the magnetic field B across turn n , generated by turn m . Its components in

the radial and axial directions are calculated from from (4-31) and (4-32), respectively. The details to derive (4-31) and (4-32) will be demonstrated in the following paragraphs.

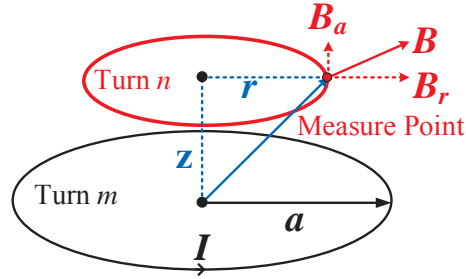


Figure 4-7. The example to calculate external field B across turn n , which is generated by turn m with excitation I . The components of B in the radial and axial directions, B_r and B_a , are calculated from (4-31) and (4-32), respectively.

According to Biot-Savart Law, the field generated by the small segment of conductor $d\vec{s}$ with length ds and excitation current I in Figure 4-8 is calculated as

$$d\vec{B} = \frac{\mu_0 I}{4\pi} \cdot \frac{d\vec{s} \times \vec{r}}{r^2} \quad (4-28)$$

where r is the distance from the segment to the measure point P; \vec{r} is the unit vector pointing from the segment to P; μ_0 is the permeability of free space.

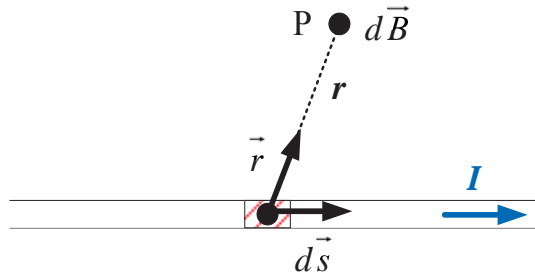


Figure 4-8. Magnetic field dB at the measure point P, generated by the small segment of conductor ds with current excitation I .

The magnetic field generated by the circular loop m in Figure 4-7 is calculated by integrating (4-28) along the loop. The magnetic fields in the radial and axial directions at the measure point in loop n are

$$B_r = \frac{\mu_0 \cdot I \cdot a \cdot z}{4\pi} \int_0^{2\pi} \frac{\sin \varphi}{(a^2 + r^2 + z^2 - 2r \cdot a \sin \varphi)^{3/2}} d\varphi \quad (4-29)$$

$$B_z = \frac{\mu_0 \cdot I \cdot a}{4\pi} \int_0^{2\pi} \frac{a - r \cdot \sin \varphi}{(a^2 + r^2 + z^2 - 2r \cdot a \cdot \sin \varphi)^{3/2}} d\varphi \quad (4-30)$$

Equations (4-29) and (4-30) are calculated to be

$$B_r = B_0 \frac{\gamma}{\pi \sqrt{Q}} \left[E(k) \frac{1 + \alpha^2 + \beta^2}{Q - 4\alpha} - K(k) \right] \quad (4-31)$$

$$B_z = B_0 \frac{1}{\pi \sqrt{Q}} \left[E(k) \frac{1 - \alpha^2 - \beta^2}{Q - 4\alpha} + K(k) \right] \quad (4-32)$$

where functions $K(k)$ and $E(k)$ are the complete elliptic integral functions of the first kind and second kind; definitions of B_0 , α , β , γ , Q , and k are

$$B_0 = \frac{\mu_0 I}{2a} \quad (4-33)$$

$$\alpha = \frac{r}{a} \quad (4-34)$$

$$\beta = \frac{z}{a} \quad (4-35)$$

$$\gamma = \frac{z}{r} \quad (4-36)$$

$$Q = \left[(1 + \alpha)^2 + \beta^2 \right] \quad (4-37)$$

$$k = \sqrt{\frac{4\alpha}{Q}} \quad (4-38)$$

where I and a are the peak current and radius of turn m , respectively; r and z are the distances in the radial and axial directions between the center of turn m and the measure point of turn n , respectively.

In summary, the values of $\langle (dB(t)/dt)^2 \rangle$ across all the turns, which are critical to calculate the proximity-effect loss of planar coil with ferrite plate in Figure 4-2(a), are derived by calculating $\langle B_{internal}^2 \rangle$ and $\langle B_{external}^2 \rangle$ in (4-25) – (4-27) with the equivalent structure in Figure 4-2(b). The proximity-effect resistance is then derived from (4-5) with all the magnetic fields as

$$r_e = \frac{\pi l_t N d_c^4 \omega^2}{128 \rho_c I^2} \cdot (\langle B_{self}^2 \rangle + \langle B_{mirror}^2 \rangle + \langle B_{external}^2 \rangle) \quad (4-39)$$

4.4. Influence of Ferrite Plate's Size

In order to derive the most accurate values of magnetic fields across the turns for the planar coil with finite size of ferrite plate, the winding currents should be mirrored about the surfaces of the ferrite plate for infinite times [94], [95]. In Figure 4-2(b), the original turns are mirrored about the upper surface of the ferrite plate for only once, as shown in Figure 4-2(b). The major benefit of the equivalent structure in Figure 4-2(b) is making the calculation of the field simpler and faster, but it's not able to predict the influence of ferrite plate's size on proximity-effect resistance. In this section, this influence is parametrically studied using an exemplary planar coil, by sweeping the size of ferrite plate.

Figure 4-9(a) shows the structure and dimensions of the exemplary planar coil for the parametrical study. The winding’s inner and outer radii are 8 mm and 45 mm, respectively. Litz wire is composed of 100 strands with 0.1 mm diameter. The thickness of ferrite plate is 5 mm.

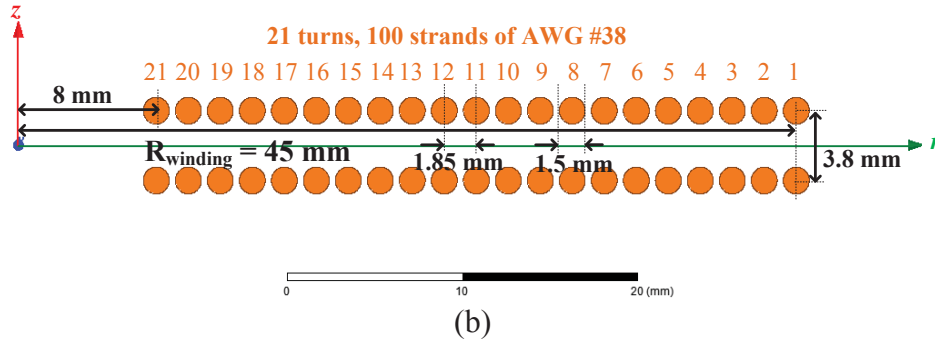
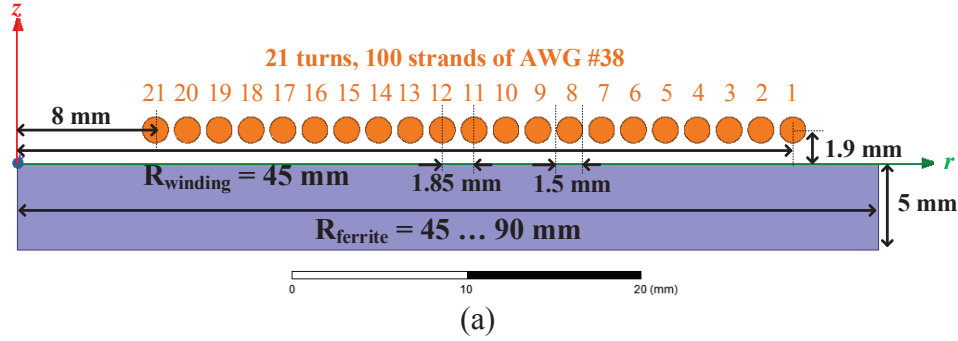


Figure 4-9. (a) Cylindrical structure of the exemplary coil with ferrite plate; (b) equivalent structure of (a) using the method of image to calculate B^2 .

Figure 4-9(b) is the equivalent structure to calculate $\langle B^2 \rangle$, using the method of image. The spacing between an original turn and its corresponding mirrored turn is 3.8 mm in the axial direction. TABLE 4-1 lists all the parameters that are used to calculate the magnetic fields in (4-25), (4-26), (4-31), and (4-32). Figure 4-10 shows the calculated $\langle B^2 \rangle$ of each original turn for the equivalent structure in Figure 4-9(b). The simulated $\langle B^2 \rangle$ using the coil with ferrite plate in Figure 4-9(a) are plotted in Figure 4-10 as well. The radius of the ferrite plate is parametrically

swept from 45 mm to 90 mm in Ansys Maxwell. The size of the ferrite plate is no smaller than that of the winding, in order to increase the coupling [46], [71] and to reduce the field emission [62] in IPT.

TABLE 4-1. Parameters Values to Calculate Magnetic Fields for the Equivalent Structure in Figure 4-9(b)

Field Equations	Variables in Equations	Values
B_{self} in (4-25)	R	1.5 mm
B_{mirror} in (4-26)	R	1.5 mm
	d	3.8 mm
$B_{external}$ in (4-31) and (4-32)	a	8 mm – 45 mm
	r	8 mm – 45 mm
	z	3.8 mm

Figure 4-10 proves that the magnetic fields are accurate for most of the inner turns. Some errors exist for the outer turns owing to the fringing, but their influences on the proximity-effect resistance is negligible, because the magnetic fields across the outer turns are much weaker than those across the inner turns. For a proper design, the inner radii of the winding is less than half of the outer radii, in order to improve the quality factor of the coil and to increase the coupling between the transmitter and receiver [71]. In this case, most turns are placed further away from the edge of the ferrite plate, and the influence of fringing is minimized.

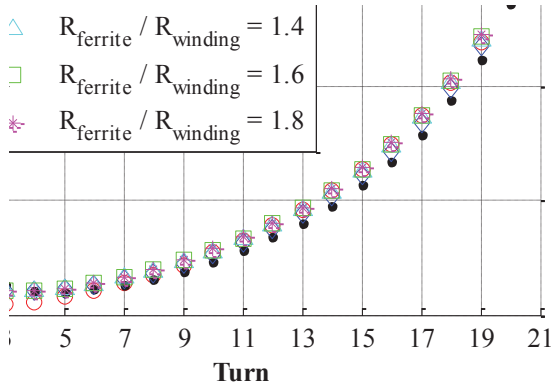


Figure 4-10. Calculated B^2 for the equivalent structure in Figure 4-9(b) and simulated B^2 for the real structure in Figure 4-9(a) with different sizes of ferrite plate.

The proximity-effect resistances in Figure 4-11 are calculated from (4-39), using the values of $\langle B^2 \rangle$ in Figure 4-10. TABLE 4-2 list the values of the parameters that are used for the calculation. The red line is the calculated resistance with the calculated $\langle B^2 \rangle$. All the other lines are calculated from the simulated $\langle B^2 \rangle$, with different radii of the ferrite plate. The frequency stops at 200 kHz because IPT for EV charging works below this frequency. Figure 4-11 shows that the differences are less than 8% between the calculation result and the simulation results. Therefore, the influence of ferrite size is negligible on the proximity-effect resistance.

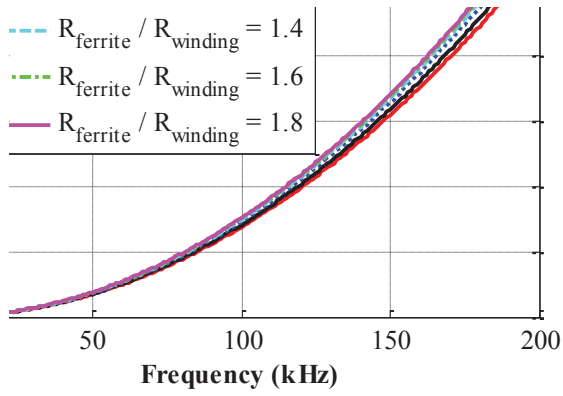


Figure 4-11. Proximity-effect resistance calculated from (4-39) using B^2 in Figure 4-10.

TABLE 4-2. Parameters Values to Calculate Proximity-Effect Loss in (4-39)

Parameters	Values
N	100
d_c	0.1 mm
ω	628318 rad/s
l_t	$2\pi * (8 \text{ mm} - 45 \text{ mm})$
$\langle B^2 \rangle$	Figure 4-10

4.5. Experimental Verification

The exemplary planar coil in Figure 4-9(a) was fabricated as shown in Figure 4-12.

Commercialized ferrite plate with dimensions of 100 mm \times 100 mm \times 5 mm is placed below the

winding. The ferrite size is larger than the winding size so the influence of its shape is negligible, according to the analysis in Section 4.4. The equivalent series resistance (ESR) of the coil was measured with impedance analyzer Agilent 4294A, from 40 Hz to 200 kHz. The measured proximity-effect resistance was derived by subtracting the DC resistance from the ESR. The DC resistance is roughly the same as the measured ESR at 40 Hz, which is the lowest frequency the impedance analyzer can be used for measurement. Figure 4-13 shows the comparison between calculation and measurement. The difference is less than 7% for ESR and less than 15% for the proximity-effect resistance.

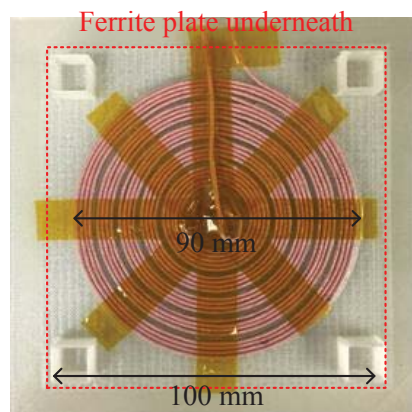


Figure 4-12. Fabricated coil of the structure in Figure 4-9 (a) with square ferrite plate of dimensions $100\text{ mm} \times 100\text{ mm} \times 5\text{ mm}$.

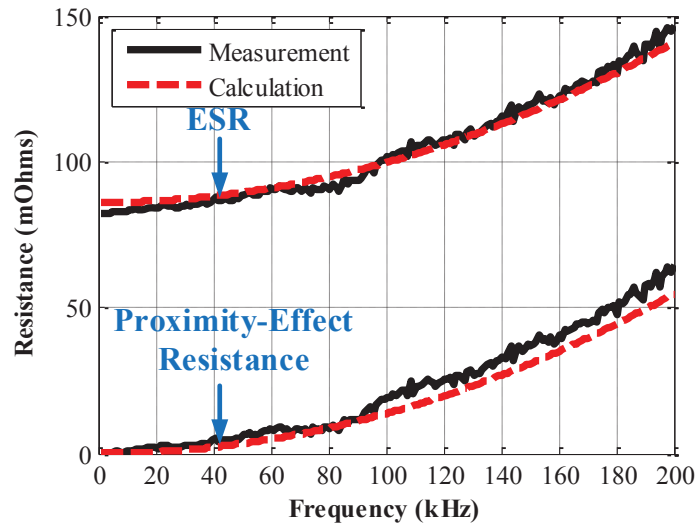


Figure 4-13. ESR and proximity-effect resistance from calculation (dashed lines) and measurement (solid lines) for the coil in Figure 4-12.

4.6. Summary

This chapter demonstrates an analytical method to approximate the magnetic field across each turn of the planar coil in IPT application, which is critical for the calculation of proximity-effect resistance. The magnetic field is decomposed into internal field and external field. The internal field is generated by the turn itself, and the external field is generated by all the other turns. They are decoupled when calculating the proximity-effect resistance.

The existence of the ferrite plate complicates the field calculation. The method of image is used for the simplification, by replacing the ferrite plate with the mirrored turns. With the equivalent structure, the internal fields are calculated from Ampere's Law, and the external fields are calculated from Biot-Savart Law. The influence of ferrite plate's size is found to be negligible on the proximity-effect resistance, as long as the plate size is no smaller than the winding size.

An exemplary planar coil was fabricated, using litz wire composed of 100 strands with 0.1 mm diameter and square ferrite plate. The dimensions of the ferrite plate are 100 mm × 100 mm × 5 mm. The winding resistance up to 200 kHz was measured with impedance analyzer. The difference of the proximity-effect resistances is less than 15% between calculation and measurement.

The resistance calculation in this chapter is useful for the fast optimization in Chapter 3. As long as the turns vectors is known, the lumped-loop model is translated back to the coils with real turns. Then the winding resistance is analytically calculated with the selected litz wire. This method is also good for the resistance calculation for planar coils with litz shield in Chapter 5.

Chapter 5. Attenuation of Stray Magnetic Field with Litz Shield

Nomenclature

I_{sh1}	RMS value of current in transmitter shield.
I_{sh2}	RMS value of current in receiver shield.
I_{w1}	RMS value of current in transmitter winding.
I_{w2}	RMS value of current in receiver winding.
L_{RX}	Equivalent self-inductance of the receiver in Figure 5-6(b).
L_{sh1}	Self-inductance of the transmitter shield in Figure 5-6(a).
L_{sh2}	Self-inductance of the receiver shield in Figure 5-6(a).
L_{TX}	Equivalent self-inductance of the transmitter in Figure 5-6(b).
L_{w1}	Self-inductance of the transmitter winding in Figure 5-6(a).
L_{w2}	Self-inductance of the receiver winding in Figure 5-6(a).
$M_{sh1,n-sh2,m}$	Mutual inductance between loop n of transmitter shield and loop m of receiver shield in Figure 5-10.
$M_{sh1-sh2}$	Mutual inductance between the transmitter and receiver shields in Figure 5-6(a).
M_{shield}	Total number of turns for the shield.
M_{TX-RX}	Equivalent mutual inductance in Figure 5-6(b).
$M_{w(i),n-sh(j),m}$	Mutual inductance between loops n of the winding i and loop m of the shield j in Figure 5-10, with i or $j = 1$ representing transmitter and i or $j = 2$ representing receiver.
$M_{w(j)-sh(i)}$	Mutual inductance between winding j and litz shield i in Figure 5-6(a), with i or $j = 1$ for transmitter and i or $j = 2$ for receiver.

$M_{w1,n-w2,m}$	Mutual inductance between loops n of transmitter winding and loop m of receiver winding in Figure 5-10.
M_{w1-w2}	Mutual inductance between the transmitter and receiver windings in Figure 5-6(a).
$N_{sh1,(n)}$	Turns number of loop n in the transmitter shield in Figure 5-9(b).
$N_{sh2,(n)}$	Turns number of loop n in the receiver shield in Figure 5-9(b).
$N_{w1,(n)}$	Turns number of loop n in the transmitter winding in Figure 5-9(b).
$N_{w2,(n)}$	Turns number of loop n in the receiver winding in Figure 5-9(b).
$N_{winding}$	Total number of turns for the winding.
$P_{e,m}$	Proximity-effect loss of turn m for the shield.
$P_{e,n}$	Proximity-effect loss of turn n for the winding.
r_{e1}	Proximity-effect resistance of the transmitter.
r_{e2}	Proximity-effect resistance of the receiver.
R_{inner}	Inner radius of the winding.
R_{outer}	Outer radius of the winding.
r_{RX}	Equivalent resistance of the receiver in Figure 5-6(b).
r_{sh1}	Resistance of the transmitter shield in Figure 5-6(a).
r_{sh2}	Resistance of the receiver shield in Figure 5-6(a).
r_{TX}	Equivalent resistance of the transmitter in Figure 5-6(b).
r_{w1}	Resistance of the transmitter winding in Figure 5-6(a).
r_{w2}	Resistance of the receiver winding in Figure 5-6(a).
$\alpha_{sh(j),n,i}$	Current-to-field coefficient in direction i for loop n of shield j in Figure 5-11, with $j = 1$ representing transmitter and $j = 2$ representing receiver, $i = X, Y, \text{ or } Z$ in Figure 3-2.

$\alpha_{w(j),n,i}$

Current-to-field coefficient in direction i for loop n of winding j in Figure 5-11, with $j = 1$ representing transmitter and $j = 2$ representing receiver, $i = X, Y,$ or Z in Figure 3-2.

5.1. Introduction

Chapter 3 describes the method to attenuate stray magnetic field by tuning the distribution of turns. The more effective method is to add metal shields to the IPT coils [53], [100]–[102]. The mostly used metal shields are the plate shield in Figure 5-1(a) and the ring shield in Figure 5-1(b). The magnetic field generated by the windings induces eddy currents in the shields, and then the stray magnetic field is reduced by the eddy currents.

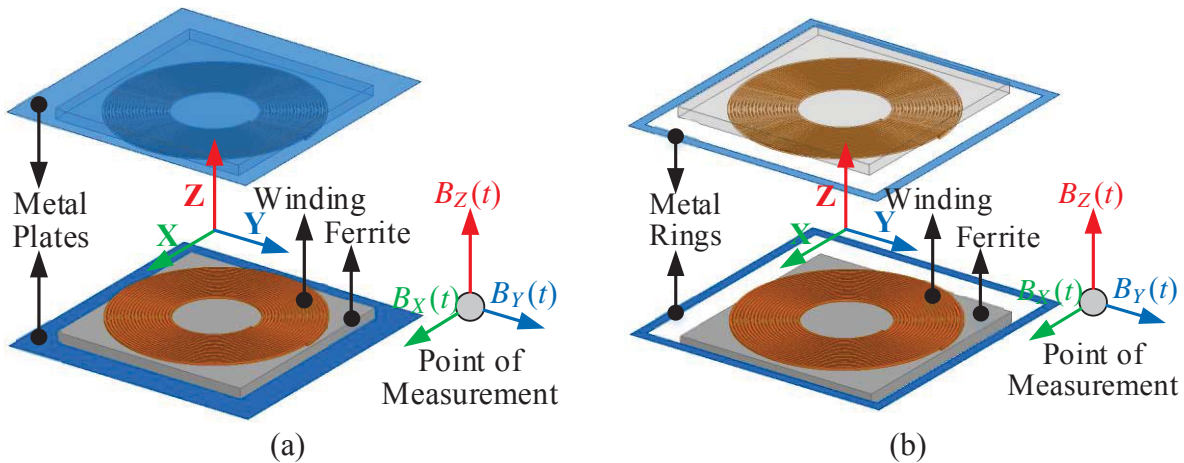


Figure 5-1. Metal shields with (a) plate structure and (b) ring structure to attenuate stray magnetic fields around the coils.

However, the induced eddy currents generate significant conduction losses owing to the skin effect. When the frequency of the current is 100 kHz, the skin depth is 0.2 mm for copper and 0.26 mm for aluminum. In this case, the shield current mostly flows on the surface and increases

conduction losses. In order to overcome this problem, litz wires are used as metal shields in this chapter. The shielding currents are uniformly distributed in the litz shields to reduce the losses.

The litz shields are categorized to two types: the shorted litz shield and the driven litz shield. Turns of litz wires are placed around the windings for shielding purpose. In the shorted litz shield, the shielding turns are self-shortened and they are not connected to the windings. The eddy current is induced on the shields for field attenuation. In the driven litz shield, the shielding turns of litz wire are connected to the windings in series, but in the reverse direction. The supplied current flows in both the winding and the driven litz shield. The induced eddy current in shorted litz shield and the supplied current in driven litz shield are evenly distributed in the shields, so the shielding losses are reduced compared to plate shield and ring shield in Figure 5-1.

Circuit models are derived to analyze the behaviors of the coils with litz shields. The litz shields are modeled as inductors coupled with the windings. The coils with litz shields are represented as four coupled inductors. The currents of windings and shields, the equivalent mutual inductance, and the equivalent series resistances (ESRs) are all calculated from the circuit models with the four coupled inductors.

Pareto fronts are used to optimize the coil-to-coil efficiency and the stray magnetic field for the coils with litz shields. The concept of lumped-loop model in Chapter 3 is used for the fast optimization, by replacing the windings and litz shields with lumped loops. As long as the number of turns for each loop is known, the inductances and magnetic field are calculated directly using the permeance matrices and current-to-field matrices. The winding resistances are calculated using the analytical method in Chapter 4. The coil-to-coil efficiency is calculated from the inductances and winding resistances afterwards. The Pareto fronts are derived using Matlab, after all the turns vectors are swept.

Section 5.2 demonstrates the structures and circuit models for the coils with litz shields. Section 5.3 shows the the fast method to derive the Pareto fronts of coil-to-coil efficiency versus stray magnetic field, using the lumped-loop model. Section 5.4 uses an example to illustrate the details of the fast method. In Section 5.5, coils with different metal shields are designed to transfer 100 W power across 40 mm gap with the same efficiency. They were fabricated and their performances were compared in experiment.

5.2. Litz Shield

5.2.1. Structures of Litz Shield

In order to attenuate the stray magnetic field on the side of the coils, the shield current flows in the opposite direction to the winding current, as shown in Figure 5-2. The current in the shield can be either induced eddy current or supplied current.

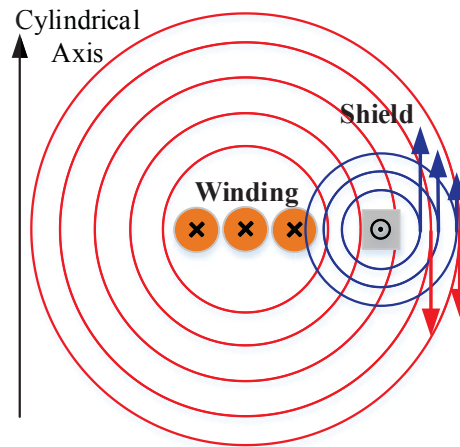


Figure 5-2. Working principle of metal shields to attenuate the stray magnetic field on the side of the coil.

Figure 5-3 shows the current-density vectors on the windings, plate shield, and ring shield. They are derived from finite-element simulation. The current densities are not uniformly distributed in the shields. The region of the shields that is closer to the winding has higher current density because the magnetic field is stronger.

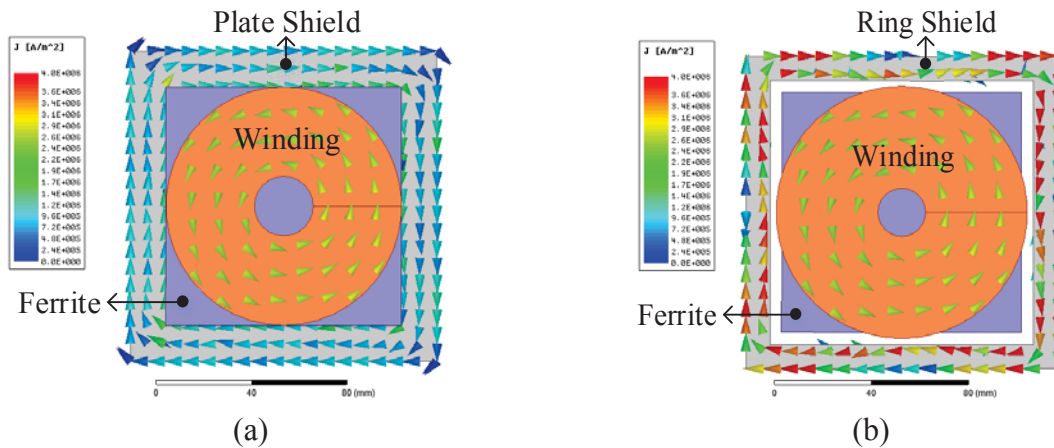


Figure 5-3. Top view of current-density vectors for coils with (a) plate shield and (b) ring shield in Figure 5-1.

The distribution of current-density magnitude for the ring shield is plotted in Figure 5-4(a), on its cross section. Most shield current flows on the surface of the ring shield, which is caused by the skin effect. The current density is higher for the region closer to the winding, because of the stronger magnetic field. The uneven distribution of the current increases the shielding loss significantly.

Figure 5-4(b) shows the structure to replace the ring shield with turns of litz wires. The shield turns are connected in series so the shielding currents are almost the same for all the turns. Because skin effect is negligible in litz wire, cross section of the shield is fully utilized so the shielding loss is reduced.

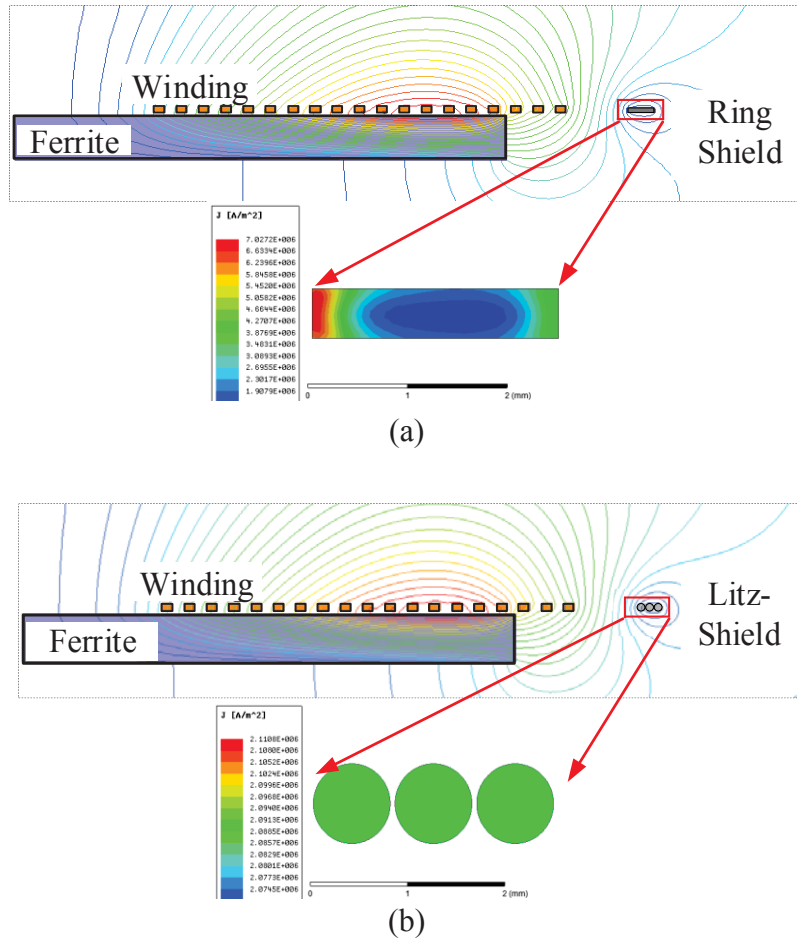


Figure 5-4. Distribution of current-density magnitudes for (a) ring shield and (b) litz shield.

Figure 5-5 demonstrates two structures of litz shields. Figure 5-5(a) is the shorted litz shield. The litz shield is self-shorted and disconnected from the winding. Eddy current is induced in shorted litz shield, which attenuates the magnetic field on the side.

Figure 5-5(b) shows the structure of driven litz shield. The litz shield is connected to the winding and driven by the winding current. Because the currents of the winding turns and shield turns flow in the opposite direction, the fields generated by the driven litz shield and that generated by the winding attenuate each other on the side of the coil.

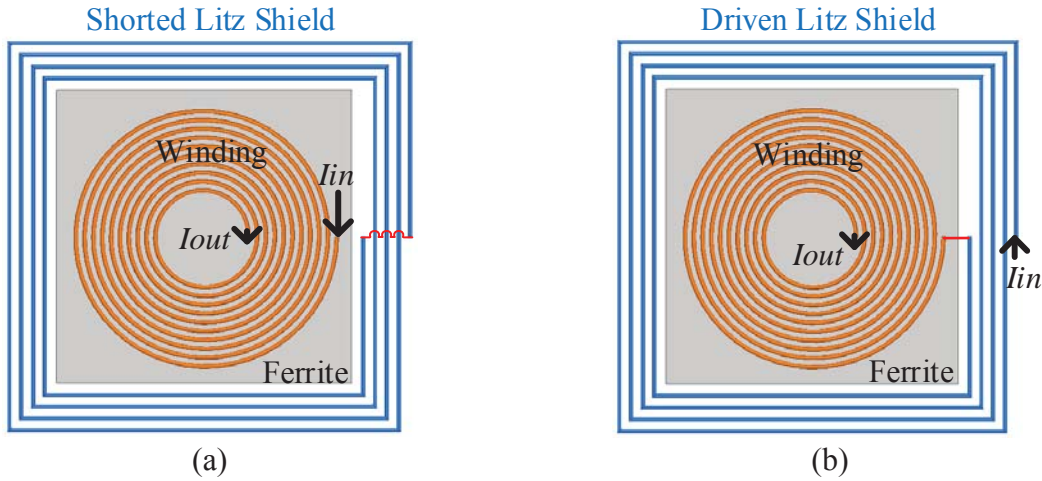


Figure 5-5. Structures of the coils with (a) shorted litz shield and (b) driven litz shield.

5.2.2. Circuit Models of Coils with Litz Shield

5.2.2.1. Circuit Models

The litz shields in Figure 5-5 behave like additional planar coils which are coupled with the windings. The circuit models for the coils with litz shields are plotted in Figure 5-6(a). The windings of transmitter and receiver are modeled as inductances L_{w1} , L_{w2} and resistances r_{w1} , r_{w2} , whereas the litz-shields are modeled as inductances L_{sh1} , L_{sh2} and resistances r_{sh1} , r_{sh2} . All of the four inductances L_{w1} , L_{w2} , L_{sh1} , L_{sh2} are coupled with each other: $M_{w(j)-sh(i)}$ is the mutual inductance between winding j and litz shield i , with i or $j = 1$ for transmitter and i or $j = 2$ for receiver; M_{w1-w2} is the mutual inductance between the windings; $M_{sh1-sh2}$ is the mutual inductance between the litz shields. All of these parameters can be extracted from finite-element simulation, but a better way for the optimization procedure is to calculate the parameters using the lumped-loop model, which will be mentioned in Section 5.3.

However, the model with four coupled inductors in Figure 5-6(a) complicates the analysis. Figure 5-6(b) shows the simplified model which uses two coupled inductors. The equivalent inductances L_{TX} , L_{RX} , M_{TX-RX} and equivalent resistances r_{TX} , r_{RX} in Figure 5-6(b) are derived from the four-coils model in Figure 5-6(a). Terminals TX₁ and TX₂ are the terminals of the transmitter winding, and RX₁, RX₂ are the terminals of the receiver winding.

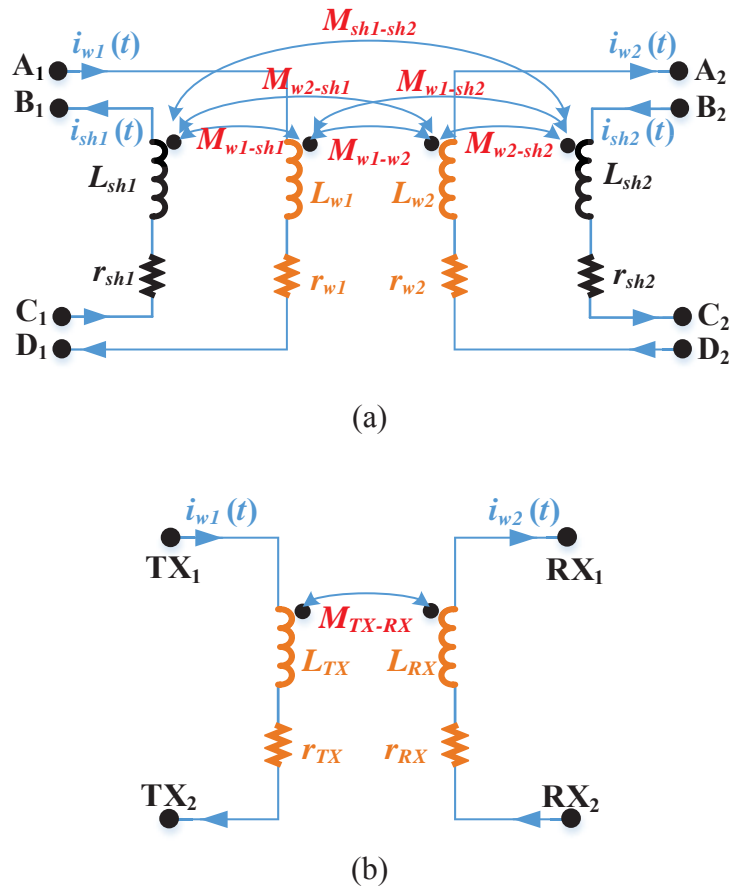


Figure 5-6. (a) Circuit model for the coils with litz shield in Figure 5-5, using four coupled inductors; (b) simplified circuit model with equivalent inductances and resistances, using two coupled inductors.

The voltages between the terminals in Figure 5-6(a) are derived according to KVL, with

$$\begin{aligned}
 V_{A_1D_1} &= j\omega L_{w1} I_{w1} - j\omega M_{w1-w2} I_{w2} - j\omega M_{w1-sh1} I_{sh1} + j\omega M_{w1-sh2} I_{sh2} \\
 V_{A_2D_2} &= j\omega M_{w1-w2} I_{w1} - j\omega L_{w2} I_{w2} - j\omega M_{w2-sh1} I_{sh1} + j\omega M_{w2-sh2} I_{sh2} \\
 V_{B_1C_1} &= j\omega M_{w1-sh1} I_{w1} - j\omega M_{w2-sh1} I_{w2} - j\omega L_{sh1} I_{sh1} + j\omega M_{sh1-sh2} I_{sh2} \\
 V_{B_2C_2} &= j\omega M_{w1-sh2} I_{w1} - j\omega M_{w2-sh2} I_{w2} - j\omega M_{sh1-sh2} I_{sh1} + j\omega L_{sh2} I_{sh2}
 \end{aligned} \tag{5-1}$$

5.2.2.2. Equivalent Parameters of Coils

For the coils with shorted litz shield in Figure 5-5(a), terminals B₁ and C₁ are shorted, and terminals B₂ and C₂ are shorted. The terminals A₁, D₁, A₂, D₂ in Figure 5-6(a) are equivalent to TX₁, TX₂, RX₁, RX₂ in Figure 5-6(b), respectively, which is expressed as

$$\begin{aligned}
 V_{A_1D_1} &= V_{TX_1TX_2} \\
 V_{A_2D_2} &= V_{RX_1RX_2} \\
 V_{B_1C_1} &= 0 \\
 V_{B_2C_2} &= 0
 \end{aligned} \tag{5-2}$$

According to (5-1) and (5-2), the equivalent inductances L_{TX} , L_{RX} , M_{TX-RX} and the equivalent resistances r_{TX} , r_{RX} in Figure 5-6(b) for shorted litz shield are derived as

$$L_{TX} = L_{w1} - \frac{M_{w1-sh2}^2}{L_{sh2}} - \frac{(L_{sh2}M_{w1-sh1} - M_{w1-sh2}M_{sh1-sh2})^2}{L_{sh2}(L_{sh1}L_{sh2} - M_{sh1-sh2}^2)} \tag{5-3}$$

$$L_{RX} = L_{w2} - \frac{M_{w2-sh1}^2}{L_{sh1}} - \frac{(L_{sh1}M_{w2-sh2} - M_{w2-sh1}M_{sh1-sh2})^2}{L_{sh1}(L_{sh1}L_{sh2} - M_{sh1-sh2}^2)} \tag{5-4}$$

$$\begin{aligned}
 M_{TX-RX} &= M_{w1-w2} - \frac{L_{sh2}M_{w2-sh1} - M_{w2-sh2}M_{sh1-sh2}}{L_{sh1}L_{sh2} - M_{sh1-sh2}^2} M_{w1-sh1} \\
 &\quad - \frac{L_{sh1}M_{w2-sh2} - M_{w2-sh1}M_{sh1-sh2}}{L_{sh1}L_{sh2} - M_{sh1-sh2}^2} M_{w1-sh2}
 \end{aligned} \tag{5-5}$$

$$r_{TX} = r_{w1} + \frac{(M_{sh1-sh2}M_{w1-sh2} - M_{w1-sh1}L_{sh2})^2}{(L_{sh1}L_{sh2} - M_{sh1-sh2}^2)^2} r_{sh1} + \frac{(M_{sh1-sh2}M_{w1-sh1} - M_{w1-sh2}L_{sh1})^2}{(L_{sh1}L_{sh2} - M_{sh1-sh2}^2)^2} r_{sh2} \quad (5-6)$$

$$r_{RX} = r_{w2} + \frac{(M_{sh1-sh2}M_{w2-sh2} - M_{w2-sh1}L_{sh2})^2}{(L_{sh1}L_{sh2} - M_{sh1-sh2}^2)^2} r_{sh1} + \frac{(M_{sh1-sh2}M_{w2-sh1} - M_{w2-sh2}L_{sh1})^2}{(L_{sh1}L_{sh2} - M_{sh1-sh2}^2)^2} r_{sh2} \quad (5-7)$$

For the winding with driven litz shield in Figure 5-6(a), terminals C₁ and D₁ are connected, and C₂ and D₂ are connected. The terminals A₁, B₁, A₂, B₂ in Figure 5-6(a) are equivalent to TX₁, TX₂, RX₁, RX₂ in Figure 5-6(b), respectively, which is equivalent to

$$\begin{aligned} V_{A_1B_1} &= V_{TX_1TX_2} \\ V_{A_2B_2} &= V_{RX_1RX_2} \\ V_{C_1D_1} &= 0 \\ V_{C_2D_2} &= 0 \end{aligned} \quad (5-8)$$

According to (5-1) and (5-8), the equivalent inductances and equivalent resistances in Figure 5-6(b) are derived for the driven litz shield as

$$L_{TX} = L_{w1} - L_{sh1} \quad (5-9)$$

$$L_{RX} = L_{w2} - L_{sh2} \quad (5-10)$$

$$M_{TX-RX} = M_{w1-w2} - M_{sh1-sh2} + M_{w1-sh2} - M_{w2-sh1} \quad (5-11)$$

$$r_{TX} = r_{w1} + r_{sh1} \quad (5-12)$$

$$r_{RX} = r_{w2} + r_{sh2} \quad (5-13)$$

Figure 5-7(a) shows an exemplary set of coils with litz shield. The dimensions are labeled in the figure. There are 25 turns in the winding. The number of turns for litz shield is changed from 1 turn to 8 turns. The same litz wire is used for both the winding and litz shield, which consists

of 100 strands of AWG number 38. The length of the square litz shield is fixed to be 130 mm. The spacing between the shield and the winding changes according to the turns of the shield. Figure 5-7(b)-(d) show the equivalent self-inductance, equivalent mutual inductance, and equivalent resistances versus different numbers of turns for the litz shields. After the shields are added, the inductances decrease and resistances increase. This is also predicted by (5-3) – (5-7) and (5-9) – (5-13).

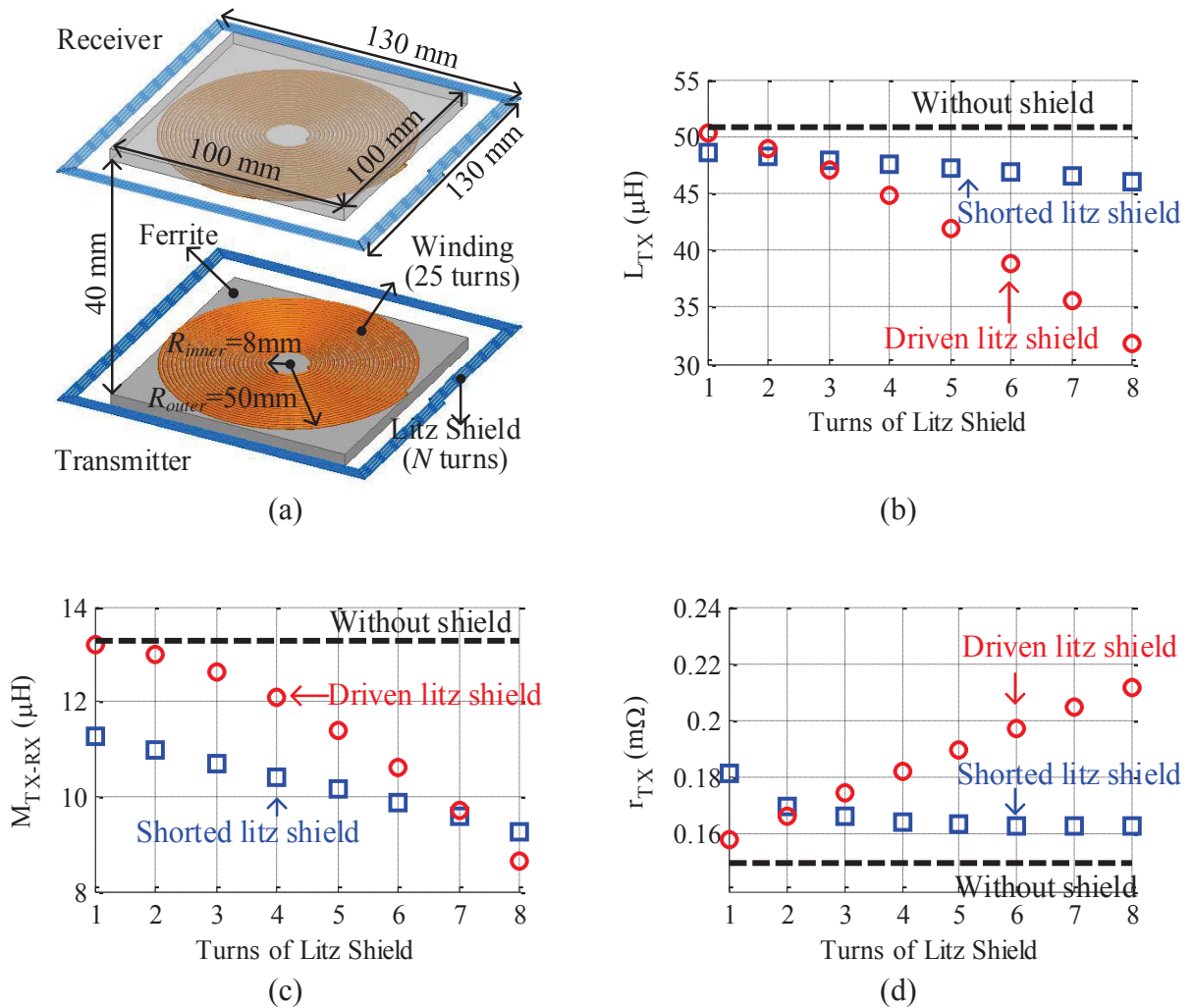


Figure 5-7. (a) An exemplary structure of coils with litz-shield; (b) equivalent self-inductances, (c) equivalent mutual inductances, and (d) equivalent winding resistances calculated for coils without shield, with shorted litz shield, and with driven litz shield.

Figure 5-8 shows the coil-to-coil efficiency which is calculated from (2-10) for the coils in Figure 5-7. The turns number of the litz shield changes from 1 turn to 8 turns. The efficiency is reduced after the shields are added, which indicates that the optimization of efficiency and field attenuation is necessary for litz shield.

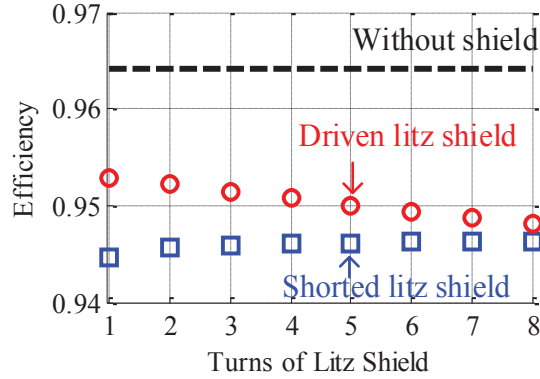


Figure 5-8. The coil-to-coil efficiency calculated from (2-10) with the parameters in Figure 5-7.

5.2.2.3. Currents of Windings and Litz Shields

The winding currents $i_{w1}(t)$ and $i_{w2}(t)$ are calculated from the equivalent circuit model in Figure 5-6(b) as

$$i_{w1}(t) = \frac{\pi R_{Lac}}{2\omega_s M_{TX-RX}} I_{out} \sin(\omega_s t) \quad (5-14)$$

$$i_{w2}(t) = \frac{\pi}{2} I_{out} \sin(\omega_s t + \frac{\pi}{2}) \quad (5-15)$$

where I_{out} is the output current which is usually determined by the system specifications.

The shielding currents are derived from the circuit model in Figure 5-6(a). For shorted litz shield, the induced eddy currents in the shields are calculated as

$$i_{sh1}(t) = \frac{M_{w1-sh1}L_{sh2} + M_{w1-sh2}M_{sh1-sh2}}{L_{sh1}L_{sh2} + M_{sh1-sh2}^2} i_{w1}(t) - \frac{M_{w2-sh1}L_{sh2} + M_{w2-sh2}M_{sh1-sh2}}{L_{sh1}L_{sh2} + M_{sh1-sh2}^2} i_{w2}(t) \quad (5-16)$$

$$i_{sh2}(t) = \frac{M_{w1-sh2}L_{sh1} - M_{w1-sh1}M_{sh1-sh2}}{L_{sh1}L_{sh2} + M_{sh1-sh2}^2} i_{w1}(t) - \frac{M_{w2-sh2}L_{sh1} - M_{w2-sh1}M_{sh1-sh2}}{L_{sh1}L_{sh2} + M_{sh1-sh2}^2} i_{w2}(t) \quad (5-17)$$

For driven litz shield, the currents in the litz shields are the same as the supplied currents in the windings, with

$$i_{sh1}(t) = i_{w1}(t) \quad (5-18)$$

$$i_{sh2}(t) = i_{w2}(t) \quad (5-19)$$

The currents $i_{w1}(t)$, $i_{w2}(t)$, $i_{sh1}(t)$, and $i_{sh2}(t)$ will be used to calculate the stray magnetic field, which is demonstrated in Section 5.3.3.

5.3. Fast Method to Derive Pareto Front

5.3.1. Lumped-loop Model and Turns Vectors

The inductances and resistances in Figure 5-6(a) can either be derived from finite-element simulation or be calculated with lumped-loop model. As mentioned in Chapter 3, the calculation with lumped-loop model is more suitable for the optimization purpose.

Figure 5-9 shows the lumped-loop model of the coils with litz shield. The windings and litz shields are replaced by several loops that are distributed on top of the ferrite plate with equal spacing. Each loop is composed of N_w or N_{sh} turns.

The turns vectors \vec{N}_{w1} and \vec{N}_{w2} describe the number of turns for each loop of the windings in the transmitter and receiver coils, respectively:

$$\vec{N}_{w1} = [N_{w1,1} \quad N_{w1,2} \quad \cdots \quad N_{w1,N}] \quad (5-20)$$

$$\vec{N}_{w2} = \begin{bmatrix} N_{w2,1} & N_{w2,2} & \cdots & N_{w2,N} \end{bmatrix} \quad (5-21)$$

where $N_{w1,(n)}$ and $N_{w2,(n)}$ represent the turns number of loop n in the transmitter and receiver, respectively, with $n = 1, 2, \dots, N$. Loop 1 represents the outermost loop and loop N represents the innermost loop of the winding, which is shown in Figure 5-9(b).

The turns vectors \vec{N}_{sh1} and \vec{N}_{sh2} describe the number of turns for each loop of the litz shields in the transmitter and receiver coils, respectively:

$$\vec{N}_{sh1} = \begin{bmatrix} N_{sh1,1} & N_{sh1,2} & \cdots & N_{sh1,M} \end{bmatrix} \quad (5-22)$$

$$\vec{N}_{sh2} = \begin{bmatrix} N_{sh2,1} & N_{sh2,2} & \cdots & N_{sh2,M} \end{bmatrix} \quad (5-23)$$

where $N_{sh1,(m)}$ and $N_{sh2,(m)}$ represent the turns number of loop n in litz shields of transmitter and receiver, respectively, with $m = 1, 2, \dots, M$. Loop 1 represents the loop that is most close to the winding and loop M represents the outermost loop of the litz shield.

The physical parameters of the coils are equivalent to the turns vectors in (5-20) – (5-23). In Figure 5-9(b), loops with dashed circles are assigned zero turn to realize the physical parameters, such as R_{inner} , R_{outer} , length of the litz shield, and the spacing between the winding and shield. The numbers of turns for the loops with solid circles represent the distribution of turns. Therefore, with lumped-loop model and turns vectors, the sweep of the physical parameters for the original coils is equivalent to the sweep of elements in the turns vectors in (5-20) – (5-23) for the lumped-loop model in Figure 5-9.

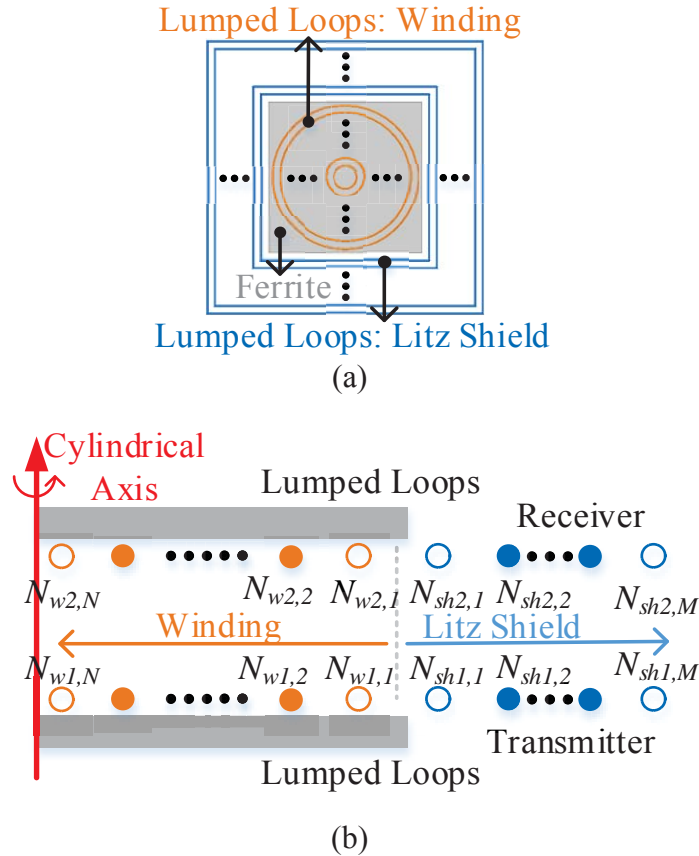


Figure 5-9. (a) Top view and (b) side view of the lumped-loop model for IPT coils with litz shield. The turns vectors are $[N_{w1,1}, N_{w1,2}, \dots, N_{w1,N}]$ and $[N_{w2,1}, N_{w2,2}, \dots, N_{w2,N}]$ for the windings, and $[N_{sh1,1}, N_{sh1,2}, \dots, N_{sh1,M}]$ and $[N_{sh2,1}, N_{sh2,2}, \dots, N_{sh2,M}]$ are for the litz shields. The distribution of turns are represented by turns vectors.

5.3.2. Calculation of Inductances with Permeance Matrices

As shown in Figure 5-9, the lumped-loop model is divided into four parts, which are the windings of transmitter and receiver, and their litz shields. Figure 5-10 shows the definitions of permeance matrices, which are used to calculate the inductances in Figure 5-6(a) with turns vectors.

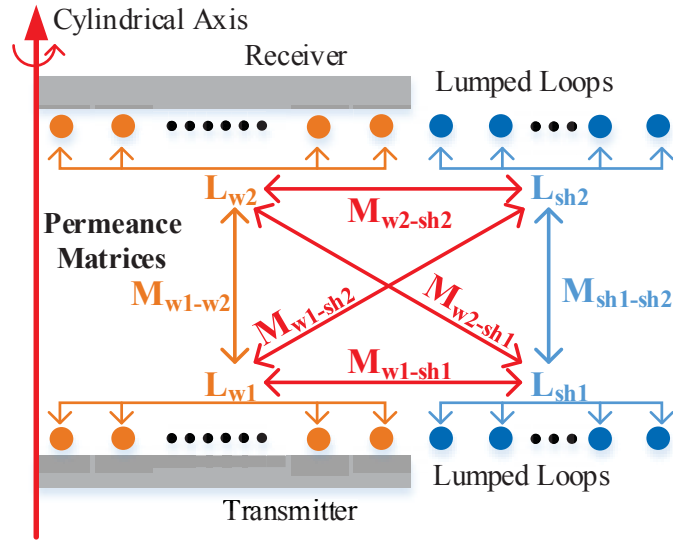


Figure 5-10. Permeance matrices L_{w1} , L_{w2} , L_{sh1} , L_{sh2} , M_{w1-w2} , $M_{sh1-sh2}$, M_{w1-sh1} , M_{w1-sh2} , M_{w2-sh1} , and M_{w2-sh2} of the lumped-loop model in Figure 5-9.

The permeance matrices $L_{w(i)}$ and $L_{sh(i)}$ are used to calculate the self-inductances of the winding i and litz shield i , with $i = 1$ representing transmitter and $i = 2$ representing receiver:

$$L_{w(i)} = \begin{bmatrix} L_{w(i),1} & M_{w(i),1-w(i),2} & \cdots & M_{w(i),1-w(i),N} \\ M_{w(i),2-w(i),1} & L_{w(i),2} & \cdots & M_{w(i),2-w(i),N} \\ \vdots & \vdots & \ddots & \vdots \\ M_{w(i),N-w(i),1} & M_{w(i),N-w(i),2} & \cdots & L_{w(i),N} \end{bmatrix} \quad (5-24)$$

$$L_{sh(i)} = \begin{bmatrix} L_{sh(i),1} & M_{sh(i),1-sh(i),2} & \cdots & M_{sh(i),1-sh(i),M} \\ M_{sh(i),2-sh(i),1} & L_{sh(i),2} & \cdots & M_{sh(i),2-sh(i),M} \\ \vdots & \vdots & \ddots & \vdots \\ M_{sh(i),M-sh(i),1} & M_{sh(i),M-sh(i),2} & \cdots & L_{sh(i),M} \end{bmatrix} \quad (5-25)$$

where $L_{w(i),n}$ and $L_{sh(i),n}$ are the self-inductances of loop n of the winding and loop n of the litz shield, respectively; $M_{w(i),n-w(i),m}$ is the mutual inductance between loops n and m of the windings; $M_{sh(i),n-sh(i),m}$ is the mutual inductance between loops n and m of the litz shields.

The permeance matrices \mathbf{M}_{w1-w2} , $\mathbf{M}_{sh1-sh2}$, \mathbf{M}_{w1-sh1} , \mathbf{M}_{w1-sh2} , \mathbf{M}_{w2-sh1} , and \mathbf{M}_{w2-sh2} are used to calculate the mutual inductances among the four parts:

$$\mathbf{M}_{w1-w2} = \begin{bmatrix} M_{w1,1-w2,1} & M_{w1,1-w2,2} & \cdots & M_{w1,1-w2,N} \\ M_{w1,2-w2,1} & M_{w1,2-w2,2} & \cdots & M_{w1,2-w2,N} \\ \vdots & \vdots & \ddots & \vdots \\ M_{w1,N-w2,1} & M_{w1,N-w2,2} & \cdots & M_{w1,N-w2,N} \end{bmatrix} \quad (5-26)$$

$$\mathbf{M}_{sh1-sh2} = \begin{bmatrix} M_{sh1,1-sh2,1} & M_{sh1,1-sh2,2} & \cdots & M_{sh1,1-sh2,M} \\ M_{sh1,2-sh2,1} & M_{sh1,2-sh2,2} & \cdots & M_{sh1,2-sh2,M} \\ \vdots & \vdots & \ddots & \vdots \\ M_{sh1,M-sh2,1} & M_{sh1,M-sh2,2} & \cdots & M_{sh1,M-sh2,M} \end{bmatrix} \quad (5-27)$$

$$\mathbf{M}_{w(i)-sh(j)} = \begin{bmatrix} M_{w(i),1-sh(j),1} & M_{w(i),1-sh(j),2} & \cdots & M_{w(i),1-sh(j),M} \\ M_{w(i),2-sh(j),1} & M_{w(i),2-sh(j),2} & \cdots & M_{w(i),2-sh(j),M} \\ \vdots & \vdots & \ddots & \vdots \\ M_{w(i),N-sh(j),1} & M_{w(i),N-sh(j),2} & \cdots & M_{w(i),N-sh(j),M} \end{bmatrix} \quad (5-28)$$

where $M_{w1,n-w2,m}$ is the mutual inductance between loops n of transmitter winding and loop m of receiver winding; $M_{sh1,n-sh2,m}$ is the mutual inductance between loops n of transmitter shield and loop m of receiver shield; $M_{w(i),n-sh(j),m}$ is the mutual inductance between loops n of the winding i and loop m of the shield j , with i or $j = 1$ representing transmitter and i or $j = 2$ representing receiver.

All of the elements for the permeance matrices in (5-24) – (5-28) are derived from one finite-element simulation of the lumped-loop model in Figure 5-10, with one turn for each loop. The inductances of the circuit models in Figure 5-6(a) are calculated from the permeance matrices and turns vectors as:

$$L_{w(i)} = \vec{N}_{w(i)} \mathbf{L}_{w(i)} \vec{N}_{w(i)}^T \quad (5-29)$$

$$L_{sh(i)} = \vec{N}_{sh(i)} \mathbf{L}_{sh(i)} \vec{N}_{sh(i)}^T \quad (5-30)$$

$$M_{w1-w2} = \vec{N}_{w1} \mathbf{M}_{w1-w2} \vec{N}_{w2}^T \quad (5-31)$$

$$M_{sh1-sh2} = \vec{N}_{sh1} \mathbf{M}_{sh1-sh2} \vec{N}_{sh2}^T \quad (5-32)$$

$$M_{w(i)-sh(j)} = \vec{N}_{w(i)} \mathbf{M}_{w(i)-sh(j)} \vec{N}_{sh(j)}^T \quad (5-33)$$

The inductances in (5-29) – (5-33) are used to calculate the currents of the windings and shields, $i_{w1}(t)$, $i_{w2}(t)$, $i_{sh1}(t)$, $i_{sh2}(t)$, from (5-14), (5-15), and (5-16) – (5-19).

5.3.3. Calculation of Stray Magnetic Field with Current-to-Field Matrices

Figure 5-11 shows the definitions of current-to-field matrices. The stray magnetic fields are calculated from winding currents using the current-to-field matrices. In Figure 5-11, the magnetic field generated by all the loops is calculated by adding the magnetic field generated by each loop, according to superposition:

$$\begin{aligned} B_i(t) = & \sum_{n=1}^N \alpha_{w1,n,i} N_{w1,n} i_{w1}(t) + \sum_{n=1}^N \alpha_{w2,n,i} N_{w2,n} i_{w2}(t) \\ & + \sum_{n=1}^M \alpha_{sh1,n,i} N_{sh1,n} i_{sh1}(t) + \sum_{n=1}^M \alpha_{sh2,n,i} N_{sh2,n} i_{sh2}(t) \end{aligned} \quad (5-34)$$

where $\alpha_{w(j),n,i}$ and $\alpha_{sh(j),n,i}$ are the current-to-field coefficients for loop n of winding j and shield j , respectively, with $j = 1$ representing transmitter and $j = 2$ representing receiver; i represents the orientations X, Y, or Z in Figure 3-2; $N_{w(j),n}$ and $N_{sh(j),n}$ are the numbers of turns for the corresponding loop, which are the elements of the turns vectors in (5-20) – (5-23); $i_{w(j)}(t)$ and $i_{sh(j)}(t)$ are the currents of winding j and litz shield j , respectively.

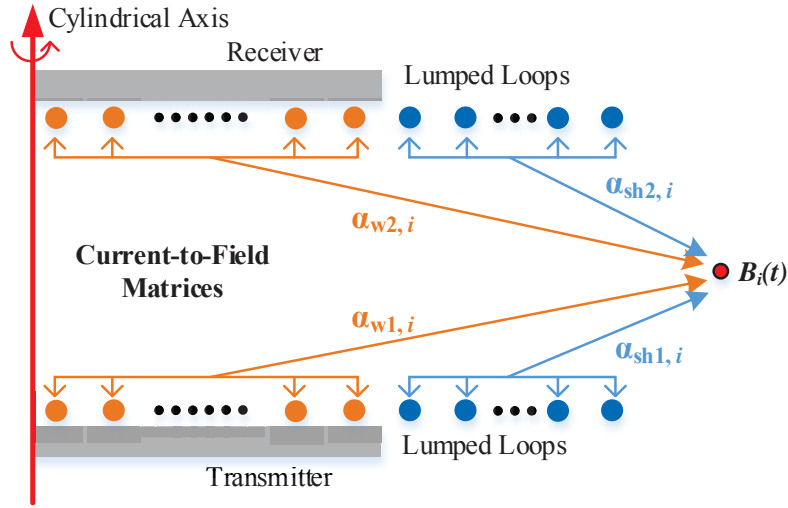


Figure 5-11. Current-to-field matrices $\alpha_{w1,i}$, $\alpha_{w2,i}$, $\alpha_{sh1,i}$, $\alpha_{sh2,i}$ of the lumped-loop model in Figure 5-9.

The current-to-field matrices $\alpha_{w1,i}$, $\alpha_{w2,i}$, $\alpha_{sh1,i}$, $\alpha_{sh2,i}$ are composed of the current-to-field coefficients in (5-34):

$$\alpha_{w(j),i} = \begin{bmatrix} \alpha_{w(j),1,i} & \alpha_{w(j),2,i} & \cdots & \alpha_{w(j),N,i} \end{bmatrix} \quad (5-35)$$

$$\alpha_{sh(j),i} = \begin{bmatrix} \alpha_{sh(j),1,i} & \alpha_{sh(j),2,i} & \cdots & \alpha_{sh(j),M,i} \end{bmatrix} \quad (5-36)$$

The current-to-field coefficients of one loop is derived by setting 1 Ampere-turn in this loop and setting 0 Ampere-turn to all the others. If there are N loops for the winding and M loops for the shield in both transmitter and receiver, $2(N + M)$ simulations are required to derive all the elements in the current-to-field matrices. After the current-to-field matrices in (5-35) and (5-36) are derived, the stray magnetic fields in X, Y, Z orientations are calculated from (5-34) with turns vector in (5-20) – (5-23), winding currents in (5-14) and (5-15), and shielding currents in (5-16) – (5-19).

5.3.4. Coil-to-Coil Efficiency

According to (2-10), the coil-to-coil efficiency is influenced by r_{TX} and r_{RX} in Figure 5-6(b). The values of r_{TX} and r_{RX} are calculated from r_{w1} , r_{w2} , r_{sh1} , r_{sh2} in Figure 5-6(a), using (5-6), (5-7), (5-12), and (5-13). The coupling power loss between the transmitter and receiver is not considered. The winding resistance r_{w1} includes the DC resistance of the transmitter winding, the proximity-effect resistance of the transmitter winding, and the reflected proximity-effect resistance of the transmitter shield. The shield resistance r_{sh1} includes only the DC resistance of the transmitter shield. The definitions of r_{w2} and r_{sh2} for the receiver are the same as r_{w1} and r_{sh1} .

The DC resistances are calculated from the cross-sectional area and the length of the litz wire. The proximity-effect resistance is calculated according to (3-22). The magnetic fields across the turns are generated by winding current $i_{w1}(t)$ and shield current $i_{sh1}(t)$. The current $i_{sh1}(t)$ is calculated from $i_{w1}(t)$ using (5-16) for shorted litz shield or using (5-18) for driven litz shield. The proximity-effect resistance r_{e1} of the transmitter is calculated from the total proximity-effect loss of the winding and shield as

$$r_{e1} = \left(\sum_{n=1}^{N_{winding}} P_{e,n} + \sum_{m=1}^{M_{shield}} P_{e,m} \right) / I_{w1}^2 \quad (5-37)$$

where I_{w1} is the RMS value of winding current; $P_{e,n}$ is the proximity-effect loss of turn n for the winding; $P_{e,m}$ is the proximity-effect loss of turn m for the shield; $N_{winding}$ is the total number of turns for the winding; M_{shield} is the total number of turns for the shield. The proximity-effect resistance of the receiver r_{e2} is calculated similarly.

To analytically calculate the magnetic fields across the turns, the lumped-loop model is translated back to coils with real turns according to the turns vectors. The same procedure as in Chapter 4 is implemented to analytically calculate the proximity-effect resistances. The ferrite

plate is replaced with mirrored turns of the winding and shield, according to the the method of image. The internal field is calculated with Ampere’s Law, and the external field is calculated with Biot-Savart Law.

After the proximity-effect resistance r_e is calculated, it is added to r_w with the DC resistance. The equivalent resistances r_{TX} and r_{RX} are calculated from (5-6) and (5-7) for the shorted litz shield and from (5-12) and (5-13) for the driven litz shield. The efficiency is then calculated from (2-10) with r_{TX} and r_{RX} .

5.3.5. Summary of the Procedure for the Fast Optimization

The optimization of efficiency and stray magnetic field is realized with Pareto fronts for the coils with litz shield. The fronts are plotted on a two-dimensional Cartesian coordinate system. The horizontal axis and vertical axis represent magnetic field and coil-to-coil efficiency, respectively. The optimal designs of the coils are selected along the fronts.

Figure 5-12 illustrates the procedure to derive the Pareto fronts using the concept of the lumped-loop model. It starts by selecting the lumped-loop model with some fixed parameters such as air gap and the size of ferrite plate. Turns vectors in (5-20) – (5-23) are swept to represent the physical parameters, such as the R_{inner} , R_{outer} , length of the shield, and the spacing between the winding and shield in Figure 5-7(a).

For each set of turns vectors, stray magnetic field and coil-to-coil efficiency are calculated following the method in 5.3.3 and 5.3.4. Stray magnetic fields are derived from (5-34) with the current-to-field matrices and the currents of windings and shields, $i_{w1}(t)$, $i_{w2}(t)$, $i_{sh1}(t)$, $i_{sh2}(t)$. These currents are calculated from (5-14), (5-15), and (5-16) – (5-19) with inductances in the circuit models of Figure 5-6. The inductances in Figure 5-6(a) are derived from the permance matrices in (5-24) – (5-28), and they are used to calculate the shield currents $i_{sh1}(t)$ and $i_{sh2}(t)$.

The inductances in Figure 5-6(b) are derived from (5-3) – (5-5) and (5-9) – (5-11), and they are used to calculate the winding currents $i_{w1}(t)$ and $i_{w2}(t)$.

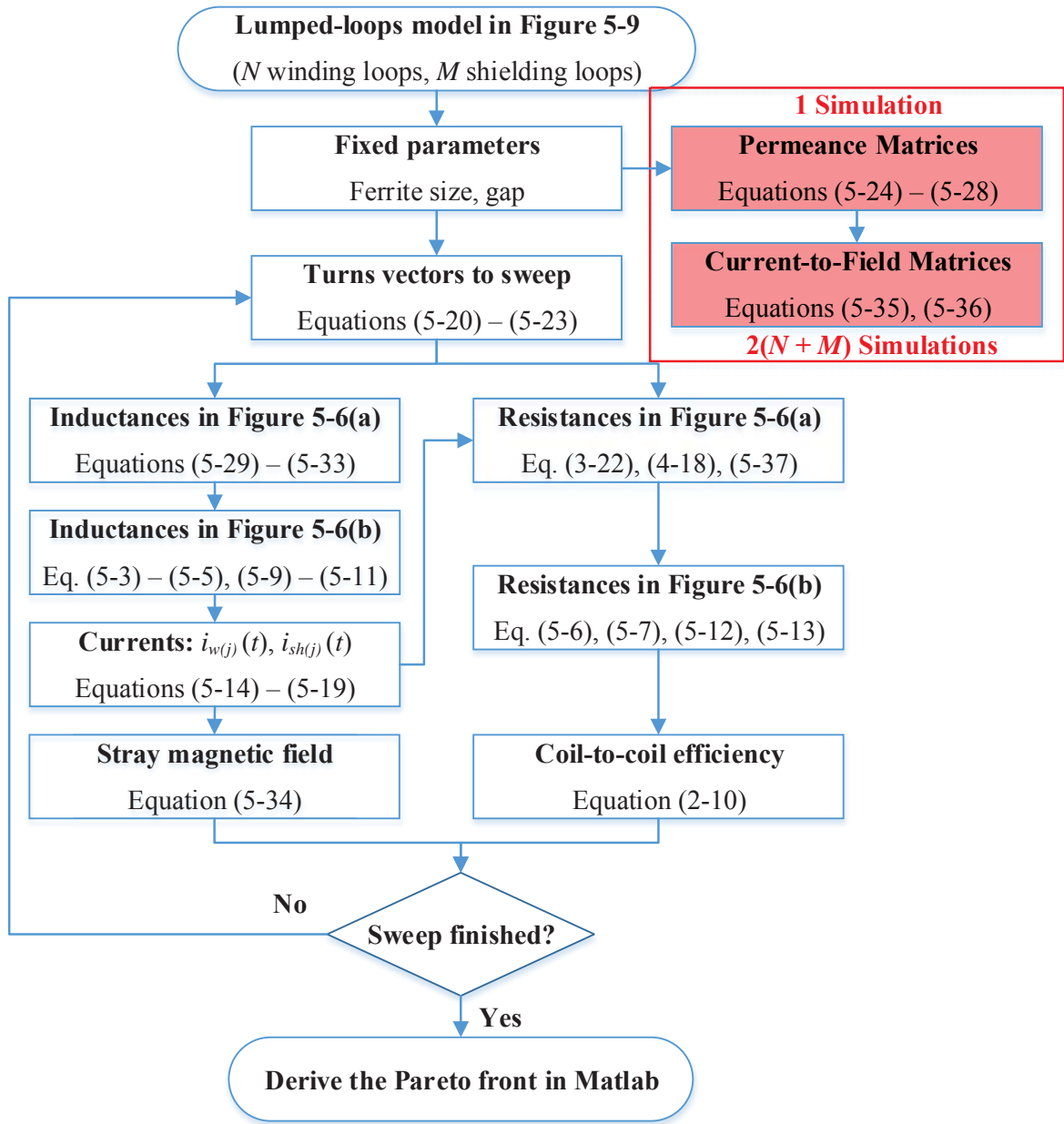


Figure 5-12. Procedure to derive the Pareto front of coil-to-coil efficiency versus stray magnetic field for the coils with litz shield, using the concept of lumped-loop model.

The coil-to-coil efficiency is calculated from (2-10). The equivalent resistances r_{TX} and r_{RX} in Figure 5-6(b) are calculated from (5-6), (5-7), (5-12), and (5-13), with the resistances r_{w1} , r_{w2} , r_{sh1} , r_{sh2} in Figure 5-6(a). The winding resistance r_w includes three parts: DC resistance of the winding, proximity-effect resistance of the winding, and reflected proximity-effect resistance of the shield. The shielding resistance r_{sh} includes only the DC resistance of the shield. The proximity-effect resistance is calculated from (4-39) and (5-37).

After the coil-to-coil efficiencies and stray magnetic fields for all the turns vectors are calculated, the results are marked on the two-dimensional Cartesian coordinate system. The Pareto fronts are derived using Matlab.

5.4. Design Example for Coils with Shorted Litz Shield

This section uses an example to demonstrate how to use the lumped-loop model to derive the Pareto front for the coils with shorted litz shield. The design specifications of this example are the same as those in Section 3.5, in order to compare the results for coils with metal shields and without metal shield.

The coils are designed for the series-series compensation with the circuit topology in Figure 2-1. The power of 100 W is transferred across 40 mm gap, with 35 V output voltage on the load and 100 kHz switching frequency of the full bridge inverter.

The structure of the coils is selected to be the same as Figure 5-7(a). Circular winding is placed on the square ferrite plate. The litz shields are placed on the side of the coils and avoid overlapping with the ferrite plate. This is to fully utilize the ferrite for shield purpose. The material of 3C96 is used for the ferrite, and the dimensions of the plate are 100 mm by 100 mm, with the thickness of 5 mm. The maximum length is 130 mm, which means the dimensions of the coils with litz shield should be smaller than 130 mm by 130 mm.

Figure 5-13 is the lumped-loop model for the coils with litz shield. The grey plates are made of ferrite. The circular loops are the lumped loops of the winding. The loops w1,1 to w1,10 are the 10 lumped loops of the transmitter winding, and the loops w2,1 to w2,10 are the lumped loops of the receiver winding. The blue square loops around the coils are the lumped loops of the litz shields. Loops sh1,1 to sh1, 4 represent the litz shield of the transmitter, and loops sh2,1 to sh2, 4 represent the litz shield of the receiver.

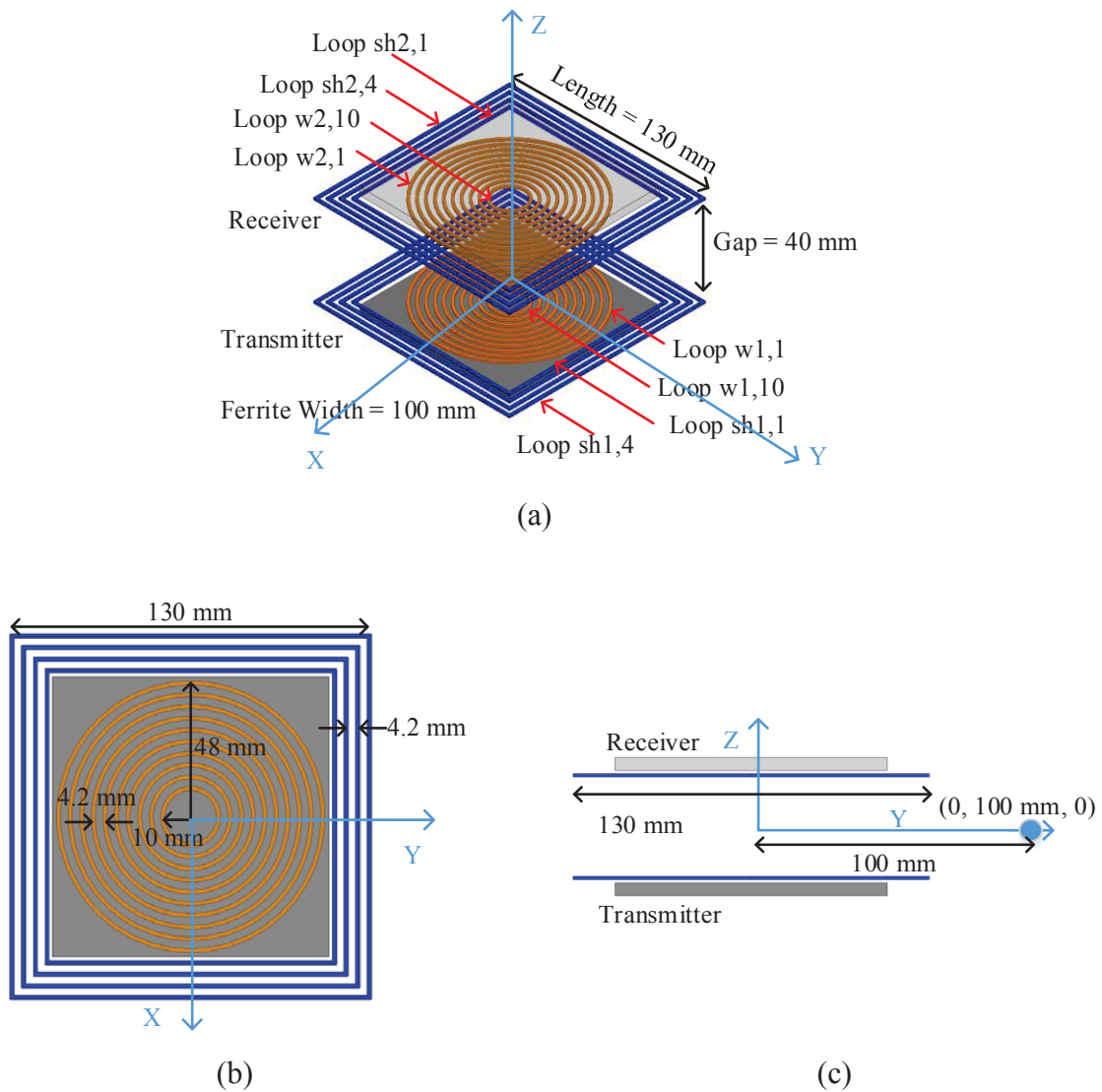


Figure 5-13. Lumped-loop model of the design example for the coils with litz shield.

By exciting all the loops in Figure 5-13 with stranded excitation in Ansys Maxwell, the permeance matrices L_{w1} , L_{w2} , L_{sh1} , L_{sh2} , M_{w1-w2} , $M_{sh1-sh2}$, M_{w1-sh1} , M_{w1-sh2} , M_{w2-sh1} , and M_{w2-sh2} are extracted from one simulation. They are used to calculate the inductances in Figure 5-6(a), using (5-29) – (5-33). TABLE 5-1 – TABLE 5-6 list the elements of these permeance matrices.

The current-to-field matrices, $\alpha_{w1,i}$, $\alpha_{w2,i}$, $\alpha_{sh1,i}$, $\alpha_{sh2,i}$, are extracted from 28 finite-element simulations, with 20 of them for the winding loops, and 8 of them for the shield loops. The procedure to derive the current-to-field matrices is similar to the example in in Section 3.5. Each current-to-field coefficient is derived by exciting the corresponding loop with 1 Ampere-turn, and all the other loops are excited with 0 Ampere-turn. TABLE 5-7 – TABLE 5-10 list the elements of the current-to-field matrices $\alpha_{w1,i}$, $\alpha_{w2,i}$, $\alpha_{sh1,i}$, $\alpha_{sh2,i}$, respectively.

TABLE 5-1. Permeance Matrices $L_{w(i)}$ in Figure 5-10 (Unit: nH, $i = 1$ or 2)

Loop	$w(i),1$	$w(i),2$	$w(i),3$	$w(i),4$	$w(i),5$	$w(i),6$	$w(i),7$	$w(i),8$	$w(i),9$	$w(i),10$
$w(i),1$	400	242	167	120	87	61	42	27	16	8
$w(i),2$	242	369	220	149	104	72	49	31	18	9
$w(i),3$	167	220	332	194	128	86	57	36	21	10
$w(i),4$	120	149	194	291	164	105	67	42	24	11
$w(i),5$	87	104	128	164	249	135	82	49	28	13
$w(i),6$	61	72	86	105	135	206	106	60	33	15
$w(i),7$	42	49	57	67	82	106	165	80	41	19
$w(i),8$	27	31	36	42	49	60	80	125	54	23
$w(i),9$	16	18	21	24	28	33	41	54	88	32
$w(i),10$	8	9	10	11	13	15	19	23	32	54

TABLE 5-2. Permeance Matrix M_{w1-w2} in Figure 5-10 (Unit: nH)

Loop	w1,1	w1,2	w1,3	w1,4	w1,5	w1,6	w1,7	w1,8	w1,9	w1,10
w2,1	66	62	56	48	40	31	23	16	10	5
w2,2	62	59	54	47	39	31	23	16	10	5
w2,3	56	54	50	44	37	30	23	16	10	5
w2,4	48	47	44	40	34	28	21	15	9	5
w2,5	40	39	37	34	30	24	19	13	8	4
w2,6	31	31	30	28	25	20	16	12	7	4
w2,7	23	23	23	21	19	16	13	9	6	3
w2,8	16	16	16	15	13	12	9	7	4	2
w2,9	10	10	10	9	8	7	6	4	3	2
w2,10	5	5	5	5	4	4	3	2	2	1

TABLE 5-3. Permeance Matrices $L_{sh(i)}$ in Figure 5-10 (Unit: nH, $i = 1$ or 2)

Loop	sh(i),1	sh(i),2	sh(i),3	sh(i),4
sh(i),1	422	245	191	160
sh(i),2	245	441	257	202
sh(i),3	191	257	474	275
sh(i),4	160	202	275	515

TABLE 5-4. Permeance Matrix $M_{sh1-sh2}$ in Figure 5-10 (Unit: nH)

	sh1, 1	sh1, 2	sh1, 3	sh1, 4
sh2, 1	65	66	67	68
sh2, 2	66	68	70	73
sh2, 3	67	70	74	77
sh2, 4	68	73	77	82

TABLE 5-5. Permeance Matrices $\mathbf{M}_{w(i)-sh(i)}$ in Figure 5-10 (Unit: nH, $i = 1$ or 2)

Loop	$w(i),1$	$w(i),2$	$w(i),3$	$w(i),4$	$w(i),5$	$w(i),6$	$w(i),7$	$w(i),8$	$w(i),9$	$w(i),10$
sh(i),1	157	118	89	68	51	37	25	17	10	5
sh(i),2	122	95	74	57	43	31	22	14	8	4
sh(i),3	104	82	64	50	38	28	19	13	8	4
sh(i),4	91	73	58	45	34	25	18	12	7	3

TABLE 5-6. Permeance Matrices $\mathbf{M}_{w(i)-sh(j)}$ in Figure 5-10
(Unit: nH, $i = 1, j = 2$ or $i = 2, j = 1$)

Loop	$w(i),1$	$w(i),2$	$w(i),3$	$w(i),4$	$w(i),5$	$w(i),6$	$w(i),7$	$w(i),8$	$w(i),9$	$w(i),10$
sh(j),1	61	55	47	40	32	25	18	12	7	4
sh(j),2	59	52	45	37	30	23	17	11	7	3
sh(j),3	57	51	43	36	28	22	16	11	6	3
sh(j),4	56	49	42	34	27	21	15	10	6	3

TABLE 5-7. Current-to-Field Matrix α_{w1} in Figure 5-11 (Unit: $\mu\text{T}/\text{Ampere-Turn}$)

	$w1, 1$	$w1, 2$	$w1, 3$	$w1, 4$	$w1, 5$	$w1, 6$	$w1, 7$	$w1, 8$	$w1, 9$	$w1,10$
X	0.021	0.006	0.000	0.007	0.011	0.005	0.008	0.007	0.001	0.001
Y	-0.594	-0.394	-0.229	-0.185	-0.123	-0.067	-0.049	-0.029	-0.019	-0.01
Z	1.083	0.906	0.688	0.620	0.521	0.359	0.255	0.174	0.096	0.07

TABLE 5-8. Current-to-Field Matrix α_{w2} in Figure 5-11 (Unit: $\mu\text{T}/\text{Ampere-Turn}$)

	w2, 1	w2, 2	w2, 3	w2, 4	w2, 5	w2, 6	w2, 7	w2, 8	w2, 9	w2,10
X	0.021	0.006	0.000	0.007	0.011	0.005	0.008	0.007	0.001	0.001
Y	0.594	0.394	0.229	0.185	0.123	0.067	0.049	0.029	0.019	0.01
Z	1.083	0.906	0.688	0.620	0.521	0.359	0.255	0.174	0.096	0.07

TABLE 5-9. Current-to-Field Matrix α_{sh1} in Figure 5-11 (Unit: $\mu\text{T}/\text{Ampere-Turn}$)

	sh1, 1	sh1, 2	sh1, 3	sh1, 4
X	0.001	0.005	0.025	0.009
Y	-1.033	-1.294	-1.620	-2.041
Z	1.409	1.608	1.847	2.085

TABLE 5-10. Current-to-Field Matrix α_{sh2} in Figure 5-11 (Unit: $\mu\text{T}/\text{Ampere-Turn}$)

	sh2, 1	sh2, 2	sh2, 3	sh2, 4
X	0.001	0.005	0.025	0.009
Y	1.033	1.294	1.620	2.041
Z	1.409	1.608	1.847	2.085

The turns vectors of the windings and shields for the lumped-loop model in Figure 5-13 are expressed as:

$$\vec{N}_{w1} = [N_{w1,1} \quad N_{w1,2} \quad \cdots \quad N_{w1,10}] \quad (5-38)$$

$$\vec{N}_{w2} = [N_{w2,1} \quad N_{w2,2} \quad \cdots \quad N_{w2,10}] \quad (5-39)$$

$$\vec{N}_{sh1} = \begin{bmatrix} N_{sh1,1} & N_{sh1,2} & N_{sh1,3} & N_{sh1,4} \end{bmatrix} \quad (5-40)$$

$$\vec{N}_{sh2} = \begin{bmatrix} N_{sh2,1} & N_{sh2,2} & N_{sh2,3} & N_{sh2,4} \end{bmatrix} \quad (5-41)$$

The turns vectors in (5-38) – (5-41) are swept to derive the Pareto fronts. In this example, the winding turns are assumed to be evenly distributed, and the turns in the litz shields are not evenly distributed. TABLE 5-11 shows the steps to sweep the elements of the turns vectors.

The outermost loops of \vec{N}_{w1} and \vec{N}_{w2} are swept to represent the outer radii of the windings. For the transmitter, its outermost loop $N_{w1,(o)}$ is swept from $N_{w1,1}$ to $N_{w1,5}$, whereas the outermost loop of the receiver $N_{w2,(o)}$ is swept from $N_{w2,1}$ to $N_{w2,5}$.

The innermost loops are selected according to the outermost loops $N_{w1,(o)}$ and $N_{w2,(o)}$, respectively. The innermost loop of the transmitter, $N_{w1,(i)}$, is swept from $N_{w1,(o+1)}$ to $N_{w1,10}$, and the innermost loop of the receiver, $N_{w2,(i)}$, is swept from $N_{w2,(o+1)}$ to $N_{w2,10}$.

The turns number of the windings is swept according to the wire diameter D . The value of D is selected from the datasheet of the litz wire manufactures. In this example, litz wires with AWG #38 strands are selected. The strand numbers are selected from 40, 66, 100, 162, 260, 420, 660, 1050, 1650. The corresponding wire diameters are 0.9 mm, 1.1 mm, 1.5 mm, 1.9 mm, 2.3 mm, 2.9 mm, 3.8 mm, 4.8 mm, and 6 mm. The maximum number of turns, N_{max} , is calculated from the innermost loop, outermost loop, and D . The total number of turns is swept from 1 to N_{max} . All these turns are evenly distributed between the loops $N_{w1,(i)}$ and $N_{w1,(o)}$ for the transmitter or between the loops $N_{w2,(i)}$ and $N_{w2,(o)}$ for the receiver. The other loops of windings are assigned zero turns.

The turns number of each loop for the shields is swept from 0 turns to $(4.2 \text{ mm} / D)$. The turns are not evenly distributed in the litz shields.

TABLE 5-11. Turns Vectors to Sweep for the Lumped-loop Model in Figure 5-13

Procedure	Swept Values
The outermost loop of transmitter $N_{w1, (o)}$	o : from 1 to 5
R_{outer} of the transmitter	$50 \text{ mm} - (o - 1) * 4.2 \text{ mm}$
The innermost loop of transmitter $N_{w1, (i)}$	i : from $(o + 1)$ to 10
R_{inner} of the transmitter	$50 \text{ mm} - (i - 1) * 4.2 \text{ mm}$
Wire Diameter D	From 0.9 mm to 6 mm
Sweep the turns number of the transmitter	From 1 to floor $[(R_{outer} - R_{inner}) / D]$
The outermost loop of receiver $N_{w2, (o)}$	o : from 1 to 5
R_{outer} of the receiver	$50 \text{ mm} - (o - 1) * 4.2 \text{ mm}$
The innermost loop of receiver $N_{w2, (i)}$	i : from $(o + 1)$ to 10
R_{inner} of the receiver	$50 \text{ mm} - (i - 1) * 4.2 \text{ mm}$
Sweep the turns number of the receiver	From 1 to floor $[(R_{outer} - R_{inner}) / D]$
Turns number of each loop in transmitter shield	From 0 to floor $(4.2 \text{ mm} / D)$
Turns number of each loop in receiver shield	From 0 to floor $(4.2 \text{ mm} / D)$

TABLE 5-12 shows an example of the turns vectors which is used to demonstrate the calculation with lumped-loop model for coils with litz shield. A total of 25 turns are evenly distributed in the 10 loops of winding, so each loop contains 2.5 turns. The number of turns for the 4 shield loops are 1, 0, 2, 2, respectively.

TABLE 5-12. Turns Vectors for an Exemplary Coil with Shorted Litz Shield with the Lumped-loop Model in Figure 5-13

Parameters	Values
\vec{N}_{w1}	[2.5, 2.5, 2.5, 2.5, 2.5, 2.5, 2.5, 2.5, 2.5, 2.5]
\vec{N}_{w2}	[2.5, 2.5, 2.5, 2.5, 2.5, 2.5, 2.5, 2.5, 2.5, 2.5]
\vec{N}_{sh1}	[1, 0, 2, 2]
\vec{N}_{sh2}	[1, 0, 2, 2]

With the turns vectors in TABLE 5-12, the inductances in Figure 5-6 are calculated from the permeance matrices in TABLE 5-1 – TABLE 5-6. TABLE 5-13 shows the methods and results.

TABLE 5-13. Calculation of Inductances for the Exemplary Coil with Shorted Litz Shield in TABLE 5-12

Parameters	Methods	Results
L_{w1}, L_{w2}	(5-29), with L_{w1} and L_{w2} in TABLE 5-1	53.5 μ H, 53.5 μ H
L_{sh1}, L_{sh2}	(5-30), with L_{sh1} and L_{sh2} in TABLE 5-3	8 μ H, 8 μ H
M_{w1-w2}	(5-31), with M_{w1-w2} in TABLE 5-2	13.4 μ H
$M_{sh1-sh2}$	(5-32), with $M_{sh1-sh2}$ in TABLE 5-4	1.8 μ H
M_{w1-sh1}, M_{w2-sh2}	(5-33), with M_{w1-sh1} and M_{w1-sh2} in TABLE 5-5	5.3 μ H, 5.3 μ H
M_{w1-sh2}, M_{w2-sh1}	(5-33), with M_{w2-sh1} and M_{w2-sh2} in TABLE 5-6	3.4 μ H, 3.4 μ H
L_{TX}	(5-3)	49.3 μ H
L_{RX}	(5-4)	49.3 μ H
M_{TX-RX}	(5-5)	9.8 μ H

The resistances of the windings and shields are calculated using the methods in Chapter 4. The coils with real turns are determined by the lumped-loop model, and the magnetic fields across each turn are calculated with the method of image. TABLE 5-14 shows the calculation results. According to the inductances in TABLE 5-13 and resistances in TABLE 5-14, the coil-to-coil efficiency is calculated to be 94.5% from (2-10).

TABLE 5-14. Calculation of Resistances for the Exemplary Coil with Shorted Litz Shield in TABLE 5-12

Parameters	Methods	Results
r_{w1}, r_{w2}	(4-39), with turns vectors in TABLE 5-12	127 m Ω , 127 m Ω
r_{sh1}, r_{sh2}	(4-39), with turns vectors in TABLE 5-12	68 m Ω , 68 m Ω
r_{TX}, r_{RX}	(5-6) and (5-7)	157 m Ω , 157 m Ω

The currents of the windings and shields are calculated from the equivalent circuit models in Figure 5-6. The transmitter and receiver currents have 90 degrees' phase difference, so the phases of the shield currents are calculated accordingly. TABLE 5-15 are the calculated currents for the currents. Because each shield is coupled to both windings, so the shield current include two parts: one part is in phase with $i_{w1}(t)$, and the other part is in phase with $i_{w2}(t)$.

TABLE 5-15. Calculation of Currents for the Exemplary Coil with Shorted Litz Shield in TABLE 5-12

Parameters	Methods	Results (Unit: A)
i_{w1}	(5-15)	$7.2 * \sin(\omega t)$
i_{w2}	(5-14), $I_{out} = P_{out} / V_{out} = 2.6 \text{ A}$	$4.5 * \sin(\omega t + \pi / 2)$
i_{sh1}	(5-16)	$5.3 * \sin(\omega t) + 4 * \sin(\omega t + \pi / 2)$
i_{sh2}	(5-17)	$4 * \sin(\omega t) + 3.3 * \sin(\omega t + \pi / 2)$

The stray magnetic fields are calculated from (5-34), with the current-to-field matrices $\alpha_{w1,i}$, $\alpha_{w2,i}$, $\alpha_{sh1,i}$, $\alpha_{sh2,i}$ in TABLE 5-7 – TABLE 5-10 and the currents in TABLE 5-15. The calculation results of $B_X(t)$, $B_Y(t)$, and $B_Z(t)$ are listed in TABLE 5-16. The quantified magnetic field is 19.6 μT .

TABLE 5-16. Calculation of Stray Magnetic Field for the Exemplary Coil with Shorted Litz Shield in TABLE 5-12

Parameters	Methods	Results (Unit: μT)
$B_X(t)$	(5-34), with $\alpha_{w1,i}$, $\alpha_{w2,i}$, $\alpha_{sh1,i}$,	$0.6 * \sin(\omega t) + 0.2 * \sin(\omega t + \pi / 2)$
$B_Y(t)$	$\alpha_{sh2,i}$ in TABLE 5-7 - TABLE	$20.2 * \sin(\omega t) + 12.8 * \sin(\omega t + \pi / 2)$
$B_Z(t)$	5-10	$0.1 * \sin(\omega t) - 14.1 * \sin(\omega t + \pi / 2)$

Similar procedure is implementd to derive the Pareto front for the coils with driven litz shield. Figure 5-14 shows the fronts derived for shorted litz shield and driven litz shield, following the procedure in Figure 5-12. The Matlab code to derive the fronts is provided in Appendix B.

The Pareto fronts for the coils without metal shields, for the coils with plate shield in Figure 5-1(b), and for the coils with ring shield in Figure 5-1(c) are plotted in Figure 5-14 as well. The

dimensions for all the coils are limited to be smaller than $130 \text{ mm} \times 130 \text{ mm}$, and the gap is 40 mm. The magnetic field is optimized for the point (0, 100 mm, 0) in Figure 5-13. Figure 5-14 shows that the coil-to-coil efficiency is reduced after the shields are added, but the stray magnetic field is significantly attenuated.

The shorted litz shield attenuates the field most when the four shields are designed for the same efficiency. Compared to the plate shield and ring shield, skin effect in shorted litz shield is negligible, so the shield current of shorted litz shield is higher for the same amount of losses. Higher current in the shields helps to attenuate the stray magnetic field more. The performance of shorted litz shield is better than driven litz shield. This is because current of the driven litz shield is limited to the supplied value, while the induced eddy current in shorted litz shield is able to adjust according to the magnetic field.

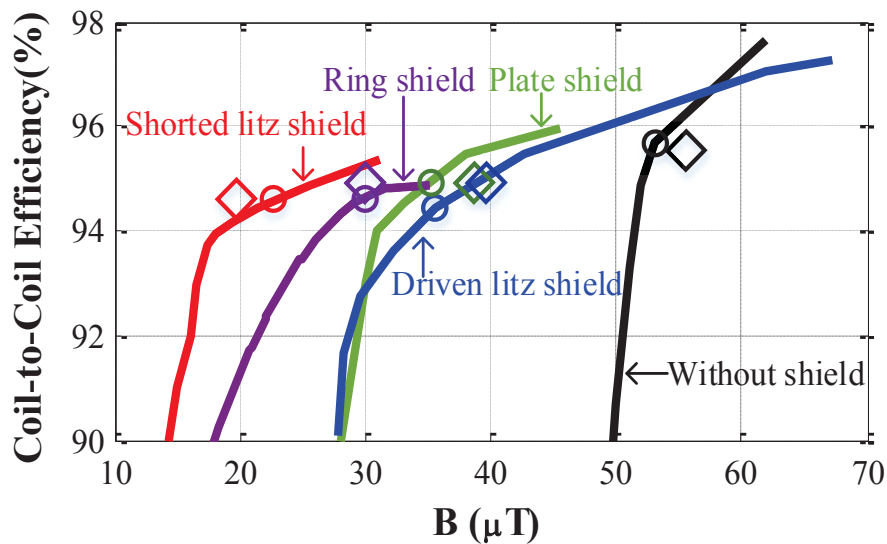


Figure 5-14. Pareto fronts of coil-to-coil efficiency versus stray magnetic field for coils with no shield, plate shield, ring shield, shorted litz shield, and driven litz shield. Horizontal axis is the stray magnetic field at point (0, 100 mm, 0) in Figure 5-13, with 100 W power transferred across 40 mm gap.

5.5. Experimental Verification

The circles along the Pareto fronts in Figure 5-14 represent coils with different shields and similar efficiency (around 94.5%). They were fabricated for experimental test. Figure 5-15 are the fabricated coils. The litz wire used for all the structures have 100 strands of AWG # 38 wires.

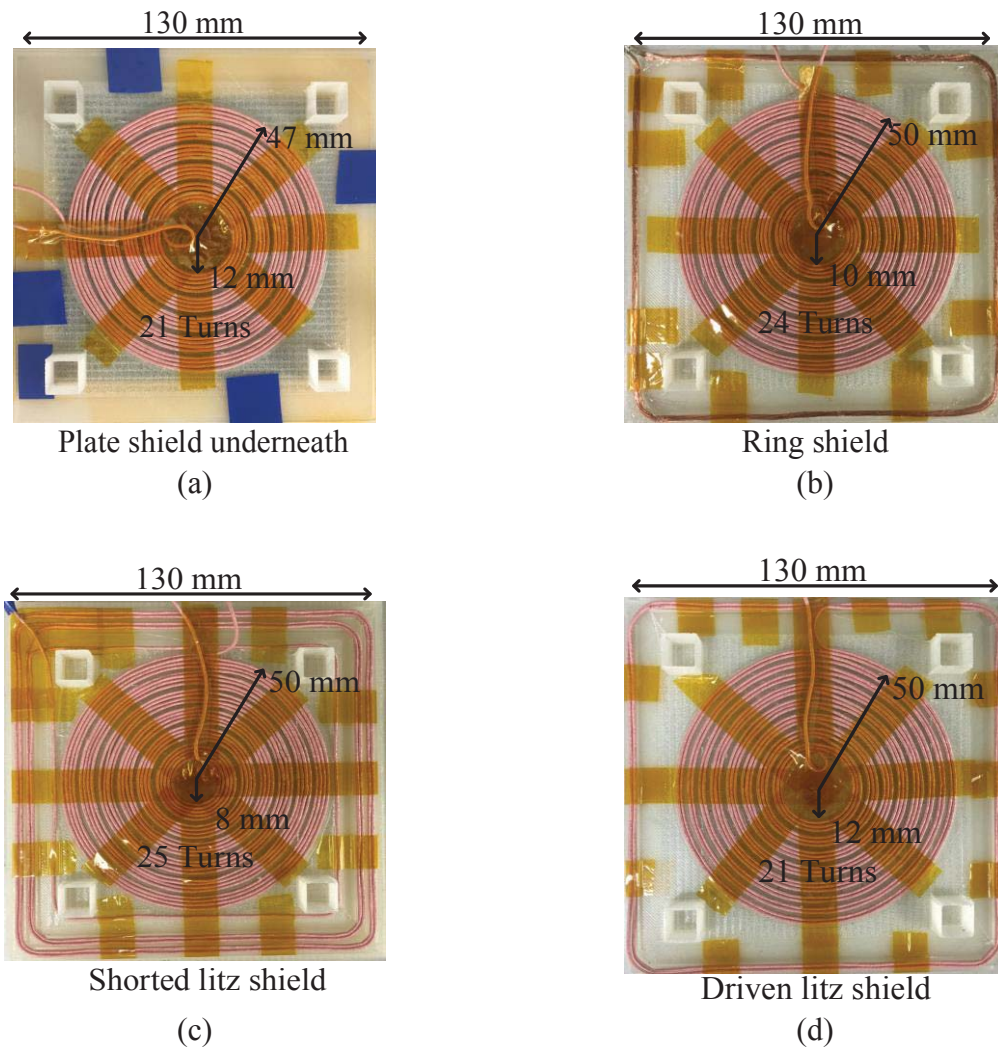


Figure 5-15. Fabricated coils for selected structures marked as circles along the Pareto fronts in Figure 5-14, with (a) plate shield, (b) ring shield, (c) shorted litz shield, and (d) driven litz shield. The coils are optimized to transfer 100 W power across 40 mm gap.

The measured inductances and resistances are listed in TABLE 5-17. The coil-to-coil efficiencies are calculated from (2-10) with the inductances and resistances. Weight breakdown of the coils is listed in TABLE 5-18. Compared to coils without shield, the increases of weight for ring shield and litz shields are negligible, while the plate shield almost doubles the weight.

The hardware setup for the field measurement is the same as in Figure 3-16(b). Figure 5-16 shows the simulated and measured waveforms of $B_Y(t)$ and $B_Z(t)$ at the point (0, 100 mm, 0). The power of 100 W was transferred from the transmitter to receiver across 40 mm gap. The difference between measurement and simulation is less than 10%. The field in Z-direction is dominant at this point. The field in X-direction is negligible so it's not plotted. Figure 5-17 is the comparison of $B_Y(t)$ and $B_Z(t)$ for coils without metal shield and with metal shields in Figure 5-15. Shorted litz shield attenuates the field more than other shields on both Y and Z directions.

TABLE 5-17. Measurement Results for Coils in Figure 5-15

Parameters	Without Shield	Plate shield	Ring shield	Shorted litz shield	Driven litz shield
L_{TX}, L_{RX} (μH)	36	40	49	45	44
M_{TX-RX} (μH)	8.7	8.8	11	9.8	9.6
r_{TX}, r_{RX} ($\text{m}\Omega$), at 100 kHz	106	125	175	160	145
Coil-to-Coil Efficiency	95.7%	94.7%	94.7%	94.4%	94.7%

TABLE 5-18. Weight Breakdown for Transmitter Coil in Figure 5-15, (Ferrite Weight = 240 g)

Parameters	Without Shield	Plate shield	Ring shield	Shorted litz shield	Driven litz shield
Winding (g)	28	31	35	36	32
Shield (g)	0	192	14	19	4

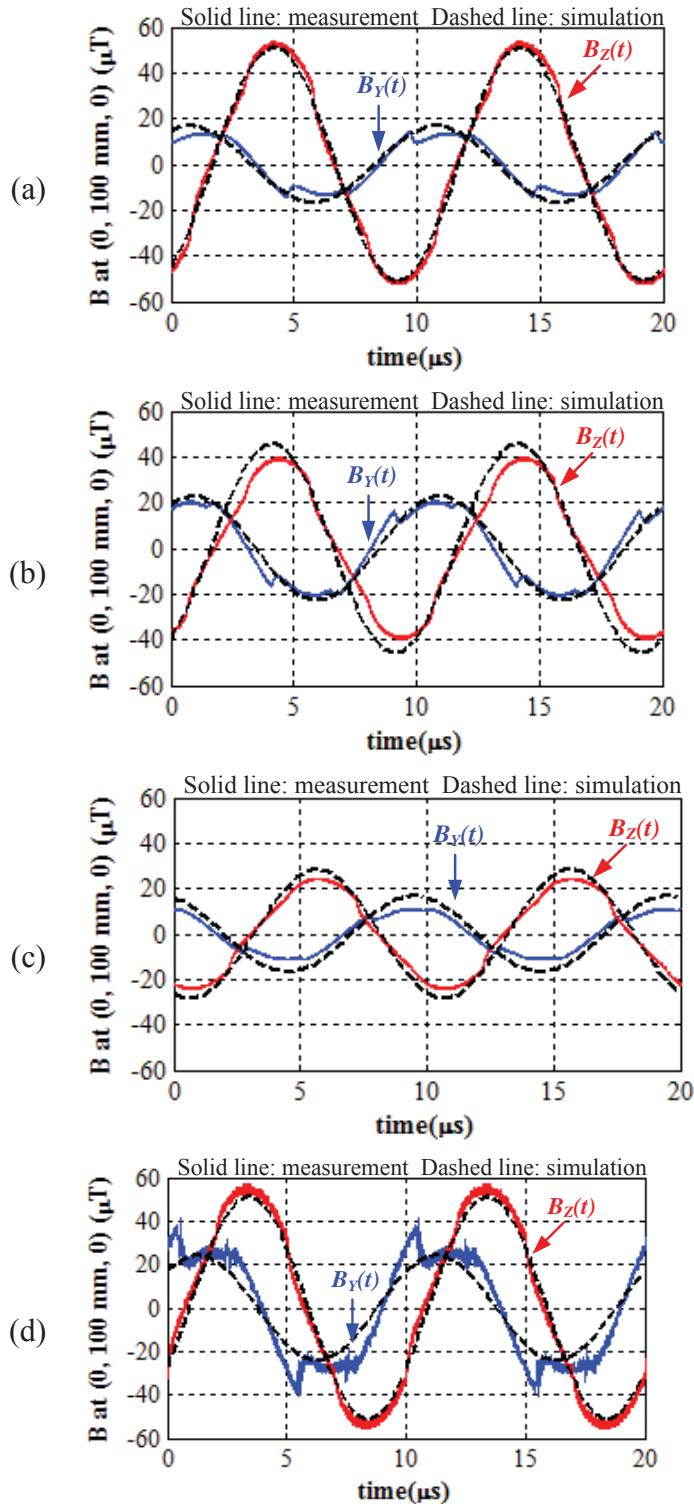


Figure 5-16. Simulated and measured waveforms of the magnetic fields $B_Y(t)$ and $B_Z(t)$ at the point $(0, 100 \text{ mm}, 0)$, for the coils in Figure 5-15 with (a) plate shield, (b) ring shield, (c) shorted litz shield, and (d) driven litz shield. The power of 100 W was transferred across 40 mm gap.

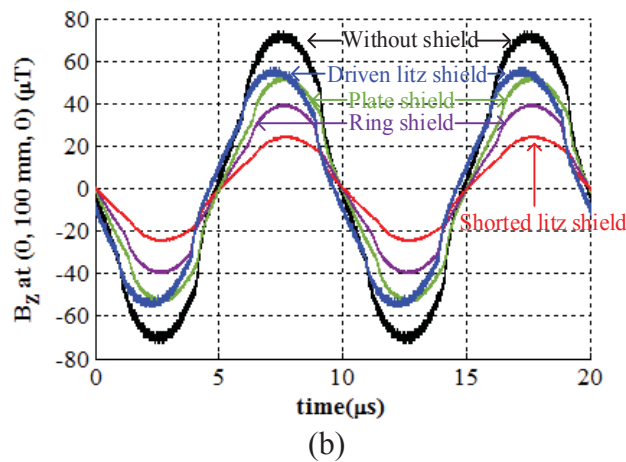
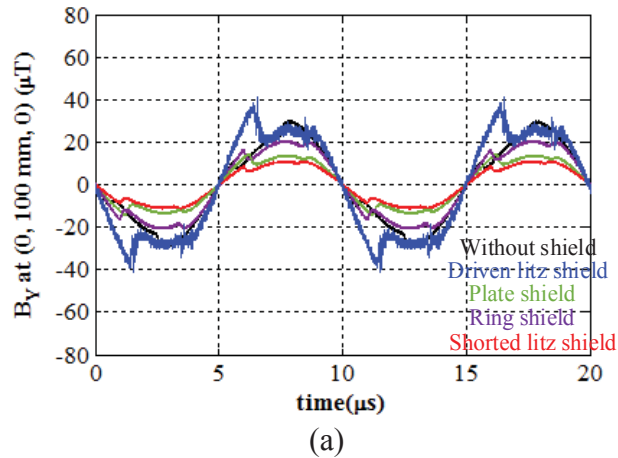


Figure 5-17. The comparison of $B_Y(t)$ and $B_Z(t)$ at point $(0, 100 \text{ mm}, 0)$ between the coils without shield and the coils with different shields in Figure 5-15. The stray magnetic fields are measured when 100 W power was transferred across 40 mm gap.

The measurement of the coil-to-coil efficiency (TABLE 5-17) and the stray magnetic fields for the coils in Figure 5-15 are plotted as diamonds in Figure 5-14. The magnetic fields were quantified using equation (3-8). The circles are the calculation results for the coils in Figure 5-15. The calculation match well with the measurement. The errors are mostly caused by the deviations of the fabrication and probe’s position.

Although the shields were optimized for the magnetic field at $(0, 100 \text{ mm}, 0)$, the stray magnetic fields at other positions are effectively attenuated as well. Figure 5-18 shows the

quantified results of the measured fields on the side of the coils along the Y axis. The stray magnetic field is attenuated by up to 65% with shorted litz shield.

100
125
150
 Distance to center (mm)

Figure 5-18. The quantified stray magnetic fields from measurement along Y axis, with the distance to the center ranging from 75 mm to 150 mm in Figure 5-13.

5.6. Summary

The litz shields are used to attenuate the stray magnetic field around the inductive-power-transfer coils in this chapter. Compared to the plate shield and ring shield, litz shield attenuates the magnetic field with smaller shield loss, because the shield current is more uniformly distributed. The increased weight due to the litz shield is negligible for the coils.

Litz shields are categorized as shorted litz shield and driven litz shield. Circuit models are derived for both categories with four coupled inductors, from which the equivalent inductances, equivalent resistances, windings currents, and shields currents are analyzed.

Pareto fronts are used to optimize the coil-to-coil efficiency and stray magnetic field for the coils with litz shields. A fast method to get the Pareto fronts using lumped-loop model is

described. The efficiency and magnetic field are calculated with permeance matrices, current-to-field matrices, and turns vectors of the lumped-loop model. Only tens of simulations are needed in the entire optimization procedure, which is much faster than the conventional method that asks for thousands of simulations.

Following the method with lumped-loop model, Pareto fronts for coils with litz shields are derived for an exemplary IPT system. The system was designed to transfer 100 W power across 40 mm gap, with 35 V output voltage and 100 kHz switching frequency. The dimensions of coils were limited to be smaller than 130 mm \times 130 mm. Pareto fronts for coils with plate shield and ring shield were derived from parametric sweep in finite-element simulation. The optimal designs of plate shield, ring shield, shorted litz shield, and driven litz shield were selected along the fronts to achieve around 94.5% coil-to-coil efficiency. The selected structures were fabricated and measured in experiment. The results from simulation and measurement match well. The shorted litz shield is most effective among all the shielding structures. It attenuates the stray magnetic field by 65% compared to the coils without metal shield. The increased weight due to the litz shields is negligible. The measured efficiencies were 94.5% and 95.5% for coils with shorted litz shield and coils without metal shield, respectively.

Chapter 6. Attenuation of Stray Magnetic Field by Controlling Phases of Winding Currents

Nomenclature

a_1	The ratio of B_{1r0} over B_{1a0} .
a_2	The ratio of B_{2r0} over B_{2a0} .
B	Quantified magnetic field.
B_1	Stray magnetic field generated by transmitter current.
B_{1a}	Components of B_1 in axial direction.
B_{1a0}	RMS value of B_{1a} when φ is 90° .
B_{1r}	Components of B_1 in radial direction.
B_{1r0}	RMS value of B_{1r} when φ is 90° .
B_2	Stray magnetic field generated by receiver current.
B_{2a}	Components of B_2 in axial direction.
B_{2a0}	RMS value of B_{2a} when φ is 90° .
B_{2r}	Components of B_2 in radial direction.
B_{2r0}	RMS value of B_{2r} when φ is 90° .
I_0	RMS value of winding current when φ is 90° and when $I_1 = I_2$.
I_1	RMS value of transmitter current.
I_2	RMS value of receiver current.
L_1	Self-inductance of the transmitter.

L_2	Self-inductance of the receiver.
M	Mutual inductance between transmitter and receiver.
P_{loss}	Total winding loss of transmitter and receiver.
P_{loss}	Output power in Figure 6-5
P_{lossN}	Normalized winding loss.
r_1	Winding resistance of transmitter at switching frequency.
r_2	Winding resistance of receiver at switching frequency.
v_1	Output voltage of the inverter in Figure 6-4.
v_{10}	Sinusoidal voltage source in Figure 6-5 to represent fundamental component of v_1 .
v_2	Input voltage of the rectifier in Figure 6-4.
v_{20}	Sinusoidal voltage source in Figure 6-5 to represent fundamental component of v_2 .
V_{in}	Input DC voltage in Figure 6-3.
V_{out}	Output DC voltage in Figure 6-3.
α_1	Pulse-width of v_1 .
α_2	Pulse-width of v_2 .
θ	Phase difference between transmitter and receiver currents.
φ	Phase difference between v_1 and v_2 .

6.1. Introduction

Chapter 5 demonstrates an effective method to attenuate the stray magnetic field by adding litz shield. In this chapter, another method to attenuate the stray magnetic field is investigated. The field is attenuated by controlling the phases of winding currents.

The magnetic field is decomposed to components in axial and radial directions [103]. The axial component decreases when the phase difference between winding currents is smaller, while the radial component exhibits the opposite property. Because the axial component of stray magnetic field around IPT coils is dominant [52], it's preferred to decrease the phase difference.

The dual-side-controlled converter is applied for circuit realization. Bridges with active switches are used for both the inverter on the transmitter side and the rectifier on the receiver side. Switching frequency equals the resonant frequency. The magnitudes of winding currents are controlled by the pulse-widths of inverter voltage and rectifier voltage. The phases of winding currents are tuned with the phases of the voltages. Equations are derived from the equivalent circuit model of the converter to predict the field attenuation. Increased winding loss is analyzed with the equivalent circuit model as well.

Section 6.2 analyzes influences of current' phases on stray magnetic field with relevant equations. Section 6.3 demonstrates the circuit realization to control phases of winding currents with dual-side-controlled converter. In Section 6.4 and 6.5, finite-element simulations and experiment were implemented to verify the theory.

6.2. Influence of Currents' Phases on Stray Magnetic Field

According to superposition, the time-varying stray magnetic field $B(t)$ around the cylindrical symmetric coils in Figure 6-1 is composed of $B_1(t)$ and $B_2(t)$. $B_1(t)$ is generated by the transmitter current $i_1(t)$, while $B_2(t)$ is generated by the receiver current $i_2(t)$. The directions of $i_1(t)$ and $i_2(t)$ are marked in Figure 6-1. Magnetic fields $B(t)$, $B_1(t)$, and $B_2(t)$ are decomposed to components in the radial direction ($B_r(t)$, $B_{1r}(t)$ and $B_{2r}(t)$) and components in the axial direction ($B_a(t)$, $B_{1a}(t)$ and $B_{2a}(t)$). According to Figure 6-1, the relationships among these components are

$$B_r(t) = B_{2r}(t) + B_{1r}(t) \quad (6-1)$$

$$B_a(t) = B_{2a}(t) - B_{1a}(t) \quad (6-2)$$

Figure 6-1. The magnetic fields generated by IPT coils from side view. According to superposition, $B_1(t)$ is generated by transmitter current $i_1(t)$, and $B_2(t)$ is generated by receiver current $i_2(t)$. $B_1(t)$ and $B_2(t)$ are decomposed to components $B_{1a}(t)$ and $B_{2a}(t)$ in the axial direction and components $B_{1r}(t)$ and $B_{2r}(t)$ in the radial direction.

According to Ampere's law, $B_1(t)$, $B_{1a}(t)$, and $B_{1r}(t)$ are proportional to $i_1(t)$, whereas $B_2(t)$, $B_{2a}(t)$, and $B_{2r}(t)$ are proportional to $i_2(t)$. Since $i_1(t)$ and $i_2(t)$ are almost sinusoidal with switching frequency in IPT application, the magnetic fields are sinusoidal as well. Therefore, the currents and fields are represented with phasors to simplify the analysis. The magnitudes of all the phasors in this chapter are the RMS values. Equations (6-1) and (6-2) are written with phasors as

$$\dot{B}_r = \dot{B}_{1r} + \dot{B}_{2r} \quad (6-3)$$

$$\dot{B}_a = \dot{B}_{2a} - \dot{B}_{1a} \quad (6-4)$$

Diagrams of phasors in Figure 6-2(b) and (c) are equivalent to (6-3) and (6-4). When the receiver current \dot{I}_2 leads transmitter current \dot{I}_1 by phase θ , fields \dot{B}_{2r} and \dot{B}_{2a} lead fields \dot{B}_{1r}

and \dot{B}_{1a} by phase θ as well. The magnitudes of phasors \dot{B}_r and \dot{B}_a are derived from Figure 6-2(b) and (c) as

$$B_r = \sqrt{B_{1r}^2 + B_{2r}^2 + 2B_{1r}B_{2r} \cos \theta} \quad (6-5)$$

$$B_a = \sqrt{B_{1a}^2 + B_{2a}^2 - 2B_{1a}B_{2a} \cos \theta} \quad (6-6)$$

(a)

(b)

(c)

Figure 6-2. (a) Phasors representing winding currents $i_1(t)$ and $i_2(t)$, with magnitudes I_1 and I_2 and phase difference θ ; phasors representing stray magnetic fields in (b) axial direction and (c) radial direction.

For cylindrical symmetric coils, the RMS value of magnetic field at one position is quantified as:

$$B = \sqrt{(B_a^2 + B_r^2)} \quad (6-7)$$

According to (6-5) and (6-6), B_r decreases with θ while B_a increases with θ , when θ changes in the range from 0° to 180° . In order to achieve a smaller value in (6-7), it's preferred to decrease θ because axial components of stray magnetic field is dominant on the side of the coils [52].

6.3. Circuit Realization with the Dual-Side-Controlled Converter

The dual-side-controlled converter in Figure 6-3 is applied in order to control the phases of winding currents on both sides. Both the inverter and rectifier are composed of full bridges with MOSFETs. The series-series compensation is used as the exemplary IPT system. In Figure 6-3, L_1 and L_2 are the self-inductances of transmitter and receiver; M is the mutual inductance; C_1 and C_2 are the resonant capacitors of L_1 and L_2 ; r_1 and r_2 are the winding resistances at switching frequency; V_{in} and V_{out} are input and output DC voltages. In order to reduce the circulating energy, switching frequencies on both sides equal resonant frequency.

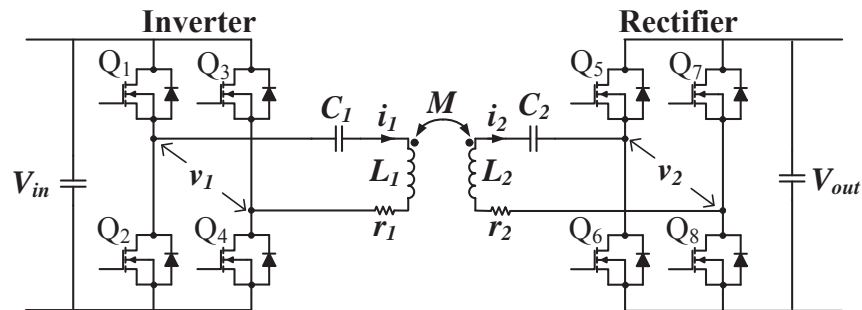


Figure 6-3. Circuit topology of series-series compensation with the dual-side control converter.

The switching sequence of the switches is shown in Figure 6-4. It controls the pulse-width α_1 for the output voltage of inverter v_1 , the pulse-width α_2 for the input voltage of rectifier v_2 , and the phase difference φ between v_1 and v_2 .

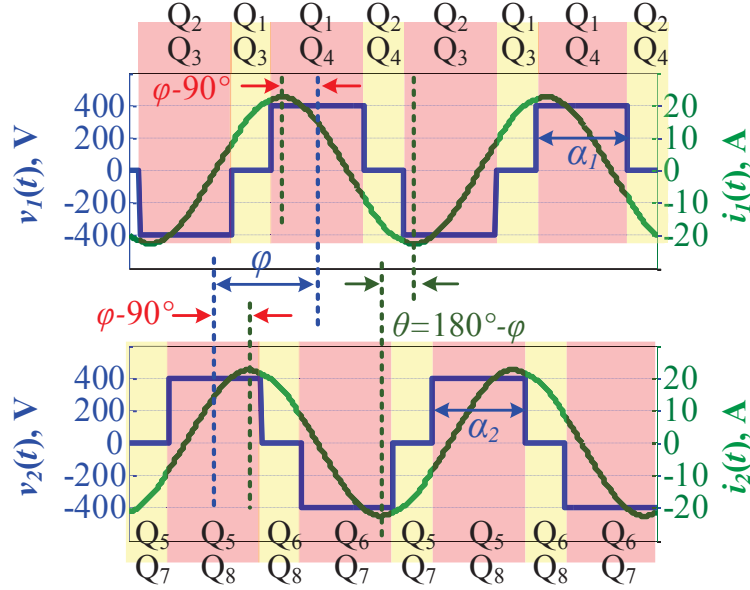


Figure 6-4. Simulated waveforms of voltages and currents on the inverter side and receiver side in Figure 6-3 ($P_{out} = 3.3 \text{ kW}$, $V_{in} = 400 \text{ V}$, $V_{out} = 400 \text{ V}$, $\varphi = 140^\circ$, $\alpha_1 = \alpha_2 = 126^\circ$).

The equivalent circuit model in Figure 6-5 is used to analyze the behavior of the topology in Figure 6-3. Under the first harmonic approximation, the input DC voltage source and the inverter are modeled as sinusoidal voltage source $v_{10}(t)$, while the output DC voltage and the rectifier are modeled as sinusoidal voltage source $v_{20}(t)$. The sources $v_{10}(t)$ and $v_{20}(t)$ are expressed as phasors \dot{V}_{10} and \dot{V}_{20} in Figure 6-5. Assuming phasor \dot{V}_{10} is aligned with real axis and its phase is 0° , the expressions of \dot{V}_{10} and \dot{V}_{20} are

$$\dot{V}_{10} = \left| \frac{2\sqrt{2}}{\pi} V_{in} \sin\left(\frac{\alpha_1}{2}\right) \right| \angle 0 \quad (6-8)$$

$$\dot{V}_{20} = \left| \frac{2\sqrt{2}}{\pi} V_{out} \sin\left(\frac{\alpha_2}{2}\right) \right| \angle \varphi \quad (6-9)$$

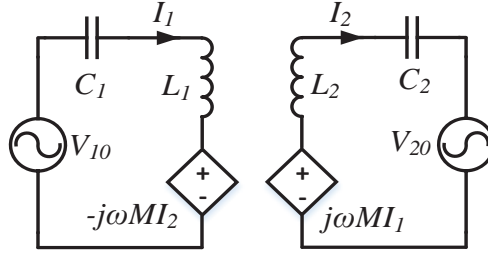


Figure 6-5. Equivalent circuit model of the topology in Figure 6-3.

The phasors \dot{I}_1 and \dot{I}_2 for the sinusoidal currents of the windings are derived from the equivalent circuit model in Figure 6-5 as

$$\dot{I}_1 = \left| \frac{2\sqrt{2}}{\pi} \frac{V_{out}}{\omega M} \sin\left(\frac{\alpha_2}{2}\right) \right| \angle(\varphi - 90^\circ) \quad (6-10)$$

$$\dot{I}_2 = \left| \frac{2\sqrt{2}}{\pi} \frac{V_{in}}{\omega M} \sin\left(\frac{\alpha_1}{2}\right) \right| \angle 90^\circ \quad (6-11)$$

According to (6-10) and (6-11), \dot{I}_1 lags \dot{V}_2 by 90° and \dot{I}_2 leads \dot{V}_1 by 90° . The phase difference θ between \dot{I}_1 and \dot{I}_2 is controlled by phase difference φ between \dot{V}_1 and \dot{V}_2 as

$$\theta = 180^\circ - \varphi \quad (6-12)$$

When neglecting the influence of r_1 and r_2 , the output power is derived from Figure 6-5 as

$$P_{out} = \frac{8}{\pi^2} \frac{V_{in} V_{out}}{\omega M} \sin\left(\frac{\alpha_1}{2}\right) \sin\left(\frac{\alpha_2}{2}\right) \sin \varphi \quad (6-13)$$

The desired output power is achieved by tuning the phases φ , as well as pulse-widths α_1 and α_2 . According to (6-10) and (6-11), the output power in (6-13) is further simplified as

$$P_{out} = I_1 I_2 \omega M \sin \varphi \quad (6-14)$$

Assuming the transmitter and receiver have the same structures, the equivalent series resistance of each coil is r . The winding loss P_{loss} is calculated from ohm's law as

$$P_{loss} = (I_1^2 + I_2^2)r \quad (6-15)$$

By combining (6-14) and (6-15), P_{loss} is expressed as:

$$P_{loss} = \left[I_1^2 + \left(\frac{P_{out}}{I_1 \cdot \omega M \cdot \sin \varphi} \right)^2 \right] r \quad (6-16)$$

By solving $\partial P_{loss} / \partial I_1 = 0$ for (6-16), the smallest P_{loss} is achieved when $I_1 = I_2$ for a given value of φ . This is equivalent to (6-17) according to (6-10) and (6-11).

$$V_{in} \sin\left(\frac{\alpha_1}{2}\right) = V_{out} \sin\left(\frac{\alpha_2}{2}\right) \quad (6-17)$$

Therefore, α_1 and α_2 are tuned to guarantee $I_1 = I_2$ and to minimize the winding loss. When phase φ between \dot{V}_1 and \dot{V}_2 is tuned to control θ between \dot{I}_1 and \dot{I}_2 , the magnitudes of the winding currents should be changed accordingly by tuning α_1 and α_2 to keep the same power transfer. Assuming I_0 is the magnitude of winding current when φ is 90° , the current should be $I_0 / \sqrt{\sin \varphi}$ for other values of φ according to (6-14). Since the magnetic field is proportional to winding currents, equations (6-5) and (6-6) are represented as:

$$B_r = \sqrt{\frac{B_{1r0}^2 + B_{2r0}^2 - 2B_{1r0}B_{2r0} \cos \varphi}{\sin \varphi}} \quad (6-18)$$

$$B_a = \sqrt{\frac{B_{1a0}^2 + B_{2a0}^2 + 2B_{1a0}B_{2a0} \cos \varphi}{\sin \varphi}} \quad (6-19)$$

where B_{1r0} , B_{2r0} , B_{1a0} , and B_{2a0} are the magnetic fields in the radial direction and axial direction when φ is 90° . The quantified field is calculated from (6-7) as

$$B = \sqrt{\frac{B_{1r0}^2 + B_{2r0}^2 - 2B_{1r0}B_{2r0} \cos \varphi + B_{1a0}^2 + B_{2a0}^2 + 2B_{1a0}B_{2a0} \cos \varphi}{\sin \varphi}} \quad (6-20)$$

Assuming a_1 is the ratio of B_{1r0} over B_{1a0} and a_2 is the ratio of B_{2r0} over B_{2a0} , (6-20) is simplified as

$$B = \sqrt{\frac{(1+a_1^2)B_{1a0}^2 + (1+a_2^2)B_{2a0}^2 + 2(1-a_1a_2)B_{1a0}B_{2a0} \cos \varphi}{\sin \varphi}} \quad (6-21)$$

Using the quantified magnetic field with $\varphi = 90^\circ$ as the base, the normalized magnetic field B_N is defined as

$$B_N = \frac{B(\varphi)}{B(\varphi = 90^\circ)} = \sqrt{\frac{(1+a_1^2)B_{1a0}^2 + (1+a_2^2)B_{2a0}^2 + 2(1-a_1a_2)B_{1a0}B_{2a0} \cos \varphi}{\sin \varphi [(1+a_1^2)B_{1a0}^2 + (1+a_2^2)B_{2a0}^2]}} \quad (6-22)$$

The normalized winding loss P_{lossN} is defined with the base of winding loss when $\varphi = 90^\circ$, which is expressed as

$$P_{lossN} = \frac{P_{loss}(\varphi)}{P_{loss}(\varphi = 90^\circ)} = \frac{1}{\sin \varphi} \quad (6-23)$$

The axial distances from the positions along the radial axis in Figure 6-1 to the transmitter and receiver are the same. When the transmitter and receiver have the same structures, the magnetic field at each position along the radial axis satisfies $B_{1a0} = B_{2a0}$, $B_{1r0} = B_{2r0}$, and $a_1 = a_2 = a$. Figure 6-6 shows B_N in (6-22) when φ changes from 90° to 140° and a changes from 0.1 to 1. With smaller a when the field component in the axial direction is more dominant, φ should be increased to reduce θ for field attenuation.

Figure 6-7 shows P_{lossN} in (6-23) when φ changes from 90° to 140° . The winding loss increases with φ . Therefore, the trade-off to attenuate the stray magnetic field by increasing φ is that the winding loss is increased as well.

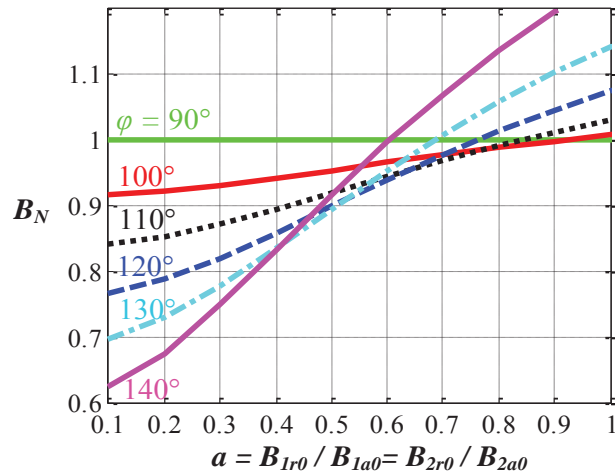


Figure 6-6. Normalized magnetic field B_N in (6-22) versus φ and a . The measurement position of magnetic field is along the radial axis.

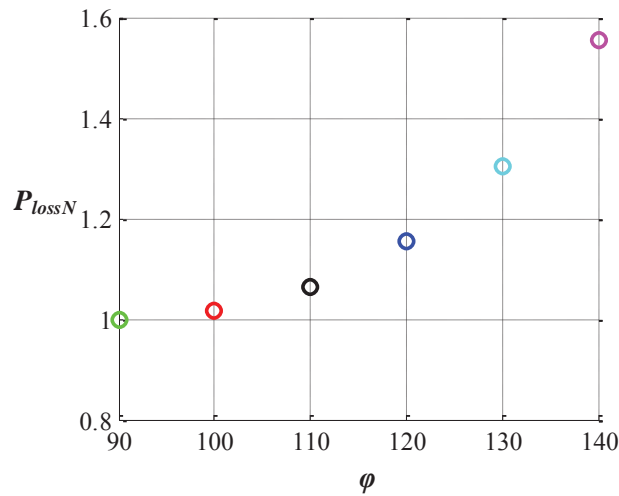


Figure 6-7. Normalized loss in (6-23) versus φ .

6.4. Simulation Verification

The effectiveness of the field attenuation by controlling the phases of winding currents is verified in finite-element simulation. The exemplary set of planar coils in Figure 6-8 was designed for a 3.3 kW IPT system. The specifications of the system are listed in TABLE 6-1.

According to the simulation, the self-inductances of the transmitter and receiver are 150.2 μH , the mutual inductance is 31.8 μH , and the coupling coefficient is 0.212. The compensation capacitors are 16.8 nF for 100 kHz resonant frequency. The stray magnetic fields at the points for field measurement along the radial axis in Figure 6-9 are compared for different values of φ with 3.3 kW power transfer.

TABLE 6-1. Specifications of the Exemplary 3.3 kW IPT system with Coils in Figure 6-8

Parameters	Values
V_{in} in Figure 6-3	400 V
V_{out} in Figure 6-3	400 V
f_s	100 kHz

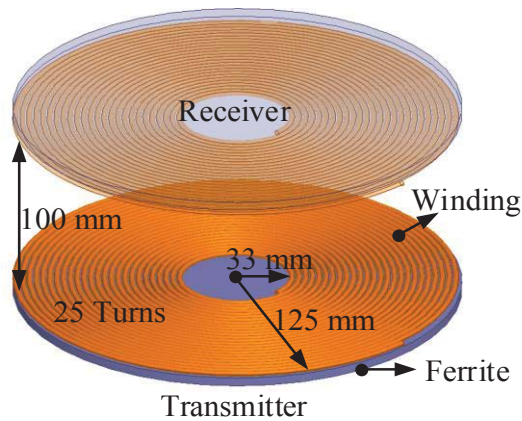


Figure 6-8. Structures and dimensions of the exemplary coils designed for the 3.3 kW IPT system in TABLE 6-1.

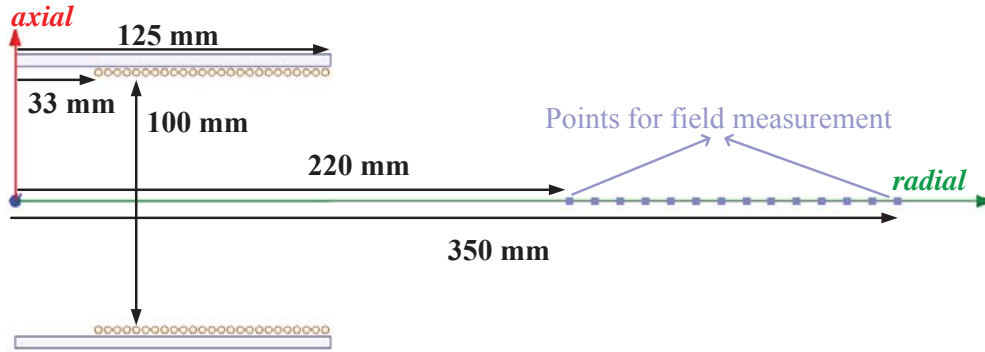


Figure 6-9. Positions for field measurement along the radial axis around the coils in Figure 6-8.

Figure 6-10 shows the values of $a = a_1 = a_2$ at the measurement positions in Figure 6-9, which represent ratios of B_{1r0} over B_{1a0} and B_{2r0} over B_{2a0} . They were derived from the simulation of the coils in Figure 6-8 by exciting the transmitter or receiver only. Circles in Figure 6-11 represent the calculated B_N versus φ at the measurement positions using (6-22) with the values of a in Figure 6-10. Solid lines in Figure 6-11 are the simulated B_N with the current excitations derived from (6-10) and (6-11). The calculation matches well with simulation. The stray magnetic field was attenuated by up to 30% and 40% when φ is 130° and 140° , respectively, which is equivalent to be $\theta = 50^\circ$ and $\theta = 40^\circ$.

The waveforms of currents and voltages the for inverter and receiver in Figure 6-3 are plotted in Figure 6-12 and Figure 6-13, for $\varphi = 90^\circ$ and $\varphi = 130^\circ$, respectively. The current and voltage are in phase when $\varphi = 90^\circ$. There is more circulating energy when $\varphi = 130^\circ$, which leads to increased winding loss.

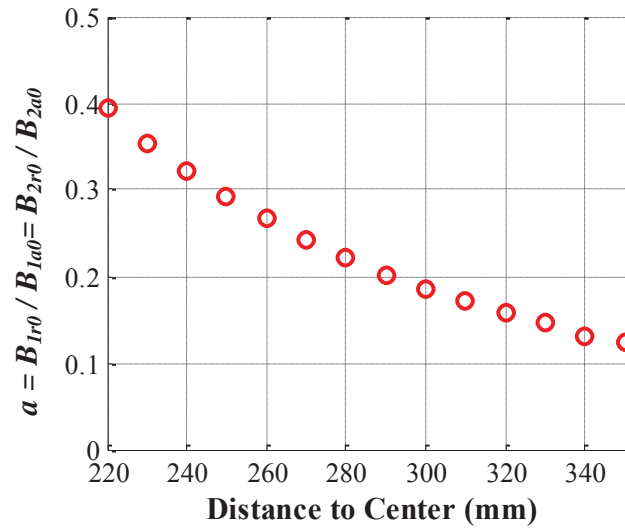


Figure 6-10. Simulated values of $\alpha = B_{1r0} / B_{1a0} = B_{2r0} / B_{2a0}$ at the positions for field measurement in Figure 6-9.

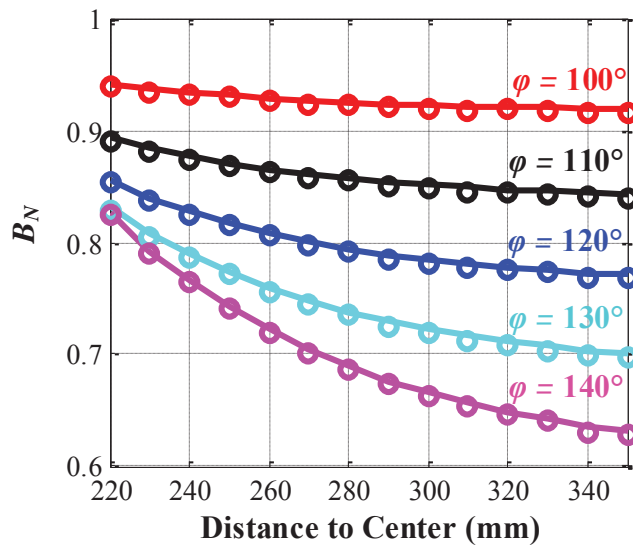


Figure 6-11. Simulated B_N (solid lines) and calculated B_N from (6-22) (circles) at the positions for field measurement in Figure 6-9.

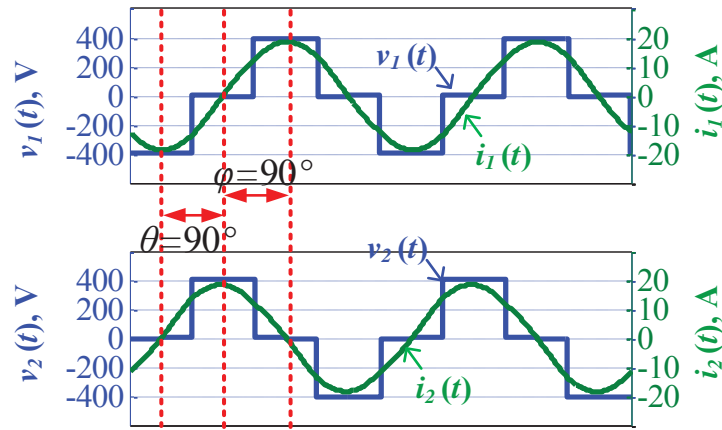


Figure 6-12. Waveforms of currents and voltages for the inverter and receiver in Figure 6-3: $\varphi = 90^\circ$, $\theta = 90^\circ$.

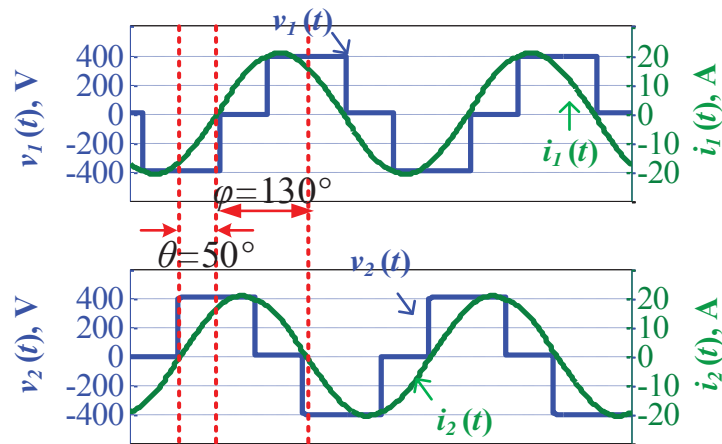


Figure 6-13. Waveforms of currents and voltages for the inverter and receiver in Figure 6-3: $\varphi = 130^\circ$, $\theta = 50^\circ$.

Figure 6-14 and Figure 6-15 show the magnitudes of the magnetic fields around the coils in finite-element simulations for these two conditions. The stray magnetic field around the coils when $\varphi = 130^\circ$ is significantly attenuated compared to the case when $\varphi = 90^\circ$.

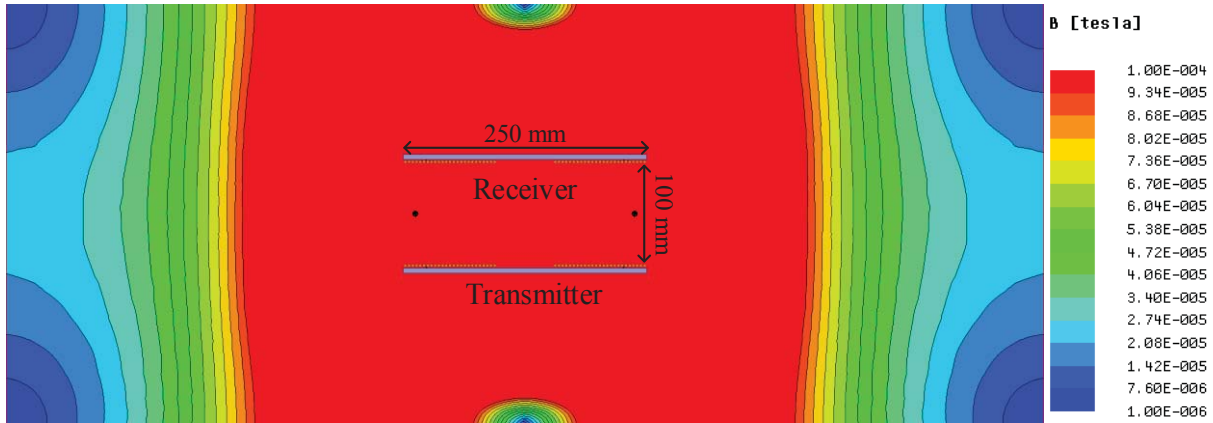


Figure 6-14. Magnitude of magnetic field around coils from finite-element simulation:
 $\varphi = 90^\circ, \theta = 90^\circ$.

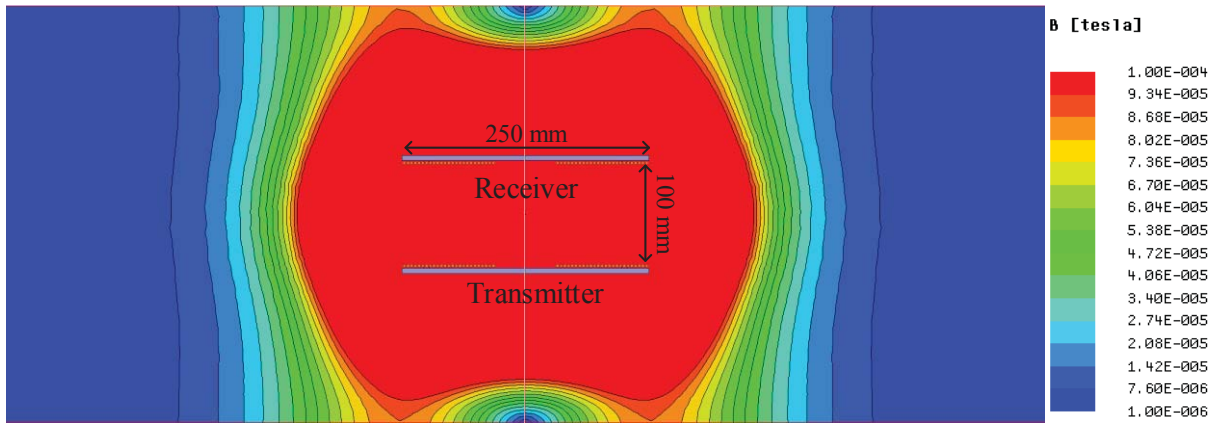


Figure 6-15. Magnitude of magnetic field around coils from finite-element simulation:
 $\varphi = 130^\circ, \theta = 50^\circ$.

6.5. Experimental Verification

A scaled-down system of TABLE 6-1 was built to verify the field attenuation by controlling the phases of winding currents. In the experiment, 100 W power was transferred across 40 mm gap, with $\varphi = 90^\circ$ and $\varphi = 130^\circ$. Figure 6-16(a) shows the structure of the coils. There are 21

turns of litz wire in the winding. The litz wire is composed of 100 strands with 0.1 mm strand-diameter. The inner radius is 10 mm, and outer radius is 45 mm. The 3C96 ferrite plate with dimensions of 100 mm by 100 mm by 5 mm is placed underneath the winding. The gap between the transmitter and receiver is 40 mm, as shown in Figure 6-16(b).

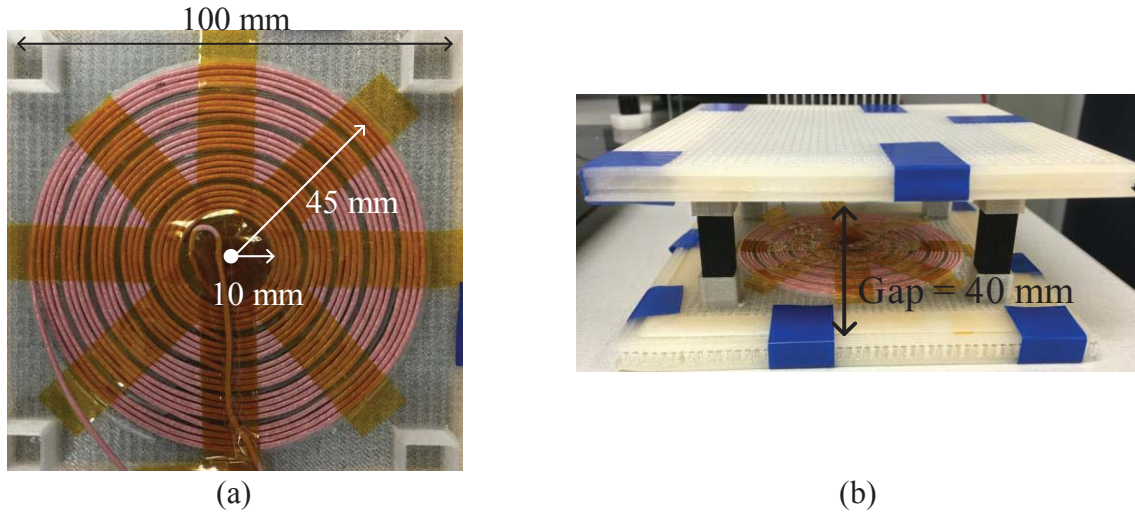


Figure 6-16. (a) Fabricated coils for the 100 W experimental verification with (b) a gap of 40 mm between transmitter and receiver.

TABLE 6-2. Inductances and Resistances for Coils in Figure 6-16

Parameter	Simulation	Measurement
L_1, L_2	36.8 μH , 36.8 μH	35.4 μH , 36.0 μH
M	8.6 μH	8.7 μH
r_1 at 100 kHz, r_2 at 100 kHz	100 m Ω , 100 m Ω	102 m Ω , 106 m Ω

Figure 6-17 shows the hardware setup for the experimental verification. Infineon IPP200N25N3 MOSFETs were used to build the inverter and rectifier. The switching frequency

and resonant frequency were both 100 kHz. The gate signals of the devices were directly supplied from two synchronized function generators. The electronic load was set to be in the constant voltage mode.



Figure 6-17. A hardware setup for field measurement around the coils.

Two conditions were tested, with $\varphi = 90^\circ$ and $\varphi = 130^\circ$. In both cases, 100 W power was transferred to the load. Figure 6-18 shows the waveforms of transmitter current $i_1(t)$ and receiver current $i_2(t)$. Figure 6-18(a) and (c) are the measurement results with the hardware setup in Figure 6-17. Figure 6-18(b) and (d) are simulated in LTSpice with the circuit topology in Figure 6-3 and coils parameters in TABLE 6-2.

When $\varphi = 90^\circ$, the receiver current is 90° leading the transmitter current. The measured RMS values of $i_1(t)$ and $i_2(t)$ are 4.5 A and 4.2 A, respectively. When $\varphi = 130^\circ$, the receiver current is 50° leading the transmitter current. The measured RMS values of $i_1(t)$ and $i_2(t)$ are 4.9 A and

4.7 A, respectively. Calculated with the winding resistances in TABLE 6-2, the winding losses are around 3.8 W for $\varphi = 90^\circ$ and 4.6 W for $\varphi = 130^\circ$.

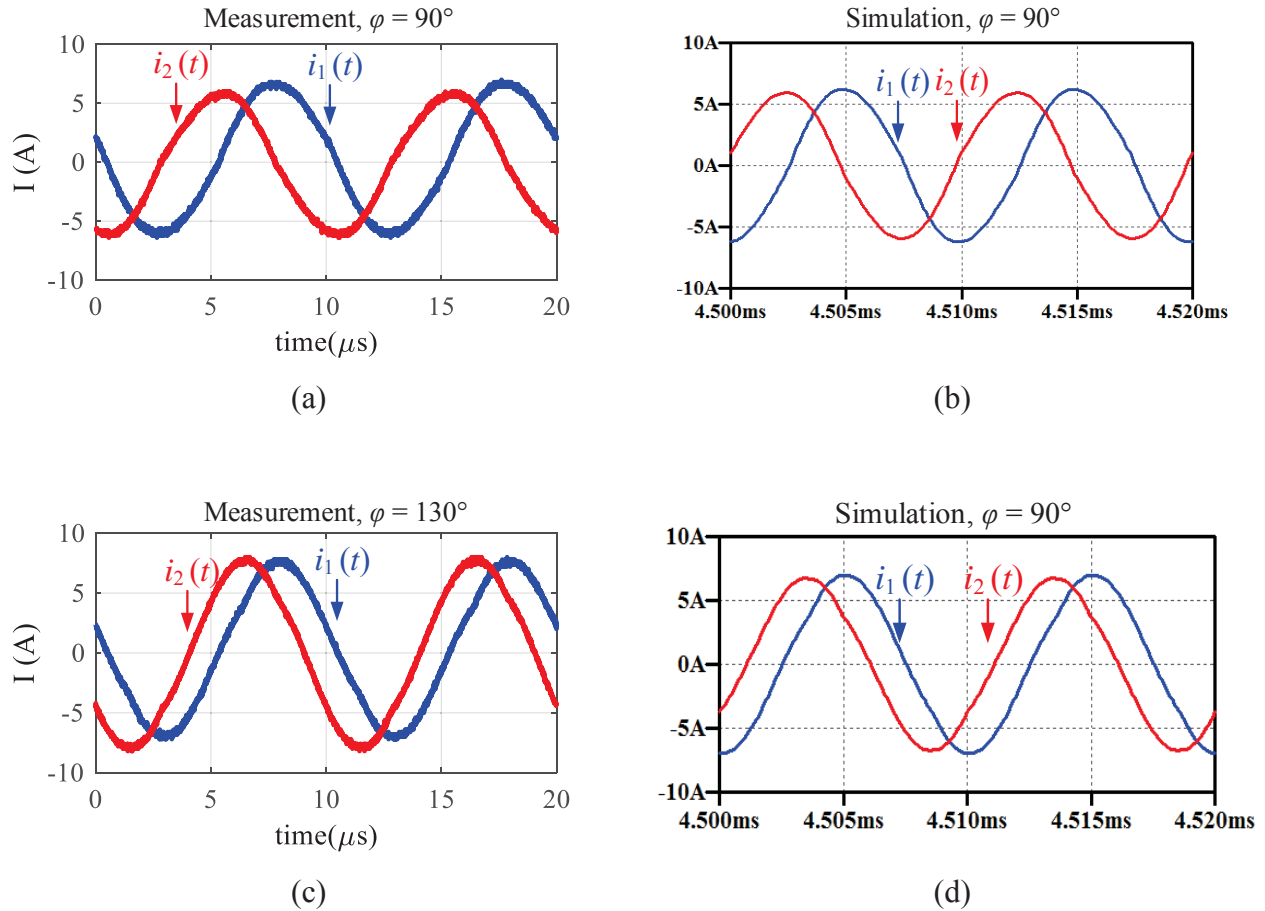


Figure 6-18. Winding currents when transferring 100 W power with the coils in Figure 6-16 and the hardware in Figure 6-17: (a) $\varphi = 90^\circ$, measurement; (b) $\varphi = 90^\circ$, simulation; ; (c) $\varphi = 130^\circ$, measurement; (d) $\varphi = 130^\circ$, simulation.

In Figure 6-17, the magnetic fields $B_a(t)$ and $B_r(t)$ were measured with the near-field probe Langer EMV LF-R 50. The stray magnetic field were measured and simulated along the r axis, as shown in Figure 6-19. The distance between the points of field measurement and the center of the coils ranges from 100 mm to 200 mm. Figure 6-20 plots the magnetic fields $B_a(t)$ and $B_r(t)$

at the point ($x = 0$, $r = 100$ mm, $a = 0$) in Figure 6-19. Figure 6-20 (a) and (c) are the measurement results with the hardware setup in Figure 6-17. Figure 6-20 (b) and (d) are the simulation results in Ansys Maxwell with the eddy current solver. The magnetic fields in X direction is negligible for the points along Y axis due to the symmetry, so they are not plotted.

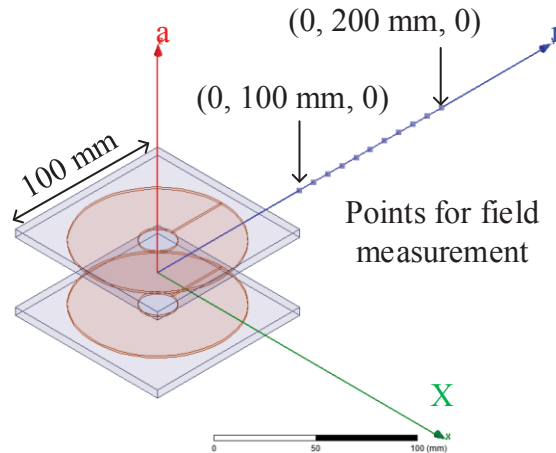


Figure 6-19. Points along the radial axis for field measurement for the coils in Figure 6-16.

Observed in Figure 6-20(a) and (c), there are harmonics for the measured magnetic fields. Therefore, FFT was implemented to derive the components at 100 kHz which is the switching frequency. When $\varphi = 90^\circ$, the RMS values of the measured $B_a(t)$ and $B_r(t)$ in Figure 6-20(a) are $50.1 \mu\text{T}$ and $13.6 \mu\text{T}$, respectively, and the quantified magnetic field is $51.7 \mu\text{T}$. Its corresponding results from simulation is $56.6 \mu\text{T}$, calculated from Figure 6-20(b). When $\varphi = 130^\circ$, the RMS values of the measured $B_a(t)$ and $B_r(t)$ in Figure 6-20(c) are $35 \mu\text{T}$ and $20.9 \mu\text{T}$, respectively. The quantified magnetic field is $40.8 \mu\text{T}$. Its corresponding results from simulation is $44.7 \mu\text{T}$, calculated from Figure 6-20(d). As shown in Figure 6-20(a) and (c), when the phase φ is increased from 90° to 130° , $B_r(t)$ is increased and $B_a(t)$ is decreased. The quantified magnetic field is decreased because $B_a(t)$ is dominant on the side of the coils.

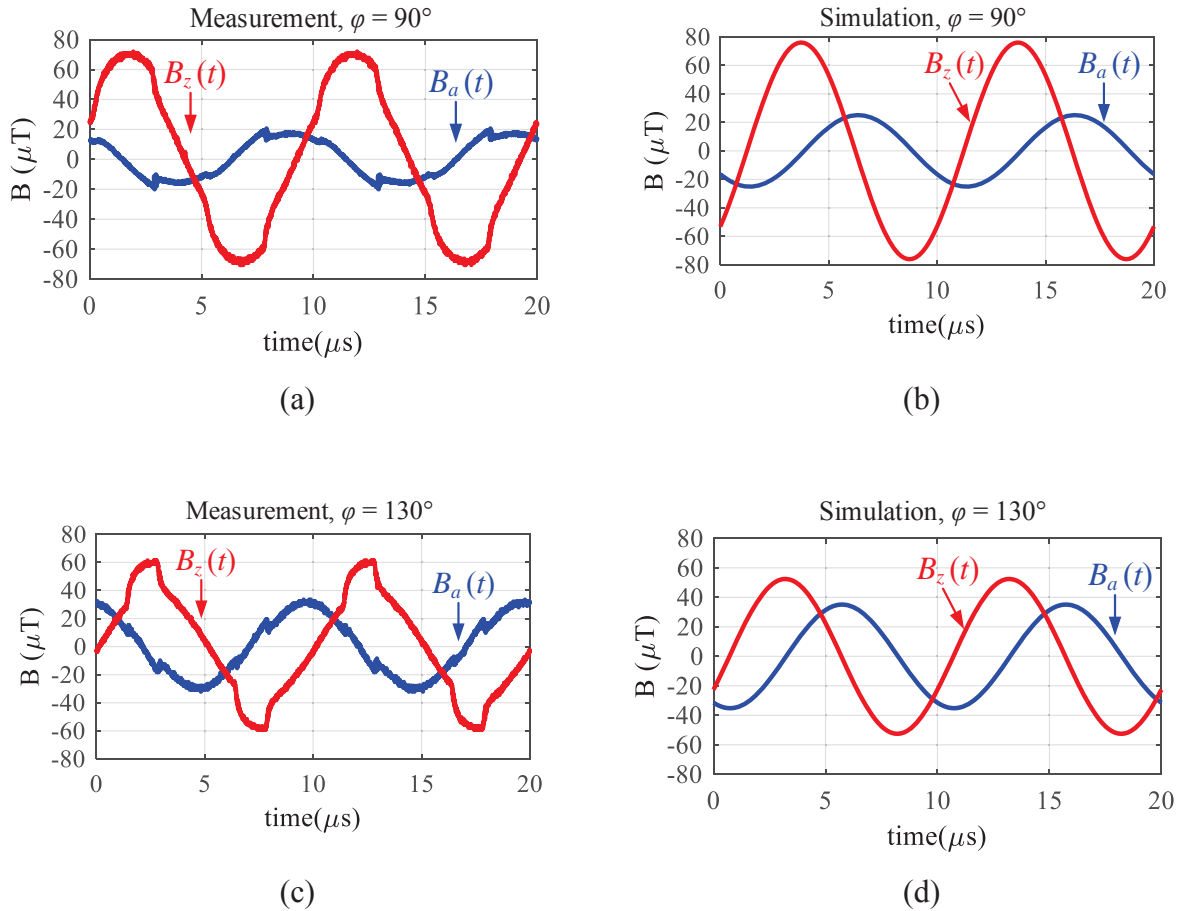


Figure 6-20. Magnetic fields $B_a(t)$ and $B_z(t)$ at the point (0, 100 mm, 0) in Figure 6-19, when transferring 100 W power with the coils in Figure 6-16 and the hardware in Figure 6-17: (a) $\varphi = 90^\circ$, measurement; (b) $\varphi = 90^\circ$, simulation; (c) $\varphi = 130^\circ$, measurement; (d) $\varphi = 130^\circ$, simulation.

Figure 6-21 shows the quantified magnetic field at the points of field measurement along the radial axis in Figure 6-19, for $\varphi = 90^\circ$ and $\varphi = 130^\circ$. The dashed lines are the simulation results, and the circles are the measurement results. They match well with each other. Figure 6-22 shows the magnitudes of the magnetic fields around coils in finite-element simulations for these two conditions. Both Figure 6-21 and Figure 6-22 prove significant attenuation of the stray magnetic field when φ is increased from 90° to 130° .

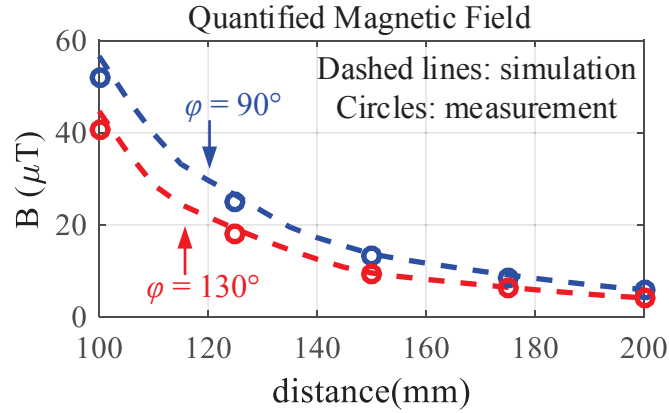
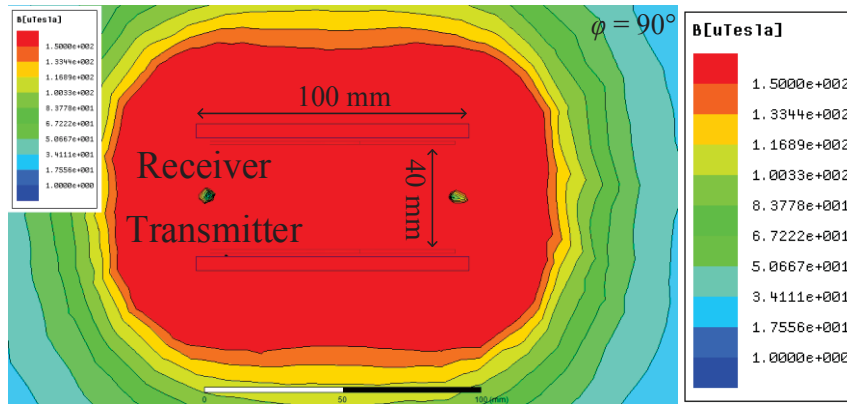
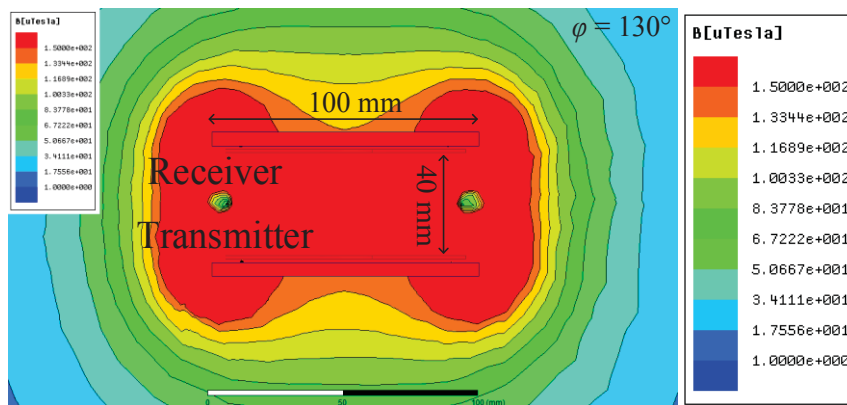


Figure 6-21. Comparison of the quantified magnetic field along radial axis in Figure 6-19, between $\phi = 90^\circ$ and $\phi = 130^\circ$. The dashed lines are from simulation using Ansys Maxwell. The circles are from measurement.



(a)



(b)

Figure 6-22. Magnitudes of magnetic field around coils from finite-element simulation: (a) $\phi = 90^\circ, \theta = 90^\circ$; (b) $\phi = 130^\circ, \theta = 50^\circ$.

6.6. Summary

The phases of winding currents are controlled to attenuate the stray magnetic field around IPT coils. The relationship between magnetic fields and phases of winding currents are derived from diagrams of phasors, by decomposing the field to the components in the axial and radial directions. The dual-side-controlled converter is applied for the circuit realization. The magnitudes of winding currents are controlled by pulse-widths of inverter voltage and rectifier voltage, while the phases of winding currents are controlled by phases of the voltages.

The effectiveness of this method was verified with a 3.3 kW IPT system using finite-element simulation and with a 100 W IPT system in experiment. Compared to the conventional series-series IPT with 90° phase difference between winding currents, stray magnetic field was attenuated by up to 30% and 40% when the phase differences of winding currents are 50° and 40° , respectively.

Chapter 7. Conclusions

7.1. Introduction

This study focuses on the synergetic attenuation of the stray magnetic field. Three methods are discussed to attenuate the stray magnetic field around the IPT coils. The first method is to tune the physical parameters of the winding, such as the inner radii, outer radii, distribution of the turns, and types of the litz wires. The second method is to add metal shields with litz wires around the IPT coils. The third method is to control the phases of winding currents.

The efficiency and stray magnetic field are optimized simultaneously for the IPT coils. Pareto front is used to realize the multi-objective optimization. The optimal designs are selected along the fronts. The performances of coils with different shield structures are compared with the Pareto fronts as well.

In this dissertation, a fast method to derive the Pareto front is demonstrated, using the lumped-loop model. The windings are replaced by several lumped loops. As long as the number of turns for each loop is known, the efficiency and magnetic field are calculated directly from the permeance matrices and current-to-field matrices. The Pareto front is derived after all the possible numbers of turns for the lumped loops are swept in calculation. Only tens of simulations are required to derive the matrices. There is no need to run the parametric sweep in finite-element simulation. This makes the optimization much faster without losing the accuracy.

An analytical method is introduced to calculate the proximity-effect resistance of the planar coils with ferrite plate, which is suitable to work together with the fast optimization. In this method, the ferrite plate is replaced by the mirrored turns according to the method of image. The

magnetic field across each turn, which is essential to calculate the proximity-effect resistance, is then derived from Ampere's Law and Biot-Savart Law.

7.2. Main Contributions and Conclusions

1. Fast optimization of efficiency and stray magnetic field using lumped-loop model.

Pareto front is applied for the synergetic attenuation of stray magnetic field. A faster method to derive the Pareto front using lumped-loop model is described. Only tens of simulations are required during the entire procedure, so this method is much faster than the conventional method which requires thousands of simulations for parametric sweep. The accuracy is verified with experimental measurement of the fabricated coils. The coil-to-coil efficiency from calculation is the same as the measurement, and the difference for stray magnetic field is less than 12.5%.

2. Calculation of proximity-effect resistance for IPT coils with ferrite plate.

The proximity-effect resistance of the litz wire in the planar coil with ferrite plate is calculated analytically. The objective of this calculation method is to work together with the fast optimization. The essence of the method is to replace the ferrite plate with mirrored turns according to the method of image. The magnetic field across each turn, which is critical to calculate the proximity-effect resistance, is then calculated from Ampere's Law and Biot-Savart Law. An exemplary planar coil was fabricated and tested. Its winding resistance was measured with impedance analyzer up to 200 kHz. The difference of its proximity-effect resistance is less than 15% between calculation and measurement.

3. Attenuation of stray magnetic field with litz shield.

Litz shield is able to attenuate the stray magnetic field with smaller shield loss compared to the conventional metal shield. This is because the shield current is more uniformly distributed. The increased weight due to the litz shield is negligible. Equivalent circuit models are derived to

analyze the two categories of litz shields: shorted litz shield and driven litz shield. The fast method with lumped-loop model is used to derive the Pareto front of coil-to-coil efficiency versus stray magnetic field for coils with litz shield. Coils with different shields were fabricated and measured in experiment. Both calculation and measurement show that shorted litz shield is most effective for field attenuation. In the exemplary system, with all the shields designed for the same efficiency, shorted litz shield attenuated the stray magnetic field by up to 65%.

4. Attenuation of stray magnetic field by controlling phases of winding currents.

Phases of winding currents are controlled to attenuate the stray magnetic field around IPT coils. The relationship between magnetic fields and phases of winding currents are derived from diagrams of phasors, by decomposing the field to the components in the axial and radial directions. The dual-side-controlled converter is applied for the circuit realization. The effectiveness of this method was verified using a 3.3 kW IPT system based on finite-element simulation and a 100 W IPT system in experiment. Compared to conventional series-series IPT with 90° phase difference between winding currents, stray magnetic field was attenuated by up to 30% and 40% when phases differences of winding currents are 50° and 40° , respectively.

5. Systematical design of IPT coils to maximize efficiency.

A sequential, non-iterative method is described to design the IPT coils for desired power transferability and efficiency. This is realized when the stray magnetic field is not considered. In this method, the electrical parameters were normalized, and the normalized parameters are designed systematically to meet the requirement of power transferability and efficiency. The physical realization of the designed electrical parameters was optimized by parametric sweep in finite-element simulation. In order to prove the effectiveness of the sequential design, coils for a 3.3 kW series-series IPT system were designed, built and tested. The measured output voltage

(200 – 400 V for 400 V input) and the coils' efficiency (98.9% at peak power) met the design specifications.

List of Publications

Journal Papers

- [1] **Ming Lu**, Khai D. T. Ngo, M. Filippa and W. Bicknell, "Model for Electromagnetic Actuator with Significant Fringing Using Minimal Fitting Parameters," in *IEEE Transactions on Magnetics*, vol. 51, no. 1, pp. 1-7, Jan. 2015.
- [2] **Ming Lu** and Khai D. T. Ngo, "Systematic Design of Coils in Series-Series Inductive Power Transfer for Power Transferability and Efficiency," in *IEEE Transactions on Power Electronics*, accepted.
- [3] **Ming Lu** and Khai D. T. Ngo, "A Fast Method to Optimize Efficiency and Stray Magnetic Field for Inductive-Power-Transfer Coils Using Lumped-loop Model", in *IEEE Transactions on Power Electronics*, accepted.
- [4] **Ming Lu** and Khai D. T. Ngo, "Attenuation of Stray Magnetic Field in Inductive Power Transfer by Controlling Phases of Windings' Currents", in *IEEE Transactions on Magnetics*, accepted.

Conference Papers

- [1] **Ming Lu** and Khai D. T. Ngo, "Sequential Design for Coils in Series-Series Inductive Power Transfer Using Normalized Parameters," *2016 IEEE PELS Workshop on Emerging Technologies: Wireless Power (WoW)*, Knoxville, TN, 2016, pp. 1-6.
- [2] **Ming Lu** and Khai D. T. Ngo, "Pareto Fronts for Coils' Efficiency Versus Stray Magnetic Field in Inductive Power Transfer," *2016 IEEE PELS Workshop on Emerging Technologies: Wireless Power (WoW)*, Knoxville, TN, 2016, pp. 1-5.

- [3] **Ming Lu** and Khai D. T. Ngo, "Synergetic optimization of efficiency and stray magnetic field for planar coils in inductive power transfer using matrix calculation," *2017 IEEE Applied Power Electronics Conference and Exposition (APEC)*, Tampa, FL, USA, 2017, pp. 3654-3660.
- [4] **Ming Lu** and Khai D. T. Ngo, "Comparison of passive shields for coils in inductive power transfer," *2017 IEEE Applied Power Electronics Conference and Exposition (APEC)*, Tampa, FL, USA, 2017, pp. 1419-1424.
- [5] **Ming Lu** and Khai D. T. Ngo, "Analytical Method to Calculate Winding Resistance of Litz Wire for Planar Coil with Ferrite Plate in Inductive Power Transfer", *2017 IEEE Energy Conversion Congress and Exposition (ECCE)*, Cincinnati, OH, 2017, accepted.
- [6] **Ming Lu** and Khai D. T. Ngo, "Attenuation of Stray Magnetic Field in Inductive Power Transfer by Controlling Phases of Winding Currents", *2017 IEEE Energy Conversion Congress and Exposition (ECCE)*, Cincinnati, OH, 2017, accepted.

Appendix A. Matlab Code for Synergetic Optimization

A.1. Coils without Shield

The following Matlab code is used to derive the Pareto front for the design example in Section 3.5.

```
% Synergetic optimization of coils with no shield (NS)
clc;
clear;
close all;
```

1.1. Import data

```
% Litz wire datasheet
Rlitz=xlspread('Litz Wire Datasheet','38AWG','F3:F14'); % DCR
Dlitz=xlspread('Litz Wire Datasheet','38AWG','E3:E14')/1000; % Diameter
Nlitz=xlspread('Litz Wire Datasheet','38AWG','A3:A14'); % Strand number

% Field matrix, Brms with 1 Arms current in TX only
MatrixB100=xlspread('FieldMatrix.xls','Field','B2:K4')/sqrt(2); %%% rms

% Inductance Matrix (Unit: H)
MatrixL=xlspread('InductanceMatrix.xls','Inductance','B2:K11')/1000;
MatrixM=xlspread('InductanceMatrix.xls','Inductance','B17:K26')/1000;
```

1.2. System parameters

```
% Lumped-Loop model
Rstep=4.2; % spacing between adjacent loops, unit: m
% length of each lumped loop
lpt=2*pi*[47.9 47.9-Rstep*1 47.9-Rstep*2 47.9-Rstep*3 47.9-Rstep*4 ...
          47.9-Rstep*5 47.9-Rstep*6 47.9-Rstep*7 47.9-Rstep*8 47.9-Rstep*9]/1000;
spacing=0.2/1000; % allowed maximum spacing between turns

% System specifications
fs=100e3; % switching frequency
w=2*pi*fs;
ACFactor=1.2; % factor to approximate total resistance
Pout=100; % output power
Vout=35; % output voltage
RLac=(8/pi^2)*(Vout^2/Pout); % equivalent load resistance
I2=sqrt(Pout/RLac); % receiver current
```

1.3. Optimization iterations

```

%%%%%%%%%%%%%%%%%%%%%%%%%%%%%%%%%%%%%%%%%%%%%%%%%%%%%%%%%%%%%%%%%%%%%%%% structure of loops %%%%%%%%%
%Outermost loop                                Innermost loop%
% IL1 IL2 IL3 IL4 IL5 IL6 IL7 IL8 IL9 IL10
%%%%%%%%%%%%%%%%%%%%%%%%%%%%%%%%%%%%%%%%%%%%%%%%%%%%%%%%%%%%%%%%%%%%%%%% structure of loops %%%%%%%%%
x=0;
a_NS=size(Nlitz);    % Sweep the strands number

for NO=1:5    % sweep outermost loops: 1, 2, 3, 4, 5
    for NI=(NO+3):10    % sweep inner most loops: NO+3, ..., 10

        % equivalent outer radii
        Router=(50-(NO-1)*Rstep)/1000;
        % equivalent inner radii
        Ri nner=(50-NI *Rstep)/1000;
        % equivalent winding width
        Wi dth=Router-Ri nner;

        % sweep Litz wire
        for Litz_NS=1:a_NS(1)
            % Max turns with the selected litz wire
            Nmax_NS= floor(Wi dth/(Di litz(Litz_NS)+spacing));
            % sweep the total number of turns
            for N_NS=1:Nmax_NS
                % Max diameter of each turn
                TurnsWi dth=Wi dth/N_NS;
                % Turns number of each loop
                TurnsPerLoop=(Rstep/1000)/TurnsWi dth;

                % Assign turns for each loop
                for i=1:10
                    if (i < NO || i > NI)
                        IL(i)=0;
                    else
                        IL(i)=TurnsPerLoop;
                    end
                end

                % turns vector (IL(1): outermost; IL(10): innermost)
                turns=[IL(1) IL(2) IL(3) IL(4) IL(5) IL(6) ...
                    IL(7) IL(8) IL(9) IL(10)];

                % calculation of inductances
                Leq=turns*Matri xL*transpose(turns);
                Meq=turns*Matri xM*transpose(turns);
                keq=Meq/Leq;

                % transmitter current
                I1=RLac/(2*pi *fs*Meq)*I2;

                if (Meq<16e-6) && (Meq>6e-6)

```

Appendix

```
% calculation of stray magnetic field
% stray magnetic field generated by the transmitter
B100_tx=MatrixB100*I1*transpose(turns);
% stray magnetic field generated by the receiver
B100_rx=MatrixB100*I2*transpose(turns);
% RMS values of BX, BY, and BZ
% BX, BY, BZ are generated by TX and RX together
B100_X=sqrt(B100_tx(1)^2+B100_rx(1)^2);
B100_Y=sqrt(B100_tx(2)^2+B100_rx(2)^2);
B100_Z=sqrt(B100_tx(3)^2+B100_rx(3)^2);
% quantified magnetic field
B100mag=sqrt(B100_X^2+B100_Y^2+B100_Z^2);

x=x+1;
% total length of wires
Length=Ipt*transpose(turns);
% simplified results of resistance
r=Rlitz(Litz_NS)*Length*ACFactor;
%
eff=1/(1+r/RLac+r/RLac*(1+r/RLac)^2/(w*Meq/RLac)^2);

% save all the results in the array optimization_NS
% total number of turns
optimization_NS(x, 1)=N_NS;
% outer radii
optimization_NS(x, 2)=Router;
% inner radii
optimization_NS(x, 3)=Rinner;
% strand number of litz wire
optimization_NS(x, 4)=Nlitz(Litz_NS);
% maximum diameter of each turn
optimization_NS(x, 5)=TurnsWidth;
% quantified magnetic field
optimization_NS(x, 6)=B100mag;
% self inductances
optimization_NS(x, 8)=Leq;
% mutual inductances
optimization_NS(x, 9)=Meq;
% coupling coefficient
optimization_NS(x, 10)=Meq/Leq;
% total length of wire
optimization_NS(x, 11)=Length;
% winding resistance
optimization_NS(x, 12)=r;
% coil-to-coil efficiency
optimization_NS(x, 13)=eff;
% transmitter current
optimization_NS(x, 14)=I1;
% winding distribution
optimization_NS(x, 15 : 24)=[IL(1) IL(2) IL(3) ...
    IL(4) IL(5) IL(6) IL(7) IL(8) IL(9) IL(10)];

end
end
```

```

%           sprintf(' NO=%d, NI =%d, x=%d' , NO, NI , x)
    end
end
end

```

1.4. Derive the Pareto front

```

ss_NS=si ze(opti mi zati on_NS(: , 10));
i =0;

% choose the parameters from optimization_NS array
for pp=1: ss_NS(1)
    if (i snan(opti mi zati on_NS(pp, 10)) == 0)
        i =i +1;
        B100_NS(i)=opti mi zati on_NS(pp, 6);
        eff_NS(i)=opti mi zati on_NS(pp, 13);
        TunrNumber_NS(i)=opti mi zati on_NS(pp, 1);
        Li tzType_NS(i)=opti mi zati on_NS(pp, 4);
        OuterRadi i_NS(i)=opti mi zati on_NS(pp, 2);
        InnerRadi i_NS(i)=opti mi zati on_NS(pp, 3);
        L_NS(i)=opti mi zati on_NS(pp, 8);
        M_NS(i)=opti mi zati on_NS(pp, 9);
        k_NS(i)=opti mi zati on_NS(pp, 10);
        I 1_NS(i)=opti mi zati on_NS(pp, 14);
    end
end

% horizontal axis: stray magnetic field
x_NS=transpose(B100_NS);
% vertical axis: efficiency
y_NS=1- transpose(eff_NS);

% derive the Pareto front using 'paretofront' function
front_NS=paretofront([x_NS y_NS]);

% number of points along the Pareto front
si ze_NS=si ze(front_NS);
i =0;
% find out the parameters of the optimal point along Pareto front
for a=1: si ze_NS(1)
    if (front_NS(a) == 1)
        i =i +1;
        Pareto_B100_NS(i)=B100_NS(a);
        Pareto_eff_NS(i)=eff_NS(a);
        Pareto_TunrNumber_NS(i)=TunrNumber_NS(a);
        Pareto_Li tzType_NS(i)=Li tzType_NS(a);
        Pareto_OuterRadi i_NS(i)=OuterRadi i_NS(a);
        Pareto_InnerRadi i_NS(i)=InnerRadi i_NS(a);
        Pareto_L_NS(i)=L_NS(a);
        Pareto_M_NS(i)=M_NS(a);
        Pareto_k_NS(i)=k_NS(a);
        Pareto_I 1_NS(i)=I 1_NS(a);
    end
end

```

```
end
end
```

1.5. Plot the Pareto front

```
% make the results in a sequence (smaller B to larger B)
% for plot purpose
[ParetoSort_B100_NS, I_NS]=sort(Pareto_B100_NS);
si ze2_NS=si ze(Pareto_B100_NS);
for a=1: si ze2_NS(2)
    i =I_NS(a);
    ParetoSort_NS(a, 1)=Pareto_B100_NS(i);
    ParetoSort_NS(a, 2)=Pareto_eff_NS(i);
    ParetoSort_NS(a, 3)=Pareto_TunrNumber_NS(i);
    ParetoSort_NS(a, 4)=Pareto_Li tzType_NS(i);
    ParetoSort_NS(a, 5)=Pareto_OuterRadi i_NS(i);
    ParetoSort_NS(a, 6)=Pareto_I nnerRadi i_NS(i);
    ParetoSort_NS(a, 7)=Pareto_L_NS(i);
    ParetoSort_NS(a, 8)=Pareto_M_NS(i);
    ParetoSort_NS(a, 9)=Pareto_k_NS(i);
    ParetoSort_NS(a, 10)=Pareto_I 1_NS(i);
end

% Curvefi tting
coeffi ci ent_NS=pol yfi t(ParetoSort_NS(:, 1), ParetoSort_NS(:, 2), 4);
CF_NS=pol yval (coeffi ci ent_NS, ParetoSort_NS(:, 1));

hFi g=fi gure(1)
set(hFi g, 'Posi ti on', [100 300 350 200])
scatter(B100_NS, eff_NS, 'b')
hold on;
h=pl ot(ParetoSort_NS(:, 1), CF_NS);
set(h, 'Col or', 'r', 'Li neWi dth', 3, 'Li neStyl e', '-');
hold off;
grid;
set(gca, 'XLi m', [45 70]);
set(gca, 'YLi m', [0.8 1]);
xx=xl abel ('B at 100 mm (\mu T)', 'FontWei ght', 'bol d', 'Col or', 'k', 'Fontsi ze', 10);
yy=yl abel ('Coil Effi ci ency', 'FontWei ght', 'bol d', 'Col or', 'k', 'Fontsi ze', 10);
set(gca, 'fontname', 'Times New Roman', 'Fontsi ze', 10)
set(xx, 'Fontname', 'Times new roman', 'fontwei ght', 'b');
set(yy, 'Fontname', 'Times new roman', 'fontwei ght', 'b');
```

A.2. Coils with Shorted Litz Shield

The following Matlab code is used to derive the Pareto front for the design example in Section 5.4.

Appendix

```
clc
clear
close all
```

2.1. Import data

```
Rlitz=xlspread('Litz Wire Datasheet','38AWG','F6:F14'); % DCR
Dlitz=xlspread('Litz Wire Datasheet','38AWG','E6:E14')/1000; % Diameter
Nlitz=xlspread('Litz Wire Datasheet','38AWG','A6:A14'); % Strand number

% Field matrices, Brms with 1 Arms current in TX only
MatrixB100=xlspread('FieldMatrix.xls','Field','B2:S4')/sqrt(2); %% rms
MatrixB150=xlspread('FieldMatrix.xls','Field','B7:S9')/sqrt(2); %% rms

% Permeance Matrices (Unit: H)
MatrixL=xlspread('InductanceMatrix.xls','Inductance','B2:O15')/1000;
MatrixM=xlspread('InductanceMatrix.xls','Inductance','B17:O30')/1000;

% Permeance matrices for equivalent circuit model with four coils
Matrix1_Ltxsh=MatrixL(11:14,11:14);
Matrix1_Ltx=MatrixL(1:10,1:10);

Matrix1_Mtx_rxsh=MatrixM(11:14,1:10);
Matrix1_Mtx_rx=MatrixM(1:10,1:10);
Matrix1_Mtx_txsh=MatrixL(11:14,1:10);
Matrix1_Mtxsh_rxsh=MatrixM(11:14,11:14);

Matrix1_Btx100=MatrixB100(1:3,1:10);
Matrix1_Btxsh100=MatrixB100(1:3,11:14);
Matrix1_Brxsh100=MatrixB100(1:3,15:18);

Matrix1_Btx150=MatrixB150(1:3,1:10);
Matrix1_Btxsh150=MatrixB150(1:3,11:14);
Matrix1_Brxsh150=MatrixB150(1:3,15:18);

% Objectives of field attenuation
turns=[3 3 3 3 3 3 1 0 0 0 ... % Inner loops 1 - 10
        0 0 0 0 0 0 0 0]; % Litz wire ring
B100=MatrixB100*5*transpose(turns);
B150=MatrixB150*5*transpose(turns);
B100mag_ori ginal =sqrt(B100(1)^2+B100(2)^2+B100(3)^2);
B150mag_ori ginal =sqrt(B150(1)^2+B150(2)^2+B150(3)^2);
```

2.2. System parameters

```
Rstep=4.2/1000; % spacing between adjacent loops
% length of each lumped loop
lpt=2*pi*[47.9 47.9-4.2*1 47.9-4.2*2 47.9-4.2*3 47.9-4.2*4 ...
          47.9-4.2*5 47.9-4.2*6 47.9-4.2*7 47.9-4.2*8 47.9-4.2*9 ...
```

Appendix

```
52. 1/(2*pi)*8 (52. 1+4. 2*1)/(2*pi)*8 (52. 1+4. 2*2)/(2*pi)*8 ...
(52. 1+4. 2*3)/(2*pi)*8]/1000;
spacing=0. 1/1000; % allowed maximum spacing between turns

% System specifications
f=100e3; % switching frequency
ACFactor=1. 2; % factor to approximate total resistance
Pout=100; % output power
Vout=35; % output voltage
R=(8/pi^2)*(Vout^2/Pout); % equivalent load resistance
Irx=sqrt(Pout/R); % receiver current
```

2.3. Optimization iterations

```
x=0;
a_SLS=size(NIitz); % Sweep of Litz wire

for NO=1:5 % sweep outermost loops of winding: 1, 2, 3, 4, 5
    for NI=(NO+3):10 % sweep inner most loops of winding: NO+3, ..., 10
        % equivalent outer radii
        Router=(50 - (NO - 1) * 4. 2) / 1000;
        % equivalent inner radii
        Rinner=(50 - NI * 4. 2) / 1000;
        % equivalent winding width
        Width=Router - Rinner;

        % sweep Litz wire
        for Litz_SLS=1:a_SLS(1)
            % Max turns with the selected litz wire
            Nmax_SLS= floor(Width / (DIitz(Litz_SLS)+spacing));
            % sweep the total number of turns
            for N_SLS=1:Nmax_SLS
                % Max diameter of each turn for winding
                TurnsWidth=Width / N_SLS;
                % Turns number of each loop for winding
                TurnsPerLoop=Rstep / TurnsWidth;
                % Max diameter of each turn for litz shield
                FALMaxTurns=fix(Rstep / TurnsWidth);

                % Assign turns for each loop
                for i=1:10
                    if (i < NO || i > NI)
                        IL(i)=0;
                    else
                        IL(i)=TurnsPerLoop;
                    end
                end

                % turns vectors
                % Winding: IL(1): outermost; IL(10): innermost
                % Shield: FAL1: closest to winding; FAL4: outermost
                for FAL1=0:FALMaxTurns
```

Appendix

```

for FAL2=0: FALMaxTurns
for FAL3=0: FALMaxTurns
for FAL4=0: FALMaxTurns
    % turns vector of TX winding
    turns_tx=[IL(1) IL(2) IL(3) IL(4) IL(5) ...
              IL(6) IL(7) IL(8) IL(9) IL(10)];
    % turns vector of RX winding
    turns_rx=[IL(1) IL(2) IL(3) IL(4) IL(5) ...
              IL(6) IL(7) IL(8) IL(9) IL(10)];
    % turns vector of TX shield
    turns_txsh=[FAL1 FAL2 FAL3 FAL4];
    % turns vector of RX shield
    turns_rxsh=[FAL1 FAL2 FAL3 FAL4];

    % calculate the inductances
    % for the equivalent circuit with four coupled coils
    Ltxsh=turns_txsh*Matrix1_Ltxsh*transpose(turns_txsh);
    Ltx=turns_tx*Matrix1_Ltx*transpose(turns_tx);
    Lrxsh=Ltxsh;
    Lrx=Ltx;
    Mtxsh_rxsh=turns_txsh*Matrix1_Mtxsh_rxsh*transpose(turns_txsh);
    Mtx_rx=turns_tx*Matrix1_Mtx_rx*transpose(turns_tx);
    Mtx_rxsh=turns_rxsh*Matrix1_Mtx_rxsh*transpose(turns_tx);
    Mtx_txsh=turns_txsh*Matrix1_Mtx_txsh*transpose(turns_tx);
    Mrx_txsh=Mtx_rxsh;
    Mrx_rxsh=Mtx_txsh;

    % calculate equivalent Leq, Meq
    % for the equivalent circuit with two coils
    Leq=Ltx-(Ltxsh*Mtx_rxsh^2+Ltxsh*Mtx_txsh^2-2 ...
             *Mtxsh_rxsh*Mtx_txsh*Mtx_rxsh)/(Ltxsh^2-Mtxsh_rxsh^2);
    Meq=Mtx_rx-Mtx_txsh*(Ltxsh*Mtx_rxsh-Mtx_txsh*Mtxsh_rxsh) ...
         /(Ltxsh^2-Mtxsh_rxsh^2)-Mtx_rxsh* ...
         (Ltxsh*Mtx_txsh-Mtx_rxsh*Mtxsh_rxsh)/(Ltxsh^2-Mtxsh_rxsh^2);
    keq=Meq/Leq;

    if (Meq<16e-6) && (Meq>6e-6)

        % calculation of currents
        % transmitter current
        Itx=R/(2*pi*f*Meq)*Irx;
        % current of transmitter shield
        % Itxsh_tx: the part in phase with Itx
        Itxsh_tx=(Mtx_txsh*Lrxsh+Mtx_rxsh*Mtxsh_rxsh)/ ...
                 (Ltxsh*Lrxsh+Mtxsh_rxsh^2)*Itx;
        % Irxsh_tx: the part in phase with Irx
        Irxsh_tx=(Mrx_txsh*Lrxsh+Mrx_rxsh*Mtxsh_rxsh)/ ...
                 (Ltxsh*Lrxsh+Mtxsh_rxsh^2)*Itx;

        % current of receiver shield
        % Itxsh_rx: the part in phase with Itx
        Itxsh_rx=(Mtx_rxsh*Ltxsh+Mtx_txsh*Mtxsh_rxsh)/ ...
                 (Ltxsh*Lrxsh+Mtxsh_rxsh^2)*Itx;
        % Irxsh_rx: the part in phase with Irx

```

Appendix

```

Irxsh_rx=(Mrx_rxsh*Ltxsh+Mrx_txsh*Mtxsh_rxsh)/ ...
(Ltxsh*Lrxsh+Mtxsh_rxsh^2)*Irx;

% magnetic field generated by TX
B100_tx=Matrix1_Btx100*I tx*transpose(turns_tx);
% magnetic field generated by TXsh
% in phase with I tx
B100_txsh_tx=Matrix1_Btxsh100*(I txsh_tx)*transpose(turns_txsh);
% magnetic field generated by RXsh
% in phase with I tx
B100_rxsh_tx=Matrix1_Brxsh100*(I rxsh_tx)*transpose(turns_rxsh);

% magnetic field generated by RX
B100_rx=Matrix1_Btx100*I rx*transpose(turns_tx);
% magnetic field generated by TXsh
% in phase with I rx
B100_txsh_rx=Matrix1_Btxsh100*(I txsh_rx)*transpose(turns_txsh);
% magnetic field generated by RXsh
% in phase with I rx
B100_rxsh_rx=Matrix1_Brxsh100*(I rxsh_rx)*transpose(turns_rxsh);

% magnetic field components, in phase with I tx
B100_I tx=B100_tx+B100_txsh_tx+B100_rxsh_tx;
% magnetic field components, in phase with I rx
B100_I rx=B100_rx+B100_txsh_rx+B100_rxsh_rx;

% quantified magnetic field
% I tx and I rx have 90 degrees phase shift
B100mag=sqrt(B100_I tx(1)^2+B100_I tx(2)^2+B100_I tx(3)^2 ...
+B100_I rx(1)^2+B100_I rx(2)^2+B100_I rx(3)^2);

% to calculate the length of winding and litz
% shields
turns1=[IL(1) IL(2) IL(3) IL(4) IL(5) IL(6) ...
IL(7) IL(8) IL(9) IL(10) 0 0 0 0];
turns2=[0 0 0 0 0 0 0 0 0 0 abs(FAL1)...
abs(FAL2) abs(FAL3) abs(FAL4)];
Length=I pt*transpose(turns1);
Length2=I pt*transpose(turns2);

% approximate the resistances
rtx=Rlitz(Litz_SLS) * Length * ACFactor;
rsh1=Rlitz(Litz_SLS) * Length2 * ACFactor;
rrx=rtx;
rsh2=rsh1;
r1=rtx+(Mtxsh_rxsh*Mtx_rxsh-Mtx_txsh*Lrxsh)^2 ...
/(Ltxsh*Lrxsh-Mtxsh_rxsh^2)^2*rsh1 ...
+(Mtxsh_rxsh*Mtx_txsh-Mtx_rxsh*Ltxsh)^2 ...
/(Ltxsh*Lrxsh-Mtxsh_rxsh^2)^2*rsh2;
r2=r1;

% coil-to-coil efficiency
eff=1/(1+r2/R+r1/R*(r2+R)^2/(2*pi *f*Meq)^2);

```

Appendix

```
% Meet the requirement of field attenuation
if (B100mag<=B100mag_ori ginal) && (eff > 0.8)

    x=x+1;
    % turns of lumped loops for litz shield
    optimization_SLS(x, 1)=FAL1;
    optimization_SLS(x, 2)=FAL2;
    optimization_SLS(x, 3)=FAL3;
    optimization_SLS(x, 4)=FAL4;
    % total number of turns for the winding
    optimization_SLS(x, 5)=N_SLS;
    % loop for outer radii
    optimization_SLS(x, 6)=Router;
    % loop for inner radii
    optimization_SLS(x, 7)=Rinner;
    % strand number
    optimization_SLS(x, 8)=Nlitz(Litz_SLS);
    % width per turn
    optimization_SLS(x, 9)=TurnsWidth;
    % quantified magnetic field
    optimization_SLS(x, 10)=B100mag;
    % equivalent inductances
    optimization_SLS(x, 12)=Leq;
    optimization_SLS(x, 13)=Meq;
    optimization_SLS(x, 14)=Meq/Leq;
    % length of winding
    optimization_SLS(x, 15)=Length;
    % resistance of winding
    optimization_SLS(x, 16)=r1;
    % length of shield
    optimization_SLS(x, 17)=Length2;
    % coil-to-coil efficiency
    optimization_SLS(x, 19)=eff;
    % distribution of turns
    optimization_SLS(x, 23 : 32)=[IL(1) IL(2) IL(3) IL(4) IL(5)
IL(6) IL(7) IL(8) IL(9) IL(10)];
        end
    end
end
end
end
end
end
    end
    sprintf(' NO=%d, NI =%d, x=%d', NO, NI , x)
end
end
end
```

2.4. Derive Pareto Front

```
ss_SLS=si ze(optimization_SLS(:, 10));
i =0;
```

Appendix

```
for pp=1:ss_SLS(1)
    if (i snan(opti mi zati on_SLS(pp, 10)) == 0)
        i=i+1;
        B100_SLS(i)=opti mi zati on_SLS(pp, 10);
        eff_SLS(i)=opti mi zati on_SLS(pp, 19);
        TunrNumber_SLS(i)=opti mi zati on_SLS(pp, 5);
        Li tzType_SLS(i)=opti mi zati on_SLS(pp, 8);
        OuterRadi i_SLS(i)=opti mi zati on_SLS(pp, 6);
        InnerRadi i_SLS(i)=opti mi zati on_SLS(pp, 7);
        L_SLS(i)=opti mi zati on_SLS(pp, 12);
        M_SLS(i)=opti mi zati on_SLS(pp, 13);
        k_SLS(i)=opti mi zati on_SLS(pp, 14);
        FAL1_SLS(i)=opti mi zati on_SLS(pp, 1);
        FAL2_SLS(i)=opti mi zati on_SLS(pp, 2);
        FAL3_SLS(i)=opti mi zati on_SLS(pp, 3);
        FAL4_SLS(i)=opti mi zati on_SLS(pp, 4);
        l txsh_SLS(i)=opti mi zati on_SLS(pp, 20);
        l rxsh_SLS(i)=opti mi zati on_SLS(pp, 21);
    end
end

% derive the points along Pareto fronts
x_SLS=transpose(B100_SLS);
y_SLS=1 - transpose(eff_SLS);
front_SLS=paretofront([x_SLS y_SLS]);
si ze_SLS=si ze(front_SLS);

i=0;
for a=1:si ze_SLS(1)
    if (front_SLS(a) == 1)
        i=i+1;
        Pareto_B100_SLS(i)=B100_SLS(a);
        Pareto_eff_SLS(i)=eff_SLS(a);
        Pareto_TunrNumber_SLS(i)=TunrNumber_SLS(a);
        Pareto_Li tzType_SLS(i)=Li tzType_SLS(a);
        Pareto_OuterRadi i_SLS(i)=OuterRadi i_SLS(a);
        Pareto_InnerRadi i_SLS(i)=InnerRadi i_SLS(a);
        Pareto_L_SLS(i)=L_SLS(a);
        Pareto_M_SLS(i)=M_SLS(a);
        Pareto_k_SLS(i)=k_SLS(a);
        Pareto_FAL1_SLS(i)=FAL1_SLS(a);
        Pareto_FAL2_SLS(i)=FAL2_SLS(a);
        Pareto_FAL3_SLS(i)=FAL3_SLS(a);
        Pareto_FAL4_SLS(i)=FAL4_SLS(a);
        Pareto_l txsh_SLS(i)=l txsh_SLS(a);
        Pareto_l rxsh_SLS(i)=l rxsh_SLS(a);
    end
end
```

2.5. Plot the Pareto front

```
[ParetoSort_B100_SLS, I_SLS]=sort(Pareto_B100_SLS);
si ze2_SLS=si ze(Pareto_B100_SLS);
for a=1: si ze2_SLS(2)
    i =I_SLS(a);
    ParetoSort_SLS(a, 1)=Pareto_B100_SLS(i);
    ParetoSort_SLS(a, 2)=Pareto_eff_SLS(i);
    ParetoSort_SLS(a, 3)=Pareto_TunrNumber_SLS(i);
    ParetoSort_SLS(a, 4)=Pareto_Li tzType_SLS(i);
    ParetoSort_SLS(a, 5)=Pareto_OuterRadi i_SLS(i);
    ParetoSort_SLS(a, 6)=Pareto_InnerRadi i_SLS(i);
    ParetoSort_SLS(a, 7)=Pareto_L_SLS(i);
    ParetoSort_SLS(a, 8)=Pareto_M_SLS(i);
    ParetoSort_SLS(a, 9)=Pareto_k_SLS(i);
    ParetoSort_SLS(a, 10)=Pareto_FAL1_SLS(i);
    ParetoSort_SLS(a, 11)=Pareto_FAL2_SLS(i);
    ParetoSort_SLS(a, 12)=Pareto_FAL3_SLS(i);
    ParetoSort_SLS(a, 13)=Pareto_FAL4_SLS(i);
    ParetoSort_SLS(a, 14)=Pareto_I txsh_SLS(i);
    ParetoSort_SLS(a, 15)=Pareto_I rxsh_SLS(i);
end

% curve fitting
coeffi ci ent_SLS=pol yfi t(ParetoSort_SLS(:, 1), ParetoSort_SLS(:, 2), 8);
CF_SLS=pol yval (coeffi ci ent_SLS, ParetoSort_SLS(:, 1));

hFi g=fi gure(1)
set(hFi g, 'Posi ti on', [100 300 350 200])
scatter(B100_SLS, eff_SLS, 'b')
hold on;
h=pl ot(ParetoSort_SLS(:, 1), CF_SLS);
set(h, 'Col or', 'r', 'Li neWi dth', 3, 'Li neStyl e', '-')
hold off;
grid;
set(gca, 'XLi m', [10 40]);
set(gca, 'YLi m', [0.8 1]);
xx=xl abel ('B at 100 mm (\mu T)', 'FontWei ght', 'bol d', 'Col or', 'k', 'Fontsi ze', 10);
yy=yl abel ('Coi l Effi ci ency', 'FontWei ght', 'bol d', 'Col or', 'k', 'Fontsi ze', 10);
set(gca, 'fontname', 'Times New Roman', 'Fontsi ze', 10)
set(xx, 'Fontname', 'Times new roman', 'fontwei ght', 'b');
set(yy, 'Fontname', 'Times new roman', 'fontwei ght', 'b');
```

A.3. Coils with Driven Litz Shield

The following Matlab code is used to derive the Pareto front for the coils with driven litz shield. The specifications are the same as the design example in Section 5.4.

```

clc
clear
close all

```

3.1. Import data

```

% Litz wire datasheet
Rlitz=xlsread('Litz Wire Datasheet', '38AWG', 'F6:F14'); % DCR
Dlitz=xlsread('Litz Wire Datasheet', '38AWG', 'E6:E14')/1000; % Diameter
Nlitz=xlsread('Litz Wire Datasheet', '38AWG', 'A6:A14'); % Strand number

% Field matrices, Brms with 1 Arms current in TX only
MatrixB100=xlsread('FieldMatrix.xls', 'Field', 'B2:S4')/sqrt(2); %% rms
MatrixB150=xlsread('FieldMatrix.xls', 'Field', 'B7:S9')/sqrt(2); %% rms

% Permeance Matrices (Unit: H)
MatrixL=xlsread('InductanceMatrix.xls', 'Inductance', 'B2:O15')/1000;
MatrixM=xlsread('InductanceMatrix.xls', 'Inductance', 'B17:O30')/1000;

% Permeance matrices for equivalent circuit model with four coils
Matrix1_Ltxsh=MatrixL(11:14, 11:14);
Matrix1_Ltx=MatrixL(1:10, 1:10);

Matrix1_Mtx_rxsh=MatrixM(11:14, 1:10);
Matrix1_Mtx_rx=MatrixM(1:10, 1:10);
Matrix1_Mtx_txsh=MatrixL(11:14, 1:10);
Matrix1_Mtxsh_rxsh=MatrixM(11:14, 11:14);

Matrix1_Btx100=MatrixB100(1:3, 1:10);
Matrix1_Btxsh100=MatrixB100(1:3, 11:14);
Matrix1_Brxsh100=MatrixB100(1:3, 15:18);

Matrix1_Btx150=MatrixB150(1:3, 1:10);
Matrix1_Btxsh150=MatrixB150(1:3, 11:14);
Matrix1_Brxsh150=MatrixB150(1:3, 15:18);

% Objectives of field attenuation
turns=[3 3 3 3 3 3 1 0 0 0 ... % Inner loops 1 - 10
        0 0 0 0 0 0 0 0]; % Litz wire ring
B100=MatrixB100*5*transpose(turns);
B150=MatrixB150*5*transpose(turns);
B100mag_ori ginal =sqrt(B100(1)^2+B100(2)^2+B100(3)^2);
B150mag_ori ginal =sqrt(B150(1)^2+B150(2)^2+B150(3)^2);

```

3.2. System parameters

```

% Lumped-loop model
Rstep=4.2/1000; % spacing between adjacent loops
% length of each lumped loop

```

Appendix

```
lpt=2*pi*[47.9 47.9-4.2*1 47.9-4.2*2 47.9-4.2*3 47.9-4.2*4 ...
47.9-4.2*5 47.9-4.2*6 47.9-4.2*7 47.9-4.2*8 47.9-4.2*9 ...
52.1/(2*pi)*8 (52.1+4.2*1)/(2*pi)*8 (52.1+4.2*2)/(2*pi)*8 ...
(52.1+4.2*3)/(2*pi)*8]/1000;
spacing=0.1/1000; % allowed maximum spacing between turns

% System specifications
f=100e3; % switching frequency
ACFactor=1.2; % factor to approximate total resistance
Pout=100; % output power
Vout=35; % output voltage
R=(8/pi^2)*(Vout^2/Pout); % equivalent load resistance
Irx=sqrt(Pout/R); % receiver current
```

3.3. Optimization iterations

```
x=0;
a_DLS=size(Nlitz); % Sweep of Litz wire

for NO=1:5 % sweep outermost loops of winding: 1, 2, 3, 4, 5
    for NI=(NO+3):10 % sweep inner most loops of winding: NO+3, ..., 10
        % equivalent outer radii
        Router=(50 - (NO - 1) * 4.2) / 1000;
        % equivalent inner radii
        Rinner=(50 - NI * 4.2) / 1000;
        % equivalent winding width
        Width=Router - Rinner;

        % sweep Litz wire
        for Litz_DLS=1:a_DLS(1)
            % Max turns with the selected Litz wire
            Nmax_DLS= floor(Width / (Dlitz(Litz_DLS)+spacing));
            % sweep the total number of turns
            for N_DLS=1:Nmax_DLS
                % Max diameter of each turn for winding
                TurnsWidth=Width / N_DLS;
                % Turns number of each loop for winding
                TurnsPerLoop=Rstep / TurnsWidth;
                % Max diameter of each turn for Litz shield
                FALMaxTurns=fix(Rstep / TurnsWidth);

                % Assign turns for each loop
                for i=1:10
                    if (i < NO || i > NI)
                        IL(i)=0;
                    else
                        IL(i)=TurnsPerLoop;
                    end
                end

                % turns vectors
                % Winding: IL(1): outermost; IL(10): innermost
```

Appendix

```
% Shield: FAL1: closest to winding; FAL4: outermost
for FAL1=0: FALMaxTurns
for FAL2=0: FALMaxTurns
for FAL3=0: FALMaxTurns
for FAL4=0: FALMaxTurns
    % turns vector of TX winding
    turns_tx=[IL(1) IL(2) IL(3) IL(4) IL(5) ...
              IL(6) IL(7) IL(8) IL(9) IL(10)];
    % turns vector of RX winding
    turns_rx=[IL(1) IL(2) IL(3) IL(4) IL(5) ...
              IL(6) IL(7) IL(8) IL(9) IL(10)];
    % turns vector of TX shield
    turns_txsh=[FAL1 FAL2 FAL3 FAL4];
    % turns vector of RX shield
    turns_rxsh=[FAL1 FAL2 FAL3 FAL4];

    % calculate the inductances
    % for the equivalent circuit with four coupled coils
    Ltxsh=turns_txsh*Matri x1_Ltxsh*transpose(turns_txsh);
    Ltx=turns_tx*Matri x1_Ltx*transpose(turns_tx);
    Lrxsh=Ltxsh;
    Lrx=Ltx;
    Mtxsh_rxsh=turns_txsh*Matri x1_Mtxsh_rxsh*transpose(turns_txsh);
    Mtx_rx=turns_tx*Matri x1_Mtx_rx*transpose(turns_tx);
    Mtx_rxsh=turns_rxsh*Matri x1_Mtx_rxsh*transpose(turns_tx);
    Mtx_txsh=turns_txsh*Matri x1_Mtx_txsh*transpose(turns_tx);
    Mrx_txsh=Mtx_rxsh;
    Mrx_rxsh=Mtx_txsh;

    % calculate equivalent Leq, Meq
    % for the equivalent circuit with two coils
    Leq=Ltx-Ltxsh;
    Meq=Mtx_rx-Mtxsh_rxsh+Mtx_rxsh-Mrx_txsh;
    keq=Meq/Leq;

    if (Meq<16e-6) && (Meq>6e-6)

        % calculation of currents
        % transmitter current
        Itx=R/(2*pi*f*Meq)*Irx;
        % current of transmitter shield
        Itxsh=Itx;
        % current of receiver shield
        Irxsh=Irx;

        % magnetic field generated by TX
        B100_tx=Matri x1_Btx100*Itx*transpose(turns_tx);
        % magnetic field generated by TXsh
        B100_txsh=Matri x1_Btxsh100*(Itxsh)*transpose(turns_txsh);
        % magnetic field generated by RX
        B100_rx=Matri x1_Brx100*Irx*transpose(turns_rx);
        % magnetic field generated by RXsh
        B100_rxsh=Matri x1_Brxsh100*(Irxsh)*transpose(turns_rxsh);
```

Appendix

```

% magnetic field components, in phase with I tx
B100_I tx=B100_tx+B100_txsh;
% magnetic field components, in phase with I rx
B100_I rx=B100_rx+B100_rxsh;

% quantified magnetic field
% I tx and I rx have 90 degrees phase shift
B100mag=sqrt(B100_I tx(1)^2+B100_I tx(2)^2+B100_I tx(3)^2 ...
+B100_I rx(1)^2+B100_I rx(2)^2+B100_I rx(3)^2);

% to calculate the length of winding and litz
% shields
turns1=[IL(1) IL(2) IL(3) IL(4) IL(5) IL(6) ...
IL(7) IL(8) IL(9) IL(10) 0 0 0 0];
turns2=[0 0 0 0 0 0 0 0 0 0 abs(FAL1)...
abs(FAL2) abs(FAL3) abs(FAL4)];
Length=l pt*transpose(turns1);
Length2=l pt*transpose(turns2);

% approximate the resistances
rtx=Rlitz(Litz_DLS) * Length * ACFactor;
rsh1=Rlitz(Litz_DLS) * Length2 * ACFactor;
rrx=rtx;
rsh2=rsh1;
r1=rtx+(Mtxsh_rxsh*Mtx_rxsh-Mtx_txsh*Lrxsh)^2 ...
/(Ltxsh*Lrxsh-Mtxsh_rxsh^2)^2*rsh1 ...
+(Mtxsh_rxsh*Mtx_txsh-Mtx_rxsh*Ltxsh)^2 ...
/(Ltxsh*Lrxsh-Mtxsh_rxsh^2)^2*rsh2;
r2=r1;

% coil-to-coil efficiency
eff=1/(1+r2/R+r1/R*(r2+R)^2/(2*pi*f*Meq)^2);

% Meet the requirement of field attenuation
if (B100mag<=B100mag_ori gi nal) && (eff > 0.8)

    x=x+1;
    % turns of lumped loops for litz shield
    optimization_DLS(x, 1)=FAL1;
    optimization_DLS(x, 2)=FAL2;
    optimization_DLS(x, 3)=FAL3;
    optimization_DLS(x, 4)=FAL4;
    % total number of turns for the winding
    optimization_DLS(x, 5)=N_DLS;
    % loop for outer radii
    optimization_DLS(x, 6)=Router;
    % loop for inner radii
    optimization_DLS(x, 7)=Ri nner;
    % strand number
    optimization_DLS(x, 8)=Nlitz(Litz_DLS);
    % width per turn
    optimization_DLS(x, 9)=TurnsWi dth;
    % quantified magnetic field
    optimization_DLS(x, 10)=B100mag;

```

Appendix

```

% equivalent inductances
optimization_DLS(x, 12)=Leq;
optimization_DLS(x, 13)=Meq;
optimization_DLS(x, 14)=Meq/Leq;
% length of winding
optimization_DLS(x, 15)=Length;
% resistance of winding
optimization_DLS(x, 16)=r1;
% length of shield
optimization_DLS(x, 17)=Length2;
% coil-to-coil efficiency
optimization_DLS(x, 19)=eff;
% distribution of turns
optimization_DLS(x, 23 : 32)=[IL(1) IL(2) IL(3) IL(4) IL(5)
IL(6) IL(7) IL(8) IL(9) IL(10)];
    end
    end
    end
    end
    end
    end
end
%      sprintf('NO=%d, NI=%d, x=%d', NO, NI, x)
end
end
end
```

3.4. Derive Pareto Front

```

ss_DLS=size(optimization_DLS(:, 10));
i=0;
for pp=1:ss_DLS(1)
    if (isnan(optimization_DLS(pp, 10)) == 0)
        i=i+1;
        B100_DLS(i)=optimization_DLS(pp, 10);
        eff_DLS(i)=optimization_DLS(pp, 19);
        TunrNumber_DLS(i)=optimization_DLS(pp, 5);
        LitzType_DLS(i)=optimization_DLS(pp, 8);
        OuterRadii_DLS(i)=optimization_DLS(pp, 6);
        InnerRadii_DLS(i)=optimization_DLS(pp, 7);
        L_DLS(i)=optimization_DLS(pp, 12);
        M_DLS(i)=optimization_DLS(pp, 13);
        k_DLS(i)=optimization_DLS(pp, 14);
        FAL1_DLS(i)=optimization_DLS(pp, 1);
        FAL2_DLS(i)=optimization_DLS(pp, 2);
        FAL3_DLS(i)=optimization_DLS(pp, 3);
        FAL4_DLS(i)=optimization_DLS(pp, 4);
        Ltxsh_DLS(i)=optimization_DLS(pp, 20);
        Lrxsh_DLS(i)=optimization_DLS(pp, 21);
    end
end
```

```

% derive the points along Pareto fronts
x_DLS=transpose(B100_DLS);
y_DLS=1 - transpose(eff_DLS);
front_DLS=paretofront([x_DLS y_DLS]);
si ze_DLS=si ze(front_DLS);

i =0;
for a=1: si ze_DLS(1)
    if (front_DLS(a) == 1)
        i =i +1;
        Pareto_B100_DLS(i)=B100_DLS(a);
        Pareto_eff_DLS(i)=eff_DLS(a);
        Pareto_TunrNumber_DLS(i)=TunrNumber_DLS(a);
        Pareto_Li tzType_DLS(i)=Li tzType_DLS(a);
        Pareto_OuterRadi i _DLS(i)=OuterRadi i _DLS(a);
        Pareto_I nnerRadi i _DLS(i)=I nnerRadi i _DLS(a);
        Pareto_L_DLS(i)=L_DLS(a);
        Pareto_M_DLS(i)=M_DLS(a);
        Pareto_k_DLS(i)=k_DLS(a);
        Pareto_FAL1_DLS(i)=FAL1_DLS(a);
        Pareto_FAL2_DLS(i)=FAL2_DLS(a);
        Pareto_FAL3_DLS(i)=FAL3_DLS(a);
        Pareto_FAL4_DLS(i)=FAL4_DLS(a);
        Pareto_I txsh_DLS(i)=I txsh_DLS(a);
        Pareto_I rxsh_DLS(i)=I rxsh_DLS(a);
    end
end

```

3.5. Plot the Pareto front

```

% make the points along the front in a sequence
[ParetoSort_B100_DLS, I_DLS]=sort(Pareto_B100_DLS);
si ze2_DLS=si ze(Pareto_B100_DLS);
for a=1: si ze2_DLS(2)
    i =I_DLS(a);
    ParetoSort_DLS(a, 1)=Pareto_B100_DLS(i);
    ParetoSort_DLS(a, 2)=Pareto_eff_DLS(i);
    ParetoSort_DLS(a, 3)=Pareto_TunrNumber_DLS(i);
    ParetoSort_DLS(a, 4)=Pareto_Li tzType_DLS(i);
    ParetoSort_DLS(a, 5)=Pareto_OuterRadi i _DLS(i);
    ParetoSort_DLS(a, 6)=Pareto_I nnerRadi i _DLS(i);
    ParetoSort_DLS(a, 7)=Pareto_L_DLS(i);
    ParetoSort_DLS(a, 8)=Pareto_M_DLS(i);
    ParetoSort_DLS(a, 9)=Pareto_k_DLS(i);
    ParetoSort_DLS(a, 10)=Pareto_FAL1_DLS(i);
    ParetoSort_DLS(a, 11)=Pareto_FAL2_DLS(i);
    ParetoSort_DLS(a, 12)=Pareto_FAL3_DLS(i);
    ParetoSort_DLS(a, 13)=Pareto_FAL4_DLS(i);
    ParetoSort_DLS(a, 14)=Pareto_I txsh_DLS(i);
    ParetoSort_DLS(a, 15)=Pareto_I rxsh_DLS(i);
end

```

```

% curve fitting
coefficients_DLS=polynomial(ParetoSort_DLS(:, 1), ParetoSort_DLS(:, 2), 8);
CF_DLS=polyval(coefficients_DLS, ParetoSort_DLS(:, 1));

hFig=figure(1)
set(hFig, 'Position', [100 300 350 200])
scatter(B100_DLS, eff_DLS, 'b')
hold on;
h=plot(ParetoSort_DLS(:, 1), CF_DLS);
set(h, 'Color', 'r', 'LineWidth', 3, 'LineStyle', '-');
hold off;
grid;
set(gca, 'XLim', [10 40]);
set(gca, 'YLim', [0.8 1]);
xx=xlabel('B at 100 mm (\muT)', 'FontWeight', 'bold', 'Color', 'k', 'FontSize', 10);
yy=ylabel('Coil Efficiency', 'FontWeight', 'bold', 'Color', 'k', 'FontSize', 10);
set(gca, 'fontname', 'Times New Roman', 'FontSize', 10)
set(xx, 'Fontname', 'Times new roman', 'fontweight', 'b');
set(yy, 'Fontname', 'Times new roman', 'fontweight', 'b');

```

A.4. Excel Files Imported for Calculation

For the codes in A.1, A.2, and A.3, three excel files should be imported in the beginning of the calculation, which are “Litz Wire Datasheet.xls” in Figure A-1, “Inductance Matrix.xls” in Figure A-2, and “Field Matrix.xls” in Figure A-3.

Figure A-1. “Litz Wire Datasheet.xls”.

Appendix

7.2E-05	6.0E-05	1.0E-04	1.4E-04	2.1E-04	1.1E-04	6.0E-05	3.3E-05	1.3E-05	3.7E-05	3.1E-05	2.8E-05	2.3E-05
4.9E-05	5.7E-05	6.7E-05	8.2E-05	1.1E-04	1.6E-04	8.0E-05	4.1E-05	1.9E-05	2.5E-05	2.2E-05	1.9E-05	1.8E-05
3.1E-05	3.6E-05	4.2E-05	4.9E-05	6.0E-05	8.0E-05	1.3E-04	5.4E-05	2.3E-05	1.7E-05	1.4E-05	1.3E-05	1.2E-05
1.8E-05	2.1E-05	2.4E-05	2.8E-05	3.3E-05	4.1E-05	5.4E-05	8.8E-05	3.2E-05	9.8E-06	8.4E-06	7.6E-06	6.9E-06
8.9E-06	1.0E-05	1.1E-05	1.3E-05	1.5E-05	1.9E-05	2.3E-05	3.2E-05	5.4E-05	4.9E-06	4.2E-06	3.8E-06	3.5E-06
1.2E-04	8.9E-05	6.8E-05	5.1E-05	3.7E-05	2.5E-05	1.7E-05	9.8E-06	4.9E-06	4.2E-04	2.5E-04	1.9E-04	1.6E-04
9.5E-05	7.4E-05	5.7E-05	4.3E-05	3.1E-05	2.2E-05	1.4E-05	8.4E-06	4.2E-06	2.5E-04	4.4E-04	2.6E-04	2.0E-04
8.2E-05	6.4E-05	5.0E-05	3.8E-05	2.8E-05	1.9E-05	1.3E-05	7.6E-06	3.8E-06	1.9E-04	2.6E-04	4.7E-04	2.8E-04
7.3E-05	5.8E-05	4.5E-05	3.4E-05	2.5E-05	1.8E-05	1.2E-05	6.9E-06	3.5E-06	1.6E-04	2.0E-04	2.8E-04	5.1E-04
w1,2	w1,3	w1,4	w1,5	w1,6	w1,7	w1,8	w1,9	w1,10	sh1,1	sh1,2	sh1,3	sh1,4
6.2E-05	5.6E-05	4.8E-05	4.0E-05	3.1E-05	2.3E-05	1.6E-05	9.7E-06	4.9E-06	6.1E-05	5.9E-05	5.7E-05	5.6E-05
5.9E-05	5.4E-05	4.7E-05	3.9E-05	3.1E-05	2.3E-05	1.6E-05	9.9E-06	5.1E-06	5.5E-05	5.2E-05	5.1E-05	4.9E-05
5.4E-05	5.0E-05	4.4E-05	3.7E-05	3.0E-05	2.3E-05	1.6E-05	9.8E-06	5.0E-06	4.7E-05	4.5E-05	4.3E-05	4.2E-05
4.7E-05	4.4E-05	4.0E-05	3.4E-05	2.8E-05	2.1E-05	1.5E-05	9.3E-06	4.8E-06	4.0E-05	3.7E-05	3.6E-05	3.4E-05
3.9E-05	3.7E-05	3.4E-05	3.0E-05	2.4E-05	1.9E-05	1.3E-05	8.5E-06	4.4E-06	3.2E-05	3.0E-05	2.8E-05	2.7E-05
3.1E-05	3.0E-05	2.8E-05	2.5E-05	2.0E-05	1.6E-05	1.2E-05	7.3E-06	3.8E-06	2.5E-05	2.3E-05	2.2E-05	2.1E-05
2.3E-05	2.3E-05	2.1E-05	1.9E-05	1.6E-05	1.3E-05	9.3E-06	5.9E-06	3.1E-06	1.8E-05	1.7E-05	1.6E-05	1.5E-05
1.6E-05	1.6E-05	1.5E-05	1.3E-05	1.2E-05	9.3E-06	6.8E-06	4.4E-06	2.4E-06	1.2E-05	1.1E-05	1.1E-05	1.0E-05
9.9E-06	9.8E-06	9.3E-06	8.5E-06	7.3E-06	5.9E-06	4.4E-06	2.9E-06	1.6E-06	7.4E-06	6.7E-06	6.3E-06	6.0E-06
5.1E-06	5.0E-06	4.8E-06	4.4E-06	3.8E-06	3.1E-06	2.4E-06	1.6E-06	8.4E-07	3.7E-06	3.4E-06	3.2E-06	3.0E-06
5.5E-05	4.7E-05	4.0E-05	3.2E-05	2.5E-05	1.8E-05	1.2E-05	7.4E-06	3.7E-06	6.5E-05	6.6E-05	6.7E-05	6.8E-05
5.2E-05	4.5E-05	3.7E-05	3.0E-05	2.3E-05	1.7E-05	1.1E-05	6.8E-06	3.4E-06	6.6E-05	6.8E-05	7.0E-05	7.3E-05
5.1E-05	4.3E-05	3.6E-05	2.8E-05	2.2E-05	1.6E-05	1.1E-05	6.3E-06	3.2E-06	6.7E-05	7.0E-05	7.4E-05	7.7E-05
4.9E-05	4.2E-05	3.4E-05	2.7E-05	2.1E-05	1.5E-05	1.0E-05	6.0E-06	3.0E-06	6.8E-05	7.3E-05	7.7E-05	8.2E-05

Figure A-2. “Inductance Matrix.xls” (unit: mH).

Figure A-3. “Field Matrix.xls” (unit: $\mu\text{T}/\text{Ampere-turn}$).

Appendix B. Simulation Tools and Conditions

B.1. Directory of raw files for simulation or drawing of each figure

The original simulation files, optimization codes, and PCB schematics and layouts in this dissertation can be found at the //ADFS directories in TABLE B-1.

TABLE B-1 Directory of Raw Files for Each Figure

Chapter	Type	Figure or Table	Directory (\\ads\ads\projects\Khai Ngo\minglu\Dissertation\Dissertation_Files\)
2	Matlab	Figure 2-6	Chapter2\Mv_eff_phi_vs_ZN_Q_fNH
2	Matlab	Figure 2-7	Chapter2\QLOpt_Qmin_vs_k_Mv_fNH
2	Matlab	Figure 2-8	Chapter2\QLOpt_Qmin_vs_k_Mv_fN_1
2	Ansys Maxwell	Figure 2-9	Chapter2\3kW_k_Q_vs_Size
2	Excel	Figure 2-10	Chapter2\k_L_Router
2	Matlab	Figure 2-11	Chapter2\physical_realization_fNH
2	Matlab	Figure 2-12	Chapter2\Q_vs_LitzWire_fNH
2	Simulink	Figure 2-13	Chapter2\FB_fN_fNH
2	Matlab	Figure 2-14	Chapter2\QLOpt_Qmin_vs_k_Mv_fN_1
2	Matlab	Figure 2-15	Chapter2\Q_vs_LitzWire_fN_1
2	Simulink	Figure 2-16	Chapter2\FB_fN_1
2	Altium	Figure 2-18	Chapter2\Primary Inverter
2	Altium	Figure 2-18	Chapter2\Secondary Rectifier
2	Altium	Figure 2-18	Chapter2\C1

Appendix

2	Altium	Figure 2-18	Chapter2\C2
3	Ansys Maxwell	TABLE 3-1, TABLE 3-2	Chapter3\Inductance Matrix
3	Ansys Maxwell	TABLE 3-3, TABLE 3-4, Figure 3-11	Chapter3\Field Matrix
3	Matlab	Figure 3-14	Chapter3\Pareto_Front\No_Shield
4	Matlab	Figure 4-10	Chapter4\ref_100W_sweep_FS
4	Ansys Maxwell	Figure 4-10	Chapter4\ref_100W_sweep_FS
4	Matlab	Figure 4-11	Chapter4\Sweep_Ferrite_Size
5	Matlab	Figure 5-7	Chapter5\Leq_Meq_req
5	Matlab	Figure 5-8	Chapter5\Leq_Meq_req
5	Ansys Maxwell	Figure 5-13, TABLE 5-1 - TABLE 5-6	Chapter5\Inductance Matrix
5	Ansys Maxwell	TABLE 5-7 - TABLE 5-10	Chapter5\Field Matrix
5	Matlab	Figure 5-14	Chapter5\Pareto_front\Driven_Litz_Shield Chapter5\Pareto_front\Shorted_Litz_Shield
5	AutoCAD	Figure 5-15	Chapter5\3D_Print
6	Matlab	Figure 6-6	Chapter6\BN_PlossN\B_vs_sin_Phi_vs_By_over_Bz
6	Matlab	Figure 6-7	Chapter6\BN_PlossN\B_vs_sin_Phi_vs_By_over_Bz
6	Ansys Maxwell	Figure 6-8 - Figure 6-11	Chapter6\3kW
6	Matlab	Figure 6-11	Chapter6\BN_PlossN\B_vs_sin_Phi_vs_By_over_Bz
6	Simulink	Figure 6-12	Chapter6\circuit simulation\phi90
6	Simulink	Figure 6-13	Chapter6\circuit simulation\phi130

B.2. Deriving Permeance Matrices in Ansys Maxwell

The permeance matrices in Section 3.4.2 and Section 5.3.2 are obtained from only one simulation using Ansys Maxwell. The lumped-loop model is drawn as Figure B-1. The circular loops and square loops represent windings and shields, respectively. The square plates are the ferrite plates. The eddy current solver in Figure B-2 is selected as the solution type for the simulation.

Figure B-1. Lumped-loop model in Ansys Maxwell for coils with litz shield (see TABLE B-1 for the original file).

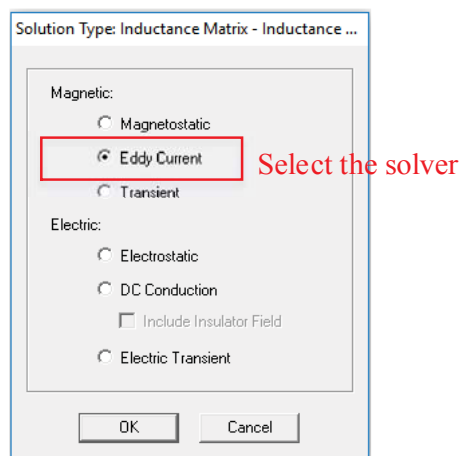


Figure B-2. Select the eddy current solver for the solution type.

All the loops are provided with stranded current excitation, as shown in Figure B-3. This is because litz wire is applied to the coils, in which the current is almost evenly distributed. Figure B-5 shows the settings for the analysis. In this study, the frequency is selected to be 100 kHz, which is the switching frequency of the inverter in Figure 2-1.

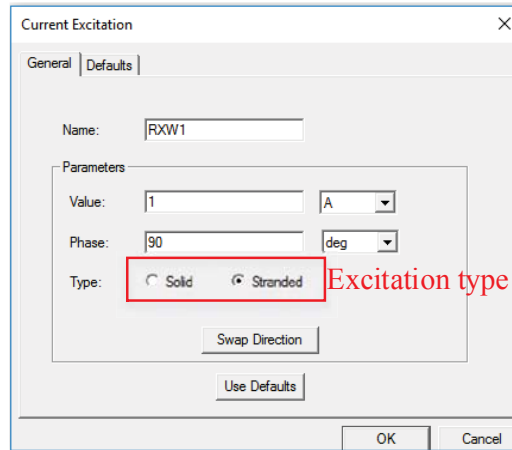


Figure B-3. Select eddy current solver for the solution type.

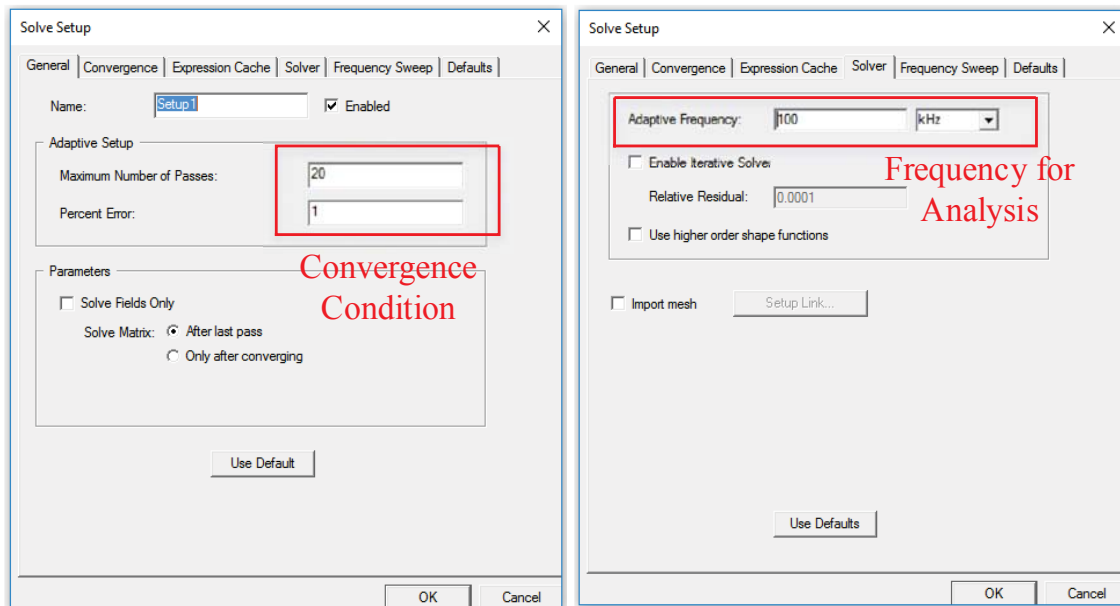


Figure B-4. Settings for the analysis.

It is important to assign proper mesh for the accurate simulation results. The adaptive meshing technique of ANSYS products uses a highly robust volumetric meshing and includes a multithreading capability that reduces the amount of memory used and speeds the simulation time. The automatic meshing is implemented in the simulation. When the simulation is complete, the result can be either plotted or shown in matrix. In this study, the matrices were used to see the results (Figure B-5).

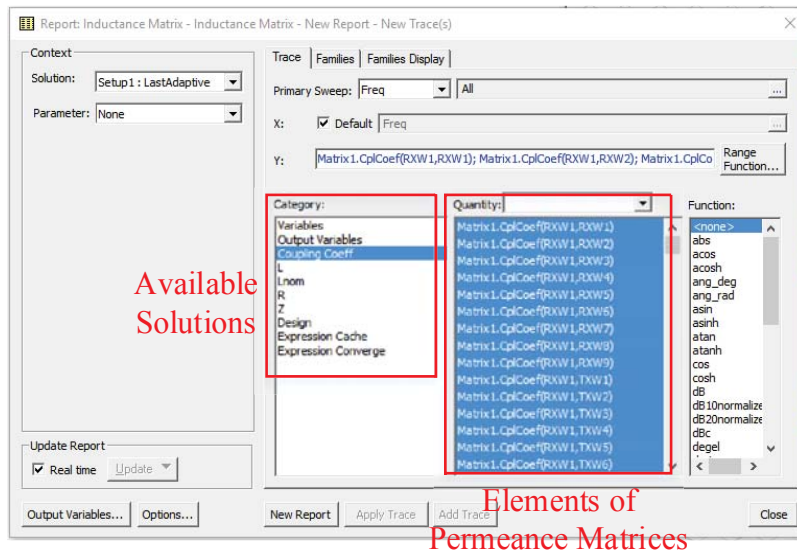


Figure B-5. Analysis of simulation and the results in matrix.

B.3. Deriving Current-to-Field Matrices in Ansys Maxwell

The current-to-field matrices in Section 3.4.2 and Section 5.3.3 are obtained from simulations using Ansys Maxwell. The lumped-loop model is the same as Figure B-1. The eddy current solver in Figure B-2 is selected as the solution type for the simulation. When deriving the current-to-field matrices for one loop, only the corresponding loop is provided with stranded current excitation of 1 A RMS, and all the other loops are provided with 0 A current. The

settings for the analysis is the same as Figure B-5. The frequency is selected to be 100 kHz, which is the switching frequency of the inverter in Figure 2-1.

For each simulation, Figure B-6 shows how to obtain the magnetic fields in X, Y, Z directions for one point of field measurement. The expressions of the fields are shown in Figure B-7. The way to derive the current-to-field coefficients from the fields and currents has been demonstrated in Figure 3-11

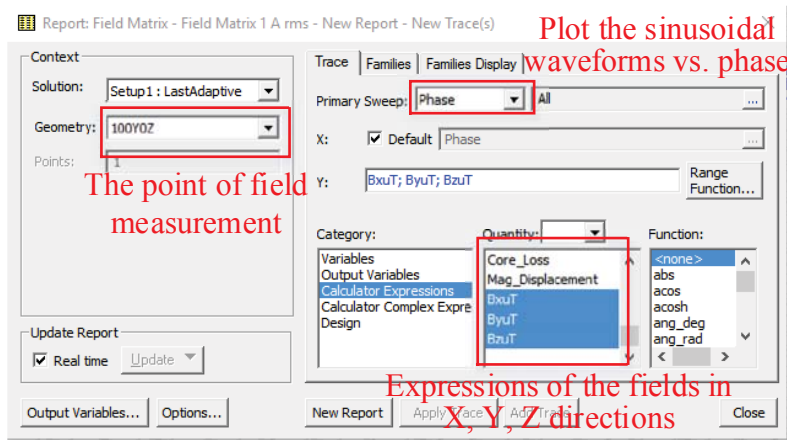


Figure B-6. Analysis of simulation and exporting the results.

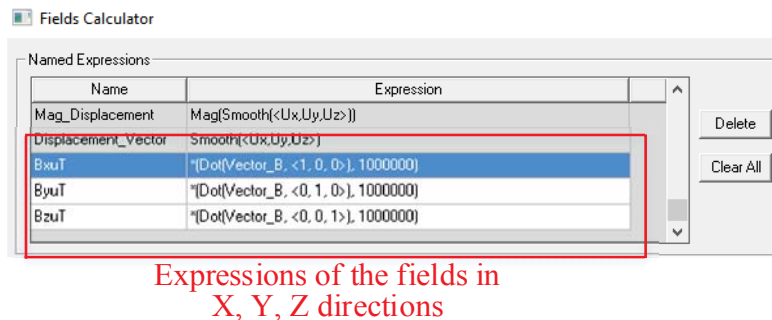


Figure B-7. Expressions of the magnetic fields in the calculator.

Appendix C. Hardware Setup for Experiment

C.1. Layout of the Inverter

Altium PCB designer was used to design the schematic in Figure C-1 and PCB layout in Figure C-2. The original design projects are saved at the directory in TABLE B-1.

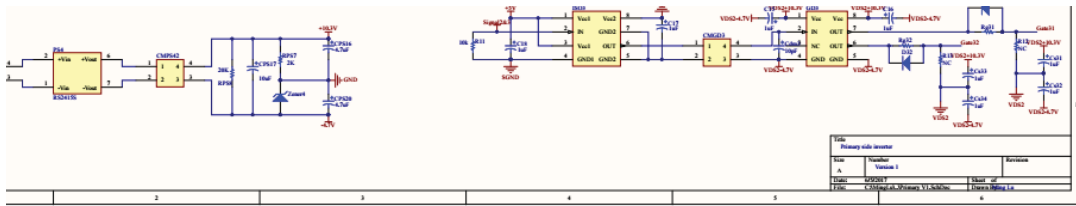
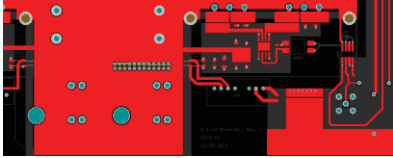


Figure C-1. Complete schematic of the inverter in Figure 2-18(a) (see TABLE B-1 for the original file).

Appendix



(a)

(b)

(c)

(d)

Figure C-2. Layout of the inverter in Figure 2-18(a): (a) top layer; (b) layer 2; (c) layer 3; (4) bottom layer (see TABLE B-1 for the original file).

C.2. Fabrication of 100 W Coils with 3D Printer

AutoCAD was used to design the fixture of the planar coil as shown in Figure C-3. The .stl file was imported to Cura for 3D printing, as shown in Figure C-4. The settings in the Cura are shown in Figure C-5.

Figure C-3. AutoCAD file of the coils' fixture for 3D printing (see TABLE B-1 for the original file).

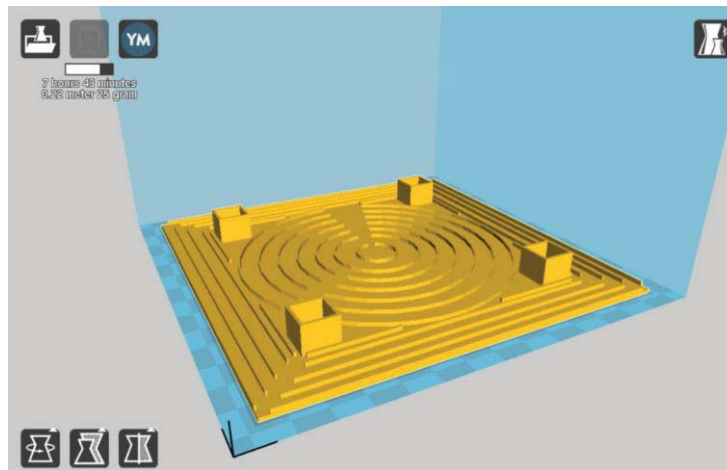


Figure C-4. Importing the .stl file in Figure C-3 to Cura for 3D printing.

Appendix

Basic	Advanced	Plugins	Start/End-GCode
Quality			
Layer height (mm)	<input type="text" value="0.1"/>		
Shell thickness (mm)	<input type="text" value="0.8"/>		
Enable retraction	<input checked="" type="checkbox"/>	<input type="button" value="..."/>	
Fill			
Bottom/Top thickness (mm)	<input type="text" value="0.3"/>		
Fill Density (%)	<input type="text" value="100"/>	<input type="button" value="..."/>	
Speed and Temperature			
Print speed (mm/s)	<input type="text" value="20"/>		
Printing temperature (C)	<input type="text" value="208"/>		
Support			
Support type	<input type="text" value="Everywhere"/>	<input type="button" value="..."/>	
Platform adhesion type	<input type="text" value="None"/>	<input type="button" value="..."/>	
Filament			
Diameter (mm)	<input type="text" value="1.75"/>		
Flow (%)	<input type="text" value="100"/>		
Machine			
Nozzle size (mm)	<input type="text" value="0.4"/>		

Basic	Advanced	Plugins	Start/End-GCode
Retraction			
Speed (mm/s)	<input type="text" value="30"/>		
Distance (mm)	<input type="text" value="1"/>		
Quality			
Initial layer thickness (mm)	<input type="text" value="0.3"/>		
Initial layer line width (%)	<input type="text" value="100"/>		
Cut off object bottom (mm)	<input type="text" value="0.0"/>		
Dual extrusion overlap (mm)	<input type="text" value="0.15"/>		
Speed			
Travel speed (mm/s)	<input type="text" value="20"/>		
Bottom layer speed (mm/s)	<input type="text" value="10"/>		
Infill speed (mm/s)	<input type="text" value="0.0"/>		
Top/bottom speed (mm/s)	<input type="text" value="0.0"/>		
Outer shell speed (mm/s)	<input type="text" value="0.0"/>		
Inner shell speed (mm/s)	<input type="text" value="0.0"/>		
Cool			
Minimal layer time (sec)	<input type="text" value="5"/>		
Enable cooling fan	<input checked="" type="checkbox"/>	<input type="button" value="..."/>	

Figure C-5. Settings in Cura for 3D printing.

Reference

- [1] Q. Chen, S. C. Wong, C. K. Tse and X. Ruan, "Analysis, design, and control of a transcutaneous power regulator for artificial hearts," *IEEE Trans. Biomedical Circuits and Systems*, vol. 3, no. 1, pp. 23-31, Feb. 2009.
- [2] H. Miura, S. Arai, Y. Kakubari, F. Sato, H. Matsuki and T. Sato, "Improvement of the transcutaneous energy transmission system utilizing ferrite cored coils for artificial hearts," *IEEE Trans. Magnetics*, vol. 42, no. 10, pp. 3578-3580, Oct. 2006.
- [3] T. Campi, S. Cruciani, F. Palandrani, V. D. Santis, A. Hirata, and M. Feliziani, "Wireless power transfer charging system for AIMDs and pacemakers," *IEEE Trans. on Microwave Theory and Techniques*, vol. 64, pp. 633-642, 2016.
- [4] T. Campi, S. Cruciani, V. D. Santis, and M. Feliziani, "EMF safety and thermal aspects in a pacemaker equipped with a wireless power transfer system working at low frequency," *IEEE Trans. on Microwave Theory and Techniques*, vol. 64, pp. 375-382, 2016.
- [5] O. Knecht, R. Bosshard and J. W. Kolar, "High-efficiency transcutaneous energy transfer for implantable mechanical heart support systems," *IEEE Trans. Power Electronics*, vol. 30, no. 11, pp. 6221-6236, Nov. 2015.
- [6] S. Y. R. Hui, W. Zhong and C. K. Lee, "A critical review of recent progress in mid-range wireless power transfer," *IEEE Trans. Power Electronics*, vol. 29, no. 9, pp. 4500-4511, Sept. 2014.
- [7] G. A. Covic and J. T. Boys, "Modern trends in inductive power transfer for transportation applications," *IEEE Journal of Emerging and Selected Topics in Power Electronics*, vol. 1, no. 1, pp. 28-41, March 2013.

- [8] U. K. Madawala and D. J. Thrimawithana, "A bidirectional inductive power interface for electric vehicles in V2G systems," *IEEE Trans. Industrial Electronics*, vol. 58, no. 10, pp. 4789-4796, Oct. 2011.
- [9] S. Li and C. C. Mi, "Wireless power transfer for electric vehicle applications," *IEEE Journal of Emerging and Selected Topics in Power Electronics*, vol. 3, no. 1, pp. 4-17, March 2015.
- [10] S. Lukic and Z. Pantic, "Cutting the cord: static and dynamic inductive wireless charging of electric vehicles," *IEEE Electrification Magazine*, vol. 1, pp. 57-64, 2013.
- [11] L. Kibok, Z. Pantic, and S. M. Lukic, "Reflexive field containment in dynamic inductive power transfer systems," *IEEE Trans. Power Electronics*, vol. 29, pp. 4592-4602, 2014.
- [12] W. C. Brown, "The history of power transmission by radio waves," *IEEE Trans. on Microwave Theory and Techniques*, vol. 32, no.9, pp. 1230-1242, Sep. 1984.
- [13] W. C. Brown, "A survey of the elements of power transmission by microwave beam," in *Proc. IRE International Conference*, 1961, pages 93-105.
- [14] W. C. Brown and E. E. Eves, "Beamed microwave power transmission and its application to space," *IEEE Trans. Microwave Theory and Techniques*, vol. 40, no. 6, pp. 1239-1250, Jun. 1992.
- [15] G. A. Landis, "Applications for space power by laser transmission," in *Proc. SPIE*, 1994, vol. 2121, pp. 252-255.
- [16] L. Summerer and O. Purcell. "Concepts for wireless energy transmission via laser," in *Proc. Europeans Space Agency - Advanced Concepts Team*, 2009.
- [17] M. P. Theodoridis, "Effective capacitive power transfer," *IEEE Trans. Power Electronics*, vol. 27, no. 12, pp. 4906-4913, Dec. 2012.
- [18] C. Liu, A. P. Hu, G. A. Covic, and N. C. Nair, "Comparative study of CCPT systems with

- two different inductor tuning positions,” *IEEE Trans. on Power Electronics*, vol. 27, no. 1, pp. 294-306, Jan. 2012.
- [19] C. Liu, A. P. Hu, N. C. Nair, and G. A. Covic, “2-D alignment analysis of capacitively coupled contactless power transfer systems,” in *Proc. IEEE Energy Conversion Congress and Exposition*, 2010, pp. 652-657.
- [20] F. Lu, H. Zhang, H. Hofmann and C. Mi, "A double-sided LCLC-compensated capacitive power transfer system for electric vehicle charging," *IEEE Trans. Power Electronics*, vol. 30, no. 11, pp. 6011-6014, Nov. 2015.
- [21] H. Zhang, F. Lu, H. Hofmann, W. Liu and C. C. Mi, "A four-plate compact capacitive coupler design and LCL-compensated topology for capacitive power transfer in electric vehicle charging application," *IEEE Trans. Power Electronics*, vol. 31, no. 12, pp. 8541-8551, Dec. 2016.
- [22] N. Tesla, "Apparatus for transmitting electrical energy," U.S. Patent 1,119,732, Dec. 1, 1914.
- [23] Robert Lomas, “The man who invented the twentieth century -Nikola Tesla -Forgotten Genius of Electricity,” *Headline 1999*, ISBN 0 7472 6265 9, p. 146.
- [24] J. C. Schuder, H. E. Stephenson, and J. F. Townsend, "High level electromagnetic energy transfer through a closed chestwall," *IRE Internet. Conv. Rec.*, pt.9, vol.9, pp. 119-126, 1961.
- [25] W. H. Ko, S. P. Liang, and C.D.F. Fung, " Design of radio-frequency powered coils for implant instruments," *Medical and Biological Engineering and Computing*, vol. 15, pp. 634-640, 1977.
- [26] E. S. Hochmair, "System optimization for improved accuracy in transcutaneous signal and power transmission," *IEEE Trans. Biomedical Engineering*, vol. BME-31, no. 2, pp. 177-186, Feb. 1984.

- [27] Chwei-Sen Wang, O. H. Stielau and G. A. Covic, "Design considerations for a contactless electric vehicle battery charger," *IEEE Trans. Industrial Electronics*, vol. 52, no. 5, pp. 1308-1314, Oct. 2005.
- [28] Chwei-Sen Wang, G. A. Covic and O. H. Stielau, "Power transfer capability and bifurcation phenomena of loosely coupled inductive power transfer systems," *IEEE Trans. Industrial Electronics*, vol. 51, no. 1, pp. 148-157, Feb. 2004.
- [29] F. Y. Lin, G. A. Covic and J. T. Boys, "Evaluation of magnetic pad sizes and topologies for electric vehicle charging," *IEEE Trans. Power Electronics*, vol. 30, no. 11, pp. 6391-6407, Nov. 2015.
- [30] A. Kamineni, G. A. Covic, and J. T. Boys, "Analysis of coplanar intermediate coil structures in inductive power transfer systems," *IEEE Trans. Power Electronics*, vol. 30, pp. 6141-6154, 2015.
- [31] G. R. Nagendra, G. A. Covic, and J. T. Boys, "Determining the physical size of inductive couplers for IPT EV systems," *IEEE Journal of Emerging and Selected Topics in Power Electronics*, vol. 2, pp. 571-583, 2014.
- [32] C. Y. Huang, J. T. Boys and G. A. Covic, "LCL pickup circulating current controller for inductive power transfer systems," *IEEE Trans. Power Electronics*, vol. 28, no. 4, pp. 2081-2093, April 2013.
- [33] O. H. Stielau and G. A. Covic, "Design of loosely coupled inductive power transfer systems," in *Proc. International Conference on Power System Technology*, 2000, pp. 85-90 vol.1.
- [34] M. Budhia, J. T. Boys, G. A. Covic and C. Y. Huang, "Development of a single-sided flux magnetic coupler for electric vehicle IPT charging systems," *IEEE Trans. Industrial*

- Electronics*, vol. 60, no. 1, pp. 318-328, Jan. 2013.
- [35] M. Budhia, G. A. Covic and J. T. Boys, "Design and optimization of circular magnetic structures for lumped inductive power transfer systems," *IEEE Trans. Power Electronics*, vol. 26, no. 11, pp. 3096-3108, Nov. 2011.
- [36] X. Liu and S. Y. Hui, "Optimal design of a hybrid winding structure for planar contactless battery charging platform," *IEEE Trans. Power Electronics*, vol. 23, pp. 455-463, 2008.
- [37] W. X. Zhong, X. Liu, and S. Y. R. Hui, "A novel single-layer winding array and receiver coil structure for contactless battery charging systems with free-positioning and localized charging features," *IEEE Trans. Industrial Electronics*, vol. 58, pp. 4136-4144, 2011.
- [38] C. K. Lee, W. X. Zhong, and S. Y. R. Hui, "Effects of magnetic coupling of nonadjacent resonators on wireless power domino-resonator systems," *IEEE Trans. Power Electronics*, vol. 27, pp. 1905-1916, 2012.
- [39] "ICNIRP guidelines for limiting exposure to time-varying electric, magnetic and electromagnetic fields (1 Hz to 100 kHz)," *Health Phys.*, vol. 99, pp. 818-836, 2010.
- [40] N. Kuyvenhoven, C. Dean, J. Melton, J. Schwannecke, and A. E. Umenei, "Development of a foreign object detection and analysis method for wireless power systems," in *Proc. IEEE Symposium on Product Compliance Engineering*, 2011, pp. 1-6.
- [41] Y. H. Sohn, B. H. Choi, E. S. Lee, G. C. Lim, C. Gyu-Hyeong, and C. T. Rim, "General unified analyses of two-capacitor inductive power transfer systems: equivalence of current-source SS and SP compensations," *IEEE Trans. Power Electronics*, vol. 30, pp. 6030-6045, 2015.
- [42] A. Kurs, A. Karalis, R. Moffatt, J. D. Joannopoulos, P. Fisher, and M. Soljačić, "Wireless power transfer via strongly coupled magnetic resonances," *Science*, vol. 317, no. 5834, pp.

- 83-86, Jul. 2007.
- [43] J. L. Villa, J. Sallan, J. F. Sanz Osorio and A. Llombart, "High-misalignment tolerant compensation topology for ICPT systems," *IEEE Trans. Industrial Electronics*, vol. 59, no. 2, pp. 945-951, Feb. 2012.
- [44] S. Li, W. Li, J. Deng, T. D. Nguyen and C. C. Mi, "A double-sided LCC compensation network and its tuning method for wireless power transfer," *IEEE Trans. Vehicular Technology*, vol. 64, no. 6, pp. 2261-2273, June 2015.
- [45] W. Zhang and C. C. Mi, "Compensation topologies of high-power wireless power transfer systems," *IEEE Trans. Vehicular Technology*, vol. 65, no. 6, pp. 4768-4778, June 2016.
- [46] R. Bosshard, J. W. Kolar, J. Muhlethaler, I. Stevanovic, B. Wunsch, and F. Canales, "Modeling and η - α -Pareto optimization of inductive power transfer coils for electric vehicles," *IEEE Journal of Emerging and Selected Topics in Power Electronics*, vol. 3, pp. 50-64, 2015.
- [47] C. Zheng *et al.*, "High-efficiency contactless power transfer system for electric vehicle battery charging application," *IEEE Journal of Emerging and Selected Topics in Power Electronics*, vol. 3, no. 1, pp. 65-74, March 2015.
- [48] R. Bosshard, U. Badstübner, J. W. Kolar and I. Stevanović, "Comparative evaluation of control methods for inductive power transfer," in *Proc. International Conference on Renewable Energy Research and Applications*, Nagasaki, 2012, pp. 1-6.
- [49] T. Diekhans and R. W. De Doncker, "A dual-side controlled inductive power transfer system optimized for large coupling factor variations and partial load," *IEEE Trans. Power Electronics*, vol. 30, no. 11, pp. 6320-6328, Nov. 2015.
- [50] R. Bosshard and J. W. Kolar, "All-SiC 9.5 kW/dm³ on-board power electronics for 50 kW/85

- kHz automotive IPT system," *IEEE Journal of Emerging and Selected Topics in Power Electronics*, vol. 5, no. 1, pp. 419-431, March 2017.
- [51] Ansys. Mar. 2012 User's Guide-Maxwell 3-D, Rev 6.0. [Online] Available: <http://ansoft-maxwell.narod.ru/english.html>.
- [52] M. Lu and K. D. T. Ngo, "Pareto fronts for coils' efficiency versus stray magnetic field in inductive power transfer," in *Proc. IEEE PELS Workshop Emerg. Technol.: Wireless Power*, Knoxville, TN, 2016, pp. 140-144.
- [53] S. Y. Choi, B. W. Gu, S. W. Lee, W. Y. Lee, Jin Huh and C. T. Rim, "Generalized active emf cancel methods for wireless electric vehicles," *IEEE Trans. Power Electronics*, vol. 29, no. 11, pp. 5770-5783, Nov. 2014.
- [54] K. Seonghwan, P. Hyun-Ho, K. Jonghoon, K. Jinguook, and A. Seungyoung, "Design and analysis of a resonant reactive shield for a wireless power electric vehicle," *IEEE Trans. Microwave Theory and Techniques*, vol. 62, pp. 1057-1066, 2014.
- [55] E. Waffenschmidt and T. Staring, "Limitation of inductive power transfer for consumer applications," in *Proc. European Conference on Power Electronics and Applications*, Barcelona, 2009, pp. 1-10.
- [56] G. Buja, M. Bertoluzzo and K. N. Mude, "Design and experimentation of wpt charger for electric city car," *IEEE Trans. Industrial Electronics*, vol. 62, no. 12, pp. 7436-7447, Dec. 2015.
- [57] R. Chen *et al.*, "Analysis and parameters optimization of a contactless ipt system for ev charger," in *Proc. IEEE Applied Power Electronics Conference and Exposition*, Fort Worth, TX, 2014, pp. 1654-1661.
- [58] M. Lu and Khai D. T. Ngo, "Systematic design of coils in series-series inductive power

- transfer for power transferability and efficiency,” *IEEE Trans. Power Electronics*, vol. PP, no. 99, pp. 1-1.
- [59] M. Lu and Khai D. T. Ngo, “Sequential design for coils in series-series inductive power transfer using normalized parameters,” in *Proc. IEEE PELS Workshop Emerg. Technol.: Wireless Power*, Knoxville, TN, 2016, pp. 21-26.
- [60] R. Bosshard, J. W. Kolar, and B. Wunsch, "Accurate finite-element modeling and experimental verification of inductive power transfer coil design," in *Proc. 2014 IEEE Applied Power Electronics Conference and Exposition*, 2014, pp. 1648-1653.
- [61] J. L. Volakis, *Antenna Engineering Handbook*, 4th edition, McGraw-Hill, 2007.
- [62] H. Kim, C. Song, J. Kim and D. Jung, "Design of magnetic shielding for reduction of magnetic near field from wireless power transfer system for electric vehicle," in *Proc. International Symposium on Electromagnetic Compatibility*, Gothenburg, 2014, pp. 53-58.
- [63] J. W. Kolar, J. Biela and J. Minibock, "Exploring the Pareto front of multi-objective single-phase PFC rectifier design optimization - 99.2% efficiency vs. 7kW/din³ power density,” in *Proc. IEEE 6th International Power Electronics and Motion Control Conference*, Wuhan, 2009, pp. 1-21.
- [64] Q. Wang, X. Zhang, R. Burgos, D. Boroyevich, A. White and M. Kheraluwala, "Design and optimization of a high performance isolated three phase AC/DC converter," in *Proc. IEEE Energy Conversion Congress and Exposition*, Milwaukee, WI, 2016, pp. 1-10.
- [65] M. Lu and K. D. T. Ngo, "Synergetic optimization of efficiency and stray magnetic field for planar coils in inductive power transfer using matrix calculation", in *Proc. IEEE Applied Power Electronics Conference and Exposition*, Tampa, FL, March 2017, pp. 3654–3660.
- [66] M. Lu and Khai D. T. Ngo, “A fast method to optimize efficiency and stray magnetic field

- for inductive-power-transfer coils using lumped-loop model”, *IEEE Trans. Power Electronics*, vol. PP, no. 99, pp. 1-1.
- [67] M. Lu and K. D. T. Ngo, "Comparison of passive shields for coils in inductive power transfer", in *Proc. 2017 IEEE Applied Power Electronics Conference and Exposition*, Tampa, FL, March 2017, pp. 1419-1124.
- [68] Sallan, J. L. Villa, A. Llombart and J. F. Sanz, "Optimal design of ICPT systems applied to electric vehicle battery charge," *IEEE Trans. Industrial Electronics*, vol. 56, no. 6, pp. 2140-2149, June 2009.
- [69] Q. Li and Y. C. Liang, "An inductive power transfer system with a high-Q resonant tank for mobile device charging," *IEEE Trans. Power Electronics*, vol. 30, no. 11, pp. 6203-6212, Nov. 2015.
- [70] J. Deng, W. Li, T. D. Nguyen, S. Li and C. C. Mi, "Compact and efficient bipolar coupler for wireless power chargers: design and analysis," *IEEE Trans. Power Electronics*, vol. 30, no. 11, pp. 6130-6140, Nov. 2015.
- [71] R. Bosshard, J. Mühlethaler, J. W. Kolar and I. Stevanović, "Optimized magnetic design for inductive power transfer coils," in *Proc. IEEE Applied Power Electronics Conference and Exposition*, Long Beach, CA, USA, 2013, pp. 1812-1819.
- [72] JS. Raju, R. Wu, M. Chan and C. P. Yue, "Modeling of mutual coupling between planar inductors in wireless power applications," *IEEE Trans. Power Electronics*, vol. 29, no. 1, pp. 481-490, Jan. 2014.
- [73] W. G. Hurley and M. C. Duffy, "Calculation of self and mutual impedances in planar magnetic structures," *IEEE Trans. Magnetics*, vol. 31, no. 4, pp. 2416-2422, Jul 1995.
- [74] W. G. Hurley and M. C. Duffy, "Calculation of self- and mutual impedances in planar

- sandwich inductors," *IEEE Trans. Magnetics*, vol. 33, no. 3, pp. 2282-2290, May 1997.
- [75] Y. P. Su, X. Liu and S. Y. Hui, "Extended theory on the inductance calculation of planar spiral windings including the effect of double-layer electromagnetic shield," *IEEE Trans. Power Electronics*, vol. 23, no. 4, pp. 2052-2061, July 2008.
- [76] Y. P. Su, X. Liu and S. Y. R. Hui, "Mutual inductance calculation of movable planar coils on parallel surfaces," *IEEE Trans. Power Electronics*, vol. 24, no. 4, pp. 1115-1123, April 2009.
- [77] C. R. Sullivan, "Optimal choice for number of strands in a litz-wire transformer winding," *IEEE Trans. Power Electronics*, vol. 14, no. 2, pp. 283-291, Mar 1999.
- [78] C. R. Sullivan, "Computationally efficient winding loss calculation with multiple windings, arbitrary waveforms, and two-dimensional or three-dimensional field geometry," *IEEE Trans. Power Electronics*, vol. 16, pp. 142-150, 2001.
- [79] I. Lope, J. Acero and C. Carretero, I. Lope, J. Acero and C. Carretero, "Analysis and optimization of the efficiency of induction heating applications with litz-wire planar and solenoidal coils," *IEEE Trans. Power Electronics*, vol. 31, no. 7, pp. 5089-5101, July 2016.
- [80] Zhang, S. C. Wong, C. K. Tse and Q. Chen, "Design for efficiency optimization and voltage controllability of series-series compensated inductive power transfer systems," *IEEE Trans. Power Electronics*, vol. 29, no. 1, pp. 191-200, Jan. 2014.
- [81] S. Raabe and G. A. Covic, "Practical design considerations for contactless power transfer quadrature pick-ups," *IEEE Trans. Industrial Electronics*, vol. 60, no. 1, pp. 400-409, Jan. 2013.
- [82] Y. Zhang, T. Lu, Z. Zhao, F. He, K. Chen and L. Yuan, "Selective wireless power transfer to multiple loads using receivers of different resonant frequencies," *IEEE Trans. Power*

- Electronics*, vol. 30, no. 11, pp. 6001-6005, Nov. 2015.
- [83] W. Zhang, J. C. White, A. M. Abraham and C. C. Mi, "Loosely coupled transformer structure and interoperability study for EV wireless charging systems," *IEEE Trans. Power Electronics*, vol. 30, no. 11, pp. 6356-6367, Nov. 2015.
- [84] R. Bosshard, U. Iruretagoyena and J. W. Kolar, "Comprehensive evaluation of rectangular and double-D coil geometry for 50 kW/85 kHz IPT system," *IEEE Journal of Emerging and Selected Topics in Power Electronics*, vol. 4, no. 4, pp. 1406-1415, Dec. 2016.
- [85] EPCOS. Manual. September, 2009. [Online] Available: <https://en.tdk.eu/download/528866/f41b4c91d03b93ec92d9d5db65741d50/pdf-n95.pdf>.
- [86] E. Waffenschmidt, "Homogeneous magnetic coupling for free positioning in an inductive wireless power system," *IEEE Journal of Emerging and Selected Topics in Power Electronics*, vol. 3, pp. 226-233, 2015.
- [87] J. A. Ferreira, "Improved analytical modeling of conductive losses in magnetic components," *IEEE Trans. Power Electronics*, vol. 9, no. 1, pp. 127-131, Jan 1994.
- [88] J. Mühlethaler, "Modeling and multi-objective optimization of inductive power components," Ph.D. dissertation, Swiss Federal Inst. Technol. Zurich, ETHZ, Zürich, The Switzerland, 2012.
- [89] Datasheet of Langer EMV LF-R 50, [Online] Available: <http://www.langer-emv.de/en/category/near-field-probes/19>
- [90] R. Erickson and D. Maksimovic, *Fundamentals of Power Electronics*, Springer, 2001.
- [91] P. L. Dowell, "Effects of eddy currents in transformer windings," in *Proc. IEE*, vol. 113, no. 8, pp. 1387-1394, August 1966.
- [92] M. Lu, K. D. T. Ngo, M. Filippa and W. Bicknell, "Model for electromagnetic actuator with

- significant fringing using minimal fitting parameters," *IEEE Trans. Magnetics*, vol. 51, no. 1, pp. 1-7, Jan. 2015.
- [93] A. V. den Bossche and V. C. Valchev, *Inductors and Transformers for Power Electronics*. Boca Raton, FL: CRC Press/Taylor Francis Group, 2005.
- [94] W. A. Roshen and D. E. Turcotte, "Planar inductors on magnetic substrates," *IEEE Trans. Magnetics*, vol. 24, no. 6, pp. 3213-3216, Nov 1988.
- [95] J. Muhlethaler, M. Schweizer, R. Blattmann, J. W. Kolar and A. Ecklebe, "Optimal design of LCL harmonic filters for three-phase PFC rectifiers," *IEEE Trans. Power Electronics*, vol. 28, no. 7, pp. 3114-3125, July 2013.
- [96] M. Curti, J. J. H. Paulides and E. A. Lomonova, "An overview of analytical methods for magnetic field computation," in *Proc. International Conference on Ecological Vehicles and Renewable Energies*, Monte Carlo, 2015, pp. 1-7.
- [97] J. C. Maxwell, *A Treatise on Electricity and Magnetism*, Oxford: Clarendon Press, 1873.
- [98] S. Ramo, J. R. Whinnery and T. Van Dum, *Fields and Waves in Communication Electronics*, New York: Wiley, 1965.
- [99] Datasheet of Ferroxcube 3C96 ferrite material, [Online] Available: <http://www.ferroxcube.com/FerroxcubeCorporateReception/datasheet/3c96.pdf>.
- [100] K. Jiseong, K. Jonghoon, K. Sunkyu, K. Hongseok, S. In-Soo, S. Nam Pyo, et al., "Coil design and shielding methods for a magnetic resonant wireless power transfer system," in *Proc. IEEE*, vol. 101, pp. 1332-1342, 2013.
- [101] Y. H. Sohn, B. H. Choi, E. S. Lee and C. T. Rim, "Comparisons of magnetic field shaping methods for ubiquitous wireless power transfer," in *Proc. IEEE PELS Workshop on Emerging Technologies: Wireless Power*, Daejeon, 2015, pp. 1-6.

Reference

- [102] T. Campi, S. Cruciani and M. Feliziani, "Magnetic shielding of wireless power transfer systems," in *Proc. International Symposium on Electromagnetic Compatibility, Tokyo, Tokyo, 2014*, pp. 422-425.
- [103] M. Lu and Khai D. T. Ngo, "Attenuation of stray magnetic field in inductive power transfer by controlling phases of windings' currents", *IEEE Trans. Magnetics*, vol. PP, no. 99, pp. 1-1.